

NKS-450  
ISBN 978-87-7893-542-7

---

Thermal Hydraulic Phenomena  
of the Suppression Pool  
Summary of 2020 activities

Pavel Kudinov<sup>1</sup>  
Xicheng Wang<sup>1</sup>  
Dmitry Grishchenko<sup>1</sup>  
Markku Puustinen<sup>2</sup>  
Antti Räsänen<sup>2</sup>  
Eetu Kotro<sup>2</sup>  
Kimmo Tielinen<sup>2</sup>  
Lauri Pyy<sup>2</sup>  
Timo Pättikangas<sup>3</sup>  
Ari Silde<sup>3</sup>  
Jouni Syrjänen<sup>3</sup>

<sup>1</sup>Division of Nuclear Engineering, Kungliga Tekniska Högskolan (KTH)  
Sweden

<sup>2</sup>Lappeenranta-Lahti University of Technology (LUT)  
Finland

<sup>3</sup>VTT Technical Research Centre of Finland Ltd

August 2021

## Abstract

Effective Momentum Source and the Effective Heat Source (EMS/EHS) models for spargers are further developed using source terms, boundary conditions and “unit cell” approaches. The models implemented in Fluent and GOTHIC have been used to support design of the sparger (H2P3) and integral (H2P4) tests series in PANDA facility in HYMERES-2 project. The progress on the image analysis for post processing the data from the SEF-POOL tests is discussed.

Steam injection tests in SEF-POOL facility at LUT University were carried out to clarify effective momentum behavior at low Mach numbers with a single and multiple hole injections. Small gas bubbles and high speed stereo imaging were used in water and steam injection tests to collect data on the jet entrainment characteristics. Also, high temporal resolution data was collected on the dynamic force measurements created by the steam injection in different regimes.

VTT studied stratification modeling capability of Apros 1D thermalhydraulic model using pseudo-2D nodalization for the PPOOLEX SPA-T3 test. The simulations showed that (i) dense nodalisation is needed to capture the sharp stratification (ii) pool mixing phase could not be predicted reasonably without a tailored to Apros’s approach. The EMS/EHS, volume of fluid (VOF) and k- $\omega$  were combined in the ANSYS Fluent v.19.5 simulation of SPA-T3 test. The simulation underpredicted the mixing of pool water to some degree. When the EMS/EHS source location was extended for the mixing phase simulation, the mixing improved considerably.

## Key words

Steam Condensation, Pool Stratification, Mixing, Pressure Suppression Pool, Thermal Hydraulic, BWR, Containment, CFD, GOTHIC

NKS-450  
ISBN 978-87-7893-542-7  
Electronic report, August 2021  
NKS Secretariat  
P.O. Box 49  
DK - 4000 Roskilde, Denmark  
Phone +45 4677 4041  
[www.nks.org](http://www.nks.org)  
e-mail [nks@nks.org](mailto:nks@nks.org)



# **Thermal Hydraulic Phenomena of the Suppression Pool Summary of 2020 activities**

## **Final Report from the NKS-THEOS (Contract: NKS\_R\_2020\_130)**

Pavel Kudinov<sup>1</sup>, Xicheng Wang<sup>1</sup>, Dmitry Grishchenko<sup>1</sup>  
Markku Puustinen<sup>2</sup>, Antti Räsänen<sup>2</sup>, Eetu Kotro<sup>2</sup>, Kimmo Tielinen<sup>2</sup>, Lauri Pyy<sup>2</sup>  
Timo Pättikangas<sup>3</sup>, Ari Silde<sup>3</sup>, Jouni Syrjänen<sup>3</sup>

<sup>1</sup>Division of Nuclear Engineering, Kungliga Tekniska Högskolan (KTH),

<sup>2</sup>Lappeenranta-Lahti University of Technology (LUT),

<sup>3</sup>VTT Technical Research Centre of Finland Ltd

## Table of contents

1.	Introduction .....	3
1.1.	BACKGROUND .....	3
1.2.	MOTIVATION AND GOALS FOR THE THEOS PROJECT .....	4
2.	Description of activities in 2020 .....	5
2.1.	SUMMARY OF ACTIVITIES AT KTH.....	5
2.2.	SUMMARY OF ACTIVITIES AT LUT .....	7
2.3.	SUMMARY OF ACTIVITIES AT VTT .....	8
3.	References .....	12

### Appendix A:

Development of the EHS/EMS models and analytical support to PANDA and SEF-POOL experiments

### Appendix B:

SEF-POOL tests on jet entrainment

### Appendix C:

Modelling of thermal stratification in suppression pool using the Apros thermahydraulic model

### Appendix D:

CFD study of condensation test SPA-T3 in PPOOLEX test vessel with VOF, k- $\omega$  turbulence and EMS/EHS condensation models

## 1. Introduction

### 1.1. Background

Containment is the last physical barrier that prevents the release of radioactive fission products into the environment. Boiling Water Reactors (BWR) employ a large water pool (Pressure Suppression Pool (PSP)) to condense steam released from the primary coolant system [1]. The PSP is used in accidents and in normal operation to control the pressure of the reactor vessel. It also serves as a water source for the Emergency Core Cooling System (ECCS), containment spray, and as a scrubber in case of a core damage accident with release of radioactive aerosols.

A thermally stratified pool has a higher temperature at the surface compared to a completely mixed pool with the same averaged temperature. The pool surface temperature determines the steam partial pressure in the containment gas space, while the bottom layer of the pool might remain cold. Higher pool temperature results in higher partial pressure of steam in the containment atmosphere and respectively to higher total containment pressure. If water temperature at the steam injection point is close to saturation, condensation can be very violent leading to large dynamic loads. If saturation conditions are reached in the vicinity of the steam injection, steam can bypass the pool without condensation. Thus, thermal stratification reduces pressure suppression capacity of the pool. For instance, containment pressure in Fukushima Daiichi Unit 3 accident was increasing much faster than the prediction done with the assumption of completely mixed PSP [7, 8].

There are several scenarios of where the PSP operation can be affected by interactions between (i) stratification and mixing phenomena, (ii) operation of emergency core cooling systems (ECCS), spray, residual heat removal system (RHR), (iii) water balance in the containment compartments, and (iv) pool behavior diagnostics and emergency operation procedures. Those scenarios include (i) different LOCAs scenarios e.g. with steam line break inside the radiation shield, broken blowdown pipes, and leaking safety relief valves (SRV); (ii) station blackout; (iii) severe accidents.

In a BWR, steam can be injected into the pool through blowdown pipes (in case of LOCA) and spargers [2]. The blowdown pipes connect the drywell to the wetwell and play an important role in LOCA accidents. Spargers connect the primary coolant system to the wetwell pool, inject steam through multiple small holes, and are used to control the pressure in the vessel. Direct Contact Condensation (DCC) of steam injected into a water pool is as a source of heat and momentum. A competition between these sources determines whether the PSP will be thermally stratified or mixed [3, 4]. Momentum depends on the steam condensation regime e.g. chugging, oscillatory bubbles, and stable jets. If steam injection results in a low momentum source incapable to overcome buoyancy forces, the heat can be deposited in the layer above the injection point, while water below remains cold [5, 6]. If steam injection results in a higher momentum source, it can lead to the development of a large scale circulation in the pool which can erode or even break the stratification [5, 6].

Validated codes are needed for the simulation of realistic accident scenarios that can adequately resolve the interplay between phenomena, safety systems and operational

procedures. However, the prediction of thermal stratification and mixing in a PSP remains a challenging task due to the lack of models for direct contact condensation phenomena [9, 10, 11] that could be effectively used to simulate large-scale pools with numerous steam injection devices operated during long-term transients.

Effective Heat Source (EHS) and Effective Momentum Source (EMS) models [3, 4, 12] have been proposed at KTH to enable the prediction of thermal stratification and mixing phenomena in a BWR containment and pressure suppression pool. The EHS/EMS models have been under development for steam injection through the blowdown pipes [3, 4, 12, 13, 14, 16, 17, 18, 19, 20, 21, 22, 23, 24, 25, 26] and the spargers [27, 28, 29, 30, 31, 32, 33, 34]. The models provide a computationally affordable approach by exploiting the gap between the spatial and temporal scales of the large pool and direct contact condensation phenomena. The models postulate that the effects of steam injection on the development of thermal stratification and mixing in a large pool can be predicted using only “effective”, i.e. time and space averaged, sources of heat and momentum created by steam injection without explicit resolution of the steam/water interfaces. The development of the EHS/EMS models was greatly supported by cooperation with the experimental teams first at Lappeenranta University of Technology (LUT) in the framework of NKS and NORTHNET RM3 projects and then with the Paul Scherrer Institute (PSI) in the framework of OECD/NEA HYMERES and HYMERES-2 projects.

## **1.2. Motivation and goals for the THEOS project**

Validation of the EHS/EMS models was done by KTH using experimental data from the PPOOLEX and SEF-POOL facilities at LUT, Finland, and the PANDA facility at PSI, Switzerland. The validated models have been applied to analysis of steam injection through spargers in a full-scale Nordic BWR Pressure Suppression Pool (PSP). The results show that strong thermal stratification of potential safety importance can develop in the pool during prototypic steam injection conditions. The analysis results suggest that further development of the EHS/EMS correlations and computational models are necessary in order to enable modeling of regimes and conditions, which have not yet been studied in experiments, but are critically important and can completely change the PSP stratification and mixing behavior. More specifically, non-condensable gases in case of steam injection through blowdown pipes can affect chugging phenomena and thus pool mixing. Steam injection regimes through spargers, azimuthal velocity distribution and turbulence generated at the sparger head and the effect of the load reduction rings are also very influential factors according to the analysis. The effects of other safety systems such as sprays and strainers have not been addressed in the experiments. In this project, KTH will provide analytical support for the new tests in the SEF-POOL and PPOOLEX facilities at LUT and in the PANDA facility at PSI (in the framework of the OECD/HYMERES-2 project). Obtained experimental data will be used by KTH for the development and validation of the models in order to address the remaining important sources of uncertainty for prediction of the pool behavior.

A set of experiments with spargers were performed in the PPOOLEX facility at LUT. The experiments were mainly focused on the oscillatory bubble regime, and exploratory tests were done in chugging and stable jet regimes. The experimental data were used by KTH to address important phenomena governing the pool behavior and to validate the computational models. A small-scale Separate Effect Facility (SEF-POOL) was built to measure directly the effective momentum induced by steam injection through a sparger. The tests provided a possibility to

quantify the effective momentum correlations that are used in the simulations performed at KTH and a validation effort of CFD models at VTT. Important variables affecting the effective momentum magnitude in full-scale plant need to be further analyzed in order to provide closures for the EMS model development for spargers by KTH. Furthermore, data on direct contact condensation gathered with the help of sophisticated instrumentation is needed for the improvement of calculation models of CFD codes at VTT. For this purpose, further development of the experimental facilities for obtaining systematic data relevant to PSP phenomena and conditions will be carried out in this project. Particularly, design for new experiments that can address possible effect of initial steam enthalpy to clarify most adequate definition of Jacob number for steam injection conditions, the effect of hole size on the value of Jacob number at which effective momentum reaches its maximum, the entrainment rate for the jet created by steam injection and respective effect of momentum distribution in azimuthal direction, turbulence generated by steam condensation and chugging regimes in spargers will be developed. Feasibility of a new experimental campaign in the PPOOLEX facility will be evaluated, considering remaining uncertainties in the phenomena such as the effect of spray activation in the drywell and/or wetwell on a thermally stratified pool, the combined effect of sparger head and load reduction rings, etc.

Computational Fluid Dynamics (CFD) simulations will be performed by VTT for the direct-contact condensation and thermal stratification experiments of LUT. The simulations will be done by using the commercial ANSYS Fluent code. The EHS/EMS models developed at KTH will be implemented in the Fluent code by using user-defined functions. In the model, the sparger of the vent pipe in the pressure suppression pool will be described with mass, heat and momentum sources. Simulations of stratification and mixing experiments performed with the PPOOLEX facility will be performed with the Fluent code. The results will be compared to the experiments of LUT and to the results calculated by KTH. In addition, possibilities to implement an approach based on the EHS/EMS model in the Apros system code will be studied. CFD calculations will be performed to validate the implemented EHS/EMS model for stratification and mixing. In addition, the implementation of the approaches based on the EHS/EMS model in the Apros system code will be tested.

## **2. Description of activities in 2020**

### **2.1. Summary of activities at KTH**

Detailed description of the project activities at KTH is provided in the Appendix A. KTH is providing analytical support to SEF-POOL and PANDA tests in order to select the most important parameters for the model development and the validation conditions and to provide necessary measurement systems. Further development and validation of the EHS/EMS models for spargers is ongoing in order to: (i) include the effect of Jacob and Mach numbers on the effective momentum rate in subsonic and sonic injection regimes (ii) include jet entrainment rate in the definition of the momentum profile around the sparger head, (iii) to implement revised EMS model for the load reduction rings and (iv) to further develop the Richardson correlation for predicting the erosion velocity of the cold stratified layer.

In this report we describe the progress achieved in addressing main technical tasks, i.e.: (i) development validation of the EHS/EMS models for spargers using OECD/HYMERES-1

PANDA HP5 test series; (ii) pre-test analysis in support of the experimental for SEF-POOL facility at LUT and PANDA facility at PSI; (iii) post-test analysis using the new test data.

In Section 3 of the Appendix A we provide an overview of the work on direct contact condensation, pool stratification/mixing phenomena and modeling approaches. The progress and the need for further development of the EHS/EMS models for spargers is described in Sections 4 of the Appendix A. Two approaches to the EMS model implementation are discussed (i) based on the source terms in the momentum equation and (ii) using boundary conditions for liquid velocity. Advantages and disadvantages of both approaches are discussed in detail. Results of the EHS/EMS models implemented using a source term approach suggest that the temperature evolutions are sensitive to the geometrical characteristics of the domains where the EHS/EMS source terms are introduced. Validation of the EHS/EMS model using steam condensation region (SCR) approach against PANDA HP5 tests suggest that this model can provide a reasonably accurate prediction of the pool behavior while avoiding uncertainty in the distribution of the momentum source.

In Section 5 of Appendix A results of “Unit Cell” (where individual injection hole is modelled individually) EHS/EMS model development and validation are discussed against PPOOLEX SPA-T3 test. The model can provide a reasonably accurate prediction of the pool behavior. Downward angles of the jets are estimated using the internal sparger flow simulations and then assessed using the temperature evolutions the thermocouple (TC) mesh measurements. Increased turbulence intensity induced by the steam condensation is modelled by either adding an extra source of  $k$  in the transport equation or providing turbulence in the boundary conditions.

In Section 6 of Appendix A application of the developed EHS/EMS models to pre-test analysis in support of the PANDA H2P3 tests with sparger injection are presented. Scoping calculations were carried out to specify geometrical setup (pool depth, elevation of the sparger and number of open LRR holes), initial pool temperature, injection procedures, arrangement of thermocouples, PIV setup, for sparger tests (H2P3-1,2,3) and LRR tests (H2P3-4,5,6).

In Section 7 of the Appendix A we present results of the pre-test analysis of the integral H2P4 test series in PANDA facility. The aim of the tests is to study the effect of pool stratification and mixing phenomena on containment pressurization. Results of the analysis are used for the selection of the test configuration, i.e. the vessels to be used and connections between them, water pool level, duration and mass flow rates for different injection phases. Results of the analysis suggest that it is feasible to achieve prototypic levels of pressurization during a reasonable time for the tests.

In Section 8 of the Appendix A the progress in development of the image analysis for the post-processing of the data from the SEF-POOL tests are presented. Gas bubbles are used in the tests in order to visualize water velocity in the vicinity of the jet induced by steam injection. The first data from the analysis of the bubbles rise in a stagnant pool was obtained and results are being analyzed. The current work is focused on the further analysis of the bubble flow during steam injection and the data from SEW-W7 and W8 tests with water jets is being processed. Further work will aim to optimize (i) experimental setup to resolve several issues related to the bubble formation and size, and (ii) image analysis and the development of reliable approach to the estimation of flow velocity and entrainment rate.

## 2.2. Summary of activities at LUT

Detailed description of the project activities at LUT University is provided in the Appendix B. Prediction of the effective momentum induced by the oscillatory bubble and oscillatory cone jet regimes is necessary for the modelling of the pool behavior. This is especially relevant for BWRs, where the development of thermal stratification or mixing during a steam injection through spargers can affect the performance of the suppression pool. In order to directly measure the effective momentum, the SEF-POOL facility was built at LUT University and an extensive test series is being carried out. The reference system for the SEF-POOL facility is an SRV sparger pipe of a BWR plant. Hence, the facility is designed in such a way that discharge of steam through the injection holes at the sparger lower end into the sub-cooled pool water can be simulated representatively.

The analysis of the previous tests by KTH has shown that oscillatory bubble motions are a very efficient mechanism of transferring the force from the steam to the mean liquid flow. The test results have been helpful for the understanding of the key effects and factors that can be neglected when the EMS/EHS models are developed further.

The main goal of the SEF-POOL tests in 2020 was to provide data on the characteristics of the small-scale phenomena, which affect the effective heat and momentum sources in case of steam injection through a sparger into a sub-cooled pool of water. Furthermore, the SEF-POOL tests support the validation effort of the DCC and interfacial area models of CFD codes for steam injection through spargers at VTT and LUT. Particular interest in the 2020 tests was in capturing good-quality high-speed camera stereo recordings of the steam jet behavior and jet entrainment visualized with the help of air bubbles injected into the pool.

Six steam injection tests were performed in the SEF-POOL facility in 2020. In addition, two water injection tests were performed. The main varied parameter was the mass flux of injected steam. The possible effect of multiple injection holes was also studied further by using a three-hole plate in some of the tests. The water injection tests were done in order to check the operation of the air bubble generator and to find the suitable camera imaging parameters and lighting conditions so that KTH can effectively use their in-house tools in the analysis of the recordings for tracking the movement of the air bubbles and thus ultimately assess the liquid velocity and the amount of jet entrainment.

The test matrix in 2020 contained tests both with a single-hole and three-hole injection plate configuration. Steam injection with the same steam mass flux through a three-hole plate produce slightly larger force measurement values than injection through a single-hole plate. However, effective momentum was significantly lower in three-hole injection. In addition, in the three-hole case the measured force curve reached its peak value at the pool temperature of about 60 °C and then turned very slightly downwards while in the single-hole case the peak occurred at the pool temperature of about 80 °C.

Earlier single-hole tests in SEF-POOL had revealed that in sub-sonic injection cases high subcooling of the pool water has an effect on the shape of the force curve. When steam injection is started, the measured force starts to follow a bending curve (instead of immediately jumping up). After the pool water temperature reaches 20 °C, the force curve starts to follow a more linear, slightly increasing trend. The tests in 2020 confirmed that the same kind of force curve shape can be found with sub-sonic injection also in the three-hole

configuration. In the single-hole sonic injection cases tested in 2019, the bending shape of the force curve was not observed. Sonic tests with the three-hole injection plate have not been done so far.

As the sub-cooling of the pool water decreases, the size of the forming steam bubbles increases. The high-speed video clips reveal that at low sub-cooling detached bubbles can move a long distance from the injection hole and allow the formation of a new bubble before they collapse. Close to saturation conditions a new developing bubble can catch up with the previous detached bubble, which has not condensed completely yet, collide with it and even merge with it.

Both in the single-hole and three-hole tests done with the smallest steam injection rate incomplete condensation occurred as the pool temperature approached saturation conditions. The forming steam bubbles were large in size and they started to rise upwards due to buoyancy forces even when they were still attached to the injection plate. The detached bubbles continued the rising movement and seemed to reach the pool surface before they collapsed. In these cases, the steam flow velocity was so small that the forming steam bubbles slowed down and they were unable to travel horizontally far from the injection plate. Instead, the buoyancy forces took control and started to lift the bubbles upwards.

Violent shaking of the sparger piping had been observed in the earlier tests as the pool water was heated over 80 °C. In the three-hole cases, this happened even with a little bit lower pool water temperature. To analyze the phenomenon in more detail GoPro and Canon EOS video clips were captured from the SEF-S34 test and delivered to KTH.

The most important outcome of the 2020 tests was the successful refining of the air bubble generator configuration and the high-speed camera set-up. Two water injection tests were carried out for this purpose. On the basis of the feedback from KTH the operation of the air injector was fine-tuned and optimal parameters for stereo imaging were selected so that the movement of the air bubbles can be tracked and finally, the liquid velocity and the amount of jet entrainment can be assessed. Additional bubble parameters, which will be estimated through the image processing of the high-speed videos of the SEF-POOL tests by KTH, include the collapse and bubble life frequencies, maximum bubble radius, bubble velocities, pressure gradients, and heat transfer coefficients.

### **2.3. Summary of activities at VTT**

Detailed description of the project activities at VTT on model development and validation is provided in the Appendix C and D for Apros and CFD respectively.

KTH has developed and validated the Effective Heat Source (EHS) and the Effective Momentum Source (EMS) models for providing computational efficiency and sufficient accuracy in the modelling of pool stratification effects. The previous work at VTT studied and summarized the prerequisites of the Apros lumped parameter containment model and thermohydraulic model for simulating stratification phenomena of suppression pool. Also the possibility to implement the EHS/EMS model in Apros was considered. The summary of the work was that the EHS/EMS model is not directly applicable in Apros LP modelling, but could possibly be utilized in the stratification calculation when using the Apros thermohydraulic model. However, the concern was that the Apros thermohydraulic model



applies to 1D flow solution, whereas the EHS/EMS model is developed to be coupled with 2D or 3D flow solver.

The goal of this work was to study stratification modeling capability of Apros 1D thermohydraulic model using so called pseudo-2D nodalisation. The PPOOLEX stratification test SPA-T3 was simulated. The sensitivity studies included e.g. the effect of nodalisation concept, loss coefficient, direction of momentum transfer from steam source, discretization scheme and steam mass flow during the pool mixing phase.

The simulation results show that the pool stratification phase was predicted well when the 2-column nodalisation was used. Sufficiently dense nodalisation is needed to capture the real sharp stratification, because the temperature is calculated as function of the solved enthalpy which still represents the average enthalpy of the node. The best agreement was obtained when using the higher order discretisation scheme for enthalpy solution and the larger loss coefficient for the horizontal branches than for the vertical ones.

The results also showed that the pool mixing phase could not be predicted reasonably. If the nodalisation is very coarse, pool mixing takes place, but it is then mostly caused by numerical diffusion or inaccuracy in modelling the real sharp stratification thermocline.

Sensitivity study showed that a significant increase in the steam mass flow (and momentum) did not improve the predicted pool mixing. Therefore, implementation of the EHS/EMS model in Apros would not probably solve alone the deficiencies found in the mixing calculation. Maybe the EHS/EMS approach should be modified or totally different approach should be tailored to the Apros's need in order to model better the pool stratification/mixing phenomena.

The Shah condensation correlation of Apros, which is the default correlation, could not model realistically the steam condensation in the pool. The Chen correlation without Vierow-Schrock correction seemed to predict reasonably well the steam condensation inside the water pool.

The stratification and mixing phases of the SPA-T3 condensing test performed in the PPOOLEX test vessel were simulated with the CFD software ANSYS Fluent v.19.5 using the volume of fluid (VOF) model for free surface and  $k-\omega$  turbulence model. The VOF model was included to describe the water surface elevation and to improve the heat transfer on the water surface, which were noted in the earlier simulation (Pättikangas, 2020). The steam jets of the SPA-T3 test were modelled with the effective momentum source and the effective heat source (EMS/EHS) models, which simplify the CFD modelling task and saves computational resources.

The model combination of EMS/EHS, VOF and  $k-\omega$  was combined in the ANSYS Fluent v.19.5 simulation. The simulation underpredicted the mixing of pool water to some degree. It suggested stronger stratification of temperature both in stratification and mixing phases of the experiment than observed. When the EMS/EHS source location was extended for the mixing phase simulation, the mixing improved considerably.

The weaker than expected mixing might have been caused partly by less accurate discretization schemes, which were used for convergence or compatibility reasons. For future

improvements, convergence might benefit from using polyhedral grid. Also,  $k-\omega$  turbulence model may predict lower level of turbulence and thus weaker heat transfer than  $k-\varepsilon$  model used in the earlier simulation [35]. Extending the EMS/EHS source location, if necessary, could be done in more optimal way. Including heat losses from the steam pipe to the EHS model and through the vessel wall would further improve the model, the latter by enhancing circulation from the top of the vessel to the bottom.

**Acknowledgements**

NKS conveys its gratitude to all organizations and persons who by means of financial support or contributions in kind have made the work presented in this report possible. The support from the Finnish nuclear safety program, the SAFIR2022-program, the Swedish Radiation Safety Authority for the work is gratefully acknowledged.

**Disclaimer**

The views expressed in this document remain the responsibility of the author(s) and do not necessarily reflect those of NKS. In particular, neither NKS nor any other organization or body supporting NKS activities can be held responsible for the material presented in this report.

### 3. References

1. Pershagen, B., 1994. Light Water Reactor Safety. Pergamon Press.
2. Lahey, R.T., Moody, F.J., 1993. The Thermal Hydraulics of a Boiling Water Nuclear Reactor, 2nd edition, American Nuclear Society, La Grange Park, Ill, USA.
3. Li, H., Kudinov, P., 2010. Effective Approaches to Simulation of Thermal Stratification and Mixing in a Pressure Suppression Pool. OECD/NEA & IAEA Workshop CFD4NRS-3, Bethesda, MD, USA, September 14-16, 2010.
4. Li, H., Villanueva, W., Kudinov, P., 2014. Approach and Development of Effective Models for Simulation of Thermal Stratification and Mixing Induced by Steam Injection into a Large Pool of Water. Science and Technology of Nuclear Installations, 2014, Article ID 108782, 11 pages.
5. Laine, J., Puustinen, M., Räsänen, A., 2013. PPOOLEX experiments on the dynamics of free water surface in the blowdown pipe. Nordic Nuclear Safety Research, NKS-281.
6. J. Laine, M. Puustinen, A. Räsänen, PPOOLEX Experiments with a Sparger, Nordic Nuclear Safety Research, 2015, NKS-334.
7. Mizokami, S., Yamada, D., Honda, T., Yamauchi, D., Yamanaka, Y., 2016. Unsolved issues related to thermal-hydraulics in the suppression chamber during Fukushima Daiichi accident progressions. Journal of Nuclear Science and Technology, 53, 630-638.
8. Mizokami, S., Yamanaka, Y., Watanabe, M., Honda, T., Fuji, T., Kojima, Y., PAIK, C.Y., Rahn, F., 2013. State of the art MAAP analysis and future improvements on TEPCO Fukushima-Daiichi NPP accident. NURETH-15: The 15th International Topical Meeting on Nuclear Reactor Thermal Hydraulics, Pisa, Italy, May 12-17, paper number 536.
9. Tanskanen, V., Jordan, A., Puustinen, M., Kyrki-Rajamäki, R., 2014. CFD simulation and pattern recognition analysis of the chugging condensation regime. Annals of Nuclear Energy, 66, 133-143.
10. Patel, G., Tanskanen, V., Hujala, E., Hyvärinen, J., 2017. Direct contact condensation modeling in pressure suppression pool system. Nuclear Engineering and Design, 321, 328-342.
11. Pellegrini, M., Naitoh, M., 2016. Application of two-phase flow DFC to the phenomena expected in Fukushima Daiichi S/C. OECD/NEA & IAEA Workshop CFD4NRS-6.
12. Li, H., Villanueva, W., Puustinen, M., Laine, J., Kudinov, P., 2014. Validation of Effective Models for Simulation of Thermal Stratification and Mixing Induced by Steam Injection into a Large Pool of Water. Science and Technology of Nuclear Installations, 2014, Article ID 752597, 18 pages.
13. Li, H., Villanueva, W., Puustinen, M., Laine, J., Kudinov, P., 2017. Thermal stratification and mixing in a suppression pool induced by direct steam injection. Annals of Nuclear Energy, 111, 487-498.
14. Villanueva, W., Li, H., Puustinen, M., Kudinov, P., 2015. Generalization of experimental data on amplitude and frequency of oscillations induced by steam injection into a subcooled pool. Nuclear Engineering and Design, 295, 155-161.
15. Li, H. and Kudinov, P., 2009. An Approach to Simulation of Mixing in a Stratified Pool with the GOTHIC code. ANS Transactions, paper 210976.
16. Li, H., Villanueva, W., Kudinov, P., 2011. Development and implementation of effective models in GOTHIC for the prediction of mixing and thermal stratification in a BWR pressure suppression pool. Proceedings of ICAPP 2011, Nice, France, May 2-5, 2011, Paper 11256.

17. Li, H. and Kudinov, P., 2008. An approach toward simulation and analysis of thermal stratification and mixing in a pressure suppression pool. NUTHOS-7, Seoul, Korea, October 5-9, Paper 243.
18. Gallego-Marcos, I., Villanueva, W., Kudinov, P., 2018. Modelling of Pool Stratification and Mixing Induced by Steam Injection through Blowdown Pipes. *Annals of Nuclear Energy*, 112, 624-639.
19. Li, H. and Kudinov, P., 2009. Condensation, Stratification and Mixing in a Boling Water Reactor Suppression Pool. NORTHNET Roadmap 3 Report, Division of Nuclear Power Safety, Royal Institute of Technology (KTH), Stockholm, Sweden, 70p.
20. Li, H., Villanueva, W., Kudinov, P., 2010. Investigation of containment behavior with activation of rupture disks in system 361/362 with GOTHIC simulation. Swedish Radiation Safety Authority (SSM) Project Report, Royal Institute of Technology (KTH), Stockholm, Sweden, 25p.
21. Li, H., Kudinov, P., Villanueva, W., 2010. Modeling of Condensation, Stratification and Mixing Phenomena in a Pool of Water. NKS Report, NKS-225, Division of Nuclear Power Safety, KTH, Stockholm, Sweden, 91p.
22. Li, H., Kudinov, P., Villanueva, W., 2010. Condensation, Stratification and Mixing in a Boling Water Reactor Suppression Pool. NORTHNET Roadmap 3 Report, Division of Nuclear Power Safety, Royal Institute of Technology (KTH), Stockholm, Sweden, 88p.
23. Li, H., Villanueva, W., Kudinov, P., 2012. Development, Implementation and Validation of EHS/EMS Models for Spargers. Westinghouse project report. Division of Nuclear Power Safety, Royal Institute of Technology (KTH), Stockholm, Sweden, 98p.
24. Li, H., Villanueva, W., Kudinov, P., 2012. Effective Momentum and Heat Flux Models for Simulation of Stratification and Mixing in a Large Pool of Water. NKS-ENPOOL Research report, NKS-266, 58p.
25. Li, H., Villanueva, W., Kudinov, P., 2012 Effective Models for Prediction of Stratification and Mixing Phenomena in a BWR Suppression Pool. NORTHNET Roadmap 3 Report, Division of Nuclear Power Safety, Royal Institute of Technology (KTH), Stockholm, Sweden, 87p.
26. Li, H., Villanueva, W., Kudinov, P., 2014. Effective Models for Simulation of Thermal Stratification and Mixing Induced by Steam Injection into a Large Pool of Water. Nordic Nuclear Safety Research, NKS-316.
27. Gallego-Marcos, I., Villanueva, W., Kapulla, R., Paranjape. S., Paladino, D., Kudinov, K., 2016. Modeling of thermal stratification and mixing induced by steam injection through spargers into a large water pool. OECD/NEA & IAEA Workshop CFD4NRS-6, Cambridge, MA, USA, September 13-15.
28. Gallego-Marcos, I., Villanueva, W., Kapulla, R., Paranjape. S., Paladino, D., Kudinov, K., 2016. Scaling and CFD Modelling of the Pool Experiments with Spargers Performed in the PANDA Facility. NUTHOS-11: The 11th International Topical Meeting on Nuclear Reactor Thermal Hydraulics, Operation and Safety Gyeongju, Korea, October 9-13, N11P0670.
29. Gallego-Marcos, I., Villanueva, W., Kudinov, P., 2016. Scaling of the Erosion of a Thermally Stratified Layer in a Large Water Pool during a Steam Injection Through Spargers. NUTHOS-11: The 11th International Topical Meeting on Nuclear Reactor Thermal Hydraulics, Operation and Safety, Gyeongju, Korea, October 9-13, N11P0525.
30. Gallego-Marcos, I., Villanueva, W., Kudinov, P., 2016. Modeling of Thermal Stratification and Mixing in a Pressure Suppression Pool Using GOTHIC. NUTHOS-11: The 11th International Topical Meeting on Nuclear Reactor Thermal Hydraulics, Operation and Safety, Gyeongju, Korea, October 9-13, N11P0524.

31. Gallego-Marcos, I., Villanueva, W., Kudinov, P., et al., 2019. Pool Stratification and Mixing Induced by Steam Injection through Spargers: CFD modeling of the PPOOLEX and PANDA experiments. *Nuclear Engineering and Design*, 347, 67-85.
32. Gallego-Marcos, I., Filich, L., Villanueva, W., Kudinov, P., 2015. Modelling of the Effects of Steam Injection through Spargers on Pool Thermal Stratification and Mixing. NKS Report 347.
33. Gallego-Marcos, I. Villanueva, W., Kudinov, P., 2016. Thermal Stratification and Mixing in a Large Pool Induced by Operation of Spargers, Nozzles, and Blowdown Pipes". NKS Report 369.
34. Gallego-Marcos, I., Villanueva, W., Kudinov, P., 2017. Modelling of a Large Water Pool during Operation of Blowdown Pipes, Spargers, and Nozzles. NKS-393.
35. Pättikangas, T. 2020. CFD analysis of pressure suppression pool by using effective heat and momentum source models, VTT Technical Research Centre of Finland, Research report VTT-R-00228-20.

## **Appendix A**

### **Development of the EHS/EMS models and analytical support to PANDA and SEF-POOL experiments**



**Development of the EHS/EMS models and analytical  
support to PANDA and SEF-POOL experiments**

**Project: Thermal Hydraulics of the Suppression Pool  
NKS-THEOS  
(Contract: NKS\_R\_2020\_130)**

Xicheng Wang, Dmitry Grishchenko, Pavel Kudinov

Royal Institute of Technology (KTH),  
Division of Nuclear Engineering  
Roslagstullsbacken 21, 106 91 Stockholm, Sweden

June 2021  
Stockholm





## Table of contents

1. INTRODUCTION .....	6
2. GOALS AND TASKS .....	12
3. STATE OF THE ART REVIEW .....	13
3.1. Experiments on direct contact condensation .....	13
3.2. Experiments on pool behavior .....	14
3.3. Modelling approaches .....	14
3.4. EHS/EMS models .....	15
4. DEVELOPMENT OF EHS/EMS MODELS FOR SPARGER .....	17
4.1. Introduction of PANDA HP5 tests .....	17
4.2. Calibration of the EHS/EMS models implemented using source terms .....	18
4.2.1. EHS/EMS models for spargers by source terms .....	18
4.2.2. Calibration of the EHS/EMS models .....	23
4.3. Development of EHS/EMS models using SCR approach .....	25
4.3.1. Single-phase turbulent jets .....	26
4.3.2. SCR model for a single jet induced by steam injection .....	27
4.3.3. Comparison of analytical and CFD results for single jet flow .....	28
4.3.4. SCR model for multiple condensed jets .....	31
4.4. Implementation of SCR for spargers in Fluent .....	32
4.4.1. Computational domain .....	32
4.4.2. Lumped velocity profile .....	33
4.4.3. Boundary conditions .....	35
4.4.4. Turbulence model .....	36
4.5. Validation against HP5 tests .....	36
4.6. Summary of EHS/EMS model development for sparger .....	40
5. MODELLING OF STEAM INJECTION THROUGH SPARGER .....	41
5.1. Introduction of PPOOLEX SPA tests .....	41
5.2. Development of EHS/EMMS models using a "Unit Cell" model .....	44
5.2.1. EMSR-BC and EMSR-DS methods .....	44
5.2.2. Effective sources of heat and momentum .....	45
5.2.3. Single-phase turbulent jets .....	46
5.2.4. Comparison of analytical and CFD results for single jet flow .....	47
5.3. Computational domain and boundary conditions .....	50
5.3.1. Computational domain .....	50
5.3.2. Boundary conditions .....	52
5.4. Downward angles .....	53
5.4.1. Internal flow model .....	54
5.4.2. Calibration by TC mesh .....	55
5.5. Turbulence model .....	57
5.5.1. Buoyancy effects on turbulence .....	58
5.5.2. Turbulence induced by steam condensation .....	59

5.5.3. Generalized $k - \omega$ model .....	60
5.5.4. TKE-BC .....	62
5.5.5. TKE distributed source model .....	65
5.6. Validation against PPOOLEX SPA-T3 test .....	69
5.7. Summary of EHS/EMS model development for sparger .....	73
6. PRE-TEST SIMULATIONS FOR PANDA H2P3 TESTS .....	74
6.1. Pre-test simulations for H2P3 spargers tests .....	74
6.1.1. Pool configuration.....	74
6.1.2. Steam injection procedure.....	77
6.1.3. 3D PIV setup.....	78
6.1.4. CFD analysis of velocity field around sparger .....	81
6.1.5. Optimization of the PIV window orientation.....	85
6.2. Pre-test simulations for H2P3 LRR tests .....	88
6.3. Summary of pre-test analysis for H2P3 test series in PANDA facility .....	91
7. PRE-TEST SIMULATIONS FOR PANDA H2P4 TESTS .....	92
7.1. Motivation and background.....	92
7.2. Initial test configuration for the H2P4 series .....	92
7.3. Model setup for H2P4 scoping analysis.....	93
7.4. Model validation .....	95
7.5. Results of the scoping analysis.....	97
7.5.1. Two-vessel configuration with open IPs.....	97
7.5.2. Two-vessel configuration with closed bottom IP .....	100
7.5.2.1. Effect of the water pool depth .....	101
7.5.2.2. Effect of initial water pool temperature.....	103
7.5.2.3. Effect of the hot layer thickness .....	104
7.5.2.4. Effect of steam injection rate.....	106
7.5.2.5. Effect of nozzle spray location .....	106
7.5.3. Pool preconditioning.....	109
7.6. Summary of H2P4 scoping analysis.....	110
8. ANALYSIS OF SEF-POOL TESTS.....	112
8.1. Motivation and background.....	112
8.2. Flow entrainment in round jets .....	112
8.2.1. Relation between axial and radial volumetric flow rate .....	112
8.2.2. Effects of <b>Sk1</b> on entrainment velocity.....	114
8.3. Experimental setup.....	116
8.4. Image calibration and error analysis .....	119
8.5. Entrainment rate analysis .....	121
8.5.1. SEF stagnant pool .....	121
8.5.2. SEF-W7 test analysis .....	124
8.6. Summary of development of image analysis for SEF-POOL experiment.....	132
9. SUMMARY.....	133

ACKNOWLEDGEMENTS.....	135
DISCLAIMER .....	136
REFERENCES.....	137

## 1. INTRODUCTION

Containment is an essential part of the reactor safety design and is the last physical barrier that prevents the release of radioactive fission products into the environment. Boiling Water Reactors (BWR) do not need to accommodate the steam generators used in Pressurized Water Reactors (PWR) and thus can be built with a smaller containment. In Loss-Of-Coolant Accident (LOCA) scenarios large amount of steam is released into the containment from reactor vessel. The smaller volume of the containment can lead to a rapid pressurization. Therefore BWRs utilize a large water pool (Pressure Suppression Pool (PSP)) where steam is condensed [1]. The PSP can be used in normal operation to reduce reactor vessel pressure and can be employed as a passive safety system for storing large amounts of decay heat in long-term transients such as Station Black Outs (SBO). It also serves as a water source for the Emergency Core Cooling System (ECCS), spray, and as a scrubber in case of a core damage accident with release of radioactive aerosols. Advanced PWRs (e.g. AP1000, APR1400, EPR, etc.) have In-containment Refuelling Water Storage Tank (IRWST) that carries out similar functions as the PSP in the BWRs [73].

The PSP and overall containment performance can be affected by physical phenomena such as mixing and stratification. A stratified pool will have higher temperature at the surface compared to completely mixed pool with the same averaged temperature. The pool surface temperature determines the steam partial pressure in the containment gas space. Higher pool temperature results in higher partial pressure of steam in the containment atmosphere and respectively higher total containment pressure, while bottom layer of the pool remains cold. If the water temperature at the steam injection point is close to saturation, condensation can be very violent leading to large dynamic loads. If saturation conditions are reached in the vicinity of the steam injection, steam can bypass the pool without condensation. Thus thermal stratification reduces pressure suppression capacity of the pool.

For instance, containment pressure in Fukushima Daiichi Unit 3 accident was rapidly increasing during the first 12 hours of the operation of the Reactor Core Isolation Cooling (RCIC) system [7, 8]. The system was driven by a steam turbine which exhaust is connected to the pressure suppression pool. The automated protection system shut down the RCIC when the pressure reached 400 kPa. The lumped parameter codes under-estimated the rate of pressure increase and resulting maximum pressure by about 160 kPa using a mixed pool assumption [7]. The underprediction was attributed to the development of thermal stratification in the suppression pool.

There are several scenarios of where PSP operation can be affected by interactions between (i) stratification and mixing phenomena, (ii) operation of emergency core cooling systems (ECCS), spray, residual heat removal system (RHR), (iii) water balance in the containment compartments, and (iv) pool behaviour diagnostics and emergency operation procedures. Those scenarios include (i) different LOCAs scenarios e.g. with steam line break inside the radiation shield, broken blowdown pipes, and leaking safety relief valves (SRV); (ii) station blackout; (iii) severe accidents.

In order to prevent build-up of thermal stratification, some designs (e.g. Nordic BWRs) employ nozzles that inject water into the pool at high momentum. However, as an active system, such nozzles will not be available in case of an SBO scenario and the state of the pool will be determined solely by steam injection phenomena.

In a BWR, steam can be injected into the pool through blowdown pipes (in case of LOCA) and spargers [2]. The large size blowdown pipes connect the drywell to the wetwell, inject steam vertically downwards, and play important role in LOCA accidents. Spargers connect the primary coolant system to the wetwell pool, inject steam through multiple small holes, and are used to control the pressure in the vessel. Direct Contact Condensation (DCC) of steam injected into a water pool is as a source of heat and momentum. A competition between these sources determines whether the PSP will be thermally stratified or mixed [3, 4]. Momentum depends on the steam condensation regime e.g. chugging, oscillatory bubbles, and stable jets. If steam injection results in a low momentum source incapable to overcome buoyancy forces, the heat can be deposited in the layer above the injection point, while water below remains cold [5, 6]. If steam injection results in a higher momentum source, leading to the development of a large scale circulation in the pool which can erode or even break the stratification [5, 6].

Validated codes are needed for simulation of realistic accident scenarios that can adequately resolve the interplay between phenomena, safety systems and operational procedures. However, the prediction of thermal stratification and mixing in a PSP remains a challenging task, due to the lack of models for direct contact condensation phenomena [9, 10, 11] that could be effectively used to simulate large-scale pools with numerous steam injection devices operated during long-term transients.

Effective Heat Source (EHS) and Effective Momentum Source (EMS) models [3, 4, 12] have been proposed to enable the prediction of thermal stratification and mixing phenomena in a BWR containment and pressure suppression pool. The EHS/EMS models have been under development for steam injection through the blowdown pipes [3, 4, 12, 13, 14, 16, 17, 18, 19, 20, 21, 22, 23, 24, 25, 26] and the spargers [27, 28, 29, 30, 31, 32, 33, 34]. The models provide a computationally affordable approach by exploiting the gap between the spatial and temporal scales of the large pool and direct contact condensation phenomena. The models postulate that the effects of steam injection on the development of thermal stratification and mixing in a large pool can be predicted using only “effective”, i.e. time and space averaged, sources of heat and momentum created by steam injection without explicit resolution of the steam/water interfaces.

The development of this models greatly benefited from the cooperation with the experimental teams first at Lappeenranta University of Technology (LUT) in the framework of NKS and NORTHNET RM3 projects and then with the Paul Scherrer Institute (PSI) in the framework of OECD/NEA HYMERES project.

After the Fukushima Daiichi BWRs research community was startled with the realization that some of the containment phenomena that have a significant impact on the accident progression could not be reliably predicted by contemporary safety analysis tools. This realization reignited the international research community with an interest in containment and pool behavior. OECD/NEA HYMERES-1 project (2014-2017) was the first internationally supported effort that addressed pressure suppression pool phenomena in a dedicated HP5 series of experiments in PANDA facility which is a unique, large-scale, multi-purpose facility well instrumented for performing thermal-hydraulics experiments on containment phenomena.

In the HP5 series of the HYMERES-1 project, tests were performed to study “thermal stratification build-up” in a first test phase and “homogenization” in a second test phase in a water pool at different initial temperatures, under the effect of steam venting through a vertical sparger or water injection through a horizontal nozzle. These two phenomena were obtained by varying the steam flow rate. For the lower steam flow rates prevailed thermal stratification

build-up and for the higher flow rate prevailed thermal homogenization of the water pool. In one test a mixture of helium/steam was vented in phase 2 and the homogenization time was drastically reduced. Also for the tests in which water was injected through a horizontal nozzle in phase 2, the water temperature was varied in different tests to enhance either buoyancy or inertia of the water jet.

KTH has started post-test validation of the Effective Heat and Momentum Source (EHS/EMS) models implemented in GOTHIC and CFD code Fluent [27, 28, 29, 30, 31, 32, 33, 34, 36]. The EHS/EMS models were extended to the condensation regimes appearing in spargers. However, more detailed post-test validation revealed potential deficiencies in current modeling approaches. Preliminary results suggest that modeling of the slow erosion of the stratified layer, observed in the PANDA experiments with spargers, requires adequate selection of numerical approaches and modifications in the turbulence modeling with respect to the buoyancy effects. Also, further development, calibration and validation of the EHS/EMS models, especially for steam injection through spargers, would require an extended experimental database. Specifically, more data would be needed in order to clarify:

- The effect of buoyancy forces across the interface of the stratified layer on turbulence;
- Stability of large scale flow structures in the pool.
- Effective momentum induced by steam injection through spargers;
- The effect of non-condensable gases on the pool mixing.

Following the success of the first phase of the OECD/NEA HYMERES-1 project, the second phase (HYMERES-2) project has been initiated (starting from October 2017) and supported by the project partners, including some new members, such as US-NRC. One of the topics of the HYMERES-2 is to address the remaining issues on pressure suppression pool and BWR systems. Specifically, it is proposed

- *“... to extend the database on the pool related phenomena. The test conditions for the new series will be selected based on scoping calculations. The effect of the following parameters will be considered: Height of the pool and depth of the sparger; sparger design including blowdown pipe; BWR containment system tests, which involve the interplay of e.g. Drywell, Wetwell, Reactor Pressure Vessel and components e.g. venting pipes, vacuum breaker, spray, etc. These tests would allow a progressive validation of computational tools dedicated to pool phenomena.”*

With respect to the HP5 series in HYMERES-1, the following parameters could be varied in HYMERES-2:

- Height of the pool and depth of the sparger.
- Sparger design including blowdown pipe.
- BWR containment system tests, which involve the inter-playing of e.g. Drywell, Wetwell, sparger, blowdown pipe, spray, vacuum breakers, etc.

A schematic for the PANDA test configuration addressing the suppression pool is shown in Figure 1. The tests involve the interplay of different compartments e.g. Drywell, Wetwell, RPV and components e.g. venting pipes, vacuum breaker, spray, etc. An example of the PANDA configuration for representing a Main Steam Line Break (MSLB) scenario is shown in Figure 2. The tests would include the,

- Cyclic mixture flow venting from the Drywell to the Wetwell
- Cyclic opening of vacuum breaker and mixture flow returning from the Wetwell to the drywell.

Tests addressing specific open issues related to the Fukushima Daiichi containment behavior identified in the last years including those which arose during the activities of the OECD/NEA Benchmark Scenarios at the Fukushima (BSAF) are also planned to be addressed in the HYMERES-2 project.

It is instructive to note that PSI experimentalist have developed advanced techniques for using particle image velocimetry that can be used in application to the two-phase flows in the pool tests.

As in the first phase of the HYMERES project, the relevance and usefulness of the experimental data for understanding of the Nordic BWR containment phenomena, for model development and validation, will be dependent on the analytical support. KTH has developed a unique team that is leading research in the area of the pressure suppression pool modeling and has experience in guiding experimental research efforts.

The project will contribute to further development and retention of the national expertise in containment thermal hydraulic phenomena and analysis methods. The work will also strengthen SSM and Swedish participation in the international cooperation in the area of containment thermal-hydraulics.

The ultimate aim of the tests and analysis is to make a significant step towards plan applications. In the preliminary discussion with the PANDA operators following topics have been identified as of high potential interest for SSM that can be addressed in the experimental and analytical work in the framework of the HYMERES-2 project.

Two groups of tests are foreseen:

- Integral effect tests (IET)
- Separate effect tests (SET).

***The aims of the IETs are:***

- Observation of the interaction between different
  - phenomena and
  - equipmentin complex scenarios relevant to different accident progression sequences.
- Development and validation of adequate modeling approaches applicable for plant conditions that combine:
  - Reduced numerical resolution.
    - To address the complete containment system behavior.
  - Reliable modeling of the key physical phenomena and equipment

In total ~2 integral tests (plus shake-down and repeatability) are expected to be carried out.

Scenarios of interest for each test are determined by relevancy to:

- LOCA scenarios
- SBO scenarios
  - With possibility of late power recovery.

Issues to be addressed in the tests are relevant to potential effects of

- Vacuum breakers.
- Spray.
- Break location.



- Location of the venting system inlet in the containment.
- Gas phase stratification.
  - Provides a link to the other test series in the projects concerned with gas phase mixing stratification and spray/cooler activation.

on performance of:

- ECCS and spray
- Pressure suppression function.
- Containment venting.
  - Potential for air ingress in the containment
    - activation of non-filtered containment venting
      - at the time when large fraction of non-condensable gases is present in the drywell.
  - Potential effect on aerosols distribution between the drywell and wetwell.
  - Non-condensable gases distribution between drywell and wetwell.

Extensive pre-test analysis with a plant model and a full model of the PANDA facility will be necessary in order to identify potentially important feedbacks and suggest how to address those in the tests.

The integral effect tests are expected to be of direct interest for SSM in interpretation and potential identification of safety issues.

***The aim of the separate effect tests (SETs) is***

- To provide necessary data for development and validation of the separate effect models.

In total about 5-6 SETs on development of stratification and mixing can be carried out using:

- High priority:
  - Sparger.
  - Blowdown pipe.
- Medium priority:
  - Spray – can be included in IET.
- Lower priority:
  - Nozzles.
  - Strainers.

The test conditions will be defined to provide necessary complementary knowledge to existing databases recently produced in the framework of the NKS projects in LUT and in HYMERES-1 project.

This report formulates goals and tasks in Section 2. An overview of previous works on direct contact condensation and pool phenomena and modeling approaches are provided in Section 3. The progress in development of the EHS/EMS models for spargers is described in Sections 4. Application of the developed EHS/EMS models in pre-test analysis for support of PANDA H2P3 tests are presented in Section 6. Pre-test analysis for the integral H2P4 test series in PANDA facility are presented in Section 7. Development of image analysis approach for post-processing the data from the SEF-POOL tests are provided in Section 8.

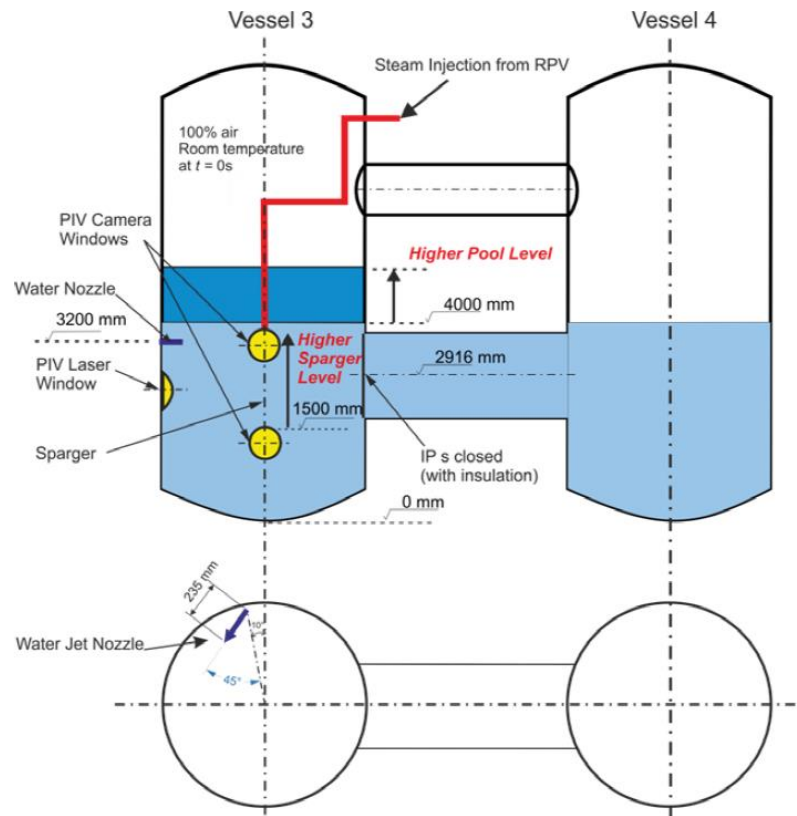


Figure 1: Example for the PANDA test configuration addressing suppression pool.

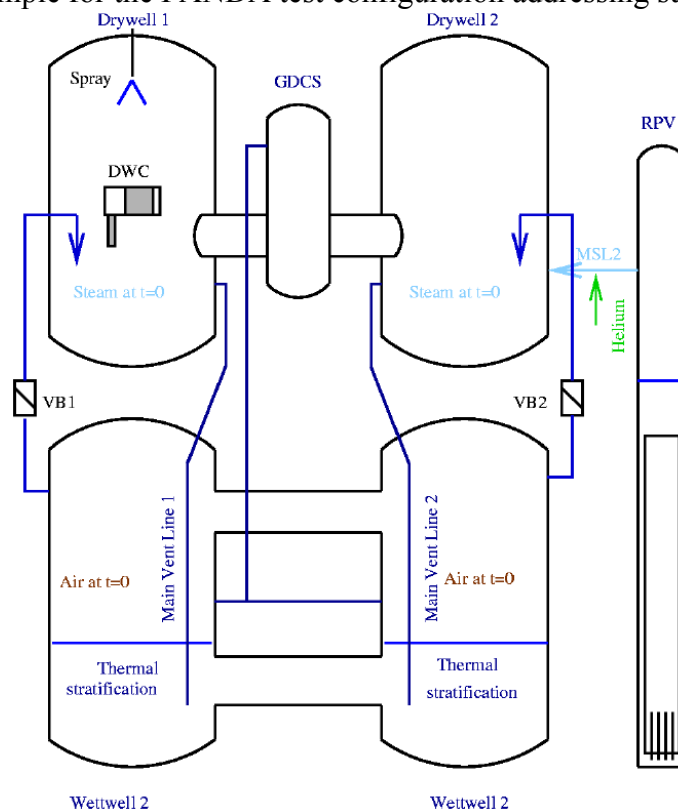


Figure 2: Example for the PANDA test configuration addressing suppression pool.

## **2. GOALS AND TASKS**

**The goal** of the project is to provide pre- and post-test analytical support to the HYMERES-2 and NKS-THEOS experimental activities in order to ensure the success of the tests and maximize the value of the tests for model development and validation.

The following main tasks to be addressed in order to achieve the goal of the project:

- Task-1: To develop EHS/EMS models for spargers and validate them against OECD/HYMERES-1 PANDA HP5 test series.
- Task-2: To provide pre-test analysis in order to support the design and selection of the test conditions for the pressure suppression pool test series in SEF-POOL facility at LUT and PANDA facility at PSI.
- Task-3: To provide post-test analysis for the tests, aiming to develop and further validate predictive capabilities for the pressure suppression pool phenomena.

### 3. STATE OF THE ART REVIEW

The behavior of the pressure suppression pool is affected by a large number of phenomena. This section provides an overview of relevant experimental data and analytical approaches.

#### 3.1. Experiments on direct contact condensation

Sonic and sub-sonic are the two main regimes of steam condensation in a pool. Sonic regimes occur when the injection pressure is about 0.53 times higher than the ambient. The high steam velocity creates large shear between liquid and vapor, which creates highly diffused interfaces before gradually turning into a single-phase jet flow. Sonic regimes are usually referred as “stable regimes” because macroscopic jet parameters such as penetration length, expansion ratio, heat transfer coefficient, etc., remain relatively constant in time. Experiments in [37] that the aforementioned parameters are mainly determined by the steam mass flux, pool subcooling, and diameter of the injection hole [37, 38, 39]. Wu et al. shown that high pressures after a shockwave cause an expansion of the jet. Steam condensation is negligible during the expansion. The jet is confined to a divergent section [40]. The expanded jet can accelerate the flow to super-sonic conditions, leading to another shockwave. Successive contraction-expansion waves can occur depending on the pressure inside the sparger and in the pool.

In the sub-sonic regime, heat transfer is smaller compared to sonic conditions [42]. Therefore a jet can expand, produce bubbles, which detach collapse and condense [43, 44], in so called oscillatory bubble regime. The frequency of the bubble growth-detach-collapse for single and multi-hole injections was observed to vary from 50 to 600 Hz [45, 46, 47], and is a function of the hole diameter and pool subcooling. Tang et al. [48] studied the mechanism of the detached bubble collapse and proposed a regime map. At low steam flux the map includes chugging regime, where the collapse of bubbles causes volumetric condensation, sudden pressure drop and rapid suction of liquid from the pool into the injection pipe [49]. The transition from the oscillatory bubble to chugging regimes is characterized by a monotonic decrease of the bubble detachment frequency which occurs in the range of steam mass flux of 20-60 kg/(m<sup>2</sup>s) [50]. Aust & Seeliger [51] showed that chugging can be suppressed in a blowdown pipe with outlet cut at 45° which prevented large bubbles from forming for steam mass fluxes up to 100 kg/(m<sup>2</sup>s). At very low steam mass fluxes all steam is condensed inside the blowdown pipe.

The condensation regime maps as functions of mass flux and pool subcooling for sub-sonic flows have been proposed in [43, 53, 54, 54]. Petrovic de With et al. [55] included the injection hole diameter as a third parameter. Gregu et al. [56] investigated different chugging regime modes. Wu et al. [57] proposed regime maps for multi-hole injection with transition from sonic to sub-sonic flow occurring at approximately 330 kg/(m<sup>2</sup>s).

In a BWR, the area of the blowdown pipes is much larger than a possible area of a break in the primary system. Therefore, steam mass fluxes are too low for transition to sonic flow. The large pressure difference between the primary coolant system and the wetwell is more likely to result in sonic flows through spargers, especially at the initial stages of the Automatic Depressurization System (ADS) activation, or during the intermittent operation of the Safety Relief Valves (SRVs). For LOCA, long-term ADS operations, or exhaust of safety systems such as the RCIC, sub-sonic regimes are expected to dominate during the transient.

Single-phase jets induced by the steam condensation were investigated by Choo et al. [58] using Particle Image Velocimetry (PIV). A self-similar feature of the liquid jet was observed after a certain distance from the orifice. Correlations were proposed to model the turbulent profile as a function of the injection conditions. Van Wissen et al. [59] measured the turbulent intensities of the liquid, which maximum values can be about 30%.

### 3.2. Experiments on pool behavior

Experiments are usually performed in reduced scale facilities. In this case, adequate scaling becomes an essential ingredient for the design of the tests and interpretation of the results [58]. The full-scale Marviken-FCSB tests [61] showed that chugging can occur during prototypic LOCA transients in a BWR Mark II containment. Thermal stratification was observed when chugging was suppressed at reduced steam mass flux. Extensive experimental campaigns were carried out by General Electric in a 1:130 reduced scale facility to for the pool swelling, pressure increase, pool temperature, etc. during a LOCA in a BWR Mark I [62], Mark II [63, 64], and Mark III [65, 66, 67]. LOCA type experiments were also performed in Japan by JAERI [62, 69] in a full size 1/18 sector of a BWR. Chugging was observed in most of the JAERI tests, but duration of the test (few hundred seconds) was too short for development of thermal stratification.

To study the development of thermal stratification and mixing at the late stages of a LOCA in ESBWR the LINX facility [70] at PSI was developed with steam injection through a single-hole 40 mm vertical sparger. Injection of pure steam lead to development of stratification with temperature differences up to 30°C [71], while adding air in concentrations above 5% in mass caused complete pool mixing. In experiments with prototypic multi-hole spargers of an APR1400 in the sonic regimes performed by Moon et al. [72] no stratified layer was observed. Zhang et al. [73] using the scaled models of the AP1000 quencher and IRWST showed that considerable thermal stratification can develop in prototypic steam injection conditions, especially for the quenchers with a low submergence.

Extensive experimental campaigns were carried out in the POOLEX/PPOOLEX facility in Lappeenranta University of Technology (LUT), Finland, and in the PANDA facility in PSI, Switzerland, using blowdown pipes [74, 75, 76, 77, 78, 79] and spargers [6, 33, 36, 139]. Separate effect experiments were conducted in these schemes to investigate the effect of parameters such as the diameter of the pipe, volume of the drywell, steam injection conditions, etc.

Solom et al. [81] studied thermal stratification that can develop during prototypic steam injections of the RCIC system. Song et al. [83] showed that the Richardson number can be used to predict transition between thermal stratification and mixing. Fernando et al. [82, 84, 86] showed that the Richardson number defines regimes of interactions between the stratified layer and turbulent eddies and that the erosion velocity of a stratified layer is a function of the Richardson number.

### 3.3. Modelling approaches

Analytical models for bubble diameter and detachment frequency in the oscillatory bubble regime were developed in [87, 88] using the Rayleigh-Plesset equation and momentum balances across the bubble. Chugging models were also developed by Aya & Nariai [49] and Pitts [89] using the conservation equations and extended to include the non-condensable gases

in [90]. Comparison to experimental data showed a good prediction of the frequency and amplitude of the oscillations. Stability analysis performed by Brennen [91] showed that chugging is usually sustained in the natural, manometer type, oscillation of the system. Pattikangas et al. [87] used ANSYS Fluent to simulate the chugging regime in the PPOOLEX experiments. An improved prediction of the heat transfer was obtained in the work done by Tanskanen et al. [9] and Patel [10]. Pellegrini et al. [11] used a Rayleigh-Taylor instability model to simulate the direct contact condensation heat transfer during chugging.

Based on the work done by Gamble et al. [93], KAERI proposed a modelling approach called Steam Condensation Region Model (SCRM) [28, 72, 94, 95, 96]. The SCRM is based on equations of mass, momentum, and energy in a control volume inside which steam condensation is assumed to be complete. This allows to introduce single-phase flow analysis and boundary conditions for the liquid velocity. The SCRM approach implemented in Star CCM+ and ANSYS Fluent showed good agreement with the results of the where complete mixing was observed. However, no thermal stratification and mixing transients were addressed with the model.

To enable prediction of the PSP performance in long-term thermal stratification and mixing transients EHS/EMS models have been proposed by Li & Kudinov [3, 4]. Similar to SCRM, EHS/EMS model aims to resolve only the effect of the direct contact condensation on the large pool. It is achieved by introducing effective sources of heat and momentum while details of the microscale phenomena at the steam/water interface are not resolved. The implementation of these models in GOTHIC [18, 34] showed good agreement with the PPOOLEX STB and MIX experiments [75, 78, 79], which were performed at different injection conditions and pool geometry, etc. The EHS/EMS models were further developed and applied to steam injection through multi-hole spargers by Gallego-Marcos et al. [31, 34, 97].

The EHS/EMS models can be implemented in a CFD code by (i) introducing volumetric momentum and heat source terms in transport equations [31], or (ii) by imposing boundary conditions on an interface (similar to the Steam Condensation Region (SCR) [72, 94, 95, 96, 138]) that render the same effective sources of heat and momentum. The method that uses the source terms has been validated against PPOOLEX [6] and PANDA tests [36], showing a good agreement with experimental data on temperature distributions in the pool, if the value of the effective momentum is properly calibrated. However, later experiments that measured the magnitude of momentum produced by steam condensation in a Separate Effect Facility (SEF) [98] suggested that the values of the effective momentum that gave good results were significantly under-estimated. Thus the need for further development of the predictive capabilities of the EHS/EMS model was identified.

### 3.4. EHS/EMS models

Explicit modeling of direct contact condensation (DCC) of steam is a challenge for contemporary codes. The small time and length scale of steam condensation behavior requires very small mesh size and time step when using CFD type analysis [9, 10, 11]. Lumped and 1D codes are inadequate for prediction of 3D, transient mixing phenomena. Thermal-hydraulic codes such as GOTHIC [99], and RELAP5 [100], do not provide a model for prediction of the effect of steam injection through blowdown pipes or spargers. Available condensation models are mostly designed for pipe flow regimes such as bubbly, churn, film, etc.

Therefore, the concept of Effective Heat Source (EHS) and Effective Momentum Source (EMS) models have been proposed to enable the prediction of the pool behavior induced by the steam condensation. The main idea of the effective models is that large scale pool behavior is not affected by the details of the DCC phenomena occurring at the small temporal and spatial scales. Therefore, only the time-averaged “effective” heat and momentum sources induced by steam in a large pool need to be modelled. The effective heat  $Q_{eff}$  and momentum  $M_{eff}$  sources can be presented as [4]

$$Q_{eff}(t) = \frac{1}{\Delta t} \int_{t-\Delta t}^t Q(\tau) d\tau \quad (1)$$

$$M_{eff}(t) = \frac{1}{\Delta t} \int_{t-\Delta t}^t M(\tau) d\tau \quad (2)$$

where the integrals represent the time-average of the instantaneous variations of the sources over a period  $\Delta t$  of time. These variations are due to the oscillatory nature of direct contact condensation. For example, the large scale motions of the liquid inside the pipe during the chugging regime, the small scale oscillatory bubble behavior, etc.

The chart for estimation of the effective heat and momentum sources in the EHS/EMS models is shown in Figure 3. First, condensation regime is estimated for the given steam injection and pool conditions, then respective heat and momentum sources are calculated.

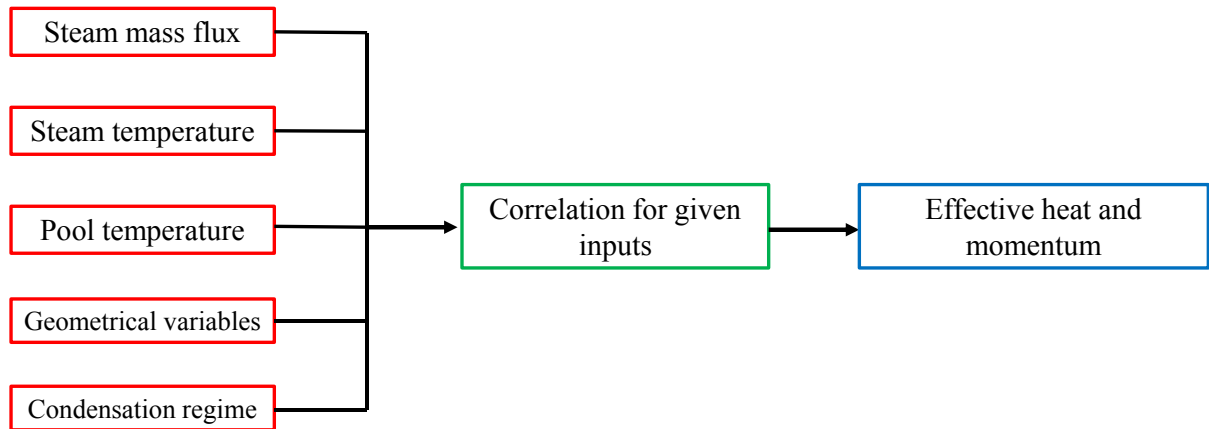


Figure 3. Chart of the EHS/EMS models.

#### 4. DEVELOPMENT OF EHS/EMS MODELS FOR SPARGER

The multi-hole spargers are used to discharge steam from the primary circuit into the PSP. They can be used in the exhaust of safety systems such as the RCIC [8] as well. The horizontal injection through multi-hole leads to different regimes compared to the blowdown pipes, and therefore, requires further development of the EHS/EMS models [34].

In this section we introduce PANDA HP5 tests and the results of calibration of EHS/EMS models implemented using source effective source terms. Then, the development of EHS/EMS models using SCR approach is discussed in Section 4.3. Finally, the implementation in Fluent together with the validation against HP5 tests are given given in Section 4.4 and Section 4.5.

##### 4.1. Introduction of PANDA HP5 tests

PANDA [108] is a multipurpose test facility designed to address containment thermal hydraulics phenomena and safety issues in LWRs. The facility consist of 2 wet well vessels and 2 dry well vessels and has a 1.5 MW steam generator. The experiments for steam injection through multi-hole spargers were done in one of the wetwell vessel as shown in Figure 4. The vessel was filled with water up to 4 m at room temperature 25°C. The interconnecting pipe (IP) was blocked by a thermally insulated lid to reduce the heat transfer between the vessels. The sparger was placed along the central axis of the pool at 1511 mm elevation above the bottom of the vessel.

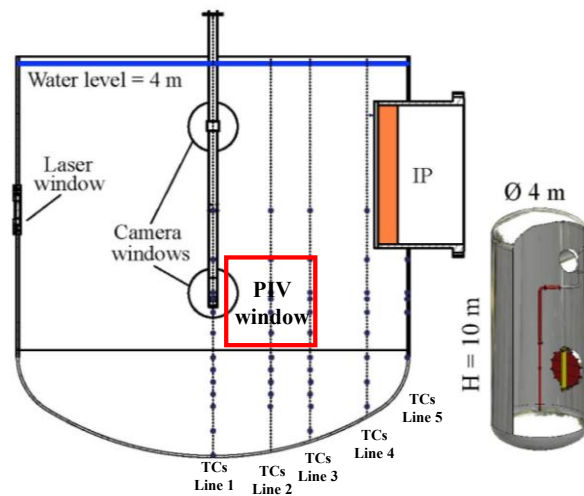


Figure 4. PANDA facility in the HP5 tests with sparger.

Five vertical trains of thermocouples (TCs) were mounted in a TC plane at different distance from the sparger (See TC points in Figure 4). The TC plane was positioned 250 mm away from the central plane. The vessel has three windows installed to enable 2D PIV measurements of the fluid velocity. One window was used to pass the laser sheet into the vessel and the other two windows were used for making video recording of the flow field with the PIV camera [109]. The geometrical characteristics of the multi-hole sparger used in the tests are shown in Figure 5. The sparger head has 32 holes arranged in 4 rings. Each hole has inner diameter of 9.5 mm and a conical chamfer.

Test matrix of selected test from the PANDA HP5 series is presented in Table 1 including steam injection procedures and initial pool temperatures. Each test had two phases for



development of thermal stratification and mixing respectively. Low steam mass flow rate (minimum flow rate avoiding the chugging regime [43, 46]) was used to develop stratification in the pool. After the temperature difference between the top and bottom of the pool reached certain value, the mass flow rate was increased to mix the pool. Further details of the experiments and their analysis can be found in [34, 36].

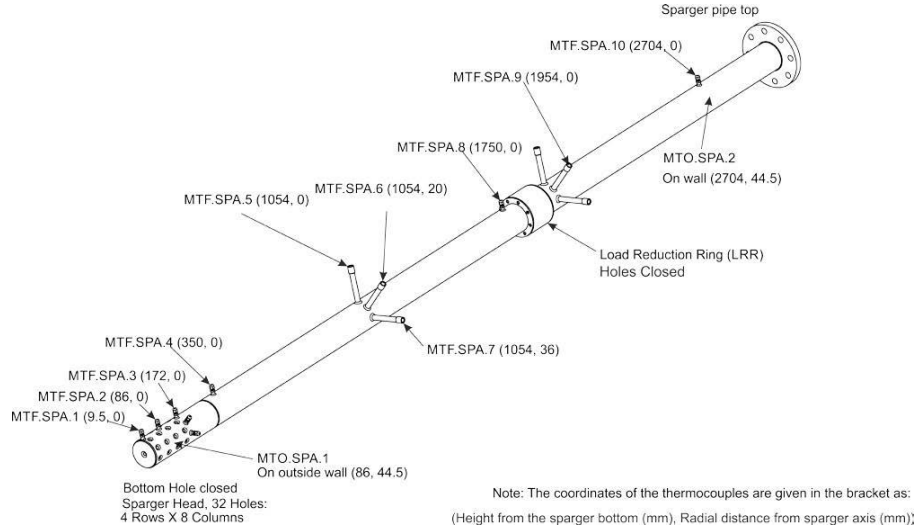


Figure 5. Geometry of sparger pipe [36].

Table 1. HP5 tests matrix

Test	Pool Initial Conditions		Phase 1: Stratification		Phase 2: Mixing	
	Temperature (°C)	Water level (m)	Flow (kg/s)	Duration (s)	Flow (kg/s)	Duration (s)
HP5-1	~25	4	0.16	6000	0.37	2500
HP5-2	~45	4	0.16	6000	0.26	5600
HP5-3	~23	4	0.16	6000	0.26	8100

#### 4.2. Calibration of the EHS/EMS models implemented using source terms

The momentum and heat induced by steam injection into the pool can be modelled in the simulation using source terms in the transport equations or using boundary conditions. A good agreement between the experiments and simulations was achieved when the source term was calibrated based on PANDA data. However, the magnitude of effective momentum source was later found to be under-estimated in the simulations [31, 98] based on the SEF-POOL data. results of EHS/EMS models calibration implemented using source terms are discussed in this section.

##### 4.2.1. Implementation of EHS/EMS models for spargers using source terms

The EMS model for multi-hole spargers requires the (i) magnitude of the momentum, (ii) downward inclination of the momentum, and (iii) profile of velocity (or momentum

distribution) in vertical and azimuthal directions. When steam is injected into a subcooled pool through the multi-hole spargers, the effective heat and momentum induced by the steam condensation can be computed by Eqs. (1) and (2) respectively [4]. With some simplifications [31], the effective momentum source can be written as:

$$\dot{M}_{eff} = C\dot{M}_{th} = C\rho_s A_0 U_s^2 \quad (3)$$

$$C = 4.28\Delta T^{-0.35} \quad (4)$$

where  $\rho_s$  and  $U_s$  are the density and velocity of steam,  $A_0$  is the injection hole area and  $\Delta T$  is water subcooling,  $C$  is the condensation regime coefficient which is introduced as a ratio of the effective momentum to the momentum of the steam. This coefficient (or the effective momentum induced by multi-hole steam injection) was not measured directly in PPOOLEX and PANDA experiments. CFD simulations [31] were used to calibrate the value of  $C$  based on the temperature evolution in the pool (see Figure 6).  $C$  was measured later in the Separate Effect Facility (SEF) [98], and approximated by an empirical correlation (4) as a function of the pool subcooling.

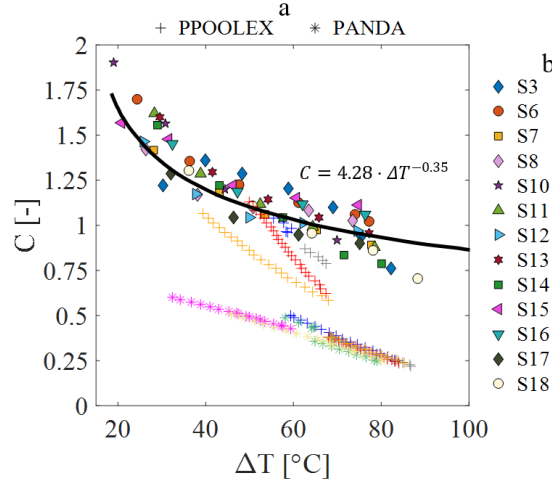


Figure 6. Comparison between  $C$  measured in the SEF facility and estimated from CFD simulations of PPOOLEX and PANDA experiments with spargers.

Comparison between the values of  $C$  estimated by CFD simulations (+, \*) and measured in SEF experiments are summarized in Figure 6. The values of  $C$  calibrated from the CFD simulations under-estimate the measurements of  $C$  by 20 – 300%. The difference might be explained by the fact that the azimuthal profile of velocity (APV) was not measured in the PANDA and PPOOLEX tests and thus is an uncertain parameter in the model. The goal of this section is to calibrate the EMS model by using the updated correlation for the  $C$  coefficient and adjusting the spatial distributions of the momentum. When correlation (4) is applied with the previous modelling setup for the spatial distribution of the momentum, increased value of the momentum is expected to intensify pool mixing.

Sensitivity studies suggest that the downward inclination has a significant effect on the motion of thermocline [31]. The jets induced by steam condensation have a downward inclination according to the TC mesh measurements in the PPOOLEX and PIV images in PANDA tests (Figure 7). The inclination is created by the downward component of the steam at the sparger hole outlet. The ratio between the area of the injection hole to the pipe cross-section area is

around 0.41 and the thickness of the wall is 4 *mm* provides an angle of 15° for both PPOOLEX and PANDA [36]. The angle was estimated to be about 10° in a separate gas-to-gas injection experiment as shown in Figure 7(a). The difference might be attributed to the secondary flows inside the sparger and buoyancy effect of the plume. The angle can be also affected by the injection conditions according to the PIV data in the PANDA tests with flow pattern determined by the competition between the jet buoyancy and inertia.

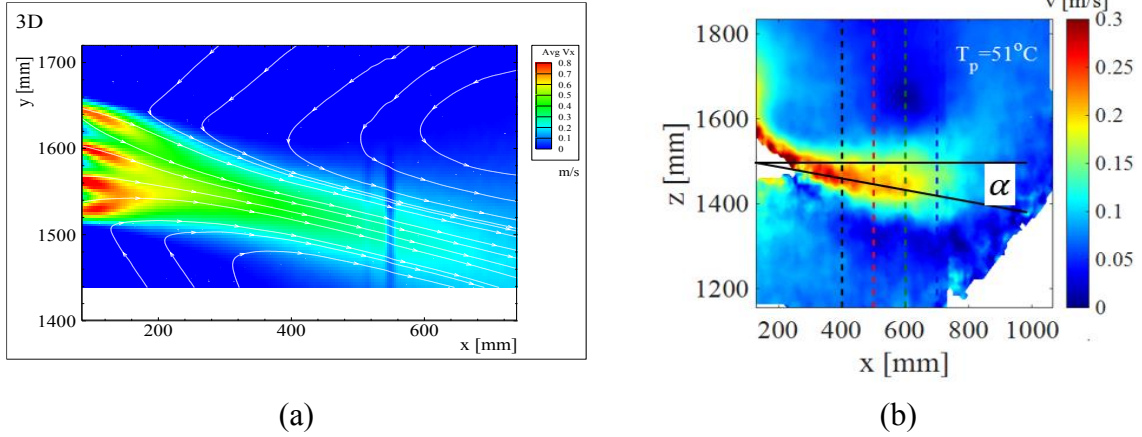


Figure 7. PIV data from (a) PANDA gas-to-gas experiment, (b) low steam injection phase of the PANDA HP5-2 experiment. Velocity data were time-averaged over 200s [36].

A single-phase jet injected into a still water develops a self-similarity velocity profile in non-dimensional coordinates. Jets injected through the adjacent nozzles have a tendency to merge into a single jet at certain distance downstream. The distance can be estimated as 3 times the pitch plus diameter [36] which agrees well with the temperature and velocity measurements in PANDA tests. Figure 7(b) shows a merged jet observed in PANDA HP5-2 test with the steam flux of 71  $kg/m^2s$ . Self-similarity of the velocity profile in the vertical cross section of the jet was also observed.

The model for the Vertical Profile of Velocity (VPV) was developed to describe the velocity profile in the vertical direction. It includes two parameters, the length of the condensation zone where the momentum is applied in the vertical direction and its distribution in this zone. According to the standard round jet equation as Eq. (5), the VPV model can be defined as:

$$U_0(x, r) = U_0(x) \exp\left(-K \frac{r^2}{x^2}\right) \quad (5)$$

The centerline velocity  $U_0(x)$  estimated by Figure 7(b), is about  $0.1/x$ . The jet expansion factors  $K$ , for round and plane jets, are 77 and 50 respectively in a single-phase flow [110, 121]. Analysis of the PIV data from PANDA experiments suggests that the  $K$  is about 40 or less (see Figure 8). The difference could be due to the effect of multi-hole sparger injection, condensation regime and turbulence. Note that all PANDA tests were performed with steam mass fluxes below 170  $kg/m^2s$ . In this work, the VPV model is kept the same as in the previous work [31]. The length of the condensation zone in vertical is assumed 50 *mm* and it starts at the height of 1560 *mm*. Since the momentum sources are distributed in a radial range of 40 – 150 *mm*, the distribution profile in the vertical can be simplified as a top-hat profile where the velocity magnitude is independent of the elevation.

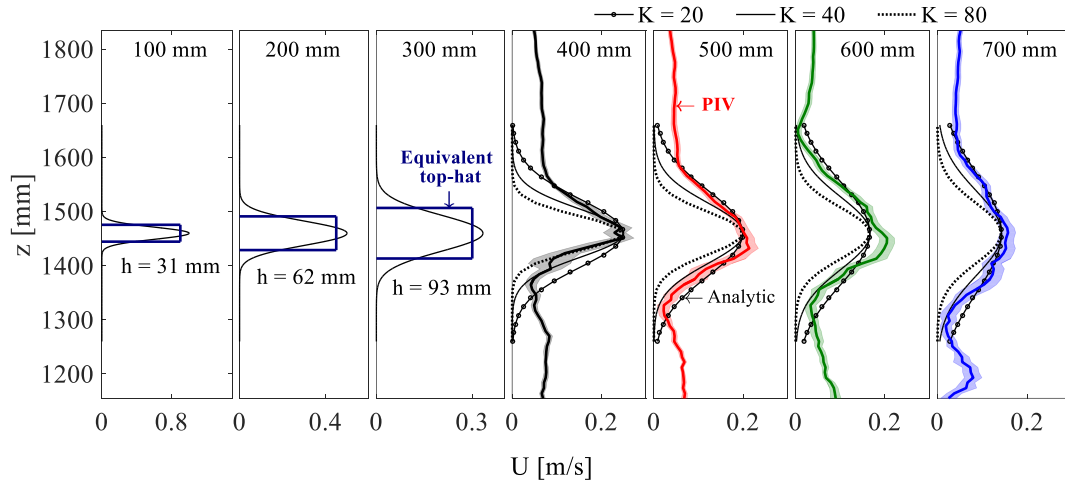


Figure 8. Comparison between the PIV data from Figure 7(b) and the analytical velocity profile described by Eq. (5) using different  $K$  [36].

Non-uniformities of the azimuthal velocity were observed in the work done by Song, et al [96]. The jet resembles a rectangular one which expands mostly in the horizontal direction. In this work, the momentum distribution in the azimuthal direction is described by the Azimuthal Profile of Velocity (APV) model. The model involves two variables, namely the length of the condensation zone in the radial direction and its distribution profile in this region.

In previous work [31], the length of the condensation zone in the radial direction was assumed as 50 mm starting at the  $r = 90$  mm as shown in Figure 9(a) and the distribution profile was estimated by (5) using  $K = 40$ . With such setup, the effective momentum coefficient  $C$  was under-estimated. In this work, the calibration of the EHS/EMS model is carried out by adjusting the distribution of the source terms in vertical and azimuthal directions using the condensation regime coefficient  $C$  defined by (4).

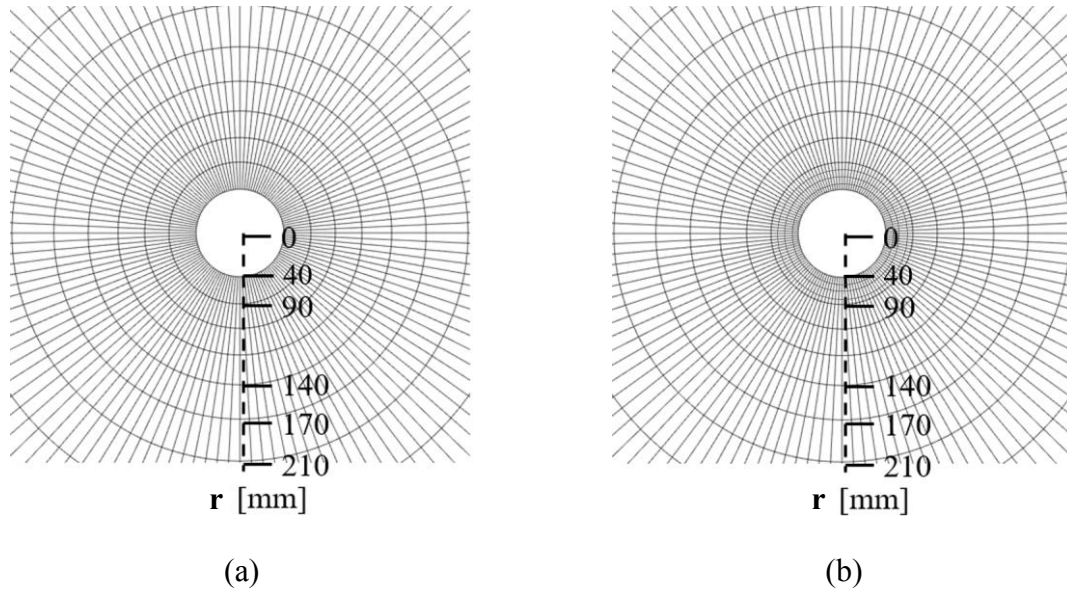


Figure 9. Top view of the azimuthal condensation zone. (a) Mesh in Fluent and (b) refined mesh within 40 – 90 mm.

Expansion factor  $K$  controls the shape of the azimuthal velocity profile. Comparison of azimuthal velocity profiles obtained using different values of  $K$  is presented in Figure 10. Note that the stepwise shape of the profiles is selected for convenient interpolation in the ANSYS Fluent. The integral of these profiles should be equal to  $2\pi$  to keep the same overall momentum for different expansion factors  $K$ . The profile becomes more homogenous as  $K$  is decreased. When  $K$  is below 5, the jets merge. The erosion velocity of the thermocline is determined by the effective momentum. Sensitivity studies using  $K = 40, 20$  and  $10$  suggest that the erosion velocity of the thermocline was slower for smaller  $K$  (Figure 11). Note that the total effective momentum was the same in all simulations, only the azimuthal velocity distribution was different.

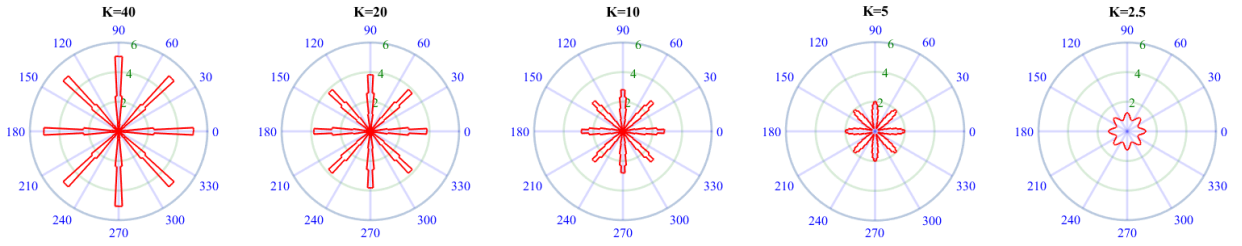


Figure 10. Comparison between the azimuthal velocity distribution profiles with different expansion factor  $K$ .

A combination of the effective momentum coefficient  $C$ , expansion coefficient  $K$ , azimuthal condensation zone length and location define intensity of the effective momentum and its impact on the erosion rate.

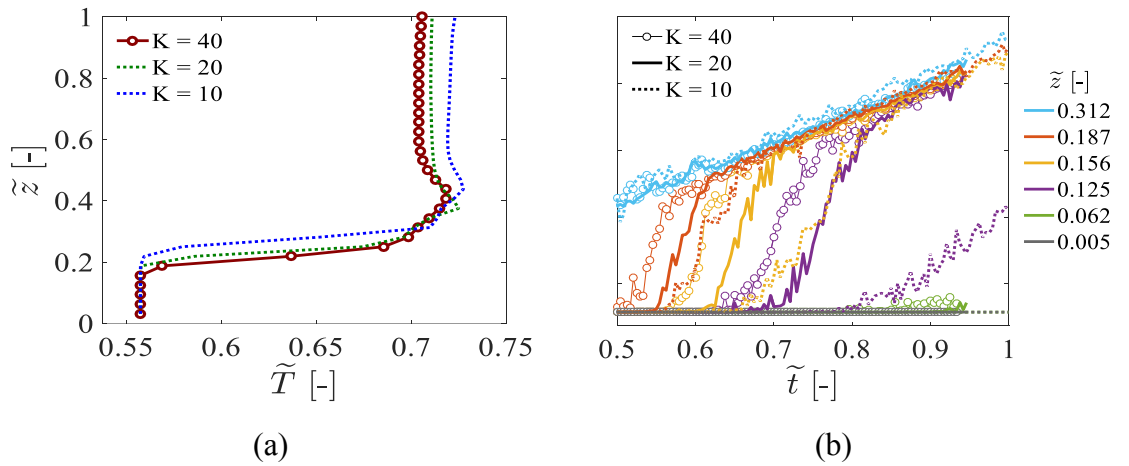


Figure 11. Effect of the expansion  $K$  on the temperature and the erosion of the pool obtained in the simulation of PANDA HP5-3. (a) Temperature profile during the low steam injection phase,  $\tilde{t} = 0.42$  and (b) temperature evolution during the high steam injection phase [31].

The Effective Heat Source (EHS) is uniformly distributed in the same region as the effective momentum. The value of the EHS is calculated by

$$\dot{q}_s = \dot{m}_s h_s \quad (6)$$

where  $\dot{m}_s$  and  $h_s$  are the mass flow rate and enthalpy of the steam.

## 4.2.2. Calibration of the EHS/EMS models

PANDA HP5-3 experiment data was used to calibrate the model. The temperature evolution of HP5-3 and results of CFD modeling using old EHS/EMS models are presented in Figure 12. In the new implementation of the EMS model following parameters can be adjusted (i) the  $C$  coefficient defined by (4), (ii) the condensation zone size and position, and (iii) the expansion factor  $K$  for the azimuthal profile. The downward inclination and the VPV model are kept the same as in the old implementation model. The cases for the old model and new models are summarized in Table 2. The mesh for case 4 (C4) is refined in the region  $40 - 90 \text{ mm}$  as shown in Figure 9(b) to enable the changes in the condensation region size and position.

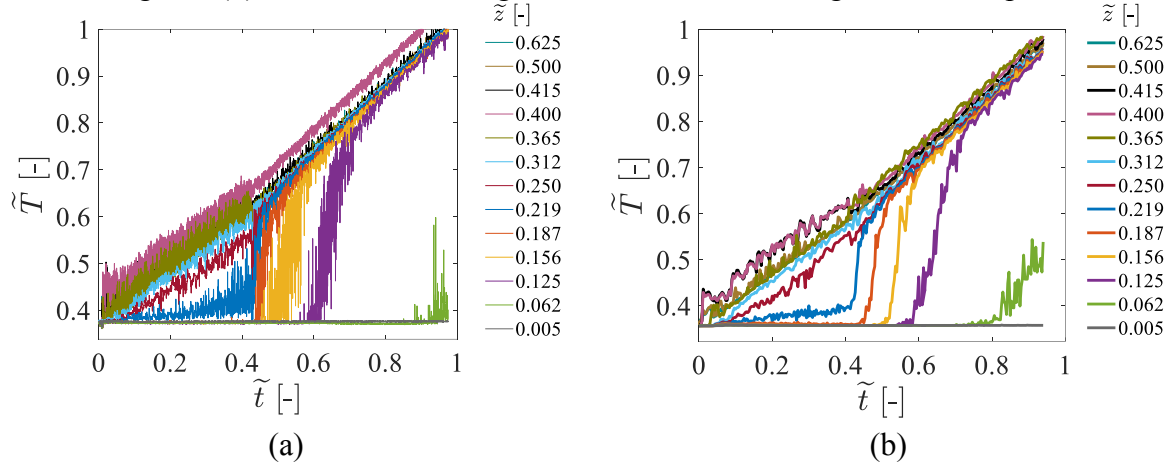


Figure 12. PANDA HP5-3 (a) experiment and (b) Fluent simulation using old EHS/EMS model with the  $C$  coefficient about  $0.24 - 0.53$  (Figure 6). Temperature evolution along a vertical line of thermocouples (TCs line 1) in the pool [31].

Implementation of the EHS/EMS models in ANSYS Fluent was introduced by Gallego-Marcos et al. [31]. Calibration of the EHS/EMS models against PANDA HP5-3 test is presented in the following part. The normalized temperature evolutions along the vertical TCs line 1 for these four cases are shown in Figure 13 and Figure 14.

Table 2. Comparison between the old and calibrated EHS/EMS models

Case name	Condensation regime coefficient $C$ [-]	APV model		VPV model	
		Condensation zone in radial [mm]	Distributed profile $K$ [-]	Condensation zone in vertical [mm]	Distributed profile [-]
Old model	0.24-0.53	90-140	40		
C1		90-140	20		
C2	$C = 4.28\Delta T^{-0.35}$	90-140	3.5	1560-1610	Top hat
C3		40-140	3.5		
C4		40-80	40		



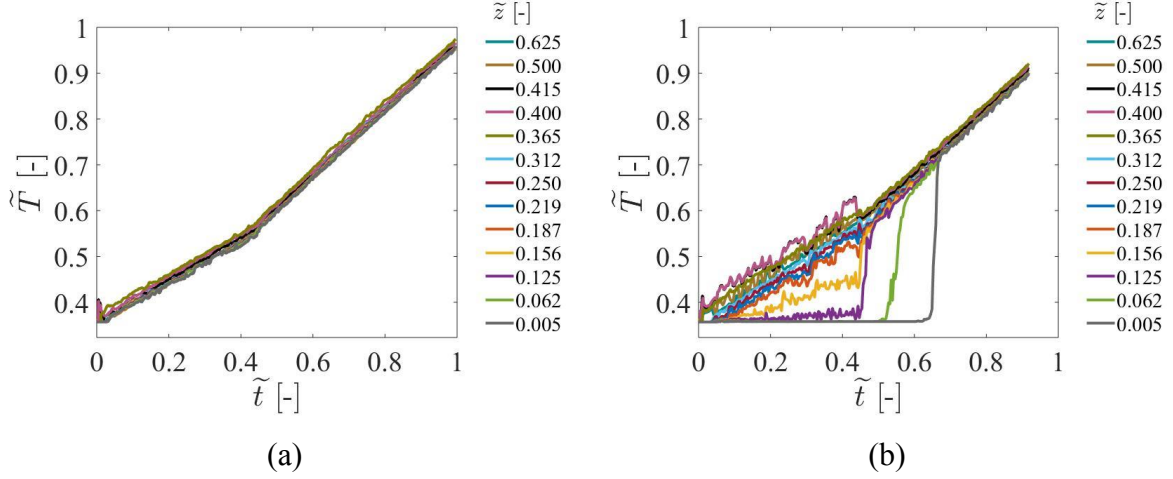


Figure 13. Pool temperature evolution (TC train 1). Fluent results of (a) C1 and (b) C2.

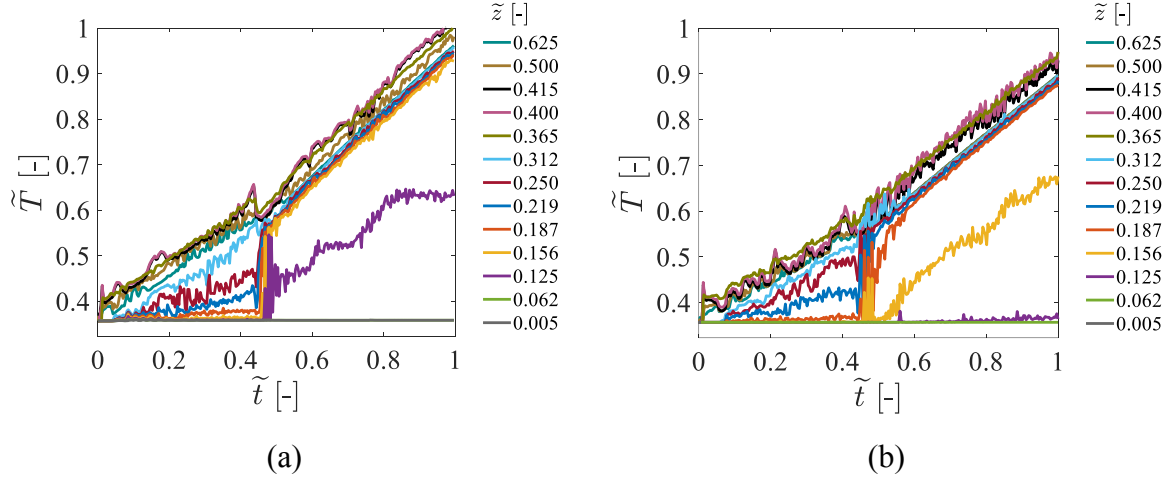


Figure 14. Pool temperature evolution (TC train 1). Fluent results for (a) C3 and (b) C4.

In C1 completely mixed pool was predicted in the simulations. This suggests that the decrease of  $K$  from 40 to 20 is not sufficient to compensate for the large increase in the magnitude of the momentum source (i.e.  $C$  coefficient). Further decrease of  $K$  from 20 to 3.5 (C2) provides a better agreement with the experimental data. However, erosion of thermocline in simulations is still faster compared to the measurements (Figure 12a). Temperature measured at the height of  $\tilde{z} = 0.219$  is increased during the first injection phase faster than in the old model in Figure 12(b). The erosion velocity of the thermocline becomes even larger in the second injection phase. The extension of the condensation zone from 90 – 140 mm to 40 – 140 mm (C3) provides a better agreement with the experiment. However, the erosion velocity of the thermocline during the high steam injection phase is slower than in the experiment. The rate of temperature increase in the locations  $\tilde{z} = 0.250$  and  $\tilde{z} = 0.125$  are small compared to the experiment.

In C4, the azimuthal condensation zone starts at the sparger wall at  $r = 40$  mm and the expansion factor  $K$  is 40. If condensation zone starts at the sparger wall, fluid can enter the condensation region only from top and bottom. Hydrodynamic resistance to fluid acceleration leads to the reduction of the magnitude of the effective momentum in this case. A good agreement is achieved between experimental data and simulations in C4 case for temperature evolution in the first injection phase was achieved. In addition, positioning of the condensation

zone starting from the sparger wall can help to reproduce the local circulation pattern which was observed in HP53 PIV measurements (Figure 15) but is not observed in the cases where condensation zone starts at  $r = 90 \text{ mm}$  (Figure 16). However, the discrepancy between experiment and simulation data for the temperature evolutions in the high steam injection phase suggest that further calibration of the EHS/EMS models with respect to the APV model, namely dependency of the azimuthal profile on the steam injection conditions such as flow rate and water subcooling is needed.

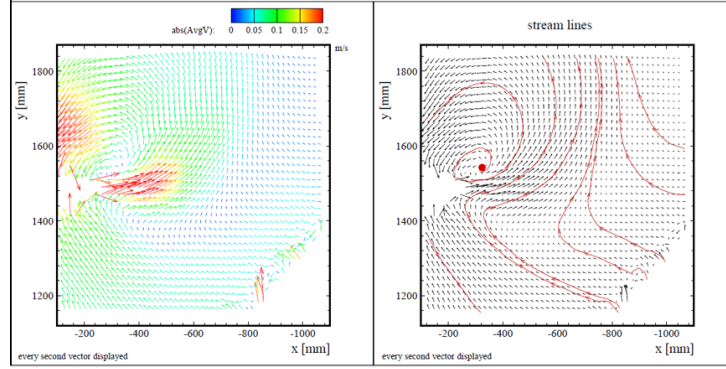


Figure 15. 2D PIV measurement of velocity at  $t = 2900s$  [132]. The blank area at the sparger exit is due to the presence of the bubbles. The data is time-averaged over 200s.

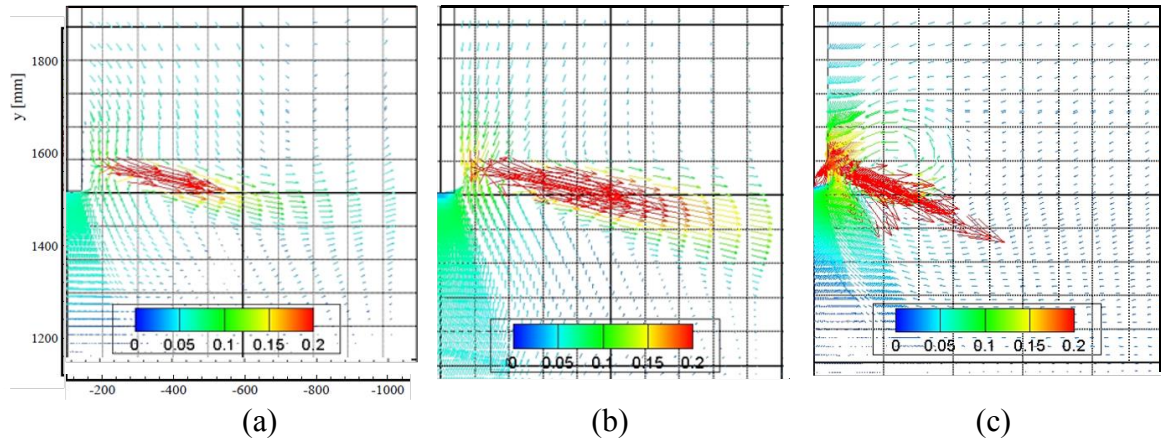


Figure 16. Velocity vectors obtained from CFD simulations of (a) old EHS/EMS models, (b) case 1, and (c) case 4 at  $T = 2900s$ .

In summary, after the uncertainty in  $C$  coefficient is reduced according to the SEF-POOL data (4), further calibration of the EHS/EMS model is needed in order to reproduce the pool behavior observed in the test. Results of calibrations show that the decreasing of expansion factor  $K$  and moving the location of the condensation region closer to the axis can help to reproduce a stratified layer at the low steam injection phase. The significant difference between experiment and simulation at high flow rate conditions suggest that the remaining calibratable parameters of the model are dependent on the steam injection regime.

#### 4.3. Development of EHS/EMS models using SCR approach

Although a good agreement between experiment and simulations can be achieved using the source terms approach to implementation of the EHS/EMS, currently available test data is insufficient for a reliable calibration of the model parameters. Specifically, characteristics of



spatial distribution of the momentum source. There are two approaches to solving this problem. One approach is to measure the azimuthal velocity profiles in the future pool tests in different steam injection regimes, as discussed in section 6.1. Another approach is to resolve in the model interactions between the jets produced by individual steam injection holes. In this case the EHS/EMS model can be implemented using boundary conditions at the surface of the sparger, or at the interface of the Steam Condensation Region (SCR).

In this section we develop implementation of the EHS/EMS models using SCR approach. In this method, a velocity profile is imposed on the interface where jets from different injection holes are fully merged. The details of steam condensation inside the condensation region are neglected. The velocity can be derived based on a “Unit Cell” model where a group of individual jets is directly modelled.

#### 4.3.1. Single-phase turbulent jets

Thermal stratification and mixing in a large pool are determined by a competition between buoyancy and momentum induced by the steam injection. The momentum created by injection through a multi-hole sparger [133] is introduced in a form of jets created by condensing steam. Characteristics of the velocity in the far-field (after condensation is finished) for such jets are similar to the single-phase turbulent jets [28, 72, 95, 133].

We consider a water jet injected through a nozzle into a large tank with stagnant water (Figure 17). The domain that contains the turbulent jet has a conical shape. Regardless of the type of fluid (water or air) and other conditions (such as nozzle diameter and discharge speed), the expansion angle is a constant [134] of  $11.8^\circ$ .

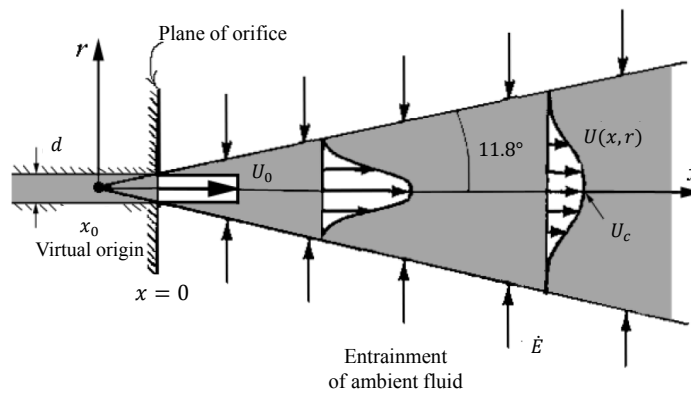


Figure 17. Schematic of a jet penetrating in a still fluid.

The mean centerline velocity  $U_c(x)$  can be expressed by Eq. (7) [121]

$$\frac{U_c(x)}{U_0} = \frac{Bd}{(x - x_0)} \quad (7)$$

where  $U_0$  is the mean exit velocity,  $B$  the decay rate,  $d$  the nozzle diameter and  $x_0$  the so called virtual origin of the jet.

The fully developed axisymmetric velocity profile obeys a law of self-similarity as given by Eq. (5). By considering the effect of virtual origin, this profile can be presented as:

$$U(x, r) = U_c(x) e^{\left(-K \frac{r^2}{(x-x_0)^2}\right)} \quad (8)$$

To integrate the square of velocity over the cross-section of the jet with the fluid density, the momentum rate of the jet is:

$$\dot{M} = \int_0^\infty \rho U(x, r)^2 2\pi r dr = \frac{1}{4} \pi d^2 \rho U_0^2 \cdot \frac{2B^2}{K} \quad (9)$$

Since the decay rate and expansion ratio are constant for a given jet, the jet momentum is conserved at any downstream cross section of the jet and equal to its initial momentum  $\pi d^2 \rho U_0^2 / 4$ . Hence, we can deduce a rough relation between  $B$  and  $K$  given by Eq. (10), which shows that a jet with faster decay of the centerline velocity should also expand faster.

$$2B^2 \sim K \quad (10)$$

Investigation of velocity characteristics induced by air, water, and steam jets shows for the fully developed jets  $2B^2/K = 0.88 \sim 1.05$  [133]. The mass flow rate  $\dot{Q}$  is not conserved because of the entrainment of ambient fluid. The jet mass flow rate can be calculated by integration (11).

$$\dot{Q} = \int_0^\infty 2\pi r \rho U(x, r) dr = \pi d \rho U_0 \frac{B}{K} \cdot (x - x_0) \quad (11)$$

The entrainment rate  $\dot{E}$  is defined as the rate at which the jet mass flow rate grows along the jet axis.

$$\dot{E} = \frac{d\dot{Q}}{dx} = \pi d \rho U_0 \frac{B}{K} \quad (12)$$

#### 4.3.2. SCR model for a single jet induced by steam injection

Before studying a group of jets and their effect on the pool behavior, it is important to understand the behavior of a single jet induced by steam injection. As shown in Figure 18, SCR model for a single jet can be characterized by two regions: the Steam Condensation Region (SCR) and the Condensed Jet Region (CJR). SCR is a control volume in which the injection steam is expected to condense completely over a short distance. The DCC phenomena in this region are not resolved, only their effects on the mean flow are taken into account by solving simplified conservation equations of mass, momentum, and energy. Downstream of SCR, the condensed jet region is a domain where single-phase turbulent jet develops. In SCR, the conservation of mass is described by:

$$\dot{m}_c = \dot{m}_s + \dot{m}_e \quad (13)$$

where  $\dot{m}_c$  is the mass flow rate of condensing jet,  $\dot{m}_s$  and  $\dot{m}_e$  are the mass flow rate of injected steam and entrained water, respectively.

The conservation of energy and momentum is achieved by the EHS/EMS models which provide the time-averaged momentum and heat transferred from the injection steam to the pool water. The equations can be found in Eqs. (3), (4) and (6). Since the velocity characteristics of the condensed jet are similar to the single-phase turbulent jet [96]. It is reasonable to describe the condensed jet velocity profile using equations (7) and (12).

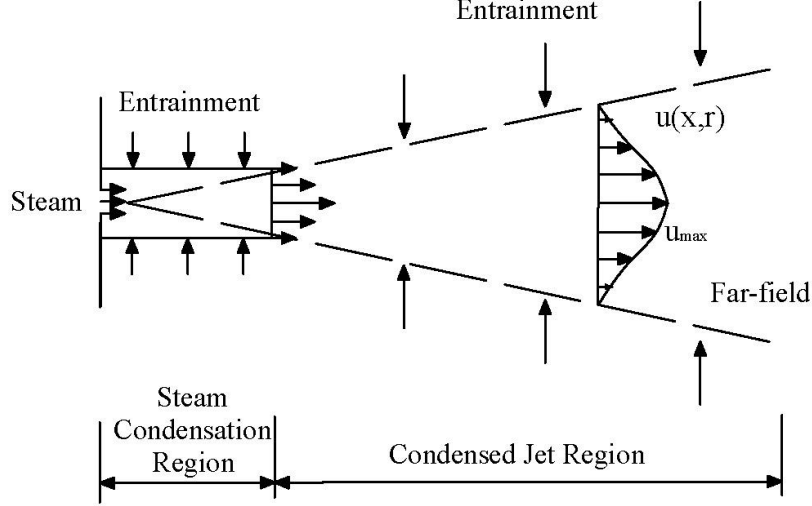


Figure 18. Schematic of SCR model for single condensing jet.

The dimensions of SCR are determined by two parameters, namely the steam penetration length  $L$  and expansion width  $\delta$ . The penetration length is a function of the steam flux, pool subcooling, and sparger geometry. Experimental works [96] showed that for Mach number  $Ma > 1$  a stable sonic jets condenses within 2 to 11 sparger hole diameters. Since the PPOOLEX and PANDA pool tests are focused on the unstable bubble regime where  $Ma < 0.8$ , its penetration length would be smaller than in the case of a sonic jet. We can define the radius  $\delta$  which contains 98% of the jet momentum in a given cross section

$$\begin{aligned} \dot{M} &= \int_0^\delta \rho U(x, r)^2 2\pi r dr = \int_0^\delta \rho U_c(x) e^{\left(-K \frac{r^2}{(x-x_0)^2}\right)^2} 2\pi r dr = 98\% M_{initial} \\ &= 0.98 \cdot \frac{1}{4} \pi d^2 \rho U_0^2 \cdot \frac{2B^2}{K} \end{aligned} \quad (14)$$

$$\delta = 2(x - x_0)/B \quad (15)$$

The radius  $\delta$  can be used to set boundary conditions for the velocity at the SCR exit surface.

#### 4.3.3. Comparison of analytical and CFD results for single jet flow

In this section we discuss comparison of predictions for a single jet by the analytical model and CFD code Fluent. In the SEF tests [98] only the effective momentum induced by steam injection was measured. Other experimental data [58, 72, 95, 96] for condensed steam jets are available in sonic and super-sonic injection regimes. The velocity profile data for a single jet induced by steam condensation in the oscillatory bubble regime is not available. Therefore, a

typical single-phase turbulent round jet [134] is used in this validation. Its main parameters are summarized in Table 3.

Table 3. Parameters of a typical turbulent round jet

	$Re$	$B$	$K$	$x_0$	$d$	$U_0$
	[-]	[-]	[-]	[mm]	[mm]	[m/s]
Theory	95500	5	40	-25	10	9.6

The dimensions of SCR and the velocity profile at the SCR exit surface are important parameters for prediction of the pool behavior. An approach to estimation of the entrainment rate in the SEF tests is under development now and will enable estimation of the decay rate  $B$  and expansion factor  $K$  as described in (12).

In this simulations the jet is injected with a uniform velocity of  $U_0 = 9.6 \text{ m/s}$  within a circular region with diameter  $d = 10 \text{ mm}$ . The  $k - \omega$  BSL model is used to resolve the turbulence characteristics. More details of the turbulence model can be found in section 4.4.4. Only the boundary conditions for the turbulence characteristics, namely, turbulence intensity and turbulent viscosity ratio, are the uncertain parameters. These two parameters are adjusted in order to fit the far-field velocity profiles according to (7) and (8). As a result the turbulence intensity of 50% and the turbulent viscosity ratio of 3000 were selected in the analysis.

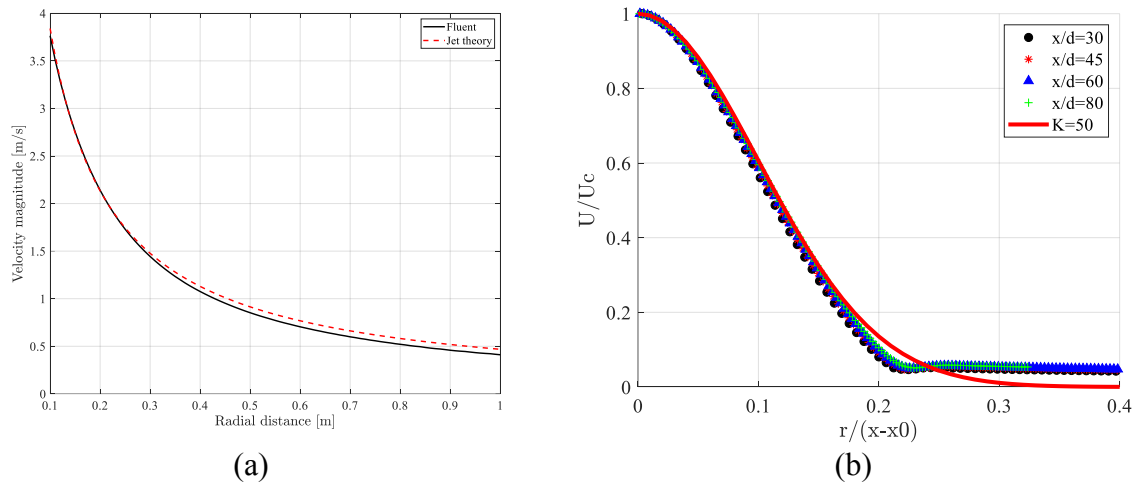


Figure 19. Comparison between Fluent and jet theory of (a) centerline velocity versus distance along the radial direction and (b) mean axial velocity versus radial distance at different slices.

A comparison of the centerline velocity profile between the Fluent and the analytical model is presented in Figure 19(a). Self-similarity of the axial velocity profile is clearly seen in different sections of the jet showing a nearly Gaussian shape (Figure 19b). The velocity is scaled by the cross-section centerline velocity and the axial distance by the distance between the jet virtual origin and the coordinate of the cross section  $x - x_0$ . Theoretical profile by Eq. (8) with  $K=50$  is plotted for comparison. Good agreement between analytical and CFD predictions for the velocity profile suggests that a single condensed jet model can be implemented in Fluent and can reproduce a round jet by appropriate selection of the turbulent characteristics, namely, the turbulence intensity and turbulent viscosity ratio. Although the simulation was carried out for

a single-phase liquid jet, the SCR approach should be applicable to simulating a jet induced by condensed steam due to the similarity of the jet characteristics in the far-field.

The momentum and entrainment integrated over different cross sections of the jet are presented in Table 4. Theoretical values are calculated by (9), (11), and (12). The momentum and entrainment rates are slowly decreasing along the jet axis, probably due to the energy dissipation or the effect of the walls in the finite computational domain. In general, we can conclude that described SCR model can be used for a single condensed jet.

Table 4. Momentum and entrainment at different slices

Distance [m]	Theory	Inlet	0.05	0.3	0.45	0.6	0.8
Momentum rate [N]	7.22	7.20	7.34	6.76	6.60	6.40	6.38
Entrainment rate [kg/ms]	30.07	29.30	30.01	25.38	24.83	24.27	24.10

## 4.3.4. SCR model for multiple condensed jets

Compared to single hole steam injection, a multi-hole sparger introduces phenomena of interactions between the jet. The interactions can be directly modelled, e.g. using SCR approach for each jet created by condensed steam from each sparger hole [141]. However resolving flow for each individual jet would require significant computational resources even for PANDA test as there are 32 holes in the PANDA sparger (Figure 20). In plant applications, the number of spargers and holes in each sparger pipe are too large making such analysis practically unfeasible. Instead we develop a model that can be used to simulate a group of condensed steam jets using approaches similar to the SCR model for a single jet.

As shown in Figure 21 two regions are introduced: the steam condensation region which includes a group of jets, and the condensed jet region. Jets injected from adjacent nozzles into undisturbed surroundings tend to merge into a single jet at a certain downstream distance. The length of SCR is no longer the steam penetration length but the downstream distance where the parallel jets are fully merged. The distance can be estimated as 3 times the pitch plus diameter [36] which agrees well with the temperature and velocity measurements in PANDA tests. For instance, Figure 7(b) shows completely merged jets in PANDA HP5-2 test with the steam flux of  $71 \text{ kg/m}^2\text{s}$  and pool subcooling of  $55^\circ\text{C}$ . The blank area around the sparger is caused by unreliable PIV data in the region with high concentration of small gas bubbles produced in the steam condensation region. This effect was especially severe at high steam flux conditions.

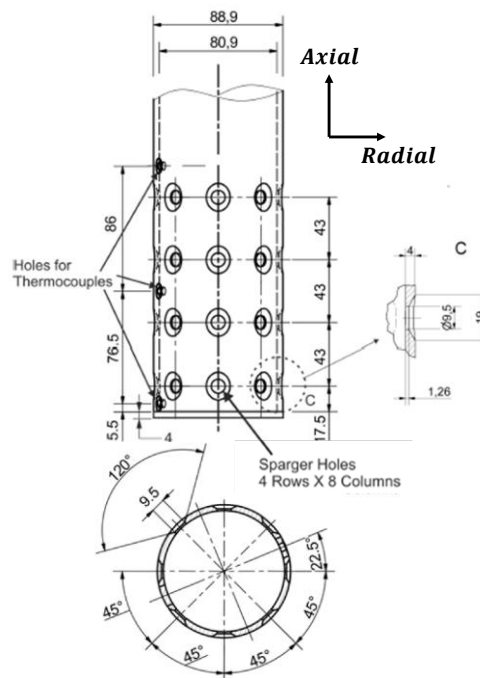


Figure 20. Geometry of multi-hole sparger head in PANDA HP5 tests [36] with a pitch to hole diameter ratio of  $p/d = 4.53$ .

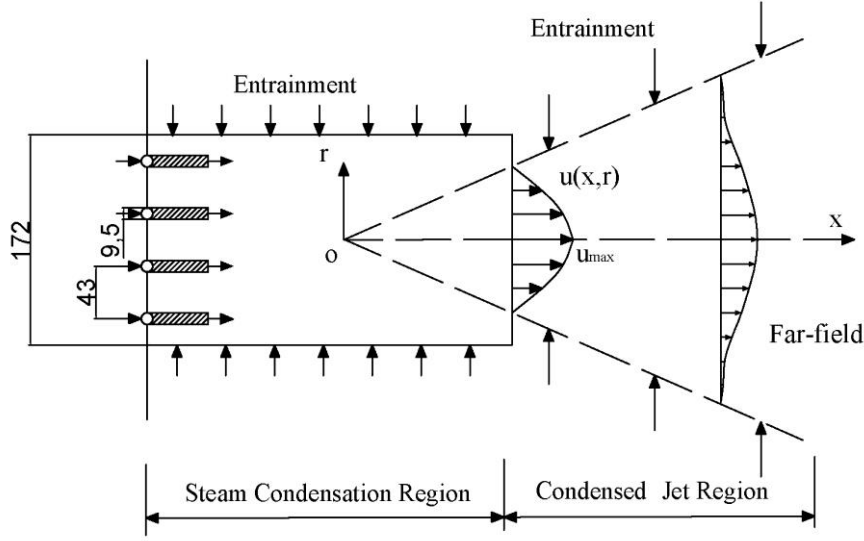


Figure 21. Schematic of SCR model for multiple jets induced by injection of condensing steam.

Self-similar behavior of the far-field velocity profile in vertical cross section was also observed for the merged jets induced by steam injection through several neighboring holes in PANDA tests. However, azimuthal profile of velocity was not measured by PIV and is expected to be non-uniform according to the results of EHS/EMS models calibration in section 4.2. The merged jet resembles a rectangular jet with little widening of the jet in the vertical direction and more intensive expansion in the horizontal (azimuthal) direction. The velocity profile for the merged condensed jet can be described by (16) by analogy with the profile of the single turbulent jet given by Eq. (8).

$$U(x, y, z) = U_c(x) \cdot e^{-\frac{K_A y^2 + K_V z^2}{(x-x_0)^2}} \quad (16)$$

where the asymmetry of velocity profile is described by the expansion ratio of  $K_A$  and  $K_V$  in azimuthal (or horizontal) and vertical directions respectively.

#### 4.4. Implementation of SCR for spargers in Fluent

SCR approach for multi-hole spargers (multiple jets) can be implemented in any CFD code. ANSYS Fluent 19.3 is used as an example in this work. In this section we describe numerical approaches to prediction of the pool behavior in PANDA HP5 test series.

##### 4.4.1. Computational domain

The computational domain for simulation of the jet induced by steam injection through a multi-hole sparger is presented in Figure 22. Several sectors ( $22.5^\circ$ ,  $180^\circ$  and  $360^\circ$ ) were used in the simulation. Data from HP51 was used to validate the models. The height of the water level and sparger head are  $4\text{ m}$  and  $1.51\text{ m}$  above the bottom of the pool. The effect of grid refinement on the solution was carried out in order to reduce sensitivity of the results to grid resolution [31]. For a full domain ( $360^\circ$ ) 128 cells in the azimuthal direction were used and the size of cells in the vertical direction above/below sparger are about  $50/25\text{ mm}$  respectively.

Steam condensation region has three boundaries, namely entrainment top, entrainment bottom, and inlet. SCR length  $L = 0.2 \text{ m}$  was selected to make sure that it is longer than the distance where jets can completely merge, which is equal to  $3 \times (43 + 9.5) = 157.5 \text{ mm}$ . According to the velocity profile at the distance  $L$  (Figure 23b), the height of  $0.08 \text{ m}$  for the condensation zone was selected. According to PIV measurements [141] the elevation of the central horizontal plane of the SCR is  $H \approx 1.475 \text{ m}$ , which is a bit lower than the geometric location of the central plane according to the simulations ( $H \approx 1.55 \text{ m}$ , Figure 23a). The discrepancy might be attributed to the single-phase modeling approach in the unit model simulations where the DCC phenomena within the condensation core region are not resolved. An increase of the injection inclination angle produced a little effect. To be consistent with the sparger geometry,  $H \approx 1.55 \text{ m}$  was used in the analysis.

Energy equation and dynamic mesh with laying method are turned on. PISO algorithm and Quick spatial discretization scheme in momentum, turbulence kinetic energy ( $k$ ), specific dissipation rate ( $\omega$ ), and energy were used. The simulation is considered fully converged when the residual was below  $1e - 6$  for energy and  $1e - 3$  for other variables.

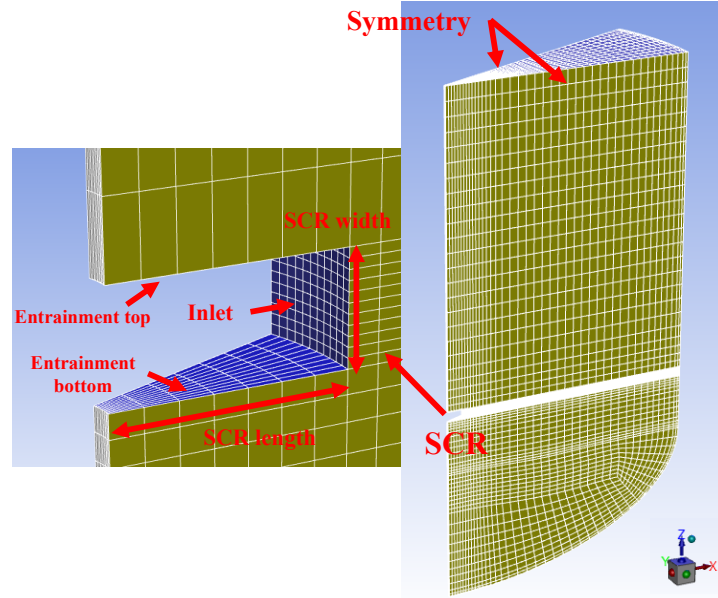


Figure 22. Hexagonal meshing grid of SCR model for multiple condensing jets.

#### 4.4.2. Lumped velocity profile

One of the most important steps in the SCR model for multiple condensed jets is to reproduce the lumped velocity profile (shown in Eq. (16)) by fitting the results from the Unit model. The Unit model [140] has a  $22.5^\circ$  sector domain with 4 injection holes (Figure 20, Figure 21). In each hole, a uniform effective velocity profile was imposed according to the EMS model and equations (3), (4), (17), and (18).

$$\dot{M}_{eff} = C\dot{M}_{th} = C\rho_s A_0 U_s^2 = \rho_l A_0 U_{eff}^2 \quad (17)$$

where  $\rho_l$  is the density of the liquid, thus:



$$U_{eff} = \sqrt{\frac{C\rho_s}{\rho_l}} U_s \quad (18)$$

Validation of the model against PANDA HP53 test with respect to the pool temperature evolution suggests that this Unit model can provide a good prediction in the low steam flux phase. However, a faster mixing was observed in the high flux phase [141]. In order to address this issue, an adjustment of the initial turbulent characteristics was done to make the jet more diffused. However, this approach resulted in numerical oscillation of the solution. The oscillations might be caused by the enforced symmetry boundary of the 22.5° domain. Therefore larger domains (1/2 and a full size) were considered. The SCR model for the merged jets was used for larger size of the domain.

The velocity profile predicted by the Unit model in a vertical cross section are shown in Figure 23. The cross section is located at  $x = 0.2 \text{ m}$  from the sparger axis (Figure 23a). Apparently the jets have merged completely prior to the selected cross section. Predicted 15° downward inclination angle for the merged jet agrees well with the PIV measurement shown in Figure 7(b) and the gas-to-gas injection case in [36].

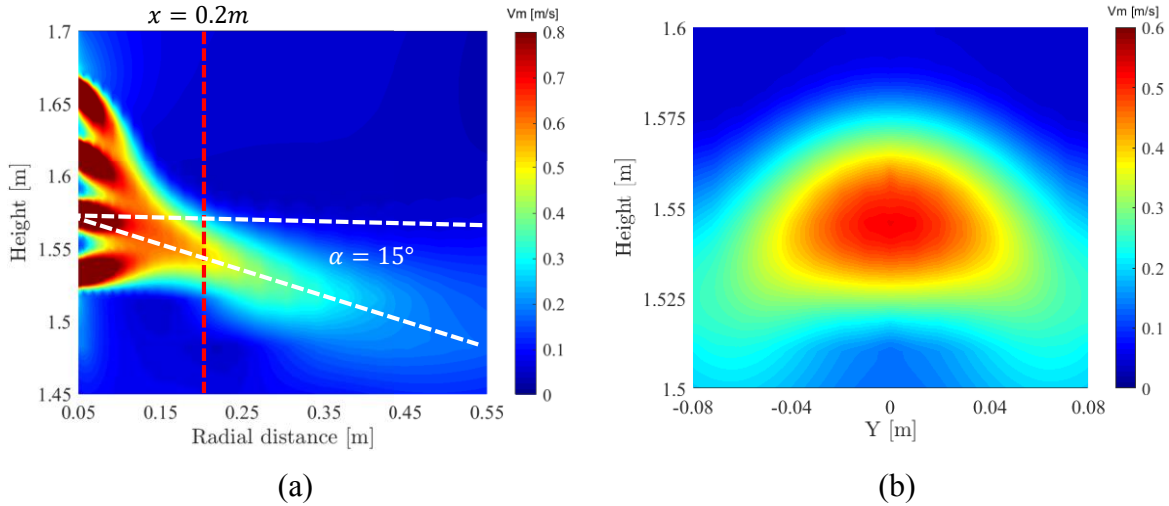


Figure 23. Velocity contours obtained in HP53 simulations by Unit model at  $\tilde{t} = 0.13$  in (a) vertical direction and (b) azimuthal direction.

The inclination of the jet is taken into account in the fitting process for calibration of the parameters in (16). A transformation from the Cartesian coordinate systems where  $x$  axis is parallel to the jet is applied (Figure 24(a)) by rotating around  $y$  axis counterclockwise by  $\alpha$  degree. The relationships between these two systems is given by (19). By substituting (19) into (16), we can obtain the jet velocity profile in the  $x'y'z'$  system (20).

$$\begin{aligned} x &= x' \cos \alpha - z' \sin \alpha \\ y &= y' \\ z &= z' \cos \alpha + x' \sin \alpha \end{aligned} \quad (19)$$

$$U(x', y', z') = U_c(x') \cdot e^{-\frac{K_A y'^2 + K_V (z' \cos \alpha + x' \sin \alpha)^2}{(x' \cos \alpha - z' \sin \alpha - x_0')^2}} \quad (20)$$

The maximum velocity  $U_c(0.2)$  over the slice at  $x = 0.2m$  served as centerline velocity is equal to  $0.53 m/s$  at  $\tilde{t} = 0.13$  and the rotation degree is about  $\alpha = 15^\circ$ . The rest of the parameters are fitted through Matlab cftool, giving  $K_A = 9.3$ ,  $K_V = 50.5$  and  $x'_0 = -0.043 m$ . A similar value for the vertical jet expansion coefficient  $K_V = 40$  was obtained in previous work [36] using fitting to PIV measurement. The velocity contours provided by the fitting equation is presented in Figure 24.

To apply this velocity profile in a transient simulation, the decay ratio  $D$  defined by the centerline velocity over the effective velocity of a single condensing jet ( $U_{eff}$ , see Eq. (18)) is used to provide the estimation of the centerline velocity  $U_c(x, t)$  at a specific distance from the sparger axis. This ratio is obtained by extracting both velocities from the Unit model results at  $\tilde{t} = 0.13$ ,  $\tilde{t} = 0.20$ ,  $\tilde{t} = 0.29$  and  $\tilde{t} = 0.46$ , resulting in a range of  $0.172 \sim 0.188$ . The averaged value  $D = 0.18$  is selected in the following simulations. The merged jet velocity profile can be described as:

$$U(x, y, z) = 0.18 \cdot U_{eff} \cdot e^{-\frac{9.3 \cdot y^2 + 50.5 \cdot z^2}{(0.2 + 0.043)^2}} \quad (21)$$

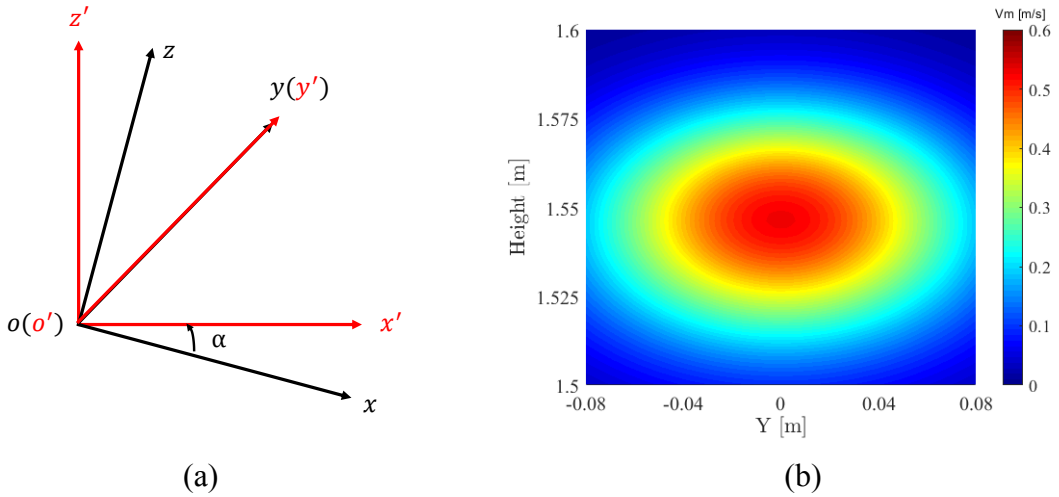


Figure 24. (a) A transformation of then Cartesian coordinate system by rotation around  $y$  by angle  $\alpha$  to an  $x'y'z'$  system, and (b) velocity contours obtained by fitting obtained profiles at  $\tilde{t} = 0.13$  with  $\alpha = 15^\circ$ .

#### 4.4.3. Boundary conditions

In the SCR approach the momentum induced by steam injection is modelled by water injection. Resulting mass flow rate of water can be many times larger than the steam flow rate. In order to preserve the mass balance, some part of the injected water should be taken out of the computational domain. We can remove the water through the surfaces named “entrainment top & bottom” (see Figure 22) with a total mass flow rate given by Eq. (22). In order to respect the heat balance, the EHS model was used with the time-averaged heat source estimated by Eq. (6). In the simulation, when mass is taken out from the entrainment surface, the energy will be removed as well. To compensate the loss of removed heat, the enthalpy of the injection water  $h_l^{in}$  should be defined by Eqs. (23), (24). The  $h_l^{in}$  is implemented by setting the inlet boundary conditions for the temperature according to Eq. (25).

$$\dot{m}_{out} = 0.5 \cdot (\dot{m}_{in} - \dot{m}_s) \quad (22)$$

$$\dot{q}_{in} = \dot{q}_s + \dot{q}_{out} \quad (23)$$

$$h_l^{in} \cdot \dot{m}_{in} = h_s \cdot \dot{m}_s + h_l^{out} \cdot \dot{m}_{out} \quad (24)$$

$$T^{in} = \frac{h_s \cdot \dot{m}_s + C_p(T^{out} - 273.15) \cdot (\dot{m}_{in} - \dot{m}_s)}{C_p \dot{m}_{in}} + 273.15 \quad (25)$$

where  $\dot{m}_{in}$  is the mass flow rate of inlet liquid, calculated by the user defined function (UDF), sub-indexes  $l$  and  $s$  are indicating liquid and steam respectively,  $in$  and  $out$  are indicating the input and output,  $C_p$  and  $T$  are the specific heat capacity and water temperature, respectively.

#### 4.4.4. Turbulence model

Stable stratification with significant temperature difference between the cold and hot layer was observed in all PPOOLEX and PANDA experiments. The development of the stratified layer is governed by the buoyancy, which is modelled by the temperature-dependent water density. In order to model the effect of buoyancy on turbulence source terms for turbulence kinetic energy  $k$  and specific dissipation rate  $\omega$  are modified respectively. Details of the turbulence model implementation can be found in [31].

The turbulence model is  $k - \omega$  BSL model with low-Re corrections which provided the best agreement between prediction and experimental temperature evolution in PANDA & PPOOLEX pool tests [31, 141]. Kato-Launder production term and production limiter are turned on to limit the build-up of  $k$  in the stagnation regions (i.e. the cold layer below the thermocline).

The flow pattern in the pool is sensitive to the boundary conditions for characteristics of turbulence [141]. Turbulence intensity and turbulent viscosity ratio are used to estimate calculate the boundary conditions for the turbulence kinetic energy and dissipation rate. Turbulence intensity in a water jet induced by steam condensation was estimated in [59] to be around 25 – 35% at 0.25  $m$  downstream from the injection orifice. These values have been further confirmed in [95, 96]. With  $I = 30\%$ , the turbulent viscosity ratio can be estimated as  $\mu_t/\mu_l = 1000$  [27]. These two values should be considered as a rough estimate. Significantly larger values were obtained in PIV data from previous PANDA tests. Further investigations of the new PIV data in the PANDA tests should be carried out to clarify.

#### 4.5. Validation against HP5 tests

Validation of the model described in the previous sections is carried out against PANDA HP51 test data using temperature evolutions and PIV measurements. The HP5 tests were done at atmospheric conditions in PANDA facility and discussed in more detail in section 4.1. The temperature evolutions obtained in HP51 TCs and Fluent simulations of 360°, 180°, and 22.5° domains are shown in Figure 25 and Figure 26. The measurements at TCs line 1 are chosen for comparison. Note that these measurements are representative for the whole pool temperature due to the uniformity of the temperature profile in the horizontal (radial) direction in the pool [36], (Figure 4).

There are noticeable differences between the three simulation cases with respect to the temperature evolution. Location of the thermocline during the first injection phase is predicted at the height between  $\tilde{z} = 0.250$  and  $\tilde{z} = 0.219$  for the  $22.5^\circ$  domain and between  $\tilde{z} = 0.219$  and  $\tilde{z} = 0.187$  for the  $180^\circ$  and  $360^\circ$  domains, which agrees well with the TCs measurements of HP51 test. Pool temperature oscillation were observed in all PANDA experiments and are also visible in the simulations with  $180^\circ$  and  $360^\circ$  domains. A similar behavior was reported by Gallego-Marcos et al. [31] where such instabilities were reproduced in a full 3D domain and not in a  $45^\circ$  sector. A faster erosion of thermocline and flow instability during the transient from low to high steam injection phases were observed in the simulations with the slice domains of  $22.5^\circ$  and  $45^\circ$  [31], respectively.

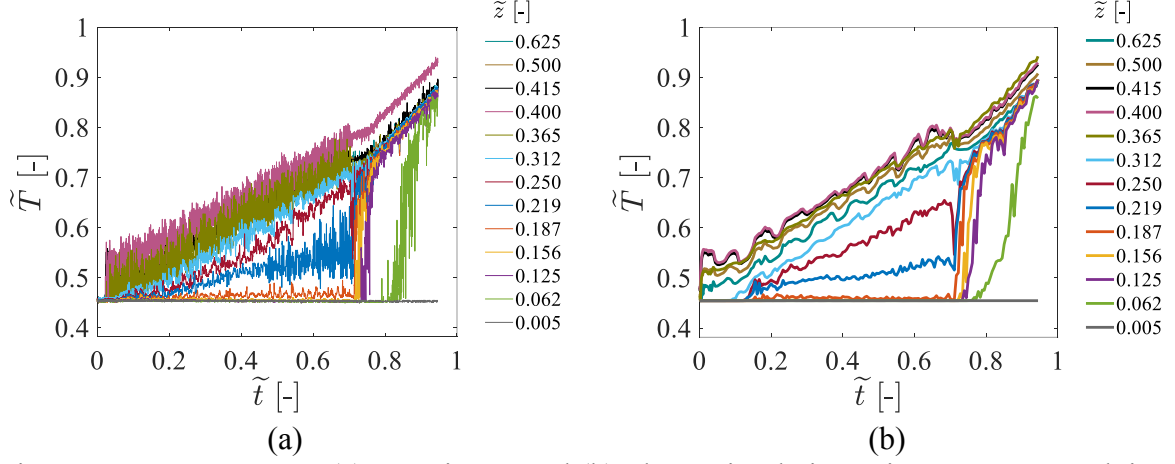


Figure 25. PANDA HP51 (a) experiment and (b) Fluent simulation using SCR approach in a  $360^\circ$  domain.

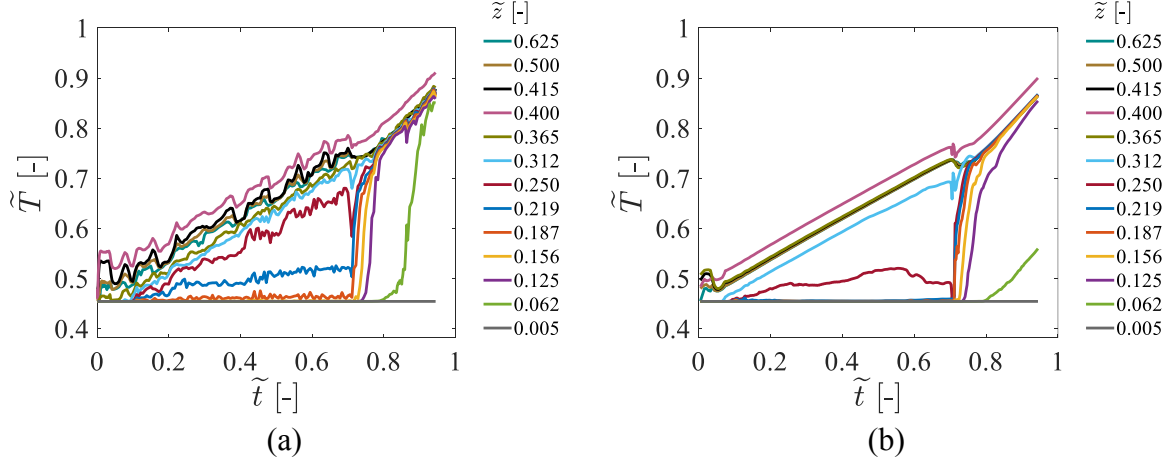


Figure 26. PANDA HP51. Fluent simulation using SCR approach in an (a)  $180^\circ$  domain and (b)  $22.5^\circ$  domain.

These observations indicate that modelling of stratification and mixing induced by steam injection through spargers in the PANDA pool requires sufficiently large 3D domain (at least  $180^\circ$ ). The artificial instabilities can be attributed to the lower degrees of freedom of reduced size 3D and 2D simulation, which prevents large scale vortices from accommodation of changes in the flow pattern. Another advantage of using the 3D model is that the effect of Inter connecting Pipe (IP) can be resolved directly. This component slightly intrudes inside the cylindrical shape of the vessel, which can serve as factor for symmetry-breaking and increased unsteadiness of the flow [31]. Therefore, a 3D domain with at least  $180^\circ$  was used in the following simulations.

HP52 and HP53 tests (Table 1) were analyzed with the same numerical setup used for simulation of HP51. Comparison of the temperature evolutions obtained in the simulations and experiments are presented in Figure 27 and Figure 28. Proposed modelling approach provides an adequate prediction of the pool behavior in different steam injection conditions. The motion of thermocline is well captured at low steam injection conditions. The large temperature gradient across the thermocline is also resolved in the high injection phase.

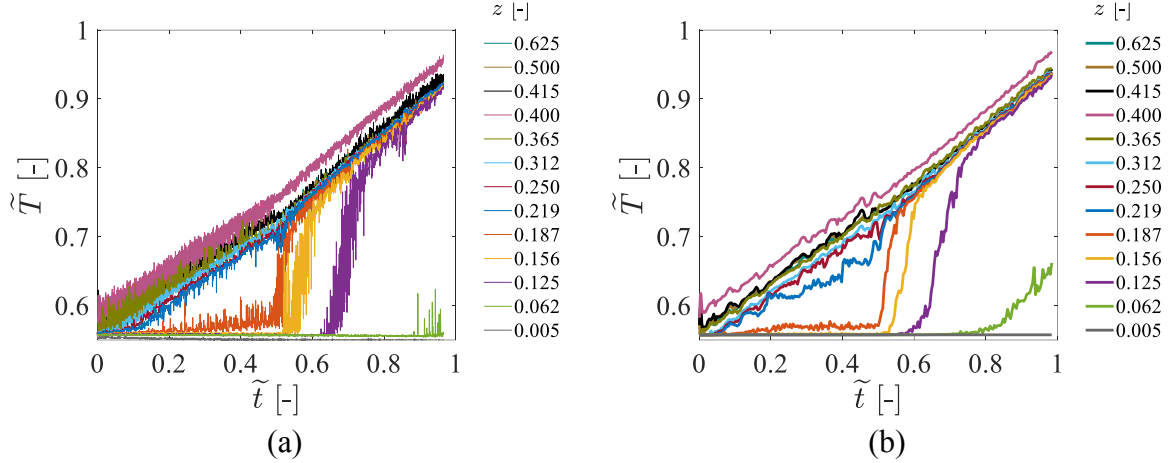


Figure 27. PANDA HP52 (a) experiment and (b) Fluent simulation using SCR approach in a  $180^\circ$  domain.

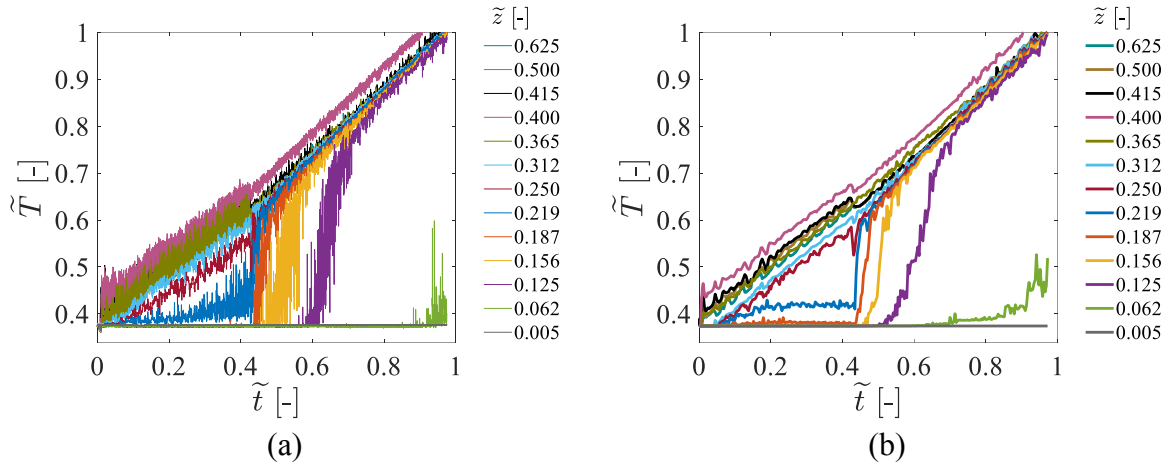


Figure 28. PANDA HP53 (a) experiment and (b) Fluent simulation using SCR approach in a  $180^\circ$  domain.

Figure 29 and Figure 30 provide a comparison of experimental (PIV) and simulation data for the velocity fields in vertical cross sections. PIV measurements were unreliable in some parts of the domain (dark blue areas) due to presence of a large number of gas bubbles. Despite the incompleteness of the PIV field of view, a reasonable agreement of simulation with the experiment on the buoyancy/inertia-driven jets in all phases of steam injection can be observed. Merging of the jets at radial distance of  $\sim 0.2$  m was observed in PIV. This confirms that selected length of SCR is reasonable. The velocity magnitude agrees well with the experiment, indicating that the merged jet velocity profile and selected boundary conditions for turbulence characteristics provide an adequate estimation. Further improvement of the simulations can be achieved by calibration of the boundary conditions for turbulence characteristics, which has considerable effect on the flow patterns (Figure 89).

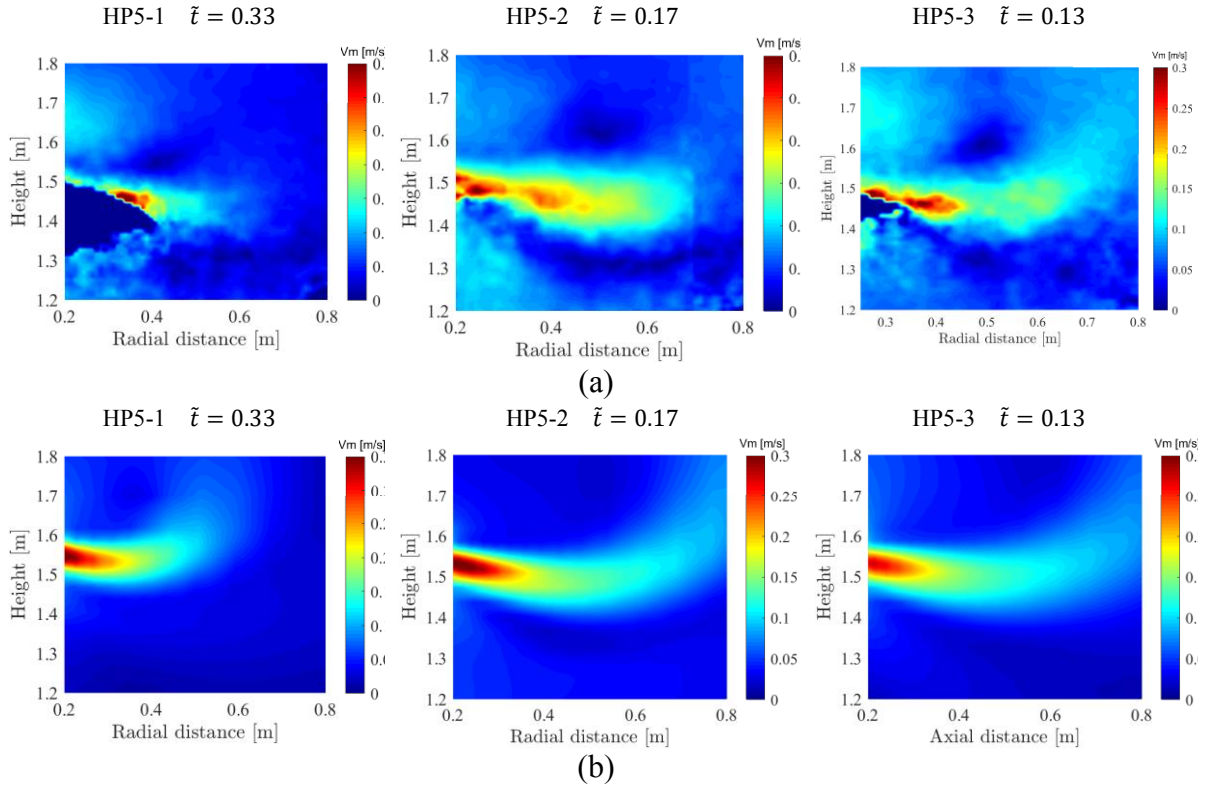


Figure 29. Velocity contours during the low steam injection phases obtained in (a) PIV data from PANDA HP5 tests and (b) Fluent simulations. Data have been time-averaged over 200s.

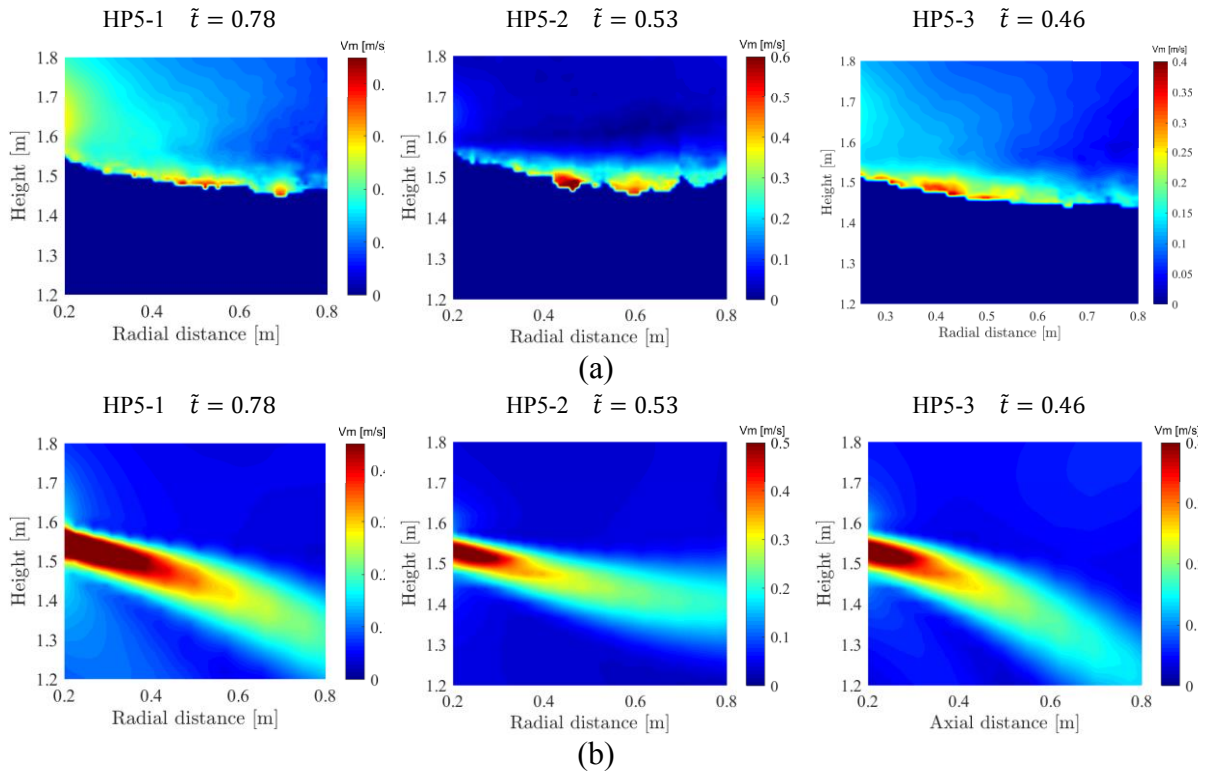


Figure 30. Velocity contours during the high steam injection phases obtained in (a) PIV data from PANDA HP5 tests and (b) Fluent simulations. Data have been time-averaged over 200s.

#### 4.6. Summary of EHS/EMS model development for sparger

In this section we present results of EHS/EMS models development for prediction of the pool behavior induced by the steam injection through a multihole sparger.

First, we discuss calibration of the EHS/EMS models implemented using a source term approach. The results suggest that the temperature evolutions are sensitive to the geometrical characteristics of the domains where EHS/EMS source terms are introduced. Although a good agreement can be achieved between simulations and experiments, a robust calibration process of the model is needed.

Second, we discuss implementation of the EHS/EMS models using steam condensation region (SCR) approach. Main findings and features of the modelling approach are listed below:

- Prototypic pool behavior has large spatial and temporal scales. Single-phase solver is used in order to achieve necessity computational efficiency in resolving the effects of steam condensation in a CFD code.
- Effective momentum is introduced by through boundary conditions and injection of liquid. The temperature of the injected liquid is defined in order to conserve the energy. In order to conserve mass excessive amount of liquid is removed from the domain through the top and bottom surfaces of the SCR.
- A 3D calculation domain with at least  $180^\circ$  is required to obtain a reasonable agreement between simulations and experiment on the temperature evolution and to avoid a large scale flow instability during transition from small to large steam flow rate.
- The velocity profile for the merged jets induced by steam condensation is derived by analytical fitting of the results obtained from the “Unit Cell” model. In this model, all individual jets and interactions between the jets are explicitly modelled.

Validation against PANDA HP5 test series suggest that this model can provide a reasonably accurate prediction of the pool behaviour. Compared to the previous modeling approach where the EHS/EMS models were implemented using source terms, SCR approach avoids uncertainty in the distribution of the momentum source, which can significantly affect temperature evolution in the pool.



## 5. MODELLING OF STEAM INJECTION THROUGH SPARGER

The multi-hole spargers are used to discharge steam from the primary circuit into the PSP, e.g. through SRVs and in the exhaust of safety systems such as the RCIC [8]. The multi-hole injection in horizontal direction results in different pool response compared to the injection in vertical direction through blowdown pipes [34], and therefore, requires further development of the EHS/EMS models.

In this chapter we introduce PPOOLEX SPA tests and the results of development of ‘Unit Cell’ EHS/EMS model. The implementation in Fluent including boundary conditions, flow downward angles and turbulence modelling is presented in Section 5.3, 5.4 and 5.5, respectively. Finally, the validation against SPA-T3 test is given in Section 5.6.

### 5.1. Introduction of PPOOLEX SPA tests

PPOOLEX [6] is a multipurpose test facility (Figure 31) designed to model thermohydraulic phenomena in a BWR containment. For the SPARger tests (SPA), the facility was equipped with a multi-hole sparger as shown in Figure 32. The main features of the facility and its instrumentation are briefly described below. More details can be found in [6].

The facility consists of a 1MW steam generator and a single stainless vessel. The vessel is divided into a wet well and a dry well. The tests were scaled to be able to resolve ranges of parameters and regimes that can capture the most significant physical behavior in plant scale. The vessel was filled with water up to 3 m at room temperature 15 – 20 °C.

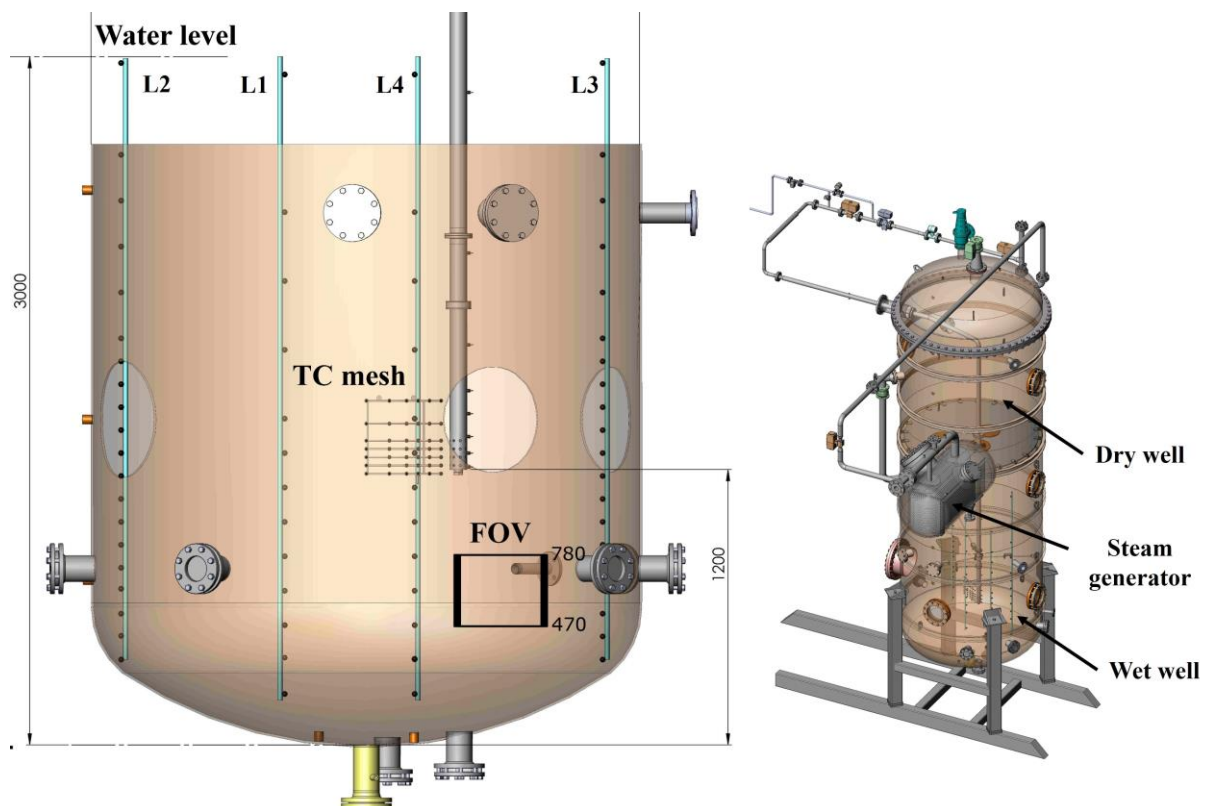


Figure 31. PPOOLEX facility in the SPA tests with sparger [6].



Four vertical trains of thermocouples (TCs, L1~ L4) were mounted in the vessel at different distances from the sparger (Figure 31). A  $6 \times 7$  grid of TC mesh (Figure 46) was placed in front of a column of injection holes of the sparger head.

The sparger was placed 420 mm away from the central axis of the pool at 1200 mm elevation above the bottom of the vessel. The diameter of the pool is about 2.4 m. The geometrical characteristics of the multi-hole sparger used in the tests are shown in Figure 32. The sparger head has 32 holes arranged in 4 rings. Each hole has an inner diameter of 8.0 mm and a conical chamfer.

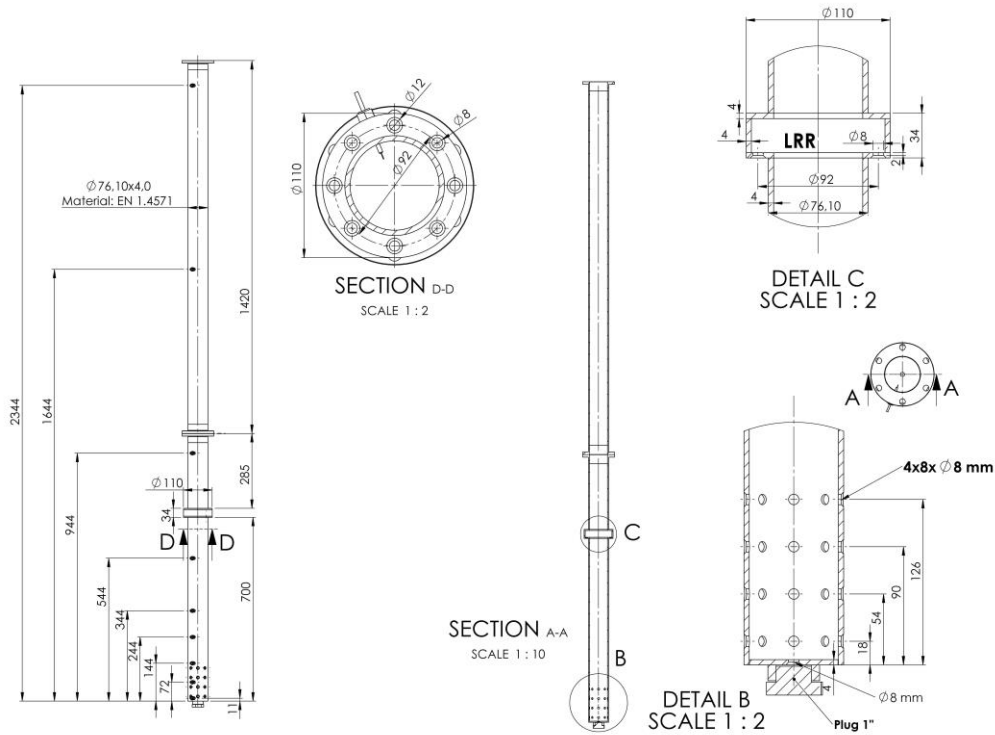


Figure 32. Geometry of PPOOLEX sparger pipe [6].

Trajectories of PPOOLEX SPA tests in terms of pool temperature and steam mass flux are presented in Figure 33. SPA-T3 test was selected for CFD validation with steam injection procedures and initial pool temperatures listed in Table 5. The test has two phases for the development of thermal stratification and two phases for mixing respectively. Low steam mass flow rate (minimum flow rate avoiding the chugging regime, Figure 33) was used to develop stratification in the pool. After the temperature difference between the top and bottom of the pool reached a certain value, the mass flow rate was increased to mix the pool.

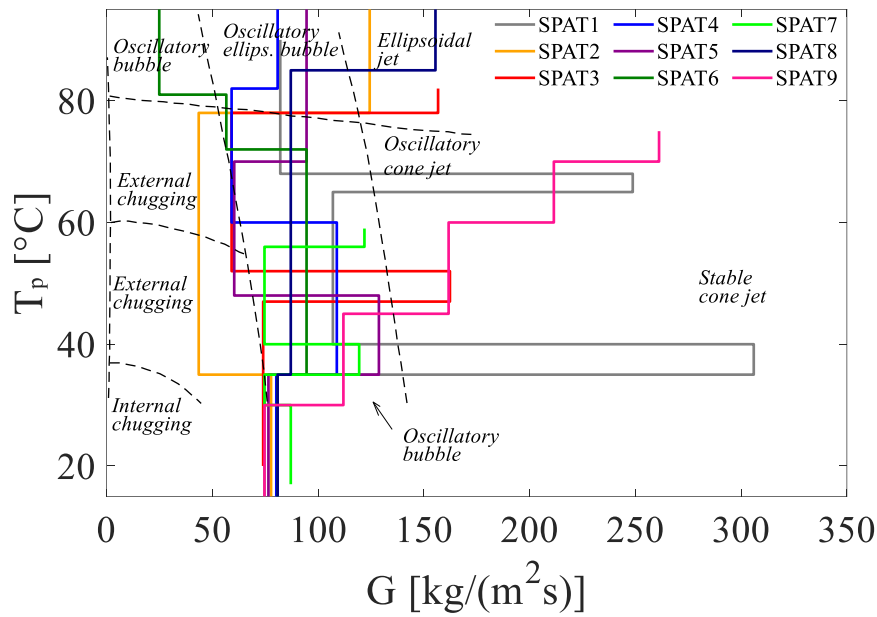


Figure 33. Trajectories of PPOOLEX SPA tests [36].  $G$  is the steam mass flux and  $T_p$  is the pool temperature. Condensation regime boundaries (dashed line) are shown from [43].

Table 5. PPOOLEX SPA-T3 test matrix

Test	Pool Initial Conditions		Phase 1&3 Stratification		Phase 2&4 Mixing	
	Temperature (°C)	Water level (m)	Flow (g/s)	Duration (s)	Flow (g/s)	Duration (s)
T3	~19	3	120	4300	260	700
			95	5800	250	900

The discrepancy between water level (Figure 34a) measurements (by pressure difference and by time integration of steam flow rate) suggests that experimental data require calibration. The steam flow rate was calibrated by multiplying measured values by 0.955 to match water level measurements by the pressure sensor [6] (which is considered more accurate than the flow meter measurements). Note that one of the pressure sensors was placed at 3.3 m thus pool depth values above this height cannot be measured.

A non-uniform temperature distribution in the pool was measured by TCs before the start of steam injection. For instance, colder temperature was measured at elevation  $z = 0.372$  m than temperature measured above and below (Figure 34b). Calibration offsets for the TCs were obtained by calculating the difference between time average temperature measured by each TC and a sum of these temperatures during the first 30 s when no steam was injected. Calibrated temperature evolutions are presented in Figure 66.

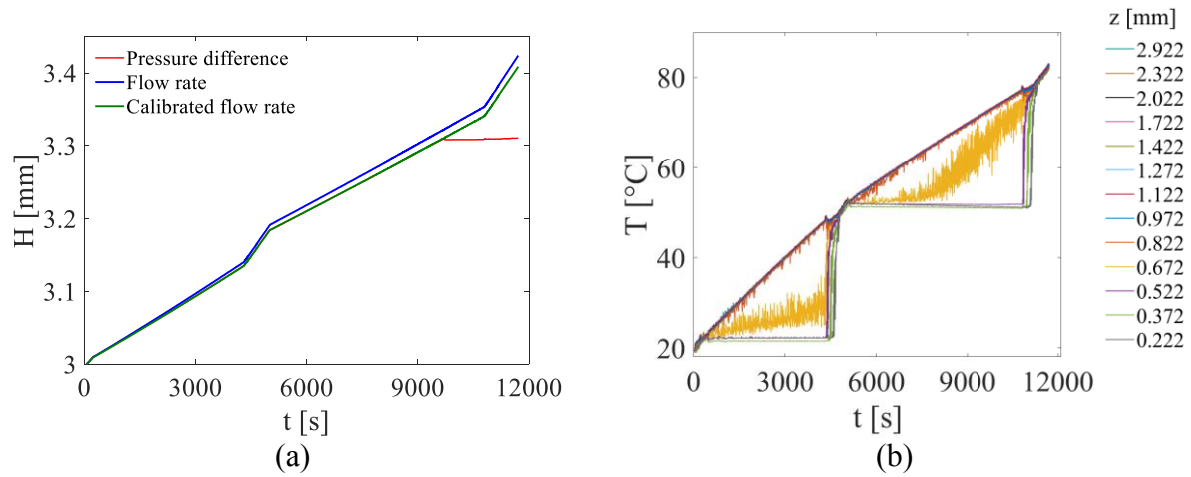


Figure 34. (a) Comparison of water level measurements and (b) temperature evolutions of TCs L1 before calibration of PPOOLEX SPA-T3.

## 5.2. Development of EHS/EMMS models using a “Unit Cell” model

### 5.2.1. EMSR-BC and EMSR-DS methods

Although a good agreement between experiment and simulations can be achieved using the source terms based implementation of the EHS/EMS, currently available test data is insufficient for reliable calibration of all the model parameters. Specifically, characteristics of the spatial distribution of the momentum source. There are two approaches to solve this problem. One is to measure the azimuthal velocity profiles in future pool tests in different steam injection regimes [137]. Another approach is to resolve the model interactions between the jets produced by individual steam injection holes.

To enable the study of such interaction, a “Unit Cell” model is developed. In this model, the liquid jets with the effective momentum and heat by Eqs. (26) (28) are introduced separately through individual holes on sparger tip as shown in Figure 35a. However, resolving each individual jet would require significant computational resources even for PPOOLEX facility with 32 injection holes (Figure 32) and can become completely impractical for plant applications with dozens of spargers and thousands of injection holes.

Fortunately, experimental data [36] from PANDA and PPOOLEX facilities suggest that jets from individual holes merge together in a relatively short distance from the sparger. Resulting fluid velocity profile of the merged jets can be obtained using data from so-called “Unit Cell” simulation model. For practical application (Figure 36), we introduce a relatively small region called EMSR Region (EMSR, Figure 35b) in the vicinity of the sparger head where the details of DCC are not resolved in this region. The effects induced by steam condensation can be modelled by using Boundary Conditions at the interface of EMSR (EMSR-BC) or adding Distributed Sources inside this region (EMSR-DS).

The EMSR-BC approach has been developed and validated against PANDA HP5 pool tests [138, 140]. The velocity profile at the EMSR interface was derived from the CFD simulations for a “Unit Cell” model [140, 141] where jets were simulated individually in a  $22.5^\circ$  sector of the pool domain. In this report, the “Unit Cell” model is further developed and validated against PPOOLEX SPA-T3 test.

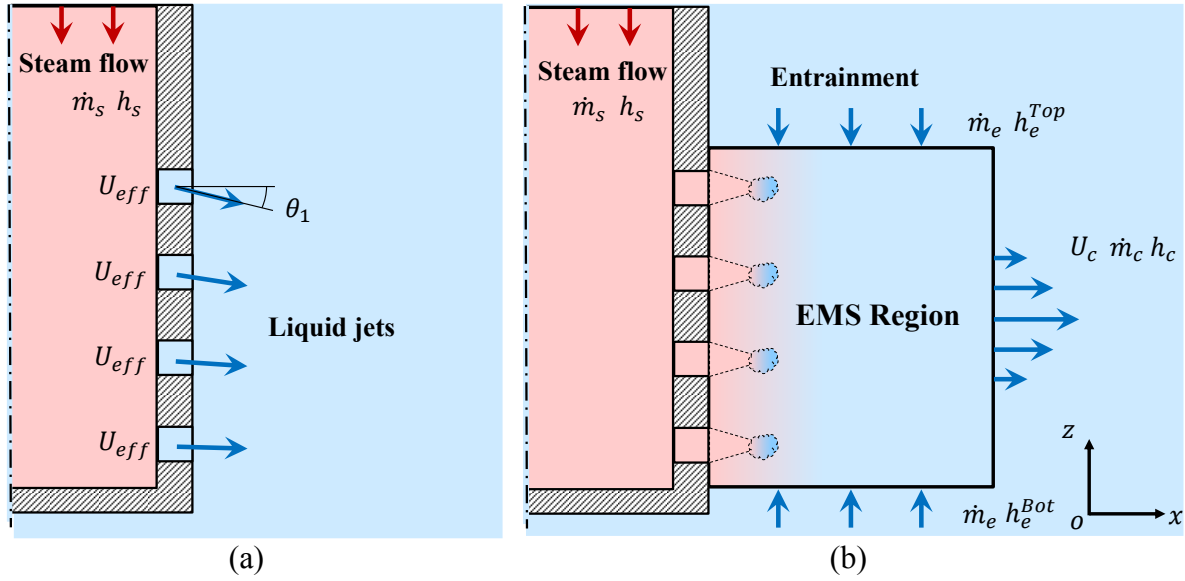


Figure 35. Schematic of (a) “Unit Cell” model and (b) EMSR-BC for steam injection through multi-hole sparger.

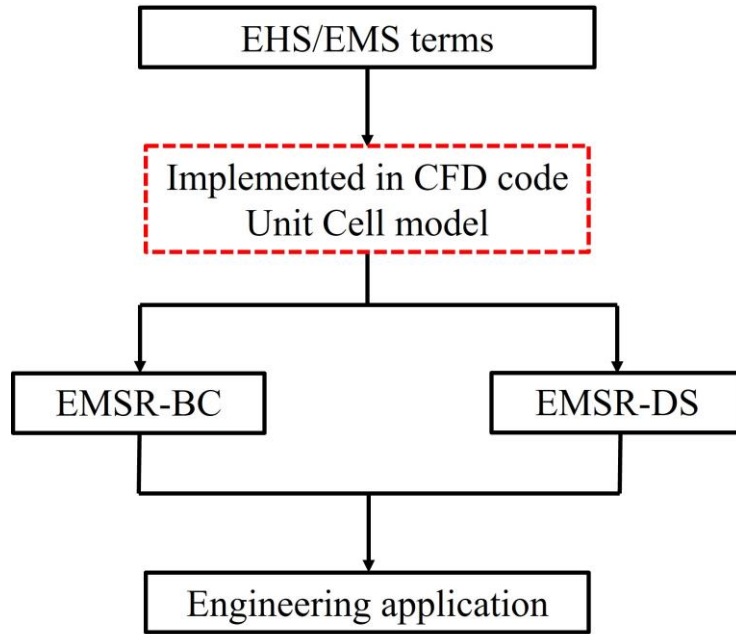


Figure 36. Flow chart of EHS/EMS models from “Unit Cell” model to engineering application.

### 5.2.2. Effective sources of heat and momentum

The effective momentum  $\dot{M}_{eff}$  rate for subsonic steam flow conditions of can be computed [98] by (26):

$$\dot{M}_{eff} = C\dot{M}_{th} = C\rho_s A_0 U_s^2 = \rho_l A_0 U_{eff}^2 \quad (26)$$

where  $C$  is the effective momentum (or condensation regime) coefficient.  $\dot{M}_{th}$  is the theoretical momentum rate of steam,  $\rho_s$  and  $\rho_l$  are the density of steam and liquid respectively;  $A_0$  is the

injection hole area,  $U_s$  is the velocity of steam in the injection hole;  $U_{eff}$  is the effective velocity of the liquid momentum source. The effective momentum rate was measured in the Separate Effect Facility (SEF) with 8 – 16 mm diameter holes [98]. Respective coefficient of the effective momentum can be approximated by an empirical correlation:

$$C = 4.28\Delta T^{-0.35} \quad (27)$$

where  $\Delta T$  is water subcooling. Note that in the previous work [31] the coefficient was estimated based on CFD simulations of PPOOLEX and PANDA experiments.

The effective heat source  $\dot{Q}$  is computed by:

$$\dot{Q} = \dot{m}_s h_s \quad (28)$$

where  $\dot{m}_s$  and  $h_s$  are the mass flow rate and enthalpy of the steam.

### 5.2.3. Single-phase turbulent jets

Thermal stratification and mixing in a large pool are determined by a competition between buoyancy and momentum induced by the steam injection. The momentum created by injection through a multi-hole sparger [133] is introduced in a form of jets created by condensing steam. Characteristics of the velocity in the far-field (after condensation is finished) for such jets are similar to the single-phase turbulent jets [28, 72, 95, 133].

We consider a water jet injected through a nozzle into a large tank with stagnant water (Figure 37). The domain that contains the turbulent jet has a conical shape. Regardless of the type of fluid (water or air) and other conditions (such as nozzle diameter and discharge speed), the expansion angle is a constant [134] of  $11.8^\circ$ .

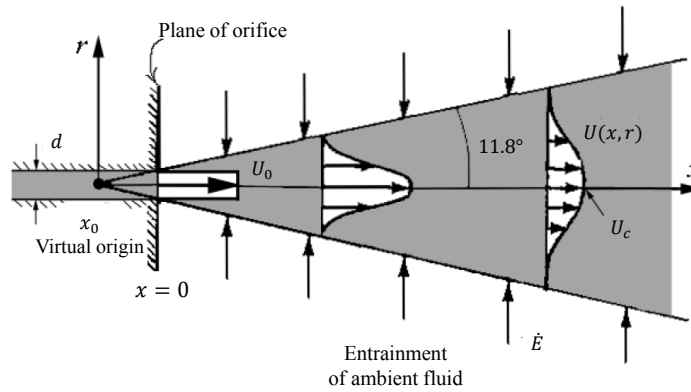


Figure 37. Schematic of a jet penetrating in a still fluid.

The mean centerline velocity  $U_c(x)$  can be expressed by Eq. (29) [121].

$$\frac{U_c(x)}{U_0} = \frac{Bd}{(x - x_0)} \quad (29)$$

where  $U_0$  is the mean exit velocity,  $B$  the decay rate,  $d$  the nozzle diameter and  $x_0$  the so called virtual origin of the jet.

The fully developed axisymmetric velocity profile obeys a law of self-similarity. By considering the effect of virtual origin, this profile can be presented as:

$$U(x, r) = U_c(x) e^{\left(-K \frac{r^2}{(x-x_0)^2}\right)} \quad (30)$$

Where  $K$  is the expansion factor, for round and plane jets, are 77 and 50 respectively in a single-phase flow [110, 121]. Analysis of the PIV data from PANDA experiments suggests that the  $K$  is about 40 or less [36] in the vertical direction. The difference could be due to the effect of multi-hole sparger injection, condensation regime, and turbulence.

The momentum rate of the jet can be obtained by integration:

$$\dot{M} = \int_0^\infty \rho U(x, r)^2 2\pi r dr = \frac{1}{4} \pi d^2 \rho U_0^2 \cdot \frac{2B^2}{K} \quad (31)$$

Since the jet momentum is conserved (if viscous energy dissipation is neglected) at any downstream cross-section of the jet and equal to its initial momentum  $\pi d^2 \rho U_0^2 / 4$ , the decay rate and expansion ratio are constant for a given jet. Hence, we can deduce a relation between  $B$  and  $K$  given by Eq. (32), which shows that a jet with faster decay of the centerline velocity should also expand faster.

$$2B^2 \sim K \quad (32)$$

Investigation of velocity characteristics induced by air, water, and steam jets shows for the fully developed jets  $2B^2/K = 0.88 \sim 1.05$  [133]. The mass flow rate  $\dot{Q}$  is not conserved because of the entrainment of ambient fluid. The jet mass flow rate can be calculated by integration (33).

$$\dot{Q} = \int_0^\infty 2\pi r \rho U(x, r) dr = \pi d \rho U_0 \frac{B}{K} \cdot (x - x_0) \quad (33)$$

The entrainment rate  $\dot{E}$  is defined as the rate at which the jet mass flow rate grows along the jet axis.

$$\dot{E} = \frac{d\dot{Q}}{dx} = \pi d \rho U_0 \frac{B}{K} \quad (34)$$

#### 5.2.4. Comparison of analytical and CFD results for single jet flow

In this section we discuss comparison of predictions for a single jet by the analytical model and CFD code Fluent. In the SEF tests [98] only the effective momentum induced by steam injection was measured. Other experimental data [58, 72, 95, 96] for condensed steam jets are available in sonic and super-sonic injection regimes. The velocity profile data for a single jet induced by steam condensation in the oscillatory bubble regime is not available. Therefore, a typical single-phase turbulent round jet [134] is used in this validation. Its main parameters are summarized in Table 6.

Table 6. Parameters of a typical turbulent round jet

	$Re$	$B$	$K$	$x_0$	$d$	$U_0$
	[-]	[-]	[-]	[mm]	[mm]	[m/s]
Theory	95500	5	50	-25	10	9.6

In this simulation, a jet is created by injection of water with a uniform velocity of  $U_0 = 9.6 \text{ m/s}$  through a cylindrical hole with diameter  $d = 10 \text{ mm}$ . The  $k - \omega$  BSL turbulence model is used, more details can be found in Section 5.5. Boundary conditions for the turbulence characteristics, namely, turbulence intensity ( $I$ ) and turbulent viscosity ratio ( $\mu_t/\mu$ ) are adjusted in order to fit the far-field velocity profiles according to Eqs. (29) and (30). As a result, the turbulence intensity of 50% and the turbulent viscosity ratio of 3000 were selected in the analysis.

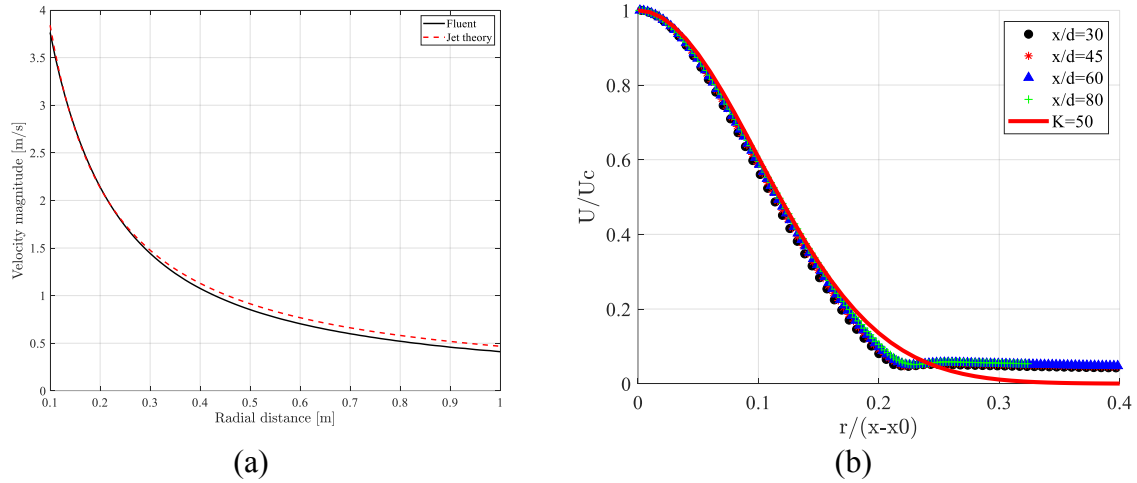


Figure 38. Comparison between Fluent and jet theory of (a) centerline velocity versus distance along the radial direction and (b) mean axial velocity versus radial distance at different slices.

A comparison of the centerline velocity profile between the Fluent and the analytical model is presented in Figure 38a. Self-similarity of the axial velocity profile is clearly seen in different sections of the jet showing a nearly Gaussian shape (Figure 38b). The velocity is scaled by the cross-section centerline velocity and the axial distance by the distance between the jet virtual origin and the coordinate of the cross-section  $x - x_0$ . Theoretical profile by Eq. (30) with  $K=50$  is plotted for comparison.

A jet induced by steam condensation is characterized by high turbulence intensity in the vicinity of steam condensation region and follows self-similarity in the far field. In this work we model such effects using a “Unit Cell” approach with a single phase jet and proper selection of the initial characteristics of turbulence ( $I$  and  $\mu_t/\mu_l$ ).

The momentum and entrainment integrated over different cross-sections of the jet are presented in Table 4. Theoretical values are calculated by Eqs (31) (33) and (34). The momentum and entrainment rates are slowly decreasing along the jet axis, probably due to the numerical dissipation and/or the effect of the walls in the finite computational domain. In general, we can

conclude that described modelling method can be used for a single phase jet induced by steam condensation.

Table 7. Momentum and entrainment at different slices

Distance [m]	Theory	Inlet	0.05	0.3	0.45	0.6	0.8
Momentum rate [N]	7.22	7.20	7.34	6.76	6.60	6.40	6.38
Entrainment rate [kg/ms]	30.07	29.30	30.01	25.38	24.83	24.27	24.10



### 5.3. Computational domain and boundary conditions

EHS/EMS models for multi-hole sparger can be implemented in any CFD code. ANSYS Fluent 2019 R3 is used as an example in this work. In this section, we describe the computational domain and boundary conditions for the “Unit Cell” model.

#### 5.3.1. Computational domain

The computational domain is shown in Figure 39. The height of the water level and sparger tip are  $3\text{ m}$  and  $1.2\text{ m}$  above the bottom of the pool. Previous study [138] suggests that a  $1/16$  sector domain ( $22.5^\circ$ ) is insufficient to resolve the flow structures and respective pool behavior. Both  $180^\circ$  and  $360^\circ$  domains can provide reasonable results with respect to temperature evolution. Thus, we use the  $180^\circ$  domain in this work to improve computational efficiency.

Two types of meshes can be applied depending on which implementation method is used to introduce the effective liquid velocity (Eq. (35)). In order to explore all possible modelling methods and improve the completeness of the work, the modelling setup and simulation results with these two meshes are introduced in this report.

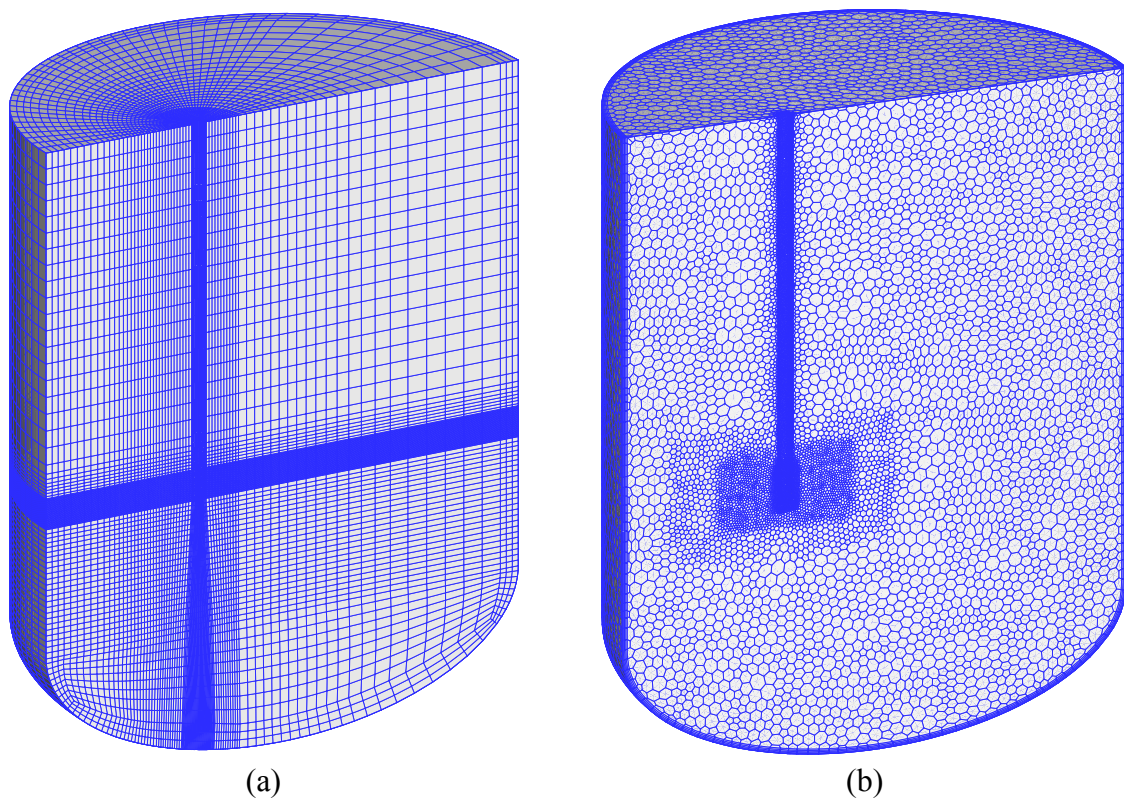


Figure 39. Computational domain with (a) hexahedral-block and (b) polyhedral mesh.

Hexahedral-block meshing can be applied if the small injection holes ( $d = 8\text{ mm}$ ) are modelled implicitly, i.e. the liquid jet is introduced by User Defined Function (UDF [126]) with uniform profiles on the sparger tip (Figure 40a). The main advantage of this method is its high quality hexahedral mesh. However, there are layers of fine size cells that extend away from the sparger head into the regions where such fine resolution is not needed. Also the non-central position of the sparger makes the mesh created relatively large cells in radial direction (Figure 39a).

The injection holes can be modelled explicitly using polyhedral [126] mesh as shown in Figure 39b. For rotating flows, the polyhedral mesh would be better than hexahedral mesh as the larger number of faces of a polyhedral cell allow it to have more chances to be aligned with the flow. The polyhedral mesh is easy to set up for the geometry of the pool and the mesh quality should be good sufficient.

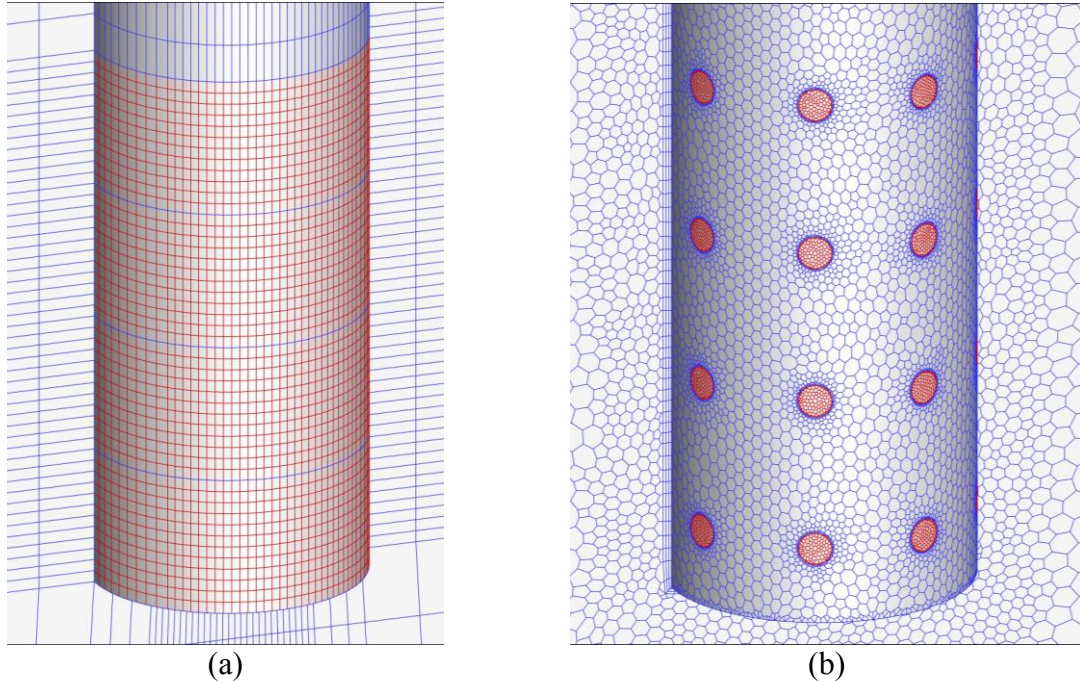


Figure 40. Sparger head with (a) hexahedral-block mesh and (b) polyhedral mesh.

For hexahedral block mesh, the effect of grid refinement on the solution was carried out to reduce the sensitivity of the results to grid resolution [31]. For a full domain ( $360^\circ$ ) 128 cells in the azimuthal direction were used and the size of cells in the vertical direction above/below sparger is about 50/25 mm respectively.

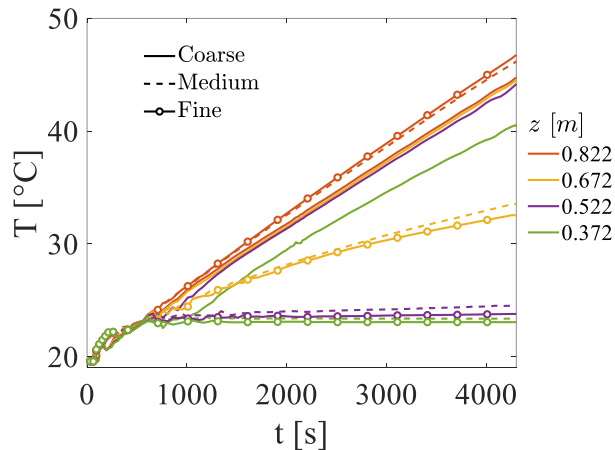


Figure 41. Effects of mesh density of polyhedral mesh on the temperature evolutions in PPOOLEX SPA-T3 phase 1. TKE-DS with  $\dot{S}_{k_1} = 60$  was used in these simulations.

For polyhedral mesh, smooth transition from the sparger tip to the surrounding wall was applied. The mesh below the sparger tip was refined in order to better capture the stratified layer. Mesh sensitivity study was performed with three different mesh densities. The coarse mesh contains 165000 cells, while the medium and fine mesh contains 362000 and 914000 cells,

respectively. From Figure 41, mesh convergence with respect to the temperature evolutions is achieved when “Medium” mesh is applied. According to the results and considering the computational time, the “Medium” mesh was decided to be used in the following simulations.

### 5.3.2. Boundary conditions

The effective liquid jet was introduced by providing the uniform velocity profile in a circular area with a diameter of 8 mm. According to Eqs. (26) and (27), the magnitude of velocity can be written as:

$$U_{eff} = \sqrt{\frac{C\rho_s}{\rho_l}} U_s \quad (35)$$

Since the momentum created by steam was modelled by water injection, the mass flow rate inlet of water was many times higher than the actual value of steam injection. To preserve the mass balance, some water should be taken out from the pool with a total mass flow rate given by Eq. (36).

$$\dot{m}_{out} = \dot{m}_{in} - \dot{m}_s \quad (36)$$

where  $\dot{m}_{in}$  is the total mass flow rate of the effective liquid jets and  $\dot{m}_s$  the mass flow rate of injected steam.  $\dot{m}_{out}$  could be implemented as a mass sink ( $\frac{\dot{m}_{out}}{V_p} \Delta V_{cell}$ ) in each cell of the domain to minimize the effect of the mass loss on the momentum distribution in the pool. However, such implementation leads to artificial cooling in the domain with mass sink. Therefore, the extra water was removed from the pool surface.

Heat balance was achieved by using the time-averaged heat source estimated by the EHS model (Eq. (28)). The enthalpy of the effective liquid  $h_l^{in}$  can be defined by Eqs (37) (38). The  $h_l^{in}$  is implemented by setting the inlet boundary conditions for the temperature according to Eq. (39).

$$\dot{q}_{in} = \dot{q}_s + \dot{q}_{out} + \dot{q}_{bc} \quad (37)$$

$$h_l^{in} \cdot \dot{m}_{in} = h_s \cdot \dot{m}_s + h_l^{out} \cdot \dot{m}_{out} + \dot{q}_{bc} \quad (38)$$

$$T^{in} = \frac{h_l^{in}}{C_p} \quad (39)$$

where  $\dot{m}_{in}$  is the mass flow rate of inlet liquid, sub-indexes  $l$  and  $s$  indicate liquid and steam respectively,  $in$  and  $out$  correspond to input and output,  $C_p$  are the specific heat capacity. In the simulation, when mass is taken out from the pool surface, the energy will be removed as well. To compensate for the loss of removed heat,  $\dot{q}_{out}$  is introduced and it can be calculated as Eq. (40).

$$h_l^{out} \cdot \dot{m}_{out} = \iint_{A_p} \rho C_p T u ds \approx \sum_{i=1}^{N_c} \rho_i u_i C_p T_i A_i \quad (40)$$

where  $A_p$  is the area of pool surface,  $N_c$  the number of cells,  $\rho_i u_i T_i A_i$  are density, velocity, temperature and area of the cell.

For the hexahedral-block mesh (Figure 39a), the areas where no velocity is introduced are not adiabatic as they are defined as velocity inlet boundaries (even if velocity is zero). Thus  $\dot{q}_{bc}$  is used to compensate the energy difference introduced by the boundary conditions as Eq. (41).

$$\dot{q}_{bc} = \dot{q}_{net}^{in} - \dot{q}_{in} \quad (41)$$

where  $\dot{q}_{net}^{in}$  is the net heat flux on the velocity inlet boundary at the sparger head (Figure 39a). It can be calculated by UDF code “BOUNDARY\_HEAT\_FLUX(f,t)”. This code is not introduced in Fluent guide book [126] but can be found in “CFD Online”[142]. Note that  $\dot{q}_{bc} = 0$  for simulations using polyhedral mesh.

From Figure 42, it can be found that the total energy estimated by four vertical lines of TCs agrees well with the EHS prediction. The relatively small difference after 6500s can be attributed to the thermal inertial of the steel of the pool and heat loss to the environment (that were not modeled in this analysis). Simulation with hexahedral mesh would achieve good agreement when  $\dot{q}_{bc}$  is considered.

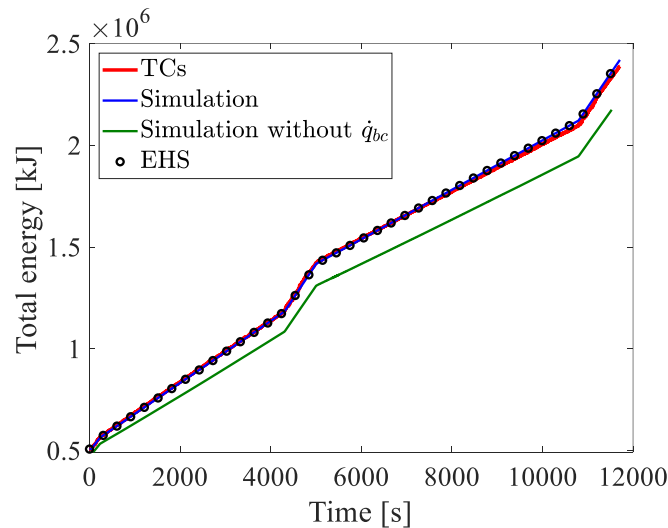


Figure 42. Total energy of PPOOLEX SPA-T3 estimated by Thermocouples (TCs), EHS model and simulations with hexahedral-block mesh using Eq. (38) with and without  $\dot{q}_{bc}$ .

Dynamic mesh is turned on to allow for the increase of liquid level in a single-phase solver [31]. The Pressure-Implicit with Splitting of Operators (PISO) with “Quick” spatial discretization scheme in momentum, Turbulence Kinetic Energy (TKE,  $k$ ), specific dissipation rate ( $\omega$ ), and energy were used. The simulation is considered fully converged when the residual was below  $1e-6$  for energy and  $1e-4$  for other variables.

#### 5.4. Downward angles

A downward inclination of the condensing jets was observed in PPOOLEX and PANDA tests [36]. It was caused by the downward part of the steam velocity at the sparger hole outlet. This angle was quantified to be about  $10^\circ$  for a merged jet induced by gas to gas injection as shown in Figure 43. As its effects cannot be ignored [31], the angles (for each hole) were firstly



estimated by an internal sparger pipe flow simulation and then were calibrated using the TC mesh measurement.

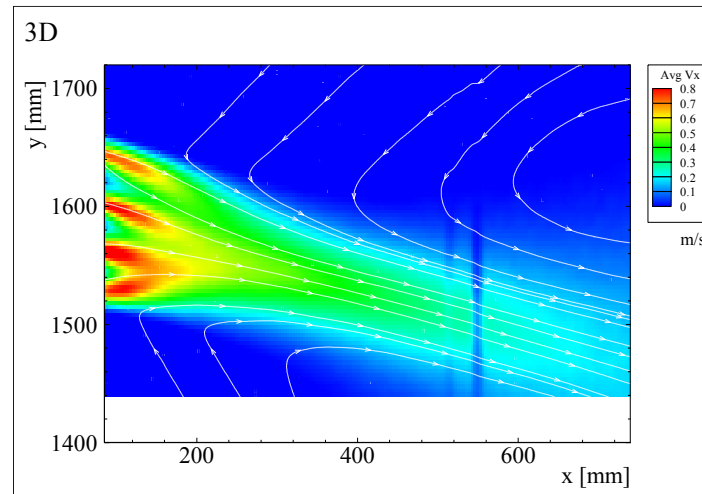


Figure 43. Velocity contours and streamlines during gas to gas test in PANDA. Data were time-averaged over 200s [36].

#### 5.4.1. Internal flow model

Figure 44 presents the domain of a 1/8 model of detailed PPOOLEX sparger geometry used to study the downward inclination and flow rate distribution for each injection hole. The steam injection was simulated by liquid injection with the same effective momentum according to nominal flow rates in SPA-T3 (Table 5). The effective velocity evaluated by Eq. (35) was applied to the inlet as shown in Figure 44a. The area-averaged velocity components of radial ( $o - x$ ) and vertical ( $o - z$ ) direction were used to solve the downward inclination.

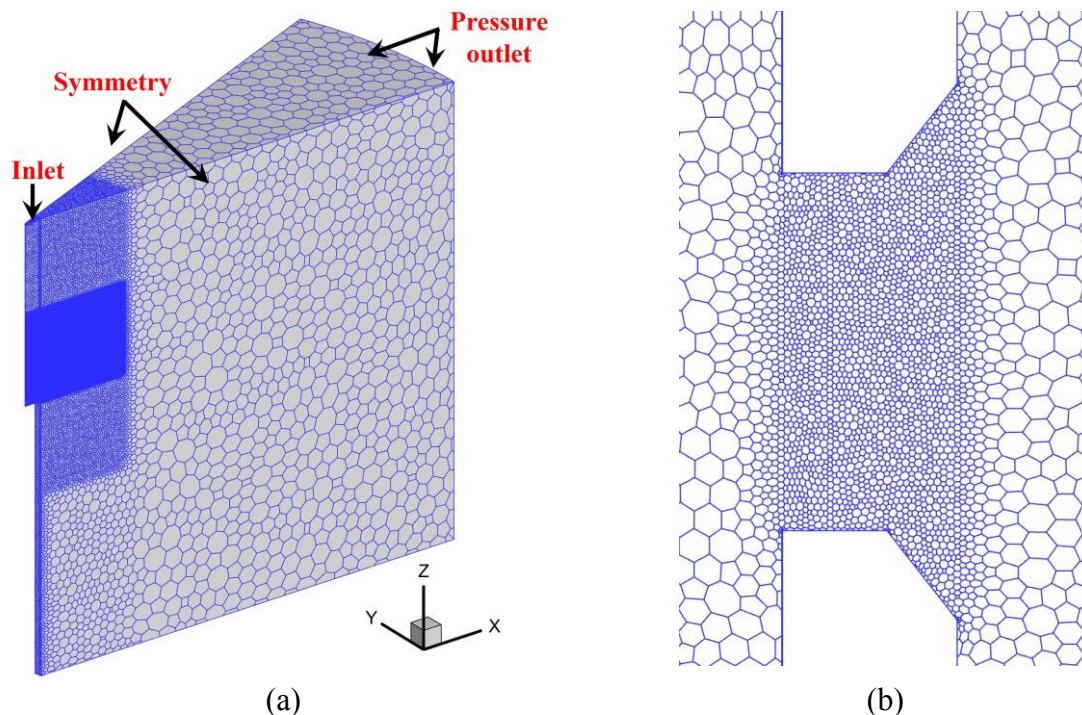


Figure 44. Computational domain of internal flow model for PPOOLEX sparger. (a) overview and (c) local hole.

The variance of flow rate between different holes is smaller than 3% thus the flow rate was assumed to be distributed evenly. As these angles vary a little with the increase of liquid velocity (Figure 45), their averaged values were considered as the input for the simulation. The values are  $14^\circ$ ,  $12^\circ$ ,  $9.5^\circ$ ,  $3^\circ$  from hole #4 (top) to hole #1 (bottom). They were applied in the simulation through the velocity inlet boundary conditions in a local cylindrical coordinate system.

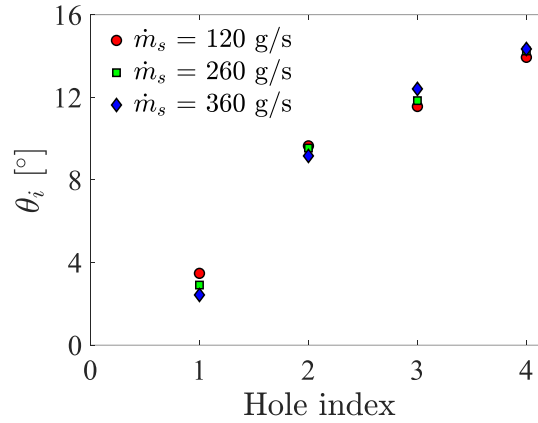


Figure 45. The effect of liquid velocity on the downward angles for each injection hole. Hole #1 represents the bottom hole on sparger head.

#### 5.4.2. Calibration by TC mesh

The downward inclinations from the internal flow model should be regarded as a rough estimate as the steam condensation was simulated by effective liquid. In this section, these angles were calibrated by TC mesh measurement. TC mesh is a group of thermocouples placed around the sparger head (Figure 46) to measure the local thermal behavior. Their measurement frequency is 20 Hz.

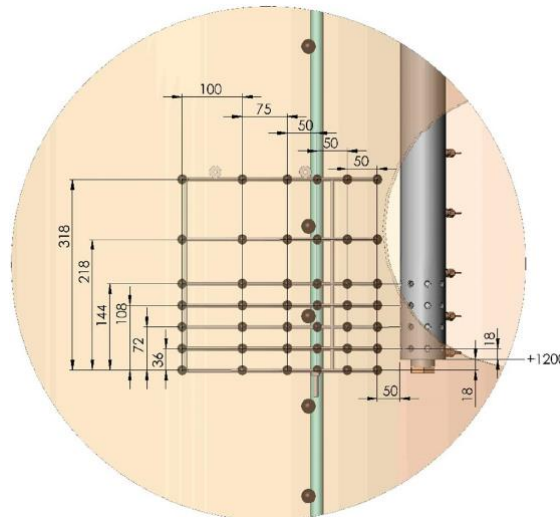


Figure 46. TC mesh (unit: mm) around the sparger head [6].

The  $\theta_i = 14^\circ, 12^\circ, 9.5^\circ, 3^\circ$  obtained by the internal flow model would result in a more inclined resultant jet in the first injection phase by comparing their temperature contours between TC mesh and simulation. Calibration was performed by reducing an identical angle ( $3^\circ$ ) for each

ring and good agreement can be achieved when using  $\theta_i = 11^\circ, 9^\circ, 6.5^\circ, 0^\circ$  (Figure 47). Meanwhile, a more inclined jet would lead to a higher vertical momentum component that prevents the jet from being bent upward by buoyancy, resulting in a delay in the establishment of thermal stratification as shown in Figure 50a. Details of TKE-BC and TKE-DS can be found in Section 5.5.

However, in the second injection phase (mixing phase), the angles  $\theta_i = 11^\circ, 9^\circ, 6.5^\circ, 0^\circ$  are not sufficient to mix the pool completely as shown in Figure 50b. Thus they were increased to  $\theta_i = 14^\circ, 12^\circ, 9.5^\circ, 3^\circ$ . The agreement of temperature evolutions (Figure 50b) and temperature contours (Figure 48) between test and simulation suggests that these angles would be appropriate during this phase. In the third and fourth injection phase (re-stratification and mixing phases), no significant difference was observed (Figure 50c) when applying these two sets of angles, therefore the angles were not changed.

Above all, we decide to use  $\theta_i = 11^\circ, 9^\circ, 6.5^\circ, 0^\circ$  in phase 1 and  $14^\circ, 12^\circ, 9.5^\circ, 3^\circ$  in the rest of the phases.

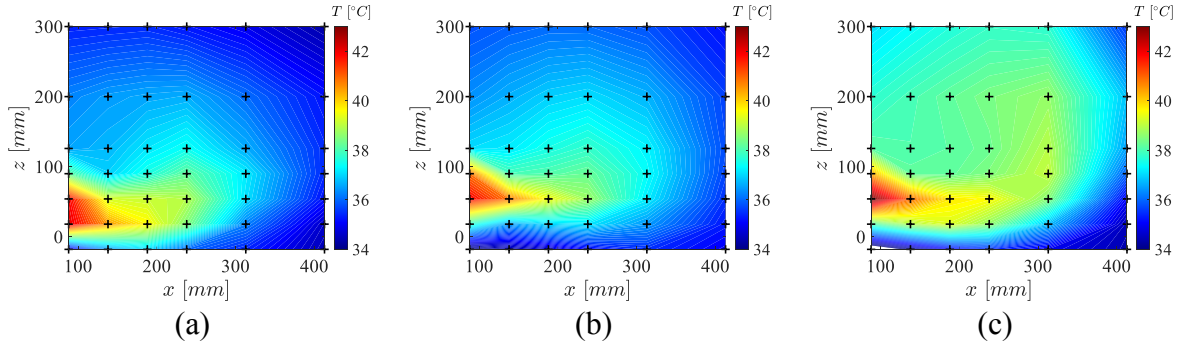


Figure 47. Temperature contours during phase 1 of SPA-T3. (a) TC mesh measurement averaged over 25s. Fluent simulation using (b) TKE-DS with  $\hat{S}_{k_1} = 60$ , and (c) TKE-BC with  $I = 800\% \mu_t/\mu = 4e4$ . Both simulations use  $\theta_i = 11^\circ, 9^\circ, 6.5^\circ, 0^\circ$ . Symbol(+) corresponds to the TC locations.

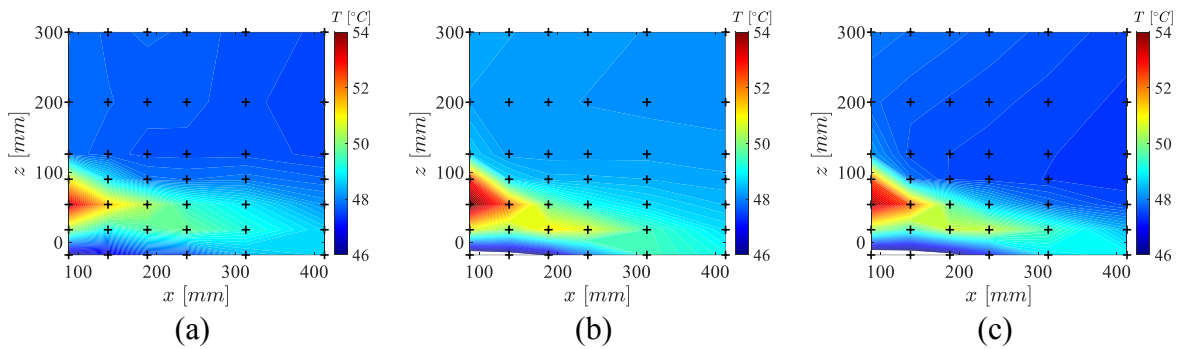


Figure 48. Temperature contours during phase 2 of SPA-T3. (a) TC mesh measurement averaged over 25s. Fluent simulation using (b) TKE-DS with  $\hat{S}_{k_1} = 60$ , and (c) TKE-BC with  $I = 200\% \mu_t/\mu = 1e4$ . Both simulations use  $\theta_i = 14^\circ, 12^\circ, 9.5^\circ, 0^\circ$ . Symbol(+) corresponds to the TC locations.

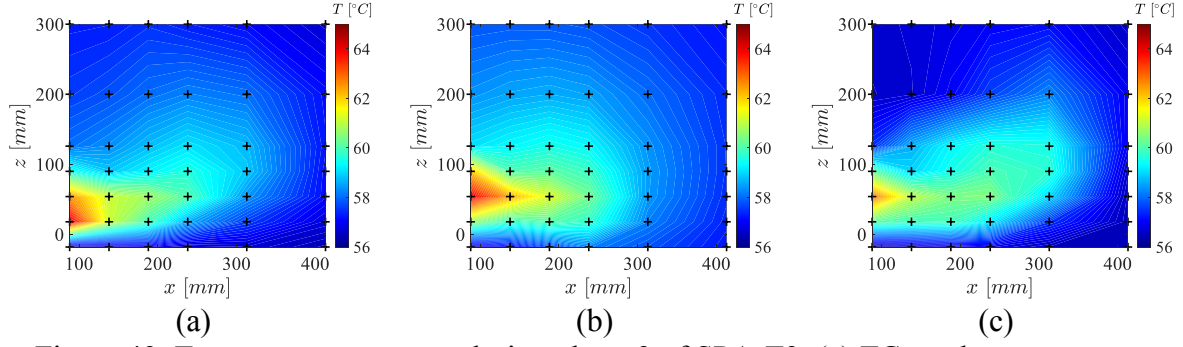


Figure 49. Temperature contours during phase 3 of SPA-T3. (a) TC mesh measurement averaged over 25s. Fluent simulation using (b) TKE-DS with  $\hat{S}_{k_1} = 60$ , and (c) TKE-BC with  $I = 200\% \mu_t/\mu = 1e4$ . Both simulations use  $\theta_i = 14^\circ, 12^\circ, 9.5^\circ, 0^\circ$ . Symbol(+) corresponds to the TC locations.

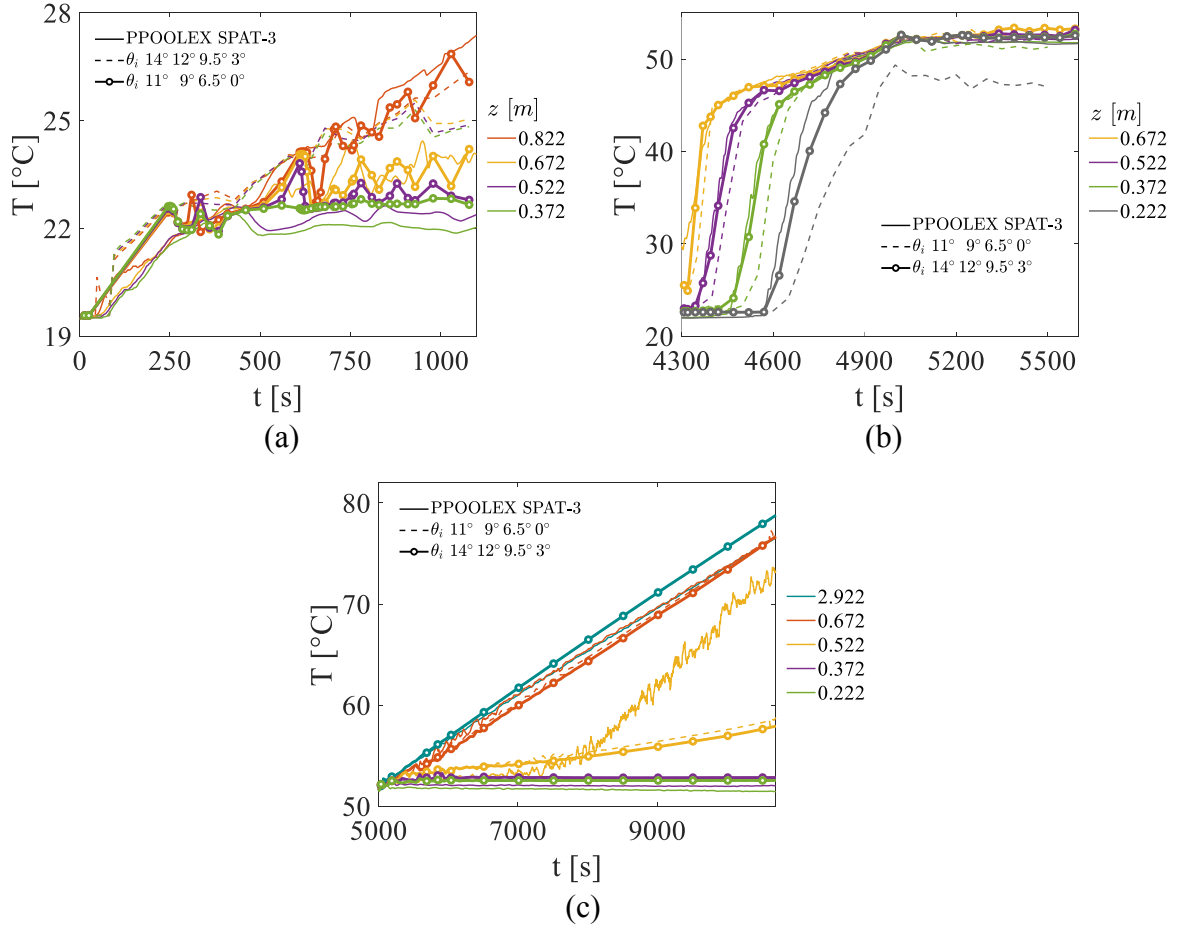


Figure 50. Effects of downward angles on temperature evolutions in (a) phase 1, (b) phase 2 and (c) phase 3. TKE-BC with  $I = 800\% \mu_t/\mu = 4e4$  was used in phase 1 and  $I = 200\% \mu_t/\mu = 1e4$  in phase 2&3.

## 5.5. Turbulence model

Modelling of turbulence is the major source of uncertainty in the “Unit Cell” implementation of the EHS/EMS models, specifically (i) selection of the base model (ii) buoyancy effects (iii) turbulence induced by steam condensation. There are several possible routes towards reduction



of the uncertainty using (i) separate effect tests to measure the turbulence characteristics of jets created by steam injection into water or (ii) pool tests data (PANDA & PPOOLEX) to calibrate turbulence model parameters according to the temperature distribution and local 2D PIV measurement.

However, reliable measurement of turbulence characteristics of steam condensation in the oscillatory bubble regime is not possible due to the motion of bubbles and temperature gradients. 3D PIV measurement was applied to HYMERES-2 PANDA H2P3 tests but failed eventually. The particle density recorded by two cameras varies significantly. It might be caused by the high temperature gradients that the light travelling from the particles experience different refractive indices during their passages towards two cameras. Therefore, we focus on the second route in this report that relies on the pool test results from previous PANDA & PPOOLEX experiments.

Validated modelling approach for buoyancy effects on turbulence is presented in Section 5.5.1. Turbulence induced by steam condensation and its modelling method are presented in the rest of the sections.

#### 5.5.1. Buoyancy effects on turbulence

Stable stratification with the cold layer remained at its initial pool temperature throughout the test, was observed in all PPOOLEX and PANDA experiments. Buoyancy and momentum sources are paramount for the development of stratification. The buoyancy is affected by the local temperature differences, which are determined by the turbulent diffusion.

We use  $k - \omega$  BSL turbulence model with low-Re corrections. Kato-Launder production term and production limiter are turned on to limit the build-up of  $k$  in the flow stagnation region of the stratified layer. This setup provided the best agreement between prediction and experimental temperature evolution in PANDA & PPOOLEX pool tests [31]. The effect of buoyancy on the  $k$  and  $\omega$  is modelled according to Eqs. (42) and (43) respectively. Details of the turbulence model implementation can be found in [31].

$$\frac{Dk}{Dt} = \mathcal{P} + \mathcal{G} - \mathcal{D}_k + \mathcal{T}_k \quad (42)$$

$$\frac{D\omega}{Dt} = C_\alpha \frac{\omega}{k} (\mathcal{P} + C_{3\varepsilon} \mathcal{G}) - C_\beta \omega^2 + \mathcal{T}_\omega \quad (43)$$

where  $\mathcal{P}$  and  $\mathcal{G}$  is the production of  $k$  due to shear and buoyancy, respectively;  $\mathcal{D}_k$  represents the dissipation.  $\mathcal{T}_k$  and  $\mathcal{T}_\omega$  are effective diffusivity of  $k$  and  $\omega$ ;  $C_\alpha$ ,  $C_\beta$  and  $C_{3\varepsilon}$  are closure coefficient for turbulence models. The Richardson number  $Ri_g$  (Eq. (44)) is used in the definition of  $C_{3\varepsilon}$  as in [31]:

$$C_{3\varepsilon} = \begin{cases} 0 & Ri_g > 1 \\ -1.25 Ri_g + 1.25 & 0.2 < Ri_g < 1 \\ 1 & Ri_g < 0.2 \end{cases} \quad (44)$$

$$Ri_g = \frac{\beta g \frac{\partial T}{\partial z}}{\left(\frac{\partial U_x}{\partial z}\right)^2 + \left(\frac{\partial U_y}{\partial z}\right)^2} \quad (45)$$

where  $\beta$  and  $g$  are thermal expansion coefficient and gravitational acceleration,  $T$  is temperature,  $U$  is mean flow velocity.

### 5.5.2. Turbulence induced by steam condensation

High turbulence intensity (Figure 51) was observed in PIV recordings obtained in PANDA tests [36, 132]. The work done by Van Wissen et al. [59] suggested that the maximum turbulence intensity in case of steam injection into the pool through a single-hole were around 30%. However, the data on steam mass fluxes in their tests was not provided. Given that the steam pressure was  $\sim 3$  bar (compared to  $\sim 1$  bar in PPOOLEX) one can expect that the injection was in a sonic regime, which would produce much more stable steam-water interface, compared to sub-sonic oscillatory bubble regimes. The interactions between neighboring jets might also be a reason for the high intensity of turbulence measured in PANDA.

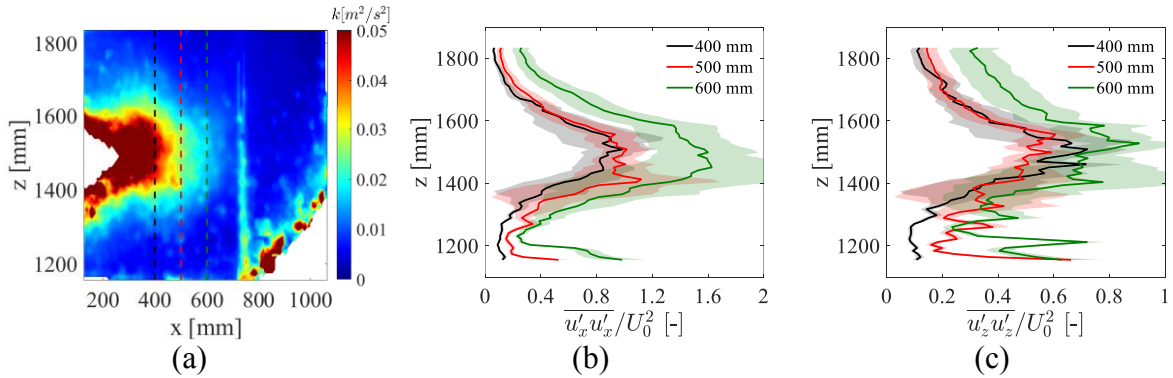


Figure 51. 2D PIV recording from the low steam injection phase ( $\tilde{t} = 0.206$ ) of the PANDA HP5-3 test. (a) Turbulence kinetic energy contours and square of turbulent intensities in the (b) axial and (c) vertical directions. Data is time-averaged over 200s. Shaded areas represent the uncertainty of the measurement.

Validation of the EMSR-DS against PPOOLEX [6] and PANDA tests [36] was done without imposing the high turbulence intensity. Results showed a reasonably good agreement between experiments and predictions of the temperature evolutions. In order to achieve that the effective momentum was calibrated [31], yet, obtained values were considerably lower compared to the measurements of effective momentum in the Separate Effect Facility (SEF) [98]. If SEF data is used to define effective momentum coefficient  $C$  (Eq. (27)), the jet becomes stronger and the pool is quickly mixed [136]. A preliminary study [138] of the EHS/EMS implementation using the EMSR-BC method suggests that higher values of turbulence intensity and viscosity ratio are required (Figure 59a) in order to capture key local phenomena (such as rapid jet diffusion and bending in upward direction) and that drive integral behavior of pool stratification development at low steam flux phase.

Generally, this high level turbulence cannot be neglected if we want to resolve the thermal behavior of the pool properly. Three avenues can be explored to model this high level turbulence, namely (i) use newly developed Generalize  $k - \omega$  (GEKO) model, (ii) provide

high initial turbulence at the Boundary Conditions (TKE-BC) and (iii) Distribute Source term of  $k$  in the vicinity of sparger tip (TKE-DS). They are introduced separately in the following sections.

### 5.5.3. Generalized $k - \omega$ model

GEKO [143] developed by Ansys is a new turbulence model group called Generalized  $k - \omega$  model. It is derived from  $k - \omega$  two-equation model but with a wide list of parameters that can be tuned to achieve different goals in different flow scenarios. Within these parameters,  $C_{MIX}$  and  $C_{JET}$  [143] are selected as most suitable for modelling of diffused free shear jets.  $C_{MIX}$  affects only free shear flows. Increasing  $C_{MIX}$  increases spreading rates of free shear flows.  $C_{JET}$  affects mostly jet flows and increasing  $C_{JET}$  (while  $C_{MIX} \neq 0$ ) decreases spreading rate for jets.

Sensitivity study of the effects of these two parameters on flow profiles was performed in a single round jet model. The computational domain for simulations of a single free jet is presented in Figure 53. The domain is designed to be large enough to contain the spatial development of the jet [144]. A nozzle ( $D = 8\text{ mm}$ , same as PPOOLEX injection hole) is placed at the centre of the smallest face (Figure 53).

A uniform velocity profile with the magnitude of  $U_0 = 2.65\text{ m/s}$  estimated by Eq. (35) in low steam injection phase in PPOOLEX SPA-T3 was applied on the injection hole. We applied  $I = 800\%$  and  $\mu_t/\mu = 4e4$  for all simulations as it can provide a proper diffused jet in the pool test simulation (Figure 59a). Other setup remained the same as the pool test simulation introduced in Section 5.3.

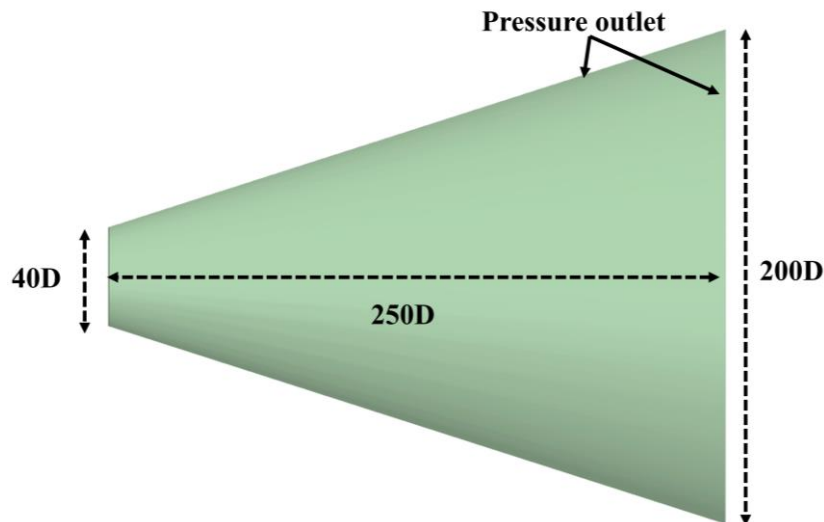


Figure 52. Geometry for simulations of a single free shear jet.

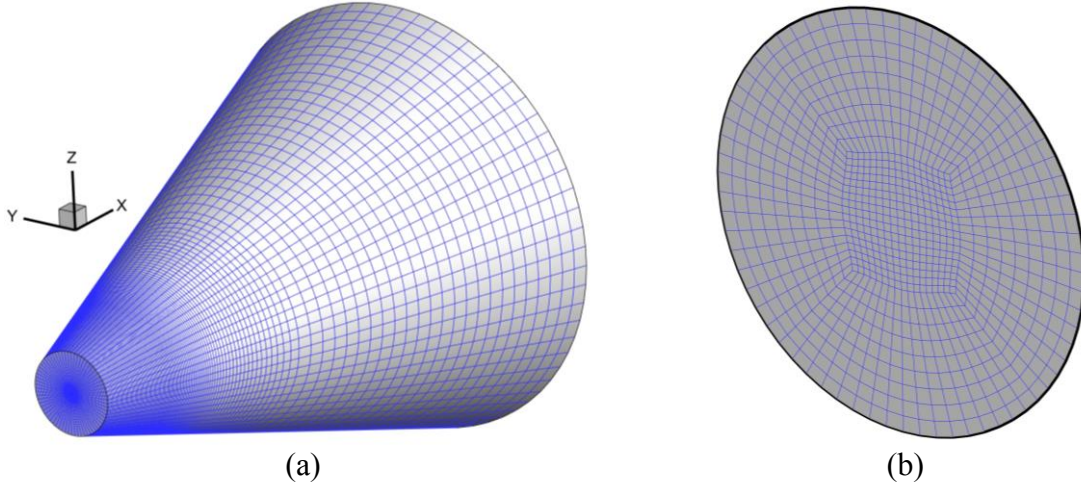


Figure 53. Computational domain for simulations of a single free shear jet of (a) overview and (c) injection hole.

Default values of  $C_{MIX}$  and  $C_{JET}$  [143] are 0.35 and 0.9. Their ranges are 0.5~1.0 and 0.0~1.0, respectively. However, these ranges are only suggestions based on previously addressed applications and there might be other situations. The centerline velocity profiles and turbulence kinetic energy of the sensitivity study are presented in Figure 54.

Compared to the case with  $k - \omega$  BSL model (Figure 59a), the default values of  $C_{MIX}$  and  $C_{JET}$  can provide similar velocity and turbulence profiles. By decreasing the  $C_{JET}$  to its minimum value (i.e.  $C_{JET} = 0$ ), a relatively diffused jet with a larger spreading rate can be obtained. To further diffuse the jet, a larger  $C_{MIX}$  is required as increasing  $C_{MIX}$  leads to higher turbulence levels in free shear flows [143]. As expected, increasing  $C_{MIX}$  from 0.35 to 3.0 would lead to larger spreading rates of the velocity profile associated with higher levels of turbulence kinetic energy (Figure 54b).

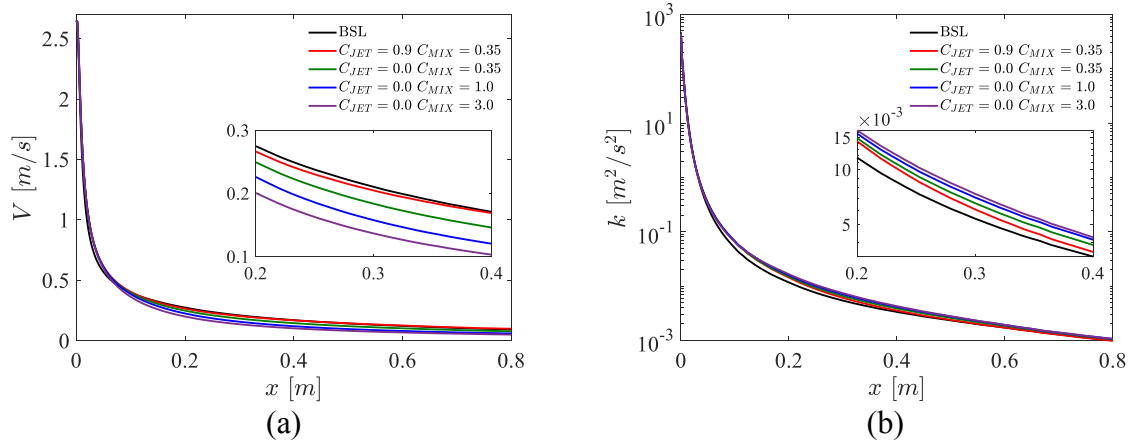


Figure 54. Effects of model parameters of GEKO on centerline profiles of (a) velocity and (b) turbulence kinetic energy.

However, the difference of velocity and turbulence characteristics between these cases is not dramatic. Meanwhile, the  $k$  of all the simulations at 200~600 mm is many times lower than the PIV measurement in PANDA (Figure 51a). Note that we expect that both PANDA and PPOOLEX tests should have similar turbulence level [36]. The main reason is the rapid decay (or dissipation) of the  $k$  in simulations as illustrated in Figure 54b. Even in the pool test

simulations with multiple jets, the rapid decay of  $k$  still cannot be avoided (Figure 72a). As we cannot benefit much from changing the turbulence model from  $k - \omega$  BSL to GEKO, the former model will be used in the rest of the simulations.

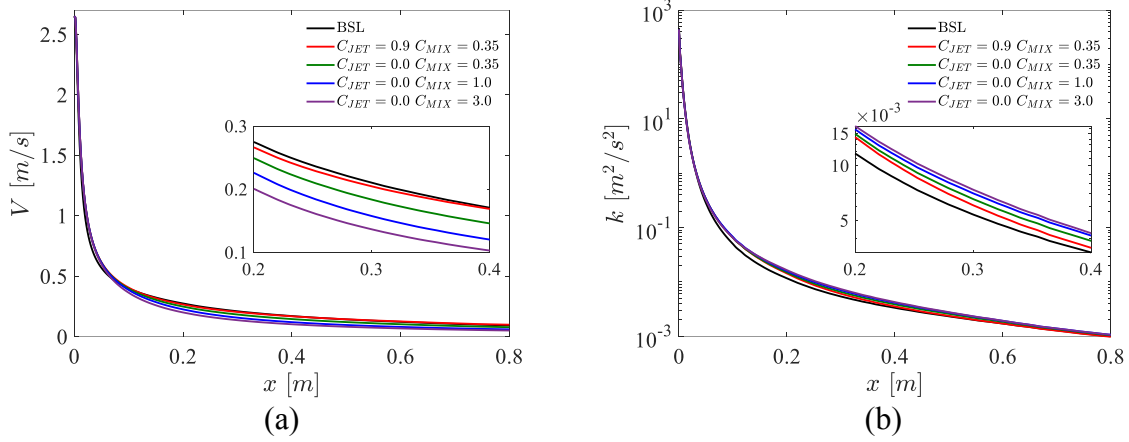


Figure 55. Effects of model parameters of GEKO on centerline profiles of (a) velocity and (b) turbulent kinetic energy.

#### 5.5.4. TKE-BC

The effect of Turbulence Kinetic Energy induced by steam condensation can be implemented in the code through (i) Boundary Condition (TKE-BC) on the sparger inlet or (ii) Distributed Source (TKE-DS) in the vicinity of the sparger head. They are discussed separately in the following two sections.

TKE-BC can be achieved in Fluent by specifying the flow boundary conditions [126]. Turbulence intensity and turbulent viscosity ratio are used to provide the boundary conditions for the turbulence kinetic energy (Eq. (48)) and dissipation rate (Eq. (49)).

$$k = \frac{3}{2} (u_{avg} I)^2 \quad (46)$$

$$\varepsilon = \rho C_\mu \frac{k^2}{\mu} \left( \frac{\mu_t}{\mu} \right)^{-1} \quad (47)$$

where  $I$  and  $u_{avg}$  are turbulence intensity and mean flow velocity;  $C_\mu$  is the empirical constant specified in the turbulence model ( $\sim 0.09$ ); and  $\mu_t/\mu$  is the turbulent viscosity ratio.

Sensitivity study of the effects of  $I$  and  $\mu_t/\mu$  on flow profiles was performed in the same single round jet model as shown in Figure 52 and Figure 53.  $k - \omega$  BSL turbulence model with low-Re corrections was used. Other setup remained the same as described in Section 5.5.3.

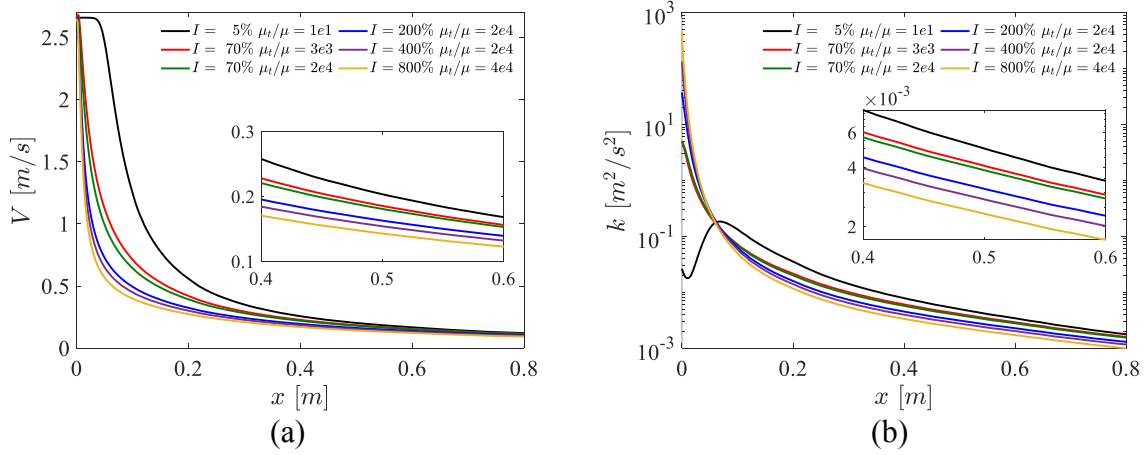


Figure 56. Effect of turbulence parameters on centerline profiles of (a) velocity and (b) turbulence kinetic energy.

A jet with velocity profile that is almost constant near the inlet and then gradually drops (Figure 56a) is observed when default values of  $I = 5\%$  and  $\mu_t/\mu = 10$  are used. However, the default values underestimate the actual  $k$  and  $\varepsilon$  in the vicinity of injection. Downstream values of  $k$  and  $\varepsilon$  are increased (Figure 57) due to generation of turbulence in the shear flow. Velocity profile varies only so slightly when the  $\mu_t/\mu$  is increased from 3000 to 20000 with  $I = 70\%$  (Figure 56a). A more diffused jet can be obtained by increasing both the turbulence intensity and viscosity ratio. Note that higher values of  $I$  and  $\mu_t/\mu$  means both more intensive initial turbulence and higher rate of turbulence dissipation. The most diffused jet is obtained by using  $I = 800\%$  and  $\mu_t/\mu = 40000$  which is far from the typical values for single phase jets. However,  $I$  and  $\mu_t/\mu$  as well as the  $k$  show an exponential decay along with the axial distance (Figure 56b, Figure 57) and eventually converge within a small range. Not only in the axial direction, this convergence is also observed in the radial direction (Figure 58).

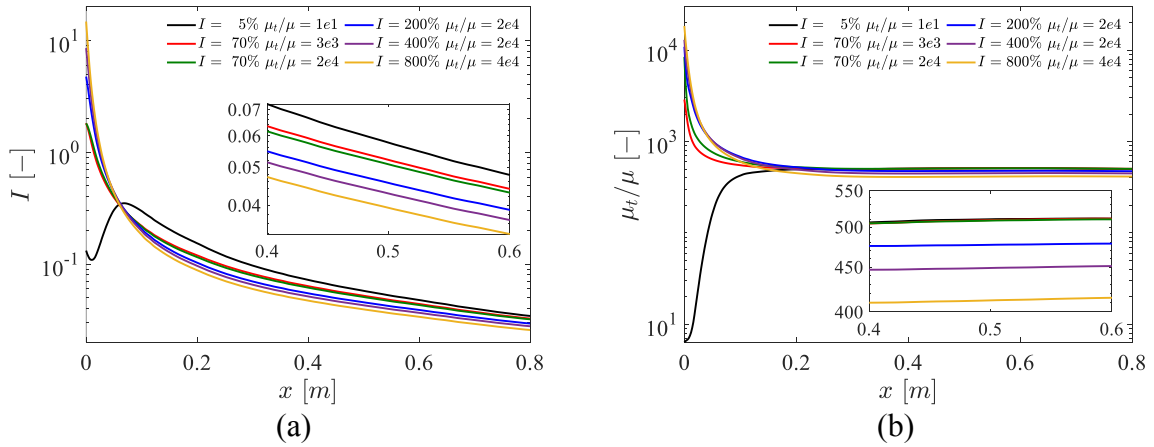


Figure 57. Effects of initial turbulent parameters on centerline profiles of (a) turbulence intensity and (b) turbulent viscosity ratio.

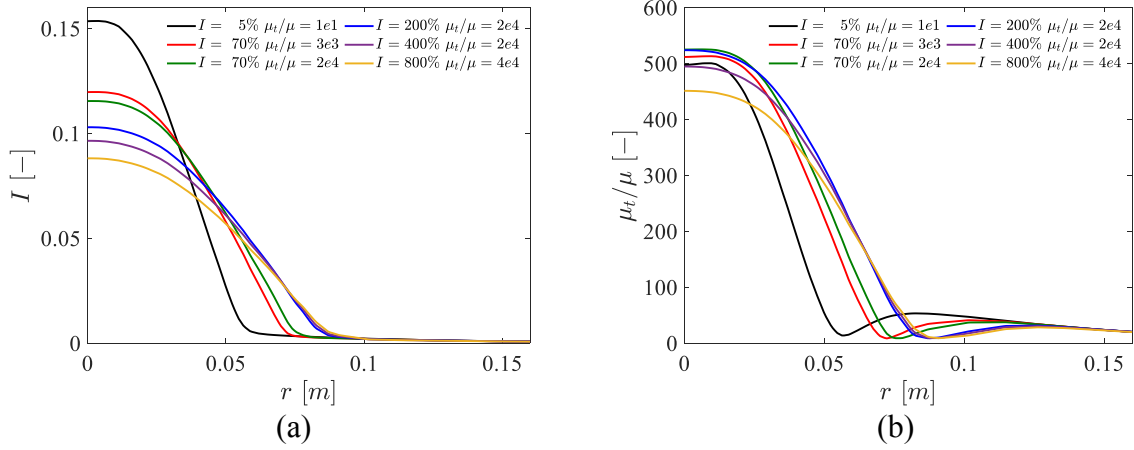


Figure 58. Effects of initial turbulent parameters on slice profiles ( $x = 0.2$  m) of (a) turbulence intensity and (b) turbulent viscosity ratio.

When the TKE-BC is applied to the pool test simulations, stratification development can be obtained (Figure 59, Figure 67) by using  $I = 800\%$  and  $\mu_t/\mu = 40000$  in phase 1 and  $I = 200\%$  and  $\mu_t/\mu = 10000$  in phase 3. The reduction of turbulence might be attributed to the decreasing of subcooling which can lead to the decreasing of bubble collapse frequency [98]. Even though these two values decrease many times in phase 3 than in phase 1, a smaller variation of the flow profiles can be expected due to the rapid decay from the previous sensitivity study.

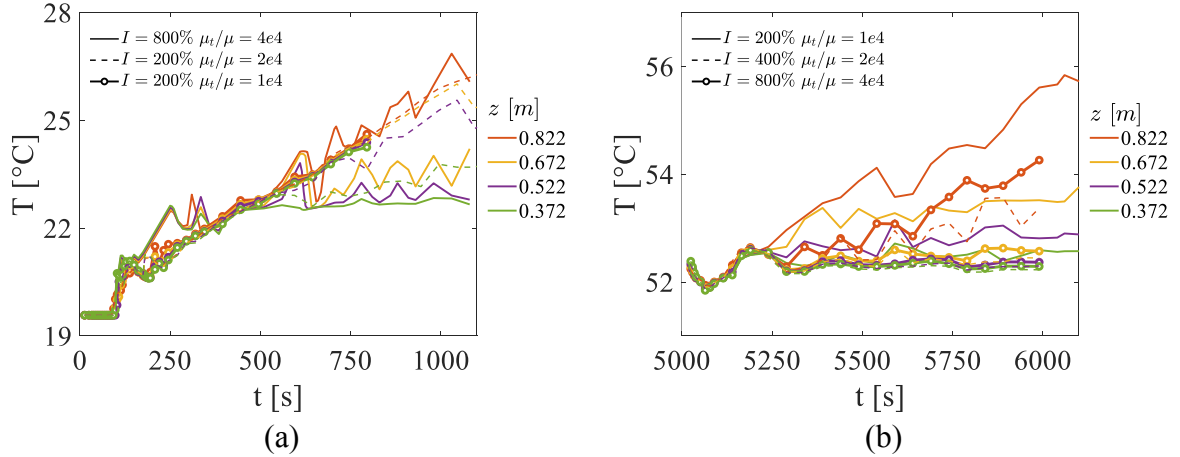


Figure 59. Effects of initial turbulent parameters on temperature evolutions of PPOOLEX SPA-T3 in (a) phase 1 and (b) phase 3.

According to the sensitivity study of the single jet, we can conclude that the thermal behavior of the pool can be resolved if the turbulence intensity and viscosity ratio are properly selected. Nevertheless, this method (TKE-BC) is unlikely to be the ultimate solution that will reconcile completely the experimental and modelling observations. The technical reason is the rapid dissipation of the turbulence, which makes it difficult to sustain significant turbulence intensity at a distance from the sparger. Such behavior is, most likely the effect of the turbulence models that we apply in the domain of conditions that are far from those for which the original models were developed and calibrated. More fundamental problem is that this approach is not physically adequate as it requires introduction of unreasonably high level of turbulence at the injection orifice. In reality, the turbulence is generated in a finite size domain where steam condenses. Therefore, another approach (i.e. TKE-DS) was proposed.



### 5.5.5. TKE distributed source model

As discussed in Section 5.5.5, the jet in the pool test simulations is much stronger than in the experiments if the turbulence induced by steam condensation is not considered. Experimental observations from PANDA and PPOOLEX seem to agree quite well with each other on the rapid diffusion of the jet at a distance of around 200 – 500 mm as shown in Figure 47, Figure 48, Figure 49 and report [144]. It could be explained if turbulence kinetic energy is still strong at these distances, which we can clearly see in PANDA PIV recording (Figure 51).

In order to address the issue of rapid decay of the  $k$ , Distributed Source of Turbulence Kinetic Energy (TKE-DS) could be introduced for the production of  $k$ , which would simulate the effect of rapid motion of the steam-water interface in the steam condensation region. This approach would help us to avoid the need for the fundamental revision of the turbulence models (e.g. GEKO) or providing extremely high initial turbulence at the orifice (i.e. TKE-BC). It is also a physically more adequate approach as the turbulence is indeed generated in the region where the steam condenses, not at the orifice of the sparger. The approach should be flexible enough to provide a better agreement between a set of all experimental observations and respective simulations, including the extended region with high levels of turbulence.

The kinetic energy of turbulence introduced by steam condensation is defined as  $\mathcal{S}_k$  in Eq. (48). The details of other terms can be found in Eq. (42).  $\mathcal{S}_k$  is assumed to be constant (Eq. (50)) in the steam condensation region (Figure 60) and decay linearly at after the exit from the region. Its azimuthal distribution is controlled by a profile factor  $\zeta$  as shown in Eqs. (49) and (51). This profile used to compute the non-uniform of  $\mathcal{S}_k$  is derived from the self-similarity characteristics of the jet [36].

$$\frac{Dk}{Dt} = \mathcal{P} + \mathcal{G} - \mathcal{D}_k + \mathcal{T}_k + \mathcal{S}_k \quad (48)$$

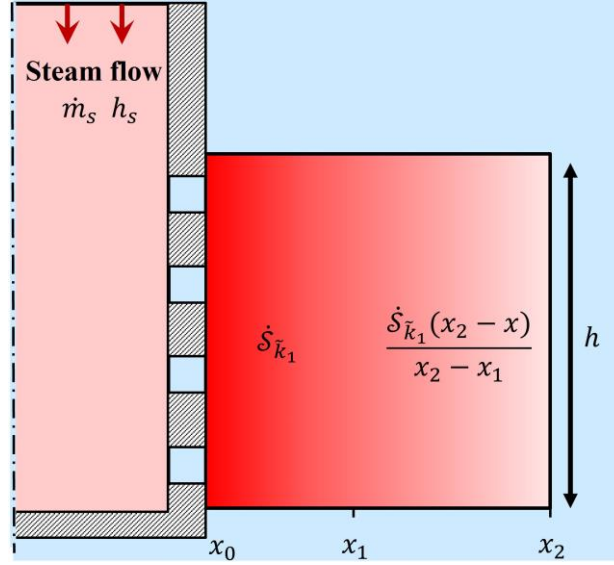
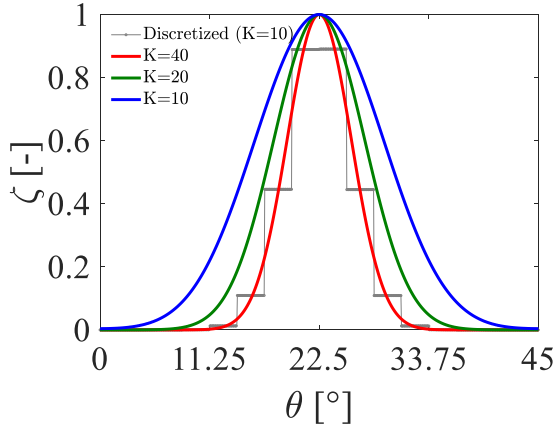
$$\mathcal{S}_k = \zeta \cdot \dot{S}_k(x) \quad (49)$$

$$\dot{S}_k(x) = \begin{cases} \dot{S}_{\bar{k}_1} & , \quad x < x_1 \\ \dot{S}_{\bar{k}_1} \frac{(x_2 - x)}{x_2 - x_1} & , \quad x_2 > x \geq x_1 \end{cases} \quad (50)$$

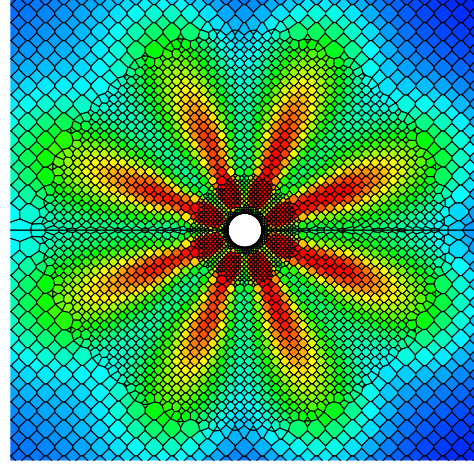
$$\zeta = \exp\left(-K \frac{r^2}{x^2}\right) \quad (51)$$

where  $x$  and  $r$  are the axial and radial coordinates;  $K$  is used to controls the standard deviation of the distribution (i.e. slenderness of the profiles, see Figure 61a). The sources were located in an annular region as illustrated in Figure 61b.



Figure 60. Schematic of the region where  $\mathcal{S}_k$  is distributed

(a)



(b)

Figure 61. (a)  $\mathcal{S}_k$  profiles at  $x = 0.1 \text{ m}$  obtained with different  $K$  values in Eq. (51) and (b) turbulence kinetic energy contour (with mirror zone) when using medium-density mesh.

Scoping analysis was performed to investigate the effects of a wide range of parameters of implementation of TKE-DS on jet profiles. The computational domain and matrix of the simulations are presented in Figure 62 and Table 8. The model setup is the same as introduced in Section 5.5.4 but with 4 injection holes.

The validation setup of the TKE-BC was included as C1 to be compared with others. For C2,  $\dot{S}_{\tilde{k}_1} = 60 \text{ kg/ms}^3$  estimated by Eq. (52) was used as a preliminary input. A too diffused jet is not expected near the orifice thus the specification of turbulence on the boundary was  $I = 30\%$  and  $\mu_t/\mu = 3000$ . The steam condensation region where  $\dot{S}_k(x)$  is constant started from sparger wall and ended at  $x_1 = 150 \text{ mm}$ . Then  $\dot{S}_k(x)$  decayed linearly to zero at  $x_2 = 500 \text{ mm}$ . The vertical height of the source region was assumed to be 4 times the pitch as  $h = 4 \times 36 = 144 \text{ mm}$ .

$$\dot{S}_{\tilde{k}_1} = \frac{\partial \mathcal{S}_{\tilde{k}_1}}{\partial t} = \frac{\partial \rho_l \tilde{k}_1}{\partial t} = \frac{990 \text{ kg/m}^3 \cdot 0.06 \text{ m}^2/\text{s}^2}{1\text{s}} \approx 60 \text{ kg/ms}^3 \quad (52)$$

where  $\rho_l$  is water density and  $\tilde{k}_1$  is the production of  $k$  induced by steam condensation.  $\tilde{k}_1 = 0.06 \text{ m}^2/\text{s}^2$  was assumed as a preliminary guess from PANDA PIV measurement (Figure 51a).

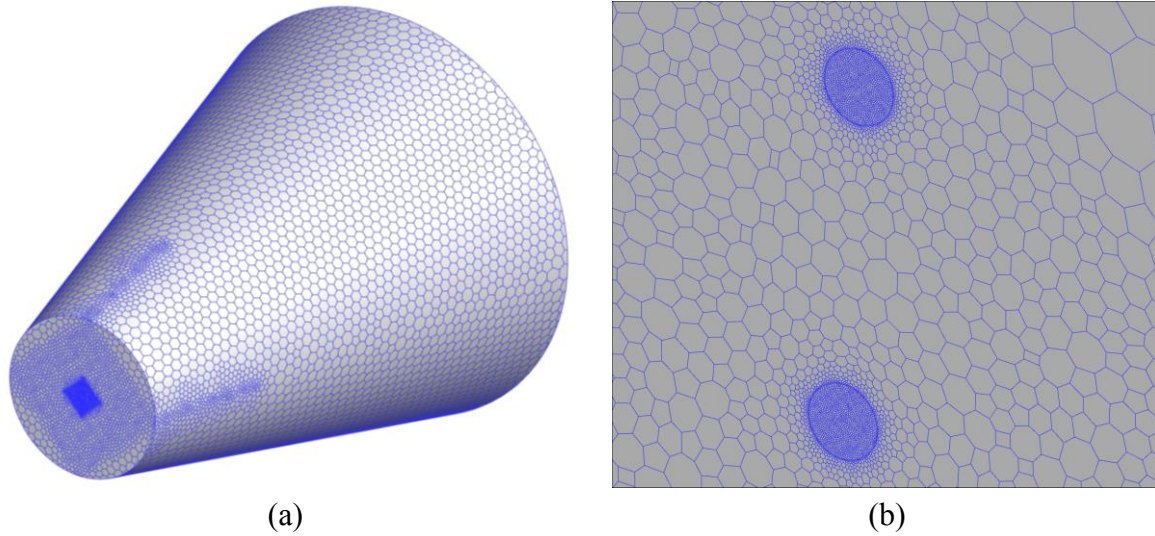


Figure 62. Computational domain for multi-hole (4 holes) simulations of (a) overview and (b) details of 2 injection holes.

Table 8 Lists of simulations performed for sensitivity analysis of implementation of TKE-DS

Case number	Initial turbulence boundary		Turbulence source $\dot{S}_{\tilde{k}_1}$ ( $\text{kg}/\text{ms}^3$ )	Source term region		
	$I$ (%)	$\mu_t/\mu$ (—)		$x_1$ (mm)	$x_2$ (mm)	$K$ (—)
C1	800	40000	0	150	500	10
C2	30	1000	60	150	500	10
C3	30	1000	180	150	500	10
C4	30	1000	360	150	500	10
C5	30	1000	180	150	500	Uniform
C6	30	1000	180	150	500	40
C7	70	3000	180	150	500	10
C8	30	1000	180	250	500	10
C9	30	1000	180	150	700	10

Scoping analysis results for the centerline profiles of velocity and turbulence kinetic energy are compared in Figure 63. A more diffused jet (C1 and C2 in Figure 64) can be obtained when TKE-DS is introduced. Rapid dissipation of  $k$  is mitigated as shown in Figure 63b where the turbulence within the region of  $x = 200 \sim 600 \text{ mm}$  is still at a relatively high level. It can be expected as the turbulence is distributed more evenly compared to the case with high turbulence at the jet injection boundary (TKE-BC). In order to achieve  $k \sim 0.05 \text{ m}^2/\text{s}^2$  in this region (Figure 51a), an increasing of  $\dot{S}_{\tilde{k}_1}$  from 60 to 180 or even higher is necessary.

The diffusion of the jet near the orifice (i.e.  $0 - 100 \text{ mm}$ ) is mainly affected by the turbulence boundary condition at the inlet. The effects of sizes of the source term region on flow profiles are minor (C3, C8, and C9). A higher spreading rate of the jet can be obtained by either

decreasing  $K$  or increasing  $\dot{S}_{k_1}$  as both methods produce more turbulence energy in the main flow as illustrated in Figure 65.

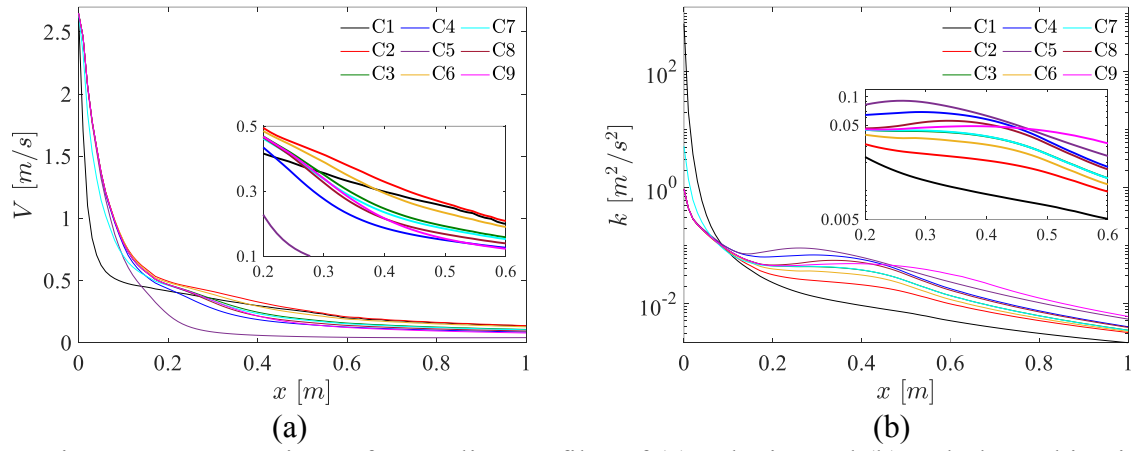


Figure 63. Comparison of centerline profiles of (a) velocity and (b) turbulence kinetic energy of scoping analysis for implementation of turbulence source.

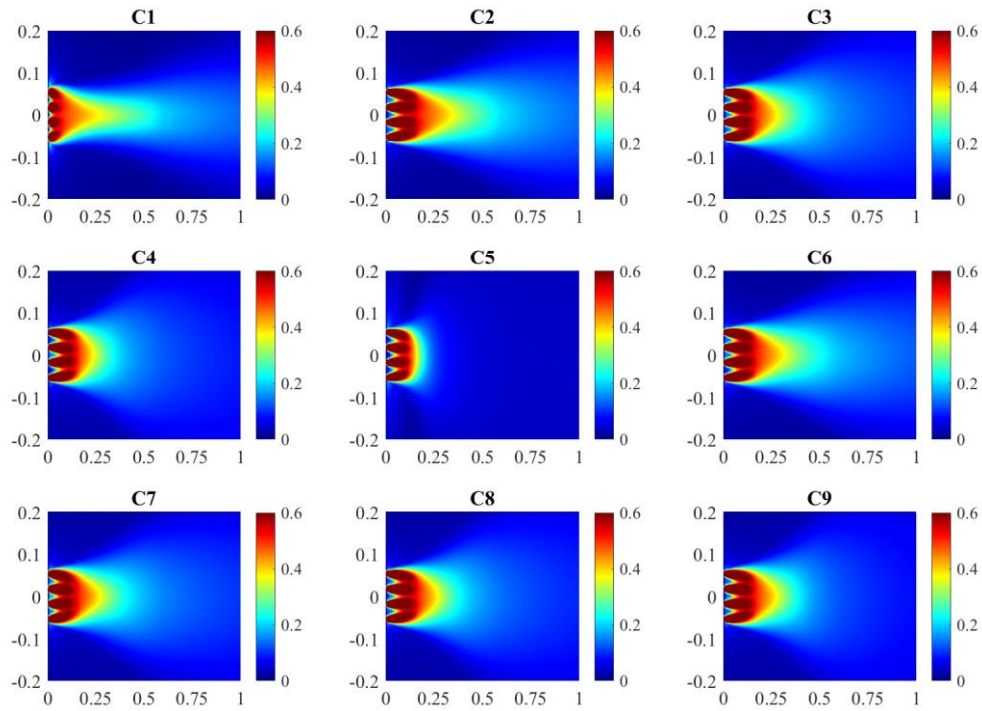


Figure 64. Comparison of velocity contours of scoping analysis for implementation of turbulence source.

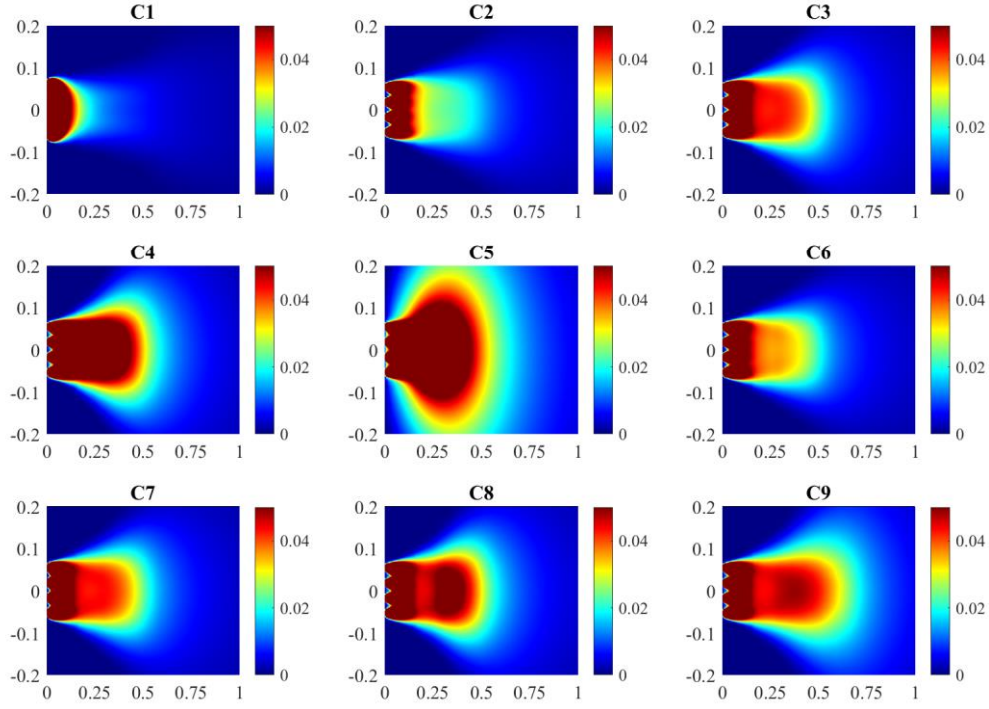


Figure 65. Comparison of TKE contours of scoping analysis for implementation of turbulence source.

### 5.6. Validation against PPOOLEX SPA-T3 test

In this section, we present the validation of EHS/EMS models for steam injection through sparger with “Unit Cell” implementation against PPOOLEX SPA-T3 tests. The details of the test and injection procedure can be found in Section 5.1 and Table 5. Comparison of the pool temperatures measured in the experiment and predicted by the “Unit Cell” model with TKE-BC and TKE-DS are presented in Figure 66 and Figure 67. Original and smoothed experimental data with a period of 50 seconds are presented in Figure 66 and Figure 66b, respectively. The comparison extracted the results from TCs at L1 (Figure 31) to the uniformity of the temperature profile in the radial direction in the pool [36].

For TKE-BC, we used  $I = 800\%$ ,  $\mu_t/u = 40000$ ,  $\theta_i = 11^\circ 9^\circ 6.5^\circ 0^\circ$  in phase 1 and  $I = 200\%$ ,  $\mu_t/u = 10000$ ,  $\theta_i = 14^\circ 12^\circ 9.5^\circ 3^\circ$  in rest phases. For TKE-DS, we used  $I = 30\%$ ,  $\mu_t/u = 1000$ ,  $\dot{S}_{\bar{k}_1} = 60 \text{ kg/ms}^3$  distributed in the region described as C3 in Table 8 in all phases, while  $\theta_i = 11^\circ 9^\circ 6.5^\circ 0^\circ$  in phase 1 and  $\theta_i = 14^\circ 12^\circ 9.5^\circ 3^\circ$  in rest phases.

The transient behavior of the pool (Figure 68 and Figure 69) is quantitatively captured by both TKE-BC and TKE-DS during the stratification development and mixing. The discrepancy of the temperature measured at  $z = 0.672 \text{ m}$  during the injection phase 3 indicates that a less diffused jet is required to further mix the pool. A notifiable difference of the temperature above the sparger tip between the test and both simulations (Figure 87) can be attributed to two aspects. The first one is that the EHS model would overshoot the total thermal energy in the pool (Figure 42) if the thermal inertia of the vessel and heat loss to the environment are ignored. Second, the higher position of the thermocline in both simulations (Figure 69) decreases the heat

capacity of the hot layer compared to the test. Nevertheless, one can conclude that the proposed modelling approach can provide an adequate prediction of the thermal behavior of the pool in different steam injection conditions.

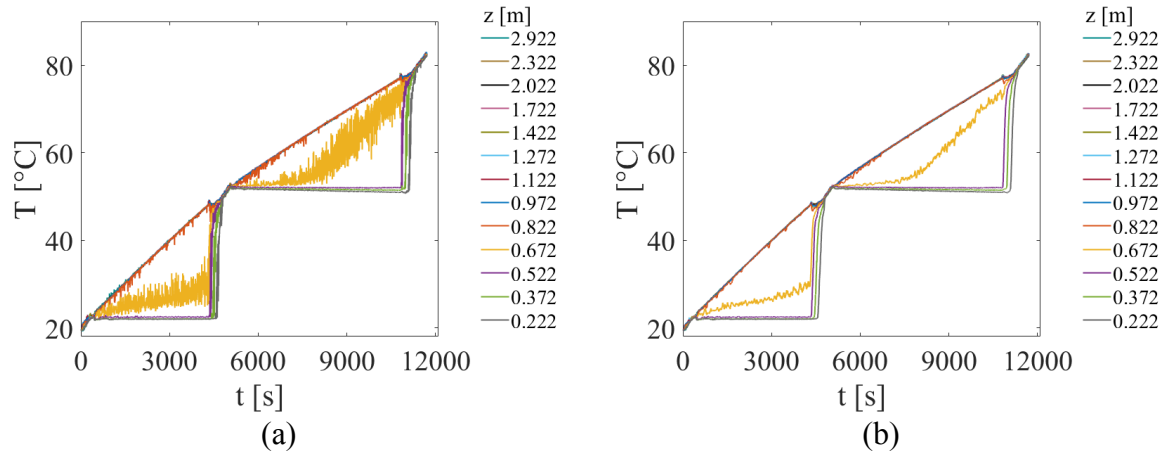


Figure 66. Evolution of pool temperature at different elevations in PPOOLEX SPA-T3 (a) experimental data and (b) experimental data averaged over 50s.

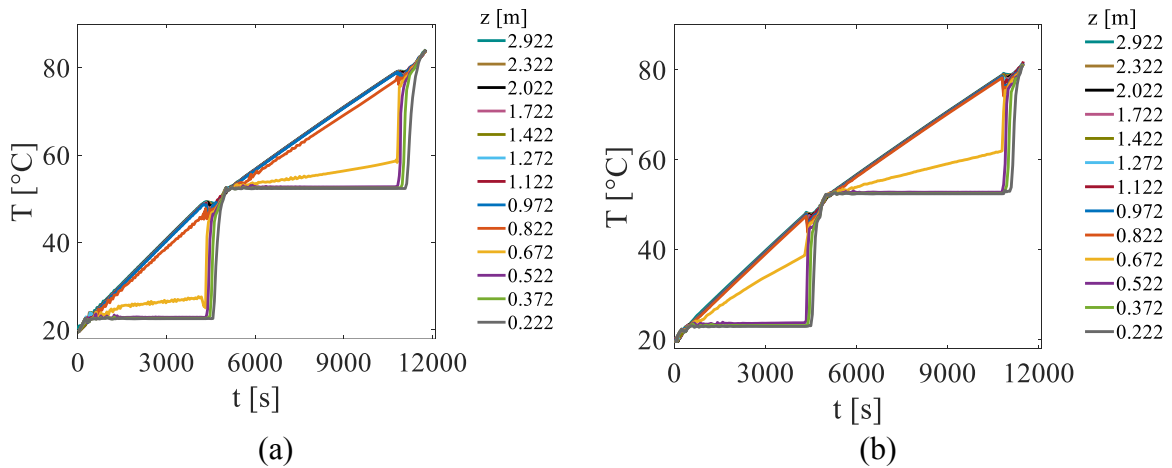


Figure 67. Evolution of pool temperature at different elevations in PPOOLEX SPA-T3. Simulation results with (a) TKE-BC and (b) TKE-DS.



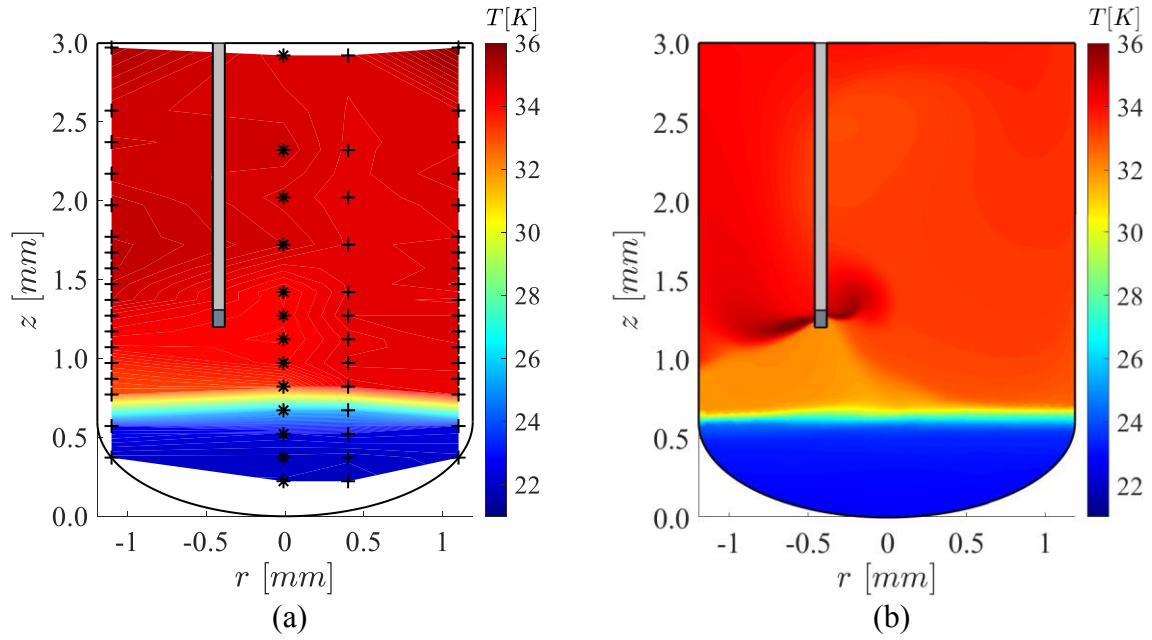


Figure 68. Temperature contour obtained by (a) TCs measurement and (b) simulation by TKE-DS at  $t = 2100s$ . ‘\*’ corresponds to the projection of TCs L4 on symmetry plane and ‘+’ indicates the rest TCs on this plane.

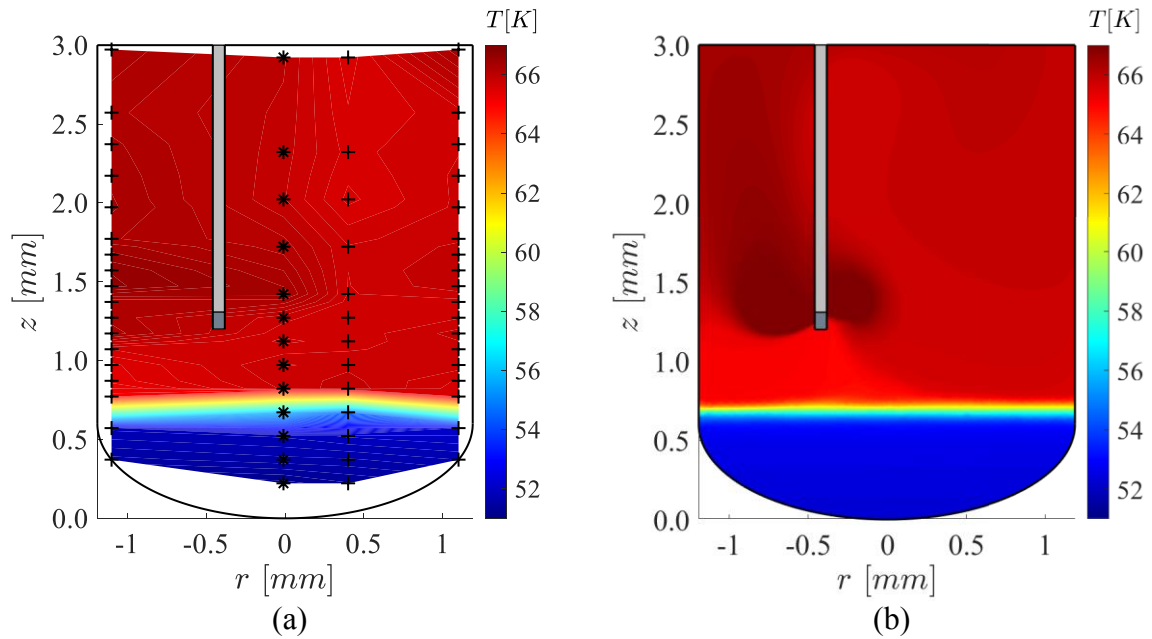


Figure 69. Temperature contour obtained by (a) TCs measurement and (b) simulation by TKE-DS at  $t = 8000s$ . ‘\*’ corresponds to the projection of TC L4 on symmetry plane and ‘+’ indicates the rest TCs on this plane.

Velocity and turbulence kinetic energy contours of simulations using TKE-BC and TKE-DS in low and high steam injection phases are compared in Figure 70~Figure 73. Although PIV measurement is not available, we can still learn from the temperature contours by TC mesh (e.g. Figure 47) that a similar jet could be observed when TKE-DS is applied. Meanwhile, the agreement of turbulence kinetic energy contour between PANDA PIV (Figure 51a) and

simulation (Figure 72b) indicates that the source term approach is a better option than the boundary condition regarding implementation of turbulence modeling.

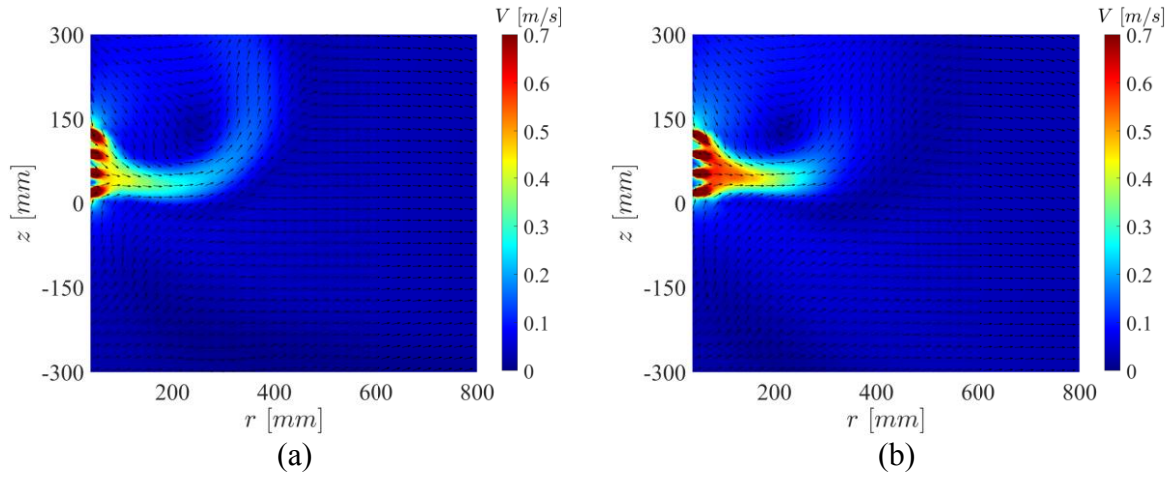


Figure 70. Velocity contours during phase 1 obtained by simulations using (a) TKE-BC and (b) TKE-DS.

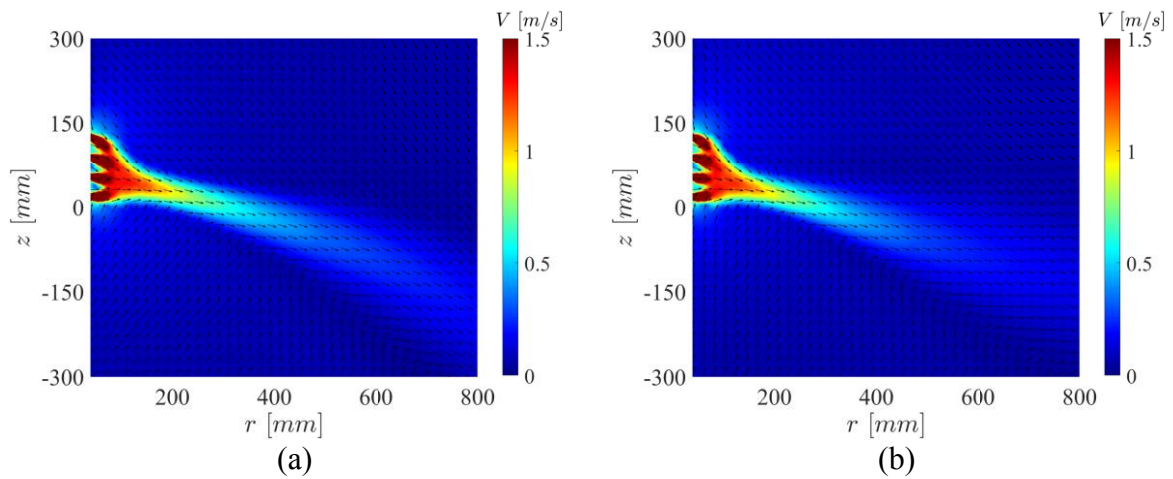


Figure 71. Velocity contours during phase 2 obtained by simulations using (a) TKE-BC and (b) TKE-DS.

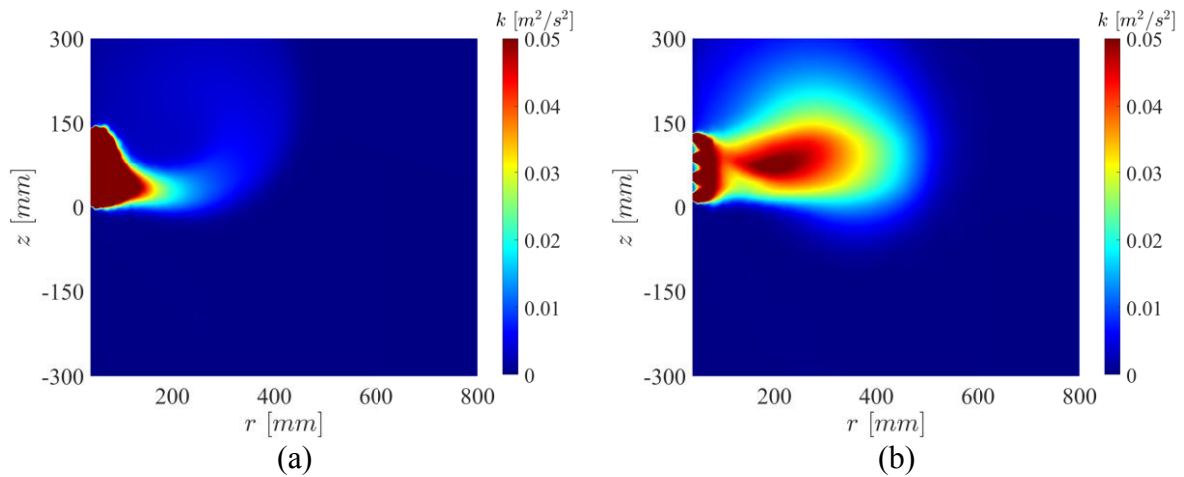


Figure 72. TKE contours during phase 1 obtained by simulations using (a) TKE-BC and (b) TKE-DS.

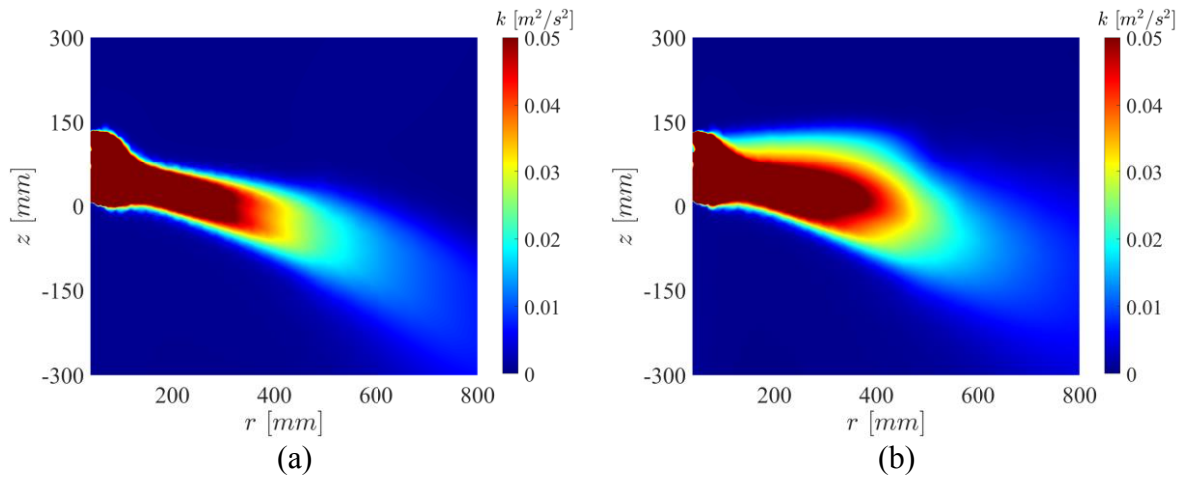


Figure 73. TKE contours during phase 2 obtained by simulations using (a) TKE-BC and (b) TKE-DS.

### 5.7. Summary of EHS/EMS model development for sparger

In this section, we present results of EHS/EMS models development and validation for prediction of the pool behavior induced by the steam injection through a multi-hole sparger.

We discuss the implementation of the EHS/EMS models in a “Unit Cell” approach and validated against PPOOLEX SPA-T3 test. Validation suggests that this model can provide a reasonably accurate prediction of the pool behavior. Main findings and features of the modelling approach are listed below:

- Prototypic pool behavior has large spatial and temporal scales. Single-phase solver is used in order to achieve necessary computational efficiency in resolving the effects of steam condensation in a CFD code.
- Interaction of the jets induced by steam injection through a multi-hole sparger is resolved by using “Unit Cell” model where the effective liquid is introduced individually through each hole.
- Velocity and temperature of the effective liquid jets are estimated by the EHS/EMS models. In order to conserve the mass, excessive amount of liquid is removed from the pool surface.
- Downward angles of the jets from the sparger head are estimated by the internal flow simulations as a preliminary input and then calibrated by the temperature evolutions and TC mesh measurement of the test.
- Buoyancy effects on turbulence are modelled by adding extra source terms of  $k$  and  $\omega$  in transport equations.
- High level turbulence induced by the steam condensation is modelled by either adding an extra  $k$  source in the transport equation (TKE-DS) or providing turbulence on boundary conditions (TKE-BC).



## 6. PRE-TEST SIMULATIONS FOR PANDA H2P3 TESTS

The OECD/NEA HYMERES-2 project aims to carry out 24 tests in PANDA facility. The tests are grouped in 6 series each addressing a set of safety-relevant containment phenomena. PANDA H2P3 pool test series is intended to study phenomena of thermal stratification development and mixing in a large water pool induced by steam injection through multi-hole spargers and Load Reduction Ring (LRR).

In order to maximize the usefulness of the experimental data for the development and validation of the containment thermal hydraulics codes and EHS/EMS models, we provide pre-test simulations and analytical support for the test design, initial and boundary conditions for the H2P3 tests. Here we present results of the pre-test analysis for H2P3 sparger tests (H2P3-1,2,3) where the steam is injected into the pool only through sparger and for H2P3 LRR tests (H2P3-4,5,6) where only LRR holes are opened for steam injection.

### 6.1. Pre-test simulations for H2P3 spargers tests

The H2P3 tests will be carried out using the same vessel and sparger as in the HP5 series (see section 4.1). The aim of the tests with steam injection through sparger head is to address (i) the effect of the distance between sparger head and thermocline on the rate of thermocline erosion; (ii) the azimuthal velocity profile and its dependence on the steam injection conditions. The pre-test simulations were carried out to support the selection of: (i) the sparger elevation above the bottom of the pool, pool depth and arrangement of TCs; (ii) the test procedure for steam injection and (iii) PIV setup for velocity measurements.

Implementation of EHS/EMS models using the source terms approach (Figure 12) was used for the analysis of the effect of the distance between sparger head and thermocline. “Unit Cell” model was used to study the velocity profile of the multiple interacting condensed steam jets [141] to support the selection of PIV setup.

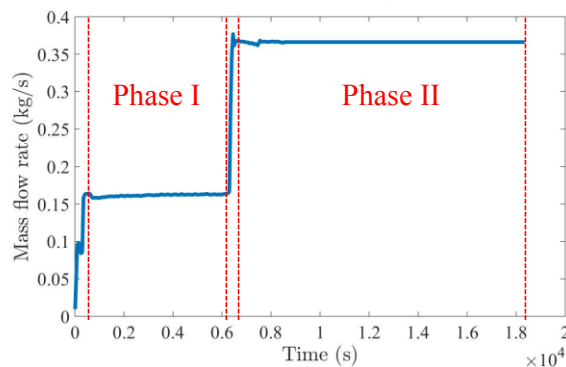


Figure 74. Steam mass flow rate in the simulations of H2P3-2.5 and H2P3-3.3.

#### 6.1.1. Pool configuration

The elevation of the sparger head should be sufficient to study the effect of the distance between the thermocline and sparger head on the erosion velocity of the stratified layer. Two options were considered with sparger elevation of 2.5 m (H2P3-2.5) and 3.3m (H2P3-3.3). The same numerical setup was used in both cases. The steam injection conditions are the same as in HP51 (Table 1) with extended duration of the second phase (Figure 74). The detailed setup including

the mesh sensitivity, turbulence model, boundary condition, numerical solver and source terms approach are described in [31].

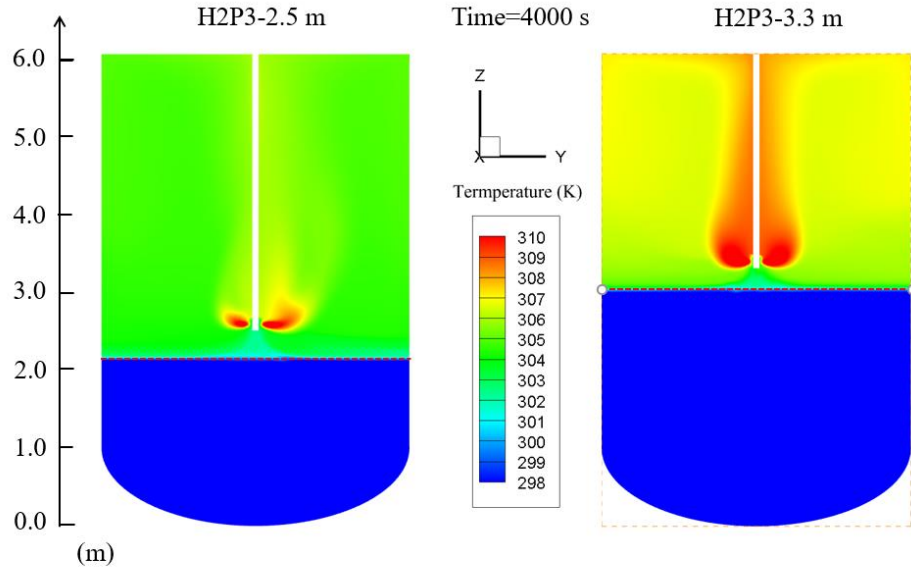


Figure 75. Comparison of temperature contours of H2P3-2.5 and H2P3-3.3 at  $T = 4000s$ .

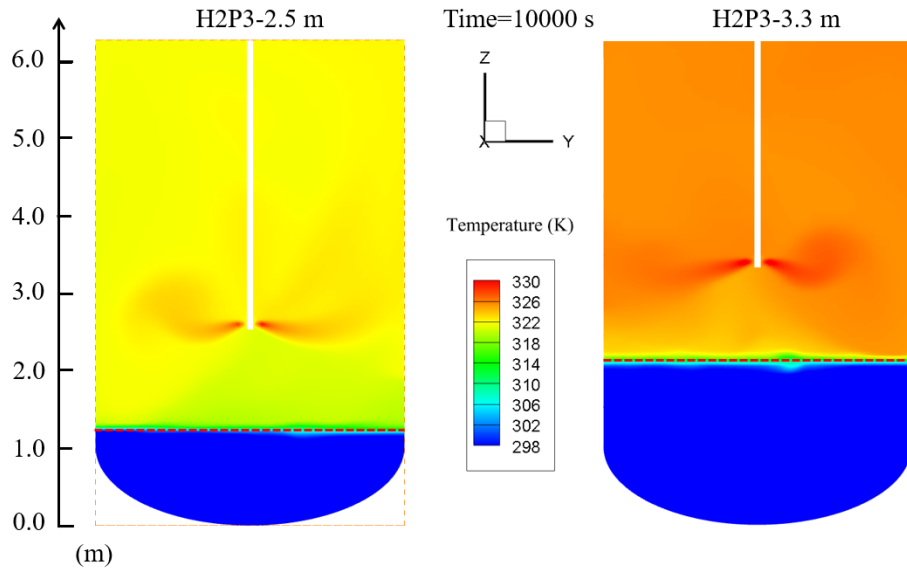


Figure 76. Comparison of temperature contours of H2P3-2.5 and H2P3-3.3 at  $T = 10000s$ .

Comparisons of the temperature fields for both cases at  $t = 4000s$  and  $t = 10000s$  (phase I and phase II respectively) are presented in Figure 75 and Figure 76. Locations of the thermocline, where the largest temperature gradient is observed, are highlighted with a red dashed line for both cases. The evolution of the thermocline elevation and velocity are shown in Figure 77. In both cases, the elevation of the thermocline decreases rapidly at the beginning of a steam injection phase, then reaches a stable position with near zero erosion velocity. Note that decreasing water subcooling slowly increases effective momentum (see (3) and (4)), which helps to maintain a certain rate of erosion of the cold layer.

The temperature evolution and motion of thermoclines in both considered cases have very similar trends (see Figure 78). The distance between the sparger head and the thermocline is

slightly smaller in case with sparger elevation of 3.3 m. This is because hot layer in this case is thinner and has higher temperature and respectively larger density difference with the cold layer at the same time moment compared to the case with 2.5 m sparger head elevation. Both options enable capturing the effect of the distance from the sparger head on the erosion rate including the regime of practical stagnation of the thermocline. Configuration with 2.5 m sparger head elevation was eventually selected for the H2P3-1,2,3 tests, considering that it was more suitable for implementing 3D PIV setup than configuration with elevation of 3.3 m.

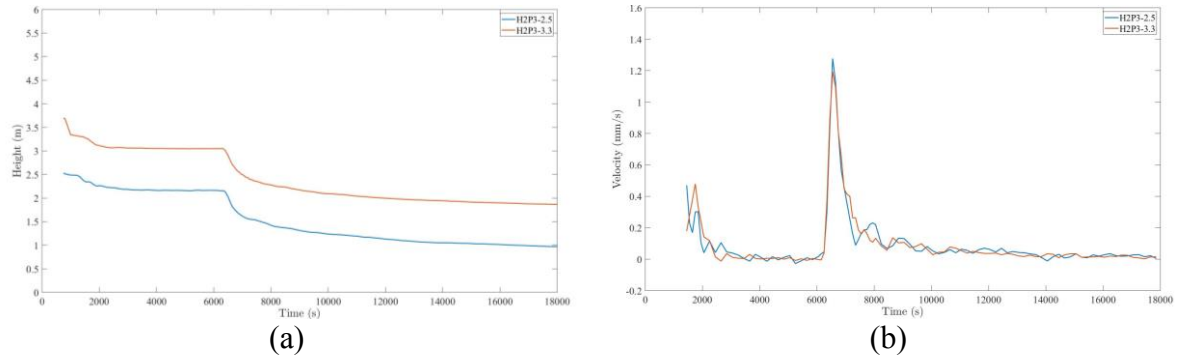


Figure 77. Comparison between H2P3-2.5 and H2P3-3.3 of (a) evolutions of thermocline and (b) erosion velocity of the stratified layer.

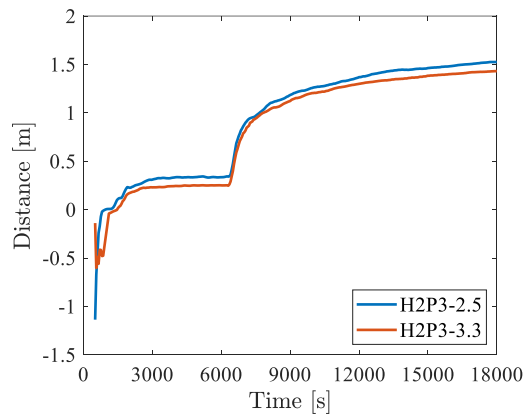


Figure 78. Comparison between H2P3-2.5 and H2P3-3.3 of the distance from the sparger head to the thermocline.

Based on the analysis results following recommendations were provided for optimization of the thermocouples (TCs) positioning. It is important to provide at least one vertical train of TCs with refined resolution (25 mm step between the TCs) below the sparger head at a distance of 250 mm away from the vertical axis of the pool (TC line 1 in Figure 4). The other two trains can be used with larger (about 100-150 mm) steps between TCs in vertical direction and be placed at a distance of 500 and 1000 mm away from the sparger. No additional TCs in the pool would be necessary due to the uniformity of the temperature profile in the radial direction [36].

## 6.1.2. Steam injection procedure

One of the goals of H2P3 was to study the effect of the distance from the sparger to thermocline and to achieve a few configurations with nearly stagnant position of the thermocline. Respectively, three cases were proposed for H2P3 (Table 9 and Figure 79). All of them involve four injection phases with different mass flow rates and durations. All tests start with injection at  $0.16 \text{ kg/s}$  which is minimum flow rate to avoid chugging [6] (Figure 79) and end with the maximum flow rate that was possible to achieve in the test. For comparison with the HP5 tests, some flow rates in H2P3 were kept similar to those in HP5 test matrix. In all cases the same boundary conditions and water pool depth of a  $6 \text{ m}$  were used. The difference was in the duration of the steam injection phases and steam mass flow rates.

Table 9. Steam injection procedures of H2P3-1,2,3.

Test	Initial conditions	Phase 1		Phase 2		Phase 3		Phase 4	
	Temperature (°C)	Flow (kg/s)	Time (s)	Flow (kg/s)	Time (s)	Flow (kg/s)	Time (s)	Flow (kg/s)	Time (s)
H2P3-1	20	0.16	4000	0.27	4000	0.37	4000	0.45	4000
H2P3-2	20	0.16	4000	0.27	4000	0.37	8000	0.45	5000
H2P3-3	45	0.16	4000	0.27	4000	0.37	4000	0.45	4000

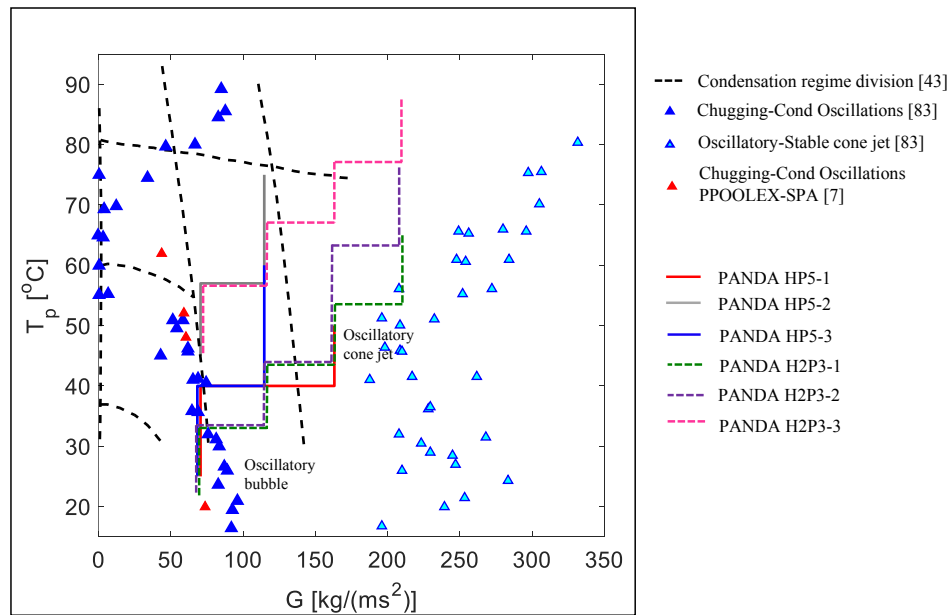


Figure 79. Condensation regime map of PANDA HP5, H2P3 tests [6, 43, 96].  $G$  is the steam mass flux through the injection holes and  $T_p$  is the pool bulk temperature.

Results of simulations presented in Figure 77 show that the stratified layer nearly stagnates at  $\sim 4000\text{s}$  after the transition. Therefore  $4000\text{s}$  is selected as a typical duration for each steam injection phase. Pre-test simulations of the H2P3-1, show that the stagnation of the thermocline in phases 3 and 4 is not observed (Figure 80). Analysis of H2P3-2 show no significant qualitative effect from extending duration of the last two injection phases. However, the extended duration of the injection phases provides a possibility to compare data from H2P3-1

and H2P3-2 at different pool configurations. Therefore, it was suggested to keep 4000s duration for each phase in H2P3-1 and perform H2P3-2 with extended injection time. In H2P3-3 a higher initial pool temperature was selected to investigate the effects of subcooling on the motion of thermocline.

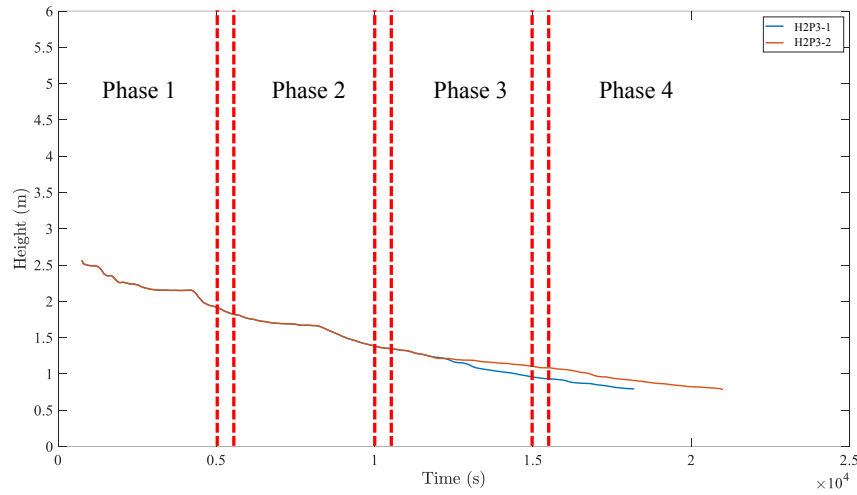


Figure 80. Evolution of thermocline elevation obtained in pre-test simulations of H2P3-1 and H2P3-2.

### 6.1.3. 3D PIV setup

Particle Image Velocimetry (PIV) was used in previous PANDA tests for measurements of the velocity profile in vertical cross section near the sparger [36]. One of the main tasks for H2P3 tests is to provide measurements that can be used to calibrate modeling approaches for the azimuthal distribution of the fluid velocity in the vicinity of the sparger. A new 3D PIV window  $\sim 1 \times 1 \text{ m}$  was prepared for this purpose. Pre-test analysis was carried out in order to optimize position of the PIV window for measurement of the merged jets velocity profiles in the azimuthal direction.

The first pre-test analysis was performed using MATLAB and equation (5) to describe the jet velocity field. The effects of the expansion factor  $K$  on the velocity profile is illustrated in Figure 81. As discussed in section 4.2.1, the azimuthal profile of velocity is smoother at smaller values of  $K$ . In Figure 82 velocity profiles are shown in different horizontal cross-sections with different distances between the PIV plane and sparger head. A horizontal PIV plane was studied as an option that provides more detailed information about dependency of the velocity on the distance from the sparger. However, small gas bubbles, usually produced in the steam condensation region, can create difficulties for measurements of the velocity near the sparger. Also there are technical difficulties with implementing a horizontal PIV plane in PANDA, therefore the option with horizontal PIV window was eventually discarded.

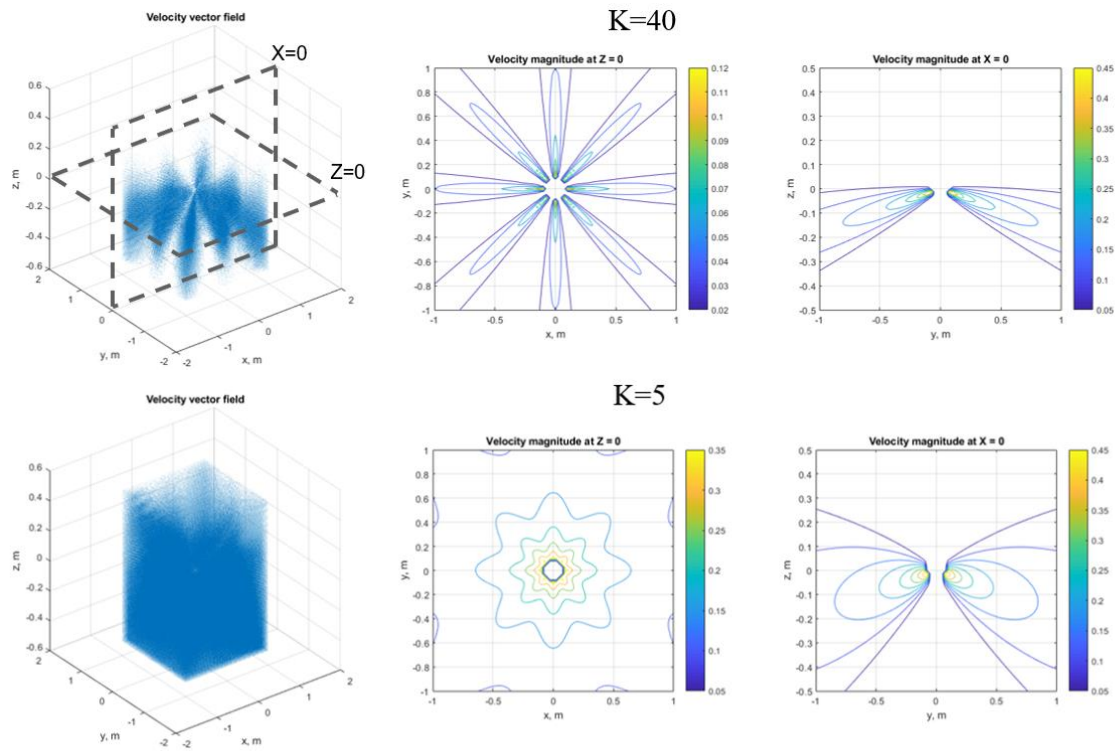


Figure 81. Characteristic map of velocity filed around a sparger with different  $K$ .

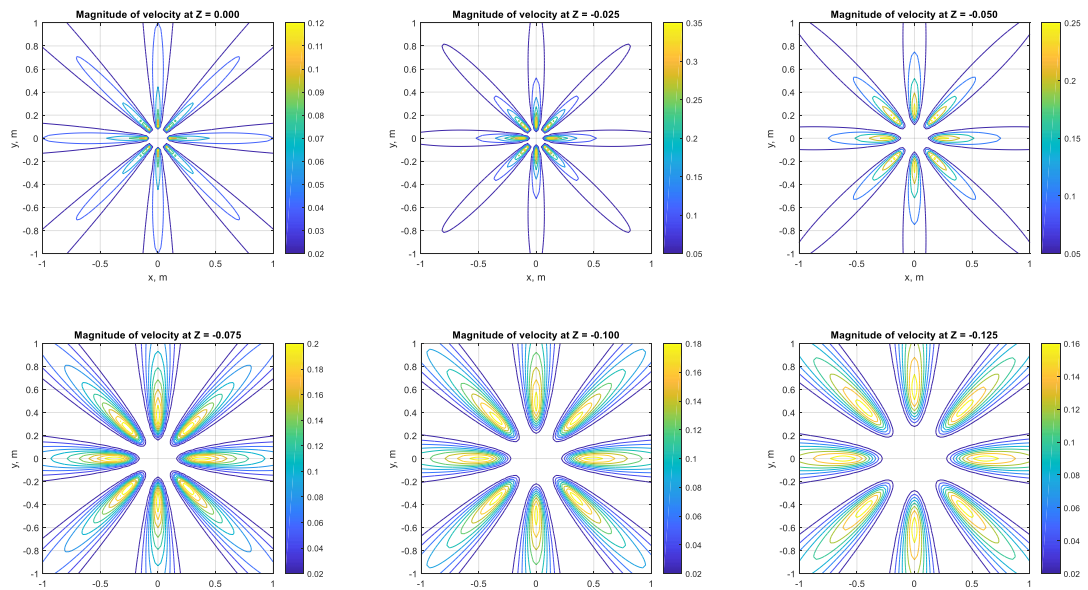


Figure 82. Horizontal cross-sections of velocity profile at the different heights using  $K = 40$ .

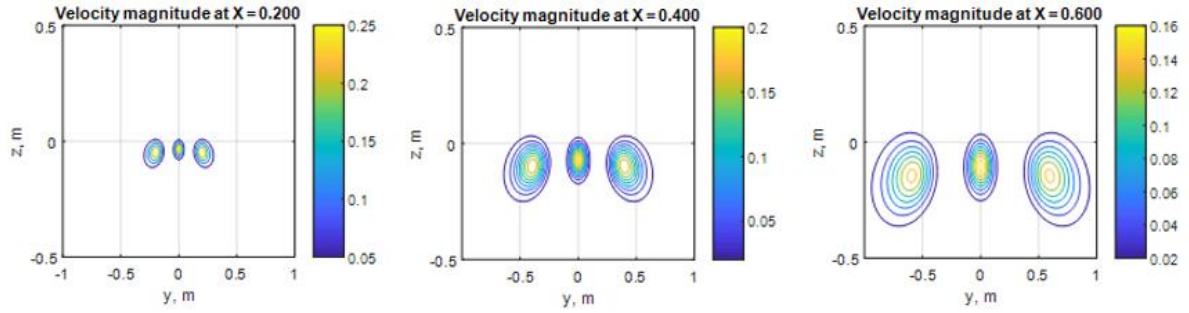


Figure 83. Vertical cross-sections of the velocity field at different distances from the sparger axis with  $K = 40$ .

Velocity profiles in vertical cross-sections with different distances from the sparger axis are shown in Figure 83. Vertical PIV plane can provide a reasonable coverage for the jet velocity field. However, given the limitation on the size of the PIV window, the coverage is significantly reduced at larger distances (e.g. larger than  $\sim 0.6$  m). An optimization of the PIV window positioning with respect to sparger is needed to maximize the value of the obtained data. The PIV plane is located in the middle section of the pool at the level of the sparger head (Figure 84). The sparger is mounted on two parallel rails and can be moved to control the distance to the PIV plane. However, the sparger can't be moved during the test.

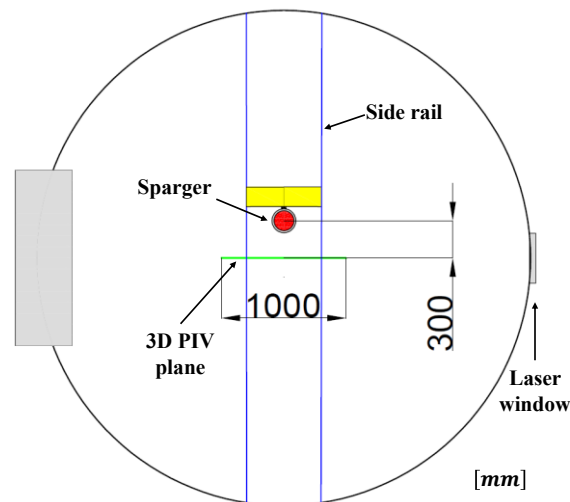


Figure 84. PIV configuration for H2P3 tests for the measurements of azimuthal velocity profiles of the jet.



## 6.1.4. CFD analysis of velocity field around sparger

To maximize the value of obtained measurements, pre-test simulations were performed to study details of the velocity field around the sparger using CFD. In this section, the “Unit Cell” model [141] with a  $22.5^\circ$  sector domain is used. Validation of the approach against PIV data from the HP53 test [132] showed a reasonable qualitative agreement with the experimental data. Comparison of the centerline velocity predicted by Fluent and obtained from PIV is shown in Figure 85.

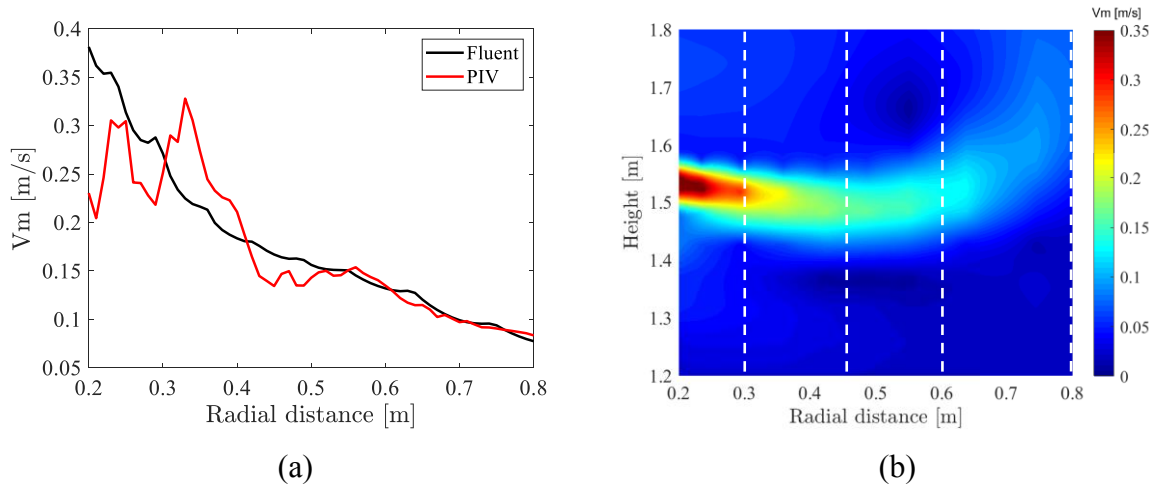


Figure 85. Velocity characteristics at  $t = 1800$ s: (a) comparison of Fluent predictions and PIV data for centerline velocity, and (b) velocity field predicted by Fluent. The data from PIV was time-averaged over 200s.

There is a noticeable deviation between experiment and simulation in the region before  $x = 0.4$  m. In Figure 29(a) the dark blue area around the sparger where no data was recorded is shown. The centerline velocity in the PIV data was defined as the maximum velocity in a cross section. Given that only part of the region is resolved, the value of the maximum velocity can be under-estimated. Further discussion regarding the measurement uncertainty can be found in [109, 132]. A good agreement in the far-field ( $x > 0.5$  m) suggests that the “Unit Cell” model can quantitatively be used to predict the far-field velocity profile induced by steam injection.

Comparison of the radial velocity profiles in different cross sections (see dashed lines in Figure 85b) is given in Figure 86. Individual jets can be seen at  $x = 0.05$  m. In reality, however, the steam jets might not be condensed yet at this point. The radial velocity profile in both PIV and simulations can be described as a single jet at the radial distances of  $x = 0.3, 0.45, 0.6$  m. A reasonable agreement between prediction and experiment is obtained with boundary conditions for turbulence intensity  $I = 50\%$  and viscosity ratio  $\nu_T/\nu_L = 3000$  (section 4.3.3). A buoyant jet is predicted by Fluent at the far-field (Figure 85(b)) agrees reasonably well with the PIV measurements (HP53 in Figure 29). These observations suggest that the “Unit Cell” model can provide an adequate prediction of the velocity field.



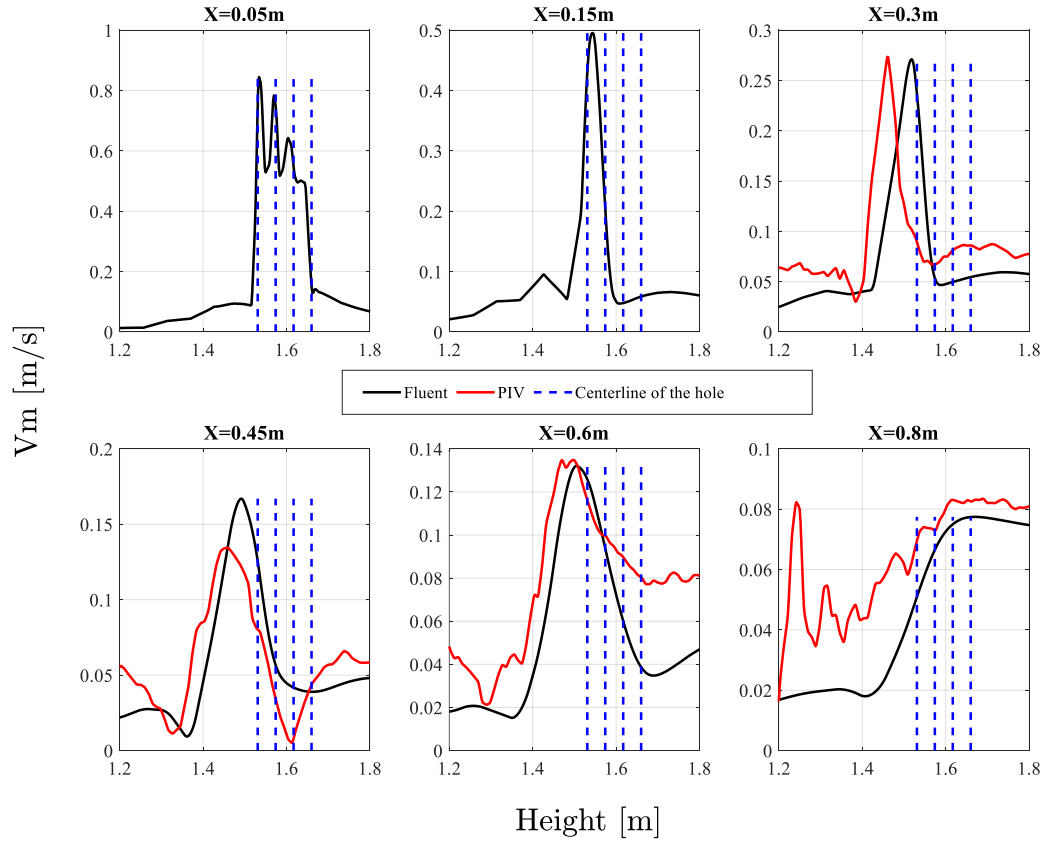


Figure 86. Comparison of radial velocity profiles between Fluent and test results over the PIV plane. The centerline of the hole drawn by blue dashed lines is used to verify the downward inclination of the jets.

The “Unit Cell” model was used in pre-test simulations to support the optimization of the PIV setup. Note that the velocity field can be affected by the pool temperature due to (i) dependency of the condensation regime coefficient  $C$  on pool subcooling, (ii) buoyancy effects on the mean flow and turbulence. According to (3) and (4) pool temperature variation in the tests will cause relatively small change of the condensation regime coefficient. Buoyancy driven jet was observed by PIV data in PANDA HP5 tests only in the low steam injection phase  $\dot{m}_s = 0.16 \text{ kg/s}$  [31, 36]. When the steam flow rate was increased to  $0.27 \text{ kg/s}$  and  $0.37 \text{ kg/s}$ , buoyancy was no longer a dominant factor. Pool temperature had little effect on the jet flow pattern. It can be expected that the differences between water temperature in H2P3 tests would not change the velocity field dramatically. Therefore, the pre-test simulations are performed using initial conditions and injection procedures of H2P3-1 (Table 9).

The velocity contours in the vertical direction obtained from the simulation are presented in Figure 87. The velocity field in H2P3-1 first phase is expected to be similar to HP53 (Figure 85(b)) that was carried out at the same conditions. A buoyancy driven jet is observed in the first injection phase where  $\dot{m}_s = 0.16 \text{ kg/s}$ , similar to the data from PIV.

After the steam flow rate was increased to  $0.27 \text{ kg/s}$ , inertia becomes the dominant factor. Simulation results at  $t = 8000 \text{ s}$  are also in a good agreement with the experimental observations (Figure 30a). Although half of the domain is invisible, one can see that jet penetration is more pronounced compared to the low steam flow rate conditions.

The main differences between the last three injection phases are the magnitude of the velocity and the inclination of the jet. The velocity is increased due to the increase of the steam flow rate and the decrease of the subcooling. The jet with higher effective momentum is less diffused and changes jet inclination angle. This is probably due to the fact that the turbulent viscosity ratio in the boundary conditions is set to 3000 during the whole transient.

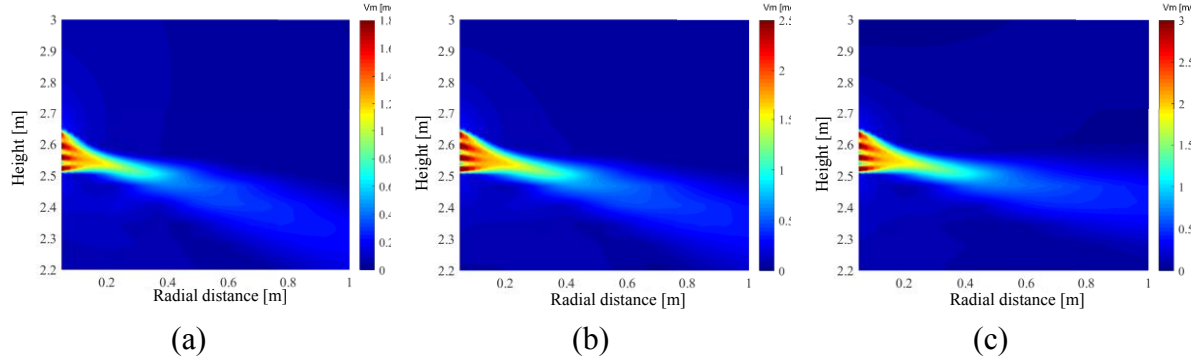


Figure 87. Velocity contours obtained in Fluent at (a)  $\dot{m}_s = 0.27 \text{ kg/s}$ ,  $t = 8000 \text{ s}$  (b)  $\dot{m}_s = 0.37 \text{ kg/s}$ ,  $t = 12000 \text{ s}$  (c)  $\dot{m}_s = 0.45 \text{ kg/s}$ ,  $t = 16000 \text{ s}$ .

The velocity fields obtained in Fluent at different cross sections are presented in Figure 88. The figure shows velocity fields at the end of each injection phase. The four condensing jets almost merge together at a distance of 150mm away from the sparger head (Figure 87, Figure 88). According to the empirical formula [36], the distance where jets merge can be estimated as three times the pitch plus hole diameter, which corresponds to 157.5 mm for PANDA sparger. Similar observation was done based on the analysis of temperature and PIV data from PANDA tests [36].

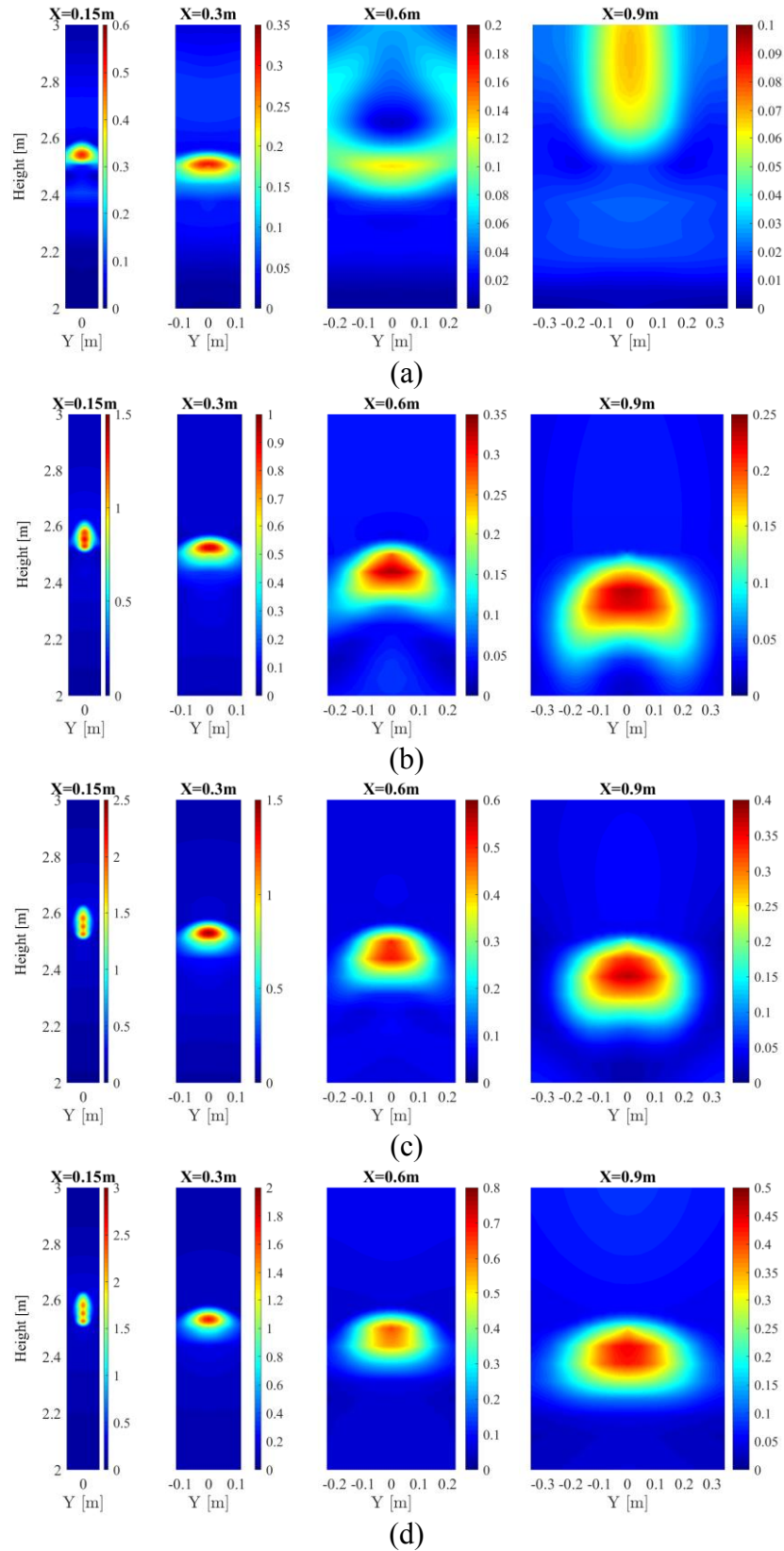


Figure 88. Velocity contours at different slices obtained in Fluent. (a)  $\dot{m}_s = 0.16 \text{ kg/s}$ ,  $t = 4000\text{s}$  (b)  $\dot{m}_s = 0.27 \text{ kg/s}$ ,  $t = 8000\text{s}$  (c)  $\dot{m}_s = 0.37 \text{ kg/s}$ ,  $t = 12000\text{s}$  (d)  $\dot{m}_s = 0.45 \text{ kg/s}$ ,  $t = 16000\text{s}$ .

Non axisymmetric velocity field is observed in Fluent simulation (Figure 88) in all injection phases. It is a typical behavior for the multiple jets. Observed profiles can be described using equation (16). As the distance from orifice increases, the jet expands in the azimuthal direction,

resulting in a change from near-planar to elliptical jet. The jet velocity profile evolution is seen in Figure 89, where the buoyancy effect and downward inclination are not modelled.

The jet at the end of the first injection phase is driven upward by the buoyancy (see sections at  $X = 0.6\text{ m}$  and  $X = 0.9\text{ m}$ ). For these conditions the PIV window should be placed closer ( $X \sim 0.3\text{ m}$ ). Inertia dominates jet behavior at higher flow rates, and no qualitative differences in the velocity profile can be seen. Turbulent diffusion effect can explain the differences between velocity profiles in the far-field obtained at different injection conditions. Higher momentum jets can penetrate farther with less diffusion.

Sensitivity of the velocity profile in azimuthal direction to the turbulent viscosity ratio was carried out (Figure 89). The jet with higher viscosity ratio result in more elliptical shape of the jet. This means that boundary conditions for turbulence characteristics have significant influence on the jet velocity field. In order to reproduce specific profile in Fluent the proper boundary conditions for turbulence are needed.

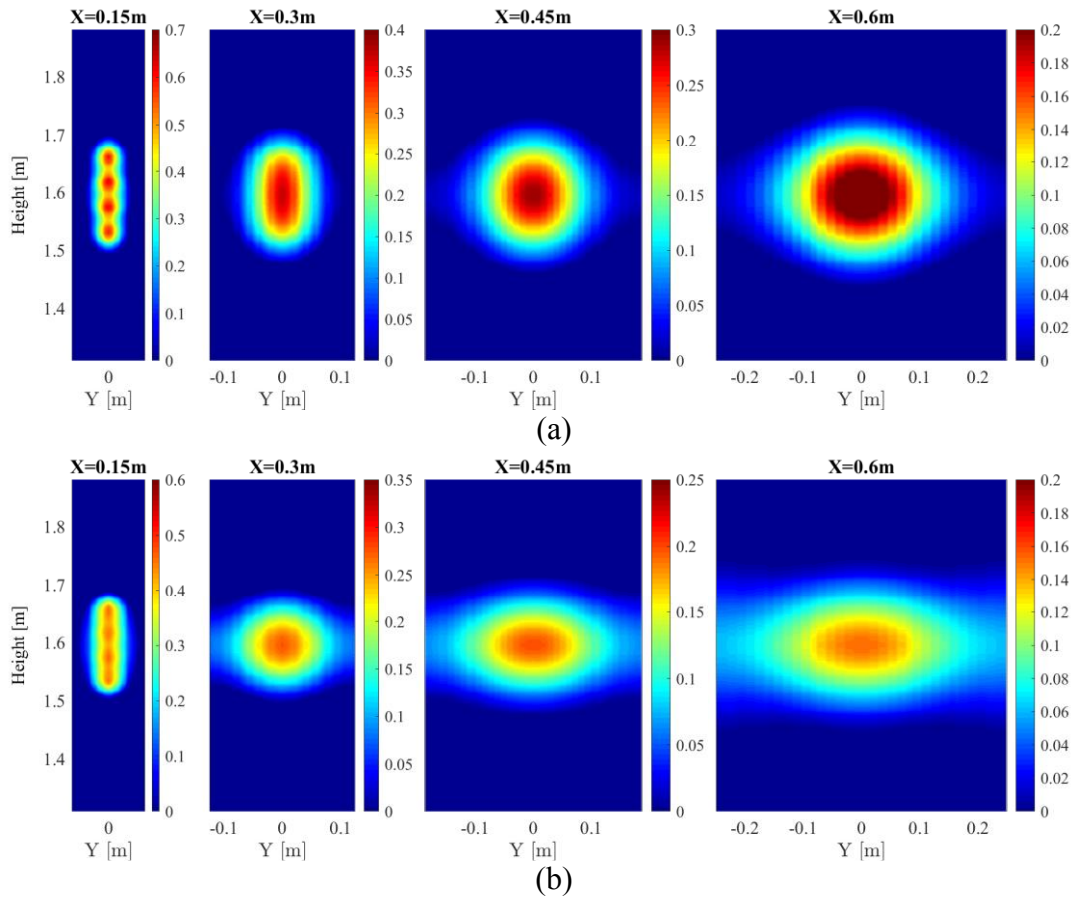


Figure 89. Velocity contours at different slices in the first injection phase, iso-thermal, and no downward inclinations. (a)  $I = 50\%$ ,  $\nu_T/\nu_L = 1000$  and (b)  $I = 50\%$ ,  $\nu_T/\nu_L = 3000$ .

#### 6.1.5. Optimization of the PIV window orientation

The sparger head position with respect to the PIV window can be optimized to maximize the value of the PIV data by measuring jet velocity with a single PIV plane in as many jet cross sections as possible. Since the centerline velocity is one of the important parameters of

calibration of the azimuthal profile model, the measurement should also capture as many centerline points of the jets as possible. The PIV setup is optimized by selecting (i) the distance  $d$  between sparger head and PIV plane, and (ii) angle  $\alpha$  of the sparger head rotation along the vertical axis. The PIV might be unreliable at close distances to the sparger. In the high steam injection phase of HP53 almost half of the PIV window becomes unusable (Figure 30(a)). In this region dense bubbles affect the passage of light from the illumination plane to the camera. Therefore a minimum distance of 300 mm between the PIV plane and the sparger is selected for the low steam injection conditions.

In order to make a quantitative optimization of PIV plane orientation we introduce an effective length. The length is defined as a sum of projections of the PIV cross sections of different jets on the centerline axes of the respective jets (Figure 90). If different jets are crossed in the same place, effective length is counted only for one of the cross sections.

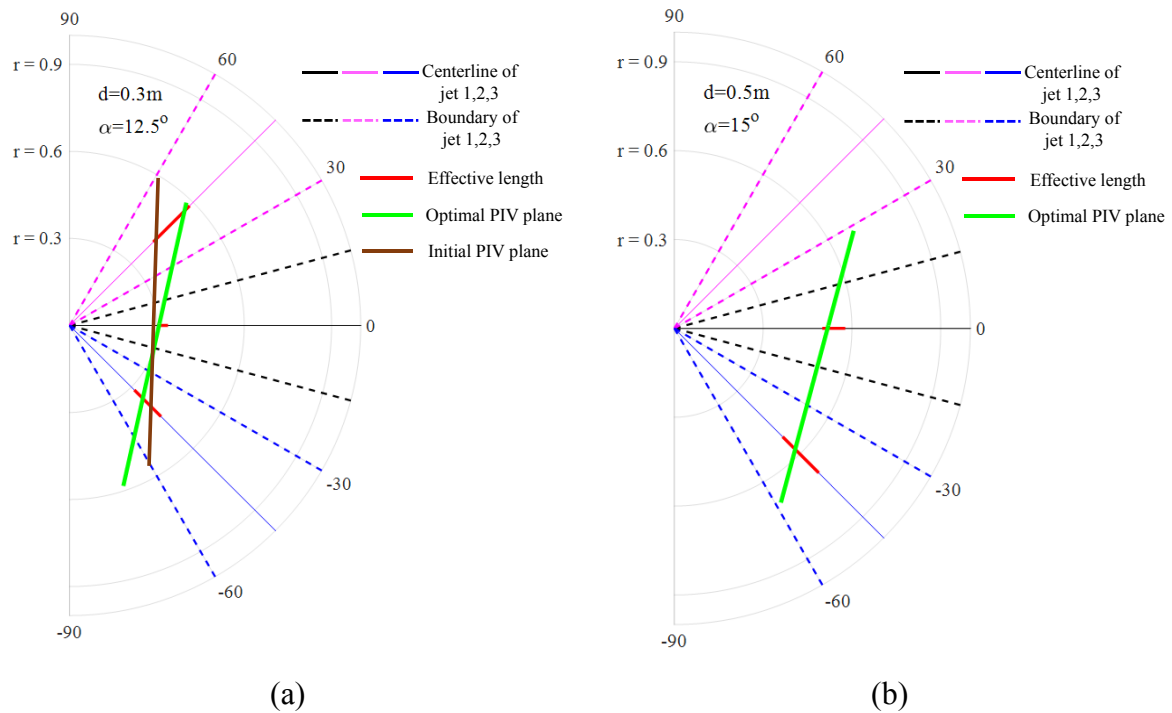


Figure 90. Optimal PIV configuration of a range of (a) 300 – 500 mm and (b) 500 – 800 mm in a view along the sparger axis.  $r$  is radial distance and the sparger at  $r = 0$ .

In the analysis we consider three turbulent jets with expansion angle  $30^\circ$  and symmetric with respect to the centerline. The PIV plane was aligned with the centerline of jet 1  $\alpha = 90^\circ$  and  $d = 0$  m (Figure 90) in the previous tests [36] to measure the velocity profile in a vertical cross section. For H2P3 measurements of the velocity distribution in azimuthal direction, the optimization is started with  $\alpha = 0^\circ$  (plane shown as brown line in Figure 90). Optimal angle of rotation depends on the distance from the sparger. Centerline velocities for three jets can be measured if the distance from the PIV plane to the sparger is in a range between 300 – 500 mm. In this case the optimization gives  $\alpha = 12.5^\circ$  and  $d = 300$  m (Figure 90(a)). The PIV plane intersection with the jet 1 centerline is 5 cm away from the edge of the PIV plane. For the range of the distances 500 – 800 mm, it is possible to measure only two centerline velocities with a 1 m wide PIV window. The optimization results in  $\alpha = 15^\circ$  and  $d = 500$  m (Figure 90(b)). At the distances larger than 900 mm only one centerline velocity can be measured.

Given the distance of the PIV window will be fixed during each test, the distribution of the above introduced three regions should be discussed. For the strongest jet (e.g. H2P3-3 last injection phase) the PIV window should be located at a distance of 900 *mm*. Sparger rotation can be set between 0° or ~43°. For the conditions of H2P3-2 second, third and fourth injection phases the PIV window can be located at the distance of 500 *mm* with rotation angle of 15°. For H2P3-1 first injection phase the PIV plane can be located at the distance of 300 *mm* with rotation angle 12.5°.

## 6.2. Pre-test simulations for H2P3 LRR tests

Three tests of H2P3-4,5,6 are planned to be carried out with LRR holes open and with the sparger head holes closed. The LRR, is located at 1800 *mm* from the bottom of the sparger (Figure 5 and Figure 91) and has 8 holes with 9.5 *mm* inner diameter, distributed in 1 ring. In this section we provide pre-test analysis to select the test conditions. The aim of the test is to maintain stratification in the pool during the whole transient and study gradual erosion of the cold layer as the steam flow rate is changed. We study the effect of (i) the elevation of LRR holes above the pool bottom, (ii) the number of open LRR holes, and (iii) the flow rate and duration in each steam injection phase.

The pre-test simulations are carried out using the EHS/EMS models implemented by SCR approach for a single jet (section 4.3.2). Results of the model validation (section 4.3.3) demonstrated that jet induced by condensing steam can be simulated by injecting liquid with a uniform velocity profile that provides the same effective momentum. Flow symmetry was assumed and a 22.5° sector was used as a computational domain with a half of the injection hole.

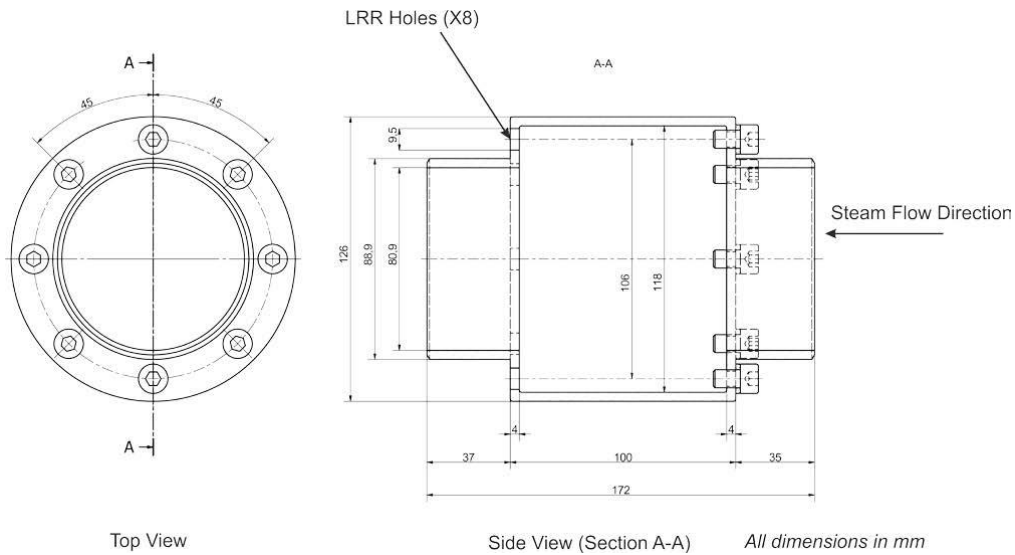


Figure 91. Details of the Load Reduction Ring (LRR).

The water pool level is 6 *m*. The pre-test analysis with LRR holes positioned at 3300 *mm* (1500 + 1800) above the pool bottom and steam injection procedure similar to H2P3 was carried out first. Results of the analysis showed that vertical jets from LRR holes can penetrate into the cold layer by about 2000 – 2500 *mm* even at relatively small flow rates. To avoid rapid mixing of the pool, the elevation of the sparger head was increased from 1.5 *m* to 2.5 *m* with elevation of LRR holes 4300 *mm*.

Further pre-test simulations with the 2.5 *m* sparger head elevation were carried out to investigate the effect of steam injection procedures. Initial pool temperature of 15°C was selected to achieve a prototypic subcooling, minimum steam flux  $G = 85 \text{ kg/m}^2\text{s}$  was chosen to avoid chugging (see regimes map in Figure 79). Temperature fields shown in Figure 92 illustrate the effect of steam mass flux increase from 85  $\text{kg/m}^2\text{s}$  to 160  $\text{kg/m}^2\text{s}$  at  $T = 4000 \text{ s}$ . A stratified layer can be observed in the first injection phase, but it is eroded rapidly by the increased momentum of the jet.

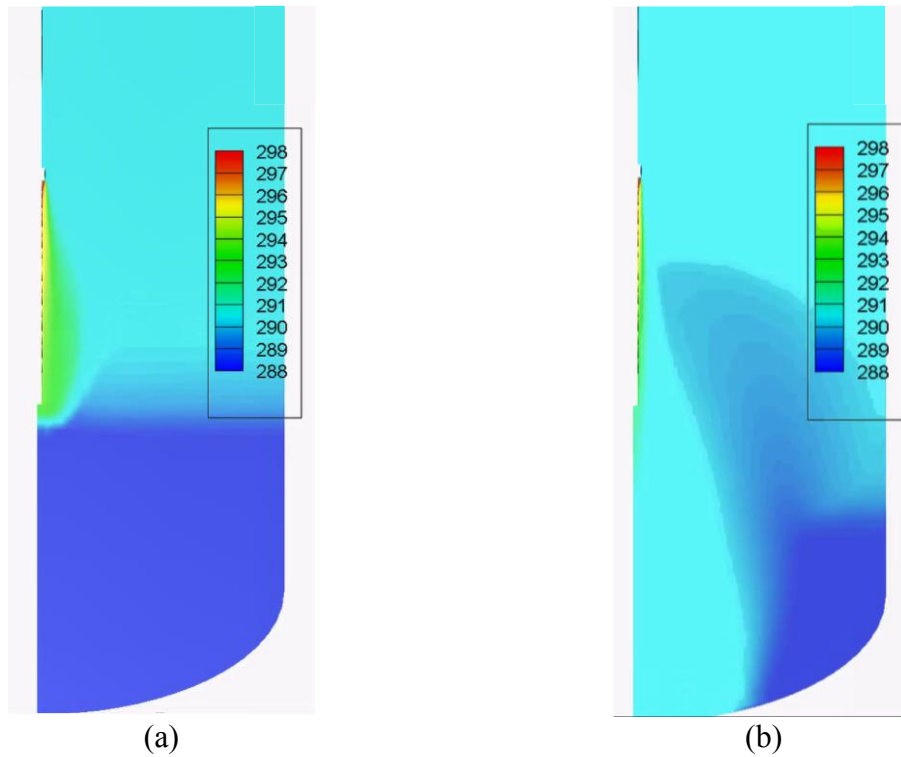


Figure 92. Temperature field predicted for H2P3 LRR tests at (a)  $t = 4000$  s with  $G = 85 \text{ kg/m}^2\text{s}$ , and (b) at  $t = 4300$  s with  $G = 160 \text{ kg/m}^2\text{s}$ .

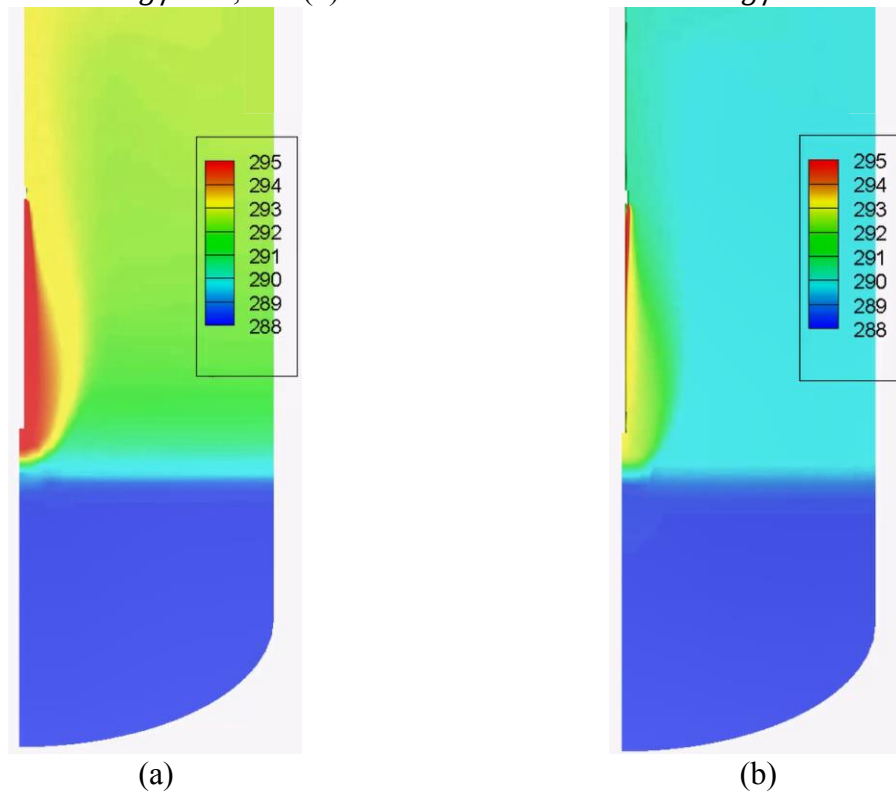


Figure 93. Temperature field predicted for H2P3 LRR tests at  $t = 6000$  s,  $G = 85 \text{ kg/m}^2\text{s}$  with (a) 8 holes open, and (b) 4 holes open.



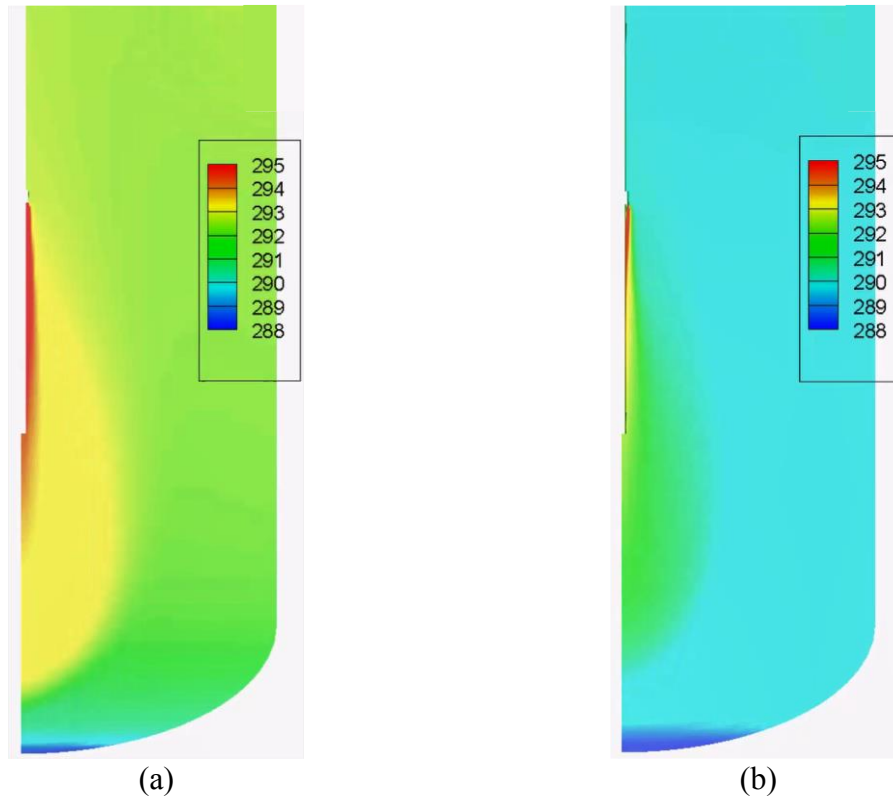


Figure 94. Temperature field predicted for H2P3 LRR tests at  $t = 7000\text{ s}$ ,  $G = 125\text{ kg/m}^2\text{s}$  with (a) 8 holes open, and (b) 4 holes open.

Based on the analysis results, it was suggested to increase the duration of the first phase to 6000 s in order to achieve a larger density (temperature) difference between the cold and the hot layers to increase resistance to the erosion at higher flow rates. In fact, 8000 s would be even better in this respect, however it was considered that the overall duration of the test still should be reasonable. The mass flux in the second phase was decreased to  $125\text{ kg/m}^2\text{s}$  in order to reduce the momentum source. Predicted temperature fields are shown in Figure 93 and Figure 94. Increased duration for the first injection phase indeed created a stronger thermocline with a larger temperature gradient (compared to the case with 4000 s for the first injection phase Figure 92). A thin layer of cold water (Figure 94a) remains at the end of the second phase, which suggests that  $G = 125\text{ kg/m}^2\text{s}$  can be used in the last phase.

We found that the effect of the number of LRR holes on the jet penetration depth at the same steam flux is minor (Figure 93b and Figure 94b). Smaller number of holes (and respectively reduced flow rate) results in increased time needed to develop a stratified layer. Therefore, it was proposed to keep 8 holes opened. The setup suggested for H2P3 LRR tests has water level 6 m, sparger head elevation 2.5 m and 8 open LRR holes. The injection procedures are summarized in Table 10 and Table 11. In total 4 injection phases are set for H2P3-4,5 and eight phases for H2P3-6. In the first phase of steam injection flux is set to  $85\text{ kg/m}^2\text{s}$  ( $0.048\text{ kg/s}$ ) in order to create a stratified pool. Then steam flow rate is increased in steps. Initial temperature in H2P3-5 is set to  $35^\circ\text{C}$ .

Amount of gas bubbles generated at small steam flow rates in the LRR tests is expected to be relatively small. There is a hope that at such conditions PIV can provide valuable data for code validation such as velocity field and turbulence characteristics of the jet. In H2P3-6 the number of the injection phases is increased to 8 and the duration of each phase is decreased to 2500 s

(Table 11). First, the flow rate is increased from 48 g/s to 60 g/s in 4 steps. The pool is expected to be almost completely mixed at that point. Then flow rate is reduced to 40 g/s. Chugging can be avoided at such small flow rates as the pool temperature is sufficiently increased. Then flow rate is increased again in several steps.

Table 10. Steam injection procedures of H2P3-4,5.

Test	Initial conditions	Phase 1		Phase 2		Phase 3		Phase 4	
	Temperature (°C)	Flow (kg/s)	Time (s)	Flow (kg/s)	Time (s)	Flow (kg/s)	Time (s)	Flow (kg/s)	Time (s)
H2P3-4	15	0.048	6000	0.053	4000	0.058	4000	0.07	4000
H2P3-5	35	0.048	6000	0.053	4000	0.058	4000	0.07	4000

Table 11. Steam injection procedures of H2P3-6.

Test	Initial conditions	Phase 1(5)		Phase 2(6)		Phase 3(7)		Phase 4(8)	
	Temperature (°C)	Flow (kg/s)	Time (s)	Flow (kg/s)	Time (s)	Flow (kg/s)	Time (s)	Flow (kg/s)	Time (s)
H2P3-6	15	0.048	2500	0.052	2500	0.056	2500	0.060	2500
		0.040	2500	0.052	2500	0.056	2500	0.060	2500

### 6.3. Summary of pre-test analysis for H2P3 test series in PANDA facility

Pre-test simulations have been carried out to support definition of the PANDA H2P3 test series. Scoping calculations are carried out to specify geometrical setup (pool depth, elevation of the sparger and number of open LRR holes), initial pool temperature, injection procedures, arrangement of thermocouples, PIV setup, for sparger tests (H2P3-1,2,3) and LRR tests (H2P3-4,5,6).

## 7. PRE-TEST SIMULATIONS FOR PANDA H2P4 TESTS

### 7.1. Motivation and background

OECD/HYMERES-2 project test series H2P4 aims to address integral phenomena of a BWR containment behavior with pressurization caused by pool stratification. We consider an SBO scenario with steam injection into wetwell at relatively small rates through a sparger. Conditions similar to those observed in the Fukushima Units 2 and 3 were taken as a reference for defining the H2P4 series of tests. Specifically, containment pressurization to ~4 bar with temperature of water ~140 °C and then activation of spray and slow depressurization of the containment.

The goal of the H2P4 test series is to provide data in relevant for plant conditions regimes for validation of code predictive capabilities for (i) development of thermal stratification in the pool induced by steam injection and condensation; (ii) containment pressurization due to development of the pool stratification with increased temperature of the pool surface and thus higher partial steam pressure in the containment gas space; (iii) the effect of spray activation on the pool stratification and containment pressure.

The primary goal of the pre-test scoping analysis is to provide basis for selection of test design options that would enable achieving within a reasonable test time: (i) pool thermal stratification, (ii) system pressurization ~4 Bar, (iii) pool temperature ~140 °C and (iv) study the effects of spray activation on pool stratification and containment pressure.

The secondary goals for the test design are: (i) to minimize the effects of irrelevant and/or not measured phenomena in the experiments, e.g. gravity driven counter current flows through the interconnecting pipes and (ii) to optimize experimental efforts, e.g. reduce facility modifications compared to H2P3 test configuration.

To achieve the goals of the scoping analysis the following tasks have been addressed: (i) to develop a fast running model, (ii) to calibrate and validate the model and (iii) to carry out scoping parametric analysis for selection of H2P4 test configuration and test matrix.

It should be mentioned that at the time of the writing of this report selection of the H2P4 test conditions has not been completed, and discussions related to the technical implementation of specific design solutions in the PANDA facility were still ongoing.

### 7.2. Initial test configuration for the H2P4 series

The H2P4 test series will be carried out in the PANDA experimental facility. The PANDA facility [135] consists of four interconnected vessels that are scaled to represent drywell and wetwell of a BWR. The facility was used to study the passive decay heat removal systems and containment response of the Simplified Boiling Water Reactor (SBWR) and the Economic Simplified Boiling Water Reactor (ESBWR) designs from General Electric (GE), as well as of the SWR1000 design from Siemens-KWU (now KERENA design from AREVA) in the case of accident transients. During the H2P4 series the injection of steam into the wetwell pool through a sparger must develop thermal stratification and with time pressurization of the drywell. The drywell vessels were disconnected in order to reduce gas volume and achieve faster pressurization within a realistic time for an experiment.

The preliminary experimental setup for the scoping analysis is comprised of two vessels (see Figure 95). The vessels are connected using two pipes one at the bottom (ID1420) and one at the top (ID928). Both vessels are filled in with water, steam injection into the pool is performed into the left (in the Figure 1) vessel through a sparger. The water pool represents the wetwell and gas gap above it – the drywell. Experimental parameters included in the scoping analysis:

- steam injection rate:
  - affects the rate of system heat-up and pool mixing / stratification.
- sparger submergence,
- water pool depth:
  - affects the volume of gas space for pressurization
- water pool initial temperature:
  - affects time required for system heat up during steam injection
  - can also affects stability of the thermocline due to temperature difference between the hot and cold layers
- configuration of the vessels:
  - single vs two vessel configuration
- spray location (vessel and elevation above water pool surface),

In addition, scoping simulations also included analysis of experimental procedures for possible pool preconditioning.

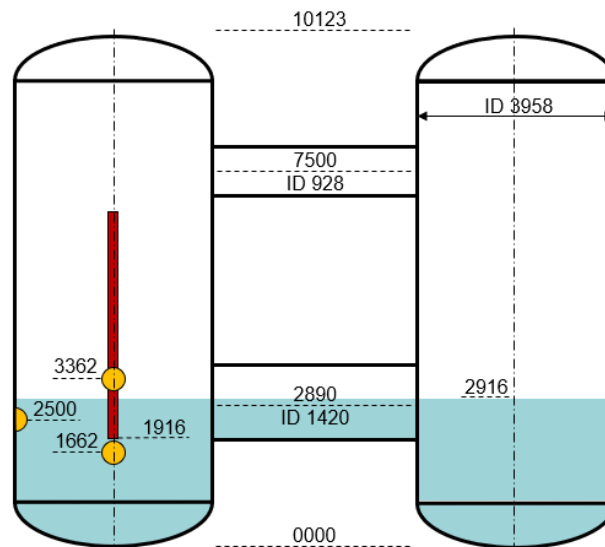


Figure 95. PANDA experimental facility for H2P4 scoping analysis

### 7.3. Model setup for H2P4 scoping analysis

GOTHIC 8.3 code was selected for the pre-test analysis. GOTHIC is a general-purpose thermal-hydraulic code used for modelling of power plant containments, confinement buildings and system components. It provides 3D capability based on Cartesian mesh and porous body approximation, has a wide validation database and is used for design and licensing applications.

To achieve required computational efficiency several simplifications were made in the model setup:

- To model sparger effect on the pool we introduced
  - Mass source: source of saturated water located in the pool cell with the sparger tip
  - Heat source: volumetric homogeneous heat source distributed vertically along the submerged section of the sparger to account for steam latent heat.
- The thickness of the hot layer (that defines position of the thermocline) was fixed in the model input to avoid the need for detailed 3D modelling of the steam momentum effect on the pool mixing.
  - The thermocline depth was varied as a part of the scoping analysis to account for available knowledge on the erosion of the cold layer by steam injection at different steam flow rates.
- In order to allow for convective energy redistribution within the hot layer a coarse 3x3x4 mesh was used.
- Convection in the gas space above the water pool was modelled using coarse 3x3x4 mesh. In the later stage of calculations nodalization in the gas space was increased to study steam transport behavior in more detail.
- Vessel walls were modelled to account for thermal inertia of the steel. Adiabatic boundary conditions were setup for all simulation cases at the external surface of the vessel covered with thermal insulation.
- The two interconnecting pipes (IPs) between the vessels were modelled using single flow paths with stratified flow option.

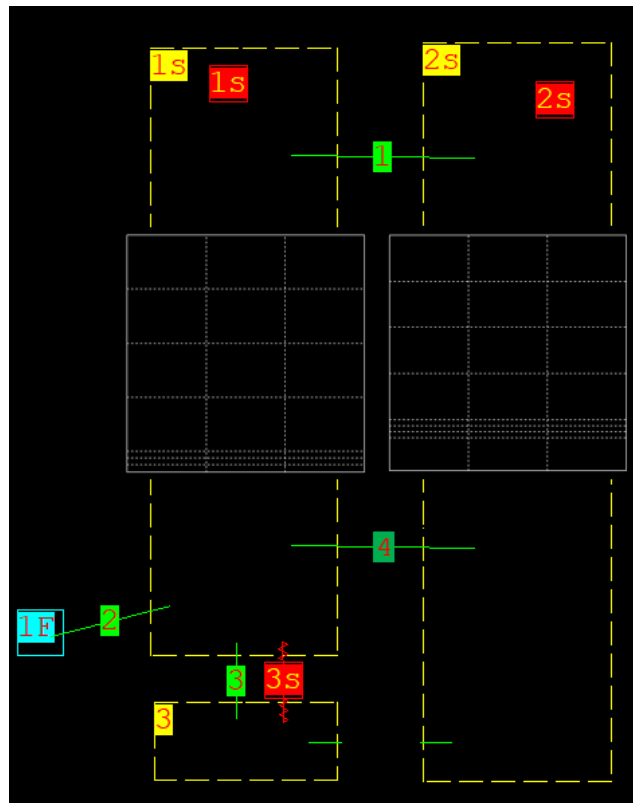


Figure 96. Initial GOTHIC model for H2P4 scoping analysis

Initial model implementation is shown in Figure 96. The two inserts in the figure show the cross-section of the nodalization for the control volumes 1s and 2s. The left vessel is modelled as two control volumes:

- control volume 3 for the cold layer of the pool and
- control volume 1s for the hot layer of the pool and the gas space above it.

Control volumes 1s and 3 are connected using a flow path and a thermal conductor. The thermal conductor is introduced to account for heat transfer between the hot and cold layer through the thermocline. The flow path is included mainly to allow for flow between the bottom of the vessel 3 and vessel 2s. The respective flow path was not used in the initial model and is not shown in the illustration.

The two interconnecting pipes are modelled as flow paths 4 and 1. Stratified flow conditions was activated to model possible counter flow of water and steam.

It should be noted that described here model corresponds to the one of several configurations studied in the scoping analysis.

#### 7.4. Model validation

The ultimate goal of the model was to assess the rate of the pool heat-up and system pressurization given conditions of steam injection and expected thermocline depth (based on previous tests and/or accompanying CFD EMS/EHS simulations).

The model was validated against Phase 1 of HP5\_1\_2 test [80]. In the test steam was injected into the left vessel through a sparger. The sparger end was positioned 1.5 m below the initial water level. The pressure in the gas space above the water pool was kept constant by opening the vessel to atmosphere. The position of the thermocline was measured in the experiment and provided as an input to the model (refer to Figure 97a and b), specifically:

- Hot layer thickness: 3 m
- Thermocline thickness: 0.25 m
- Cold layer thickness: 0.75 m

Other initial and boundary conditions:

- Water pool initial depth 4 m and temperature 25°C
- Sparger submergence 1.5 m.
- Steam injection (as equivalent mass source of saturated water and volumetric heat):
  - Flow rate: 161.74 g/s
  - Temperature: 110°C

Two relevant System Response Quantities were selected for model validation: (i) water pool heat up rate and (ii) water pool surface temperature. The latter is believed to be one of the dominating factor for vessel pressurization. The results of the model validation are provided in the Figure 98.

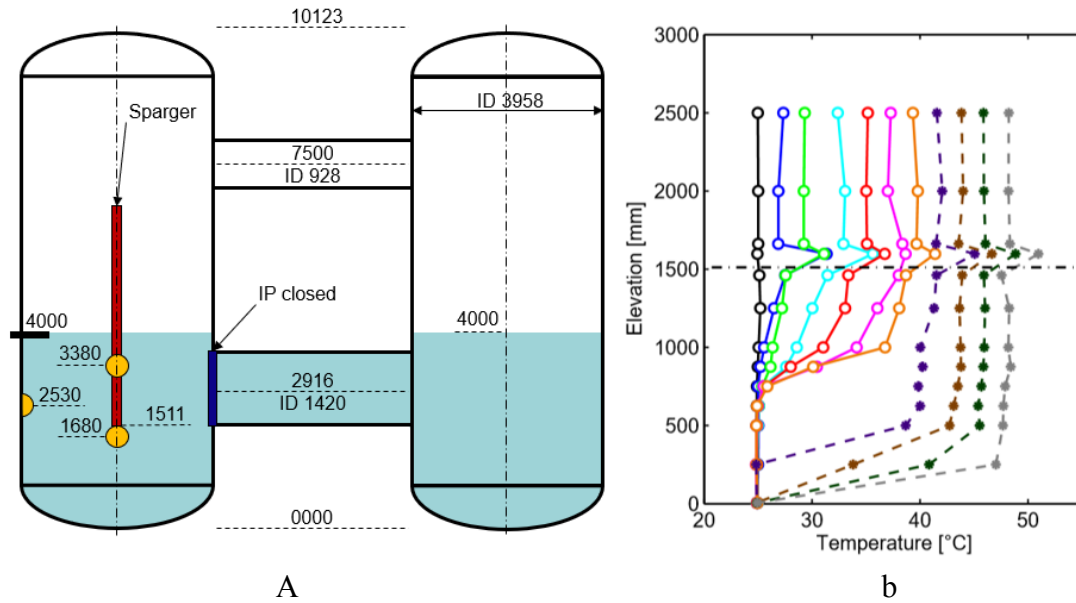


Figure 97. HP5\_1\_2 test: a – initial setup, b – temperature profile at different times for Phase 1 (solid lines) and Phase 2 (dashed lines) of the test.

The predicted rate of pool heat-up satisfactory agrees with the experimental data: at 6325 s the estimated temperature of the pool surface was 42.3°C - close to the experimental value of about 43°C. The vertical temperature difference in the hot layer was underestimated: about 2.3K in the simulation vs ~4.6K in the experiment. The discrepancy is attributed to the coarse meshing in the pool in the vertical direction (4x0.9m). The discrepancy was considered as acceptable tradeoff for the needed computations efficiency.

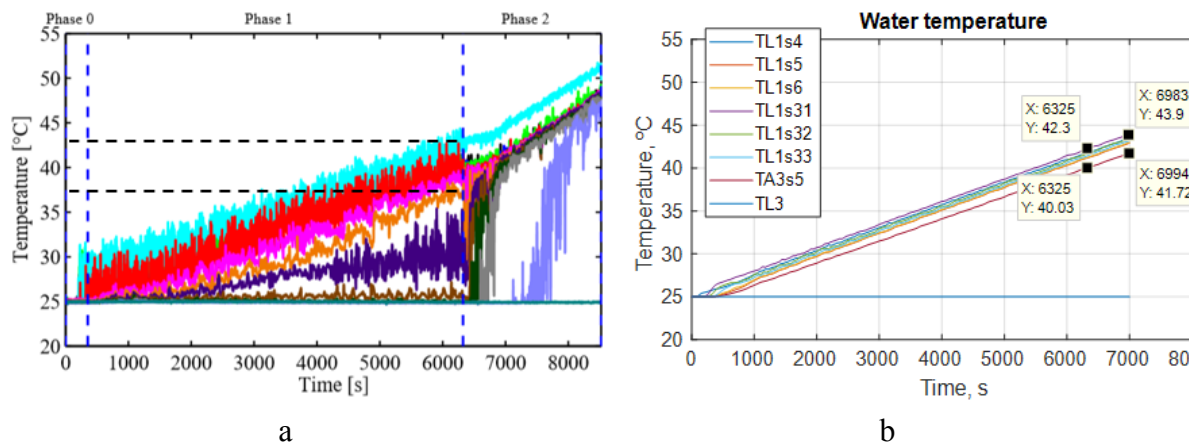


Figure 98. HP5\_1\_2 test evolution of the pool temperature: a – experiment, b – simulation.

### 7.5. Results of the scoping analysis

Preliminary heat balance calculations were carried out to estimate the magnitude of the steam injection necessary to heat the pool to 100-140°C assuming zero thermal losses and no evaporation. The results (see Table 12) suggest that scoping calculations should be performed for steam injection of 160 and 260 g/s. Higher rates of steam injection will increase the potential for complete mixing of the pool; while at lower flow rates heating and pressurization will take long time to develop.

Table 12. Heat balance calculation for different steam injection rates

Thermocline depth m	Injection rate kg/s	Time [h] to reach water pool temperature				
		100 °C	110 °C	120 °C	130 °C	140 °C
0.7	0.056	4.72	5.35	5.98	6.60	7.23
1	0.056	6.74	7.64	8.54	9.43	10.33
1.3	0.056	8.76	9.93	11.10	12.26	13.43
1.2	0.161	2.81	3.19	3.56	3.94	4.31
1.5	0.161	3.52	3.98	4.45	4.92	5.39
1.8	0.161	4.22	4.78	5.34	5.91	6.47
1.5	0.262	2.16	2.45	2.74	3.02	3.31
1.9	0.262	2.74	3.10	3.47	3.83	4.20
2.2	0.262	3.17	3.59	4.01	4.44	4.86

#### 7.5.1. Two-vessel configuration with open IPs

The first set of GOTHIC calculations was carried out for the two-vessel configuration (as show in Figure 99) for conditions listed in Table 13. For Cases 1-3 the depth of the hot layer as function of the steam injection rate was obtained from HP5\_3 experiment. For Case 4 hot layer thickness was reduced by reducing water pool depth and raising the sparger elevation.

Table 13. Calculation cases for two-vessel configuration with open top and bottom interconnecting pipes

#	Pool depth m	Sparger position m	Steam injection rate g/s	Hot layer thickness m	Initial water pool temperature °C
1	4	1.5	161	3.0	25
2	4	1.5	262	3.4	25
3	4	1.5	161	3.0	45
4	2.9	1.9	161	1.5	25



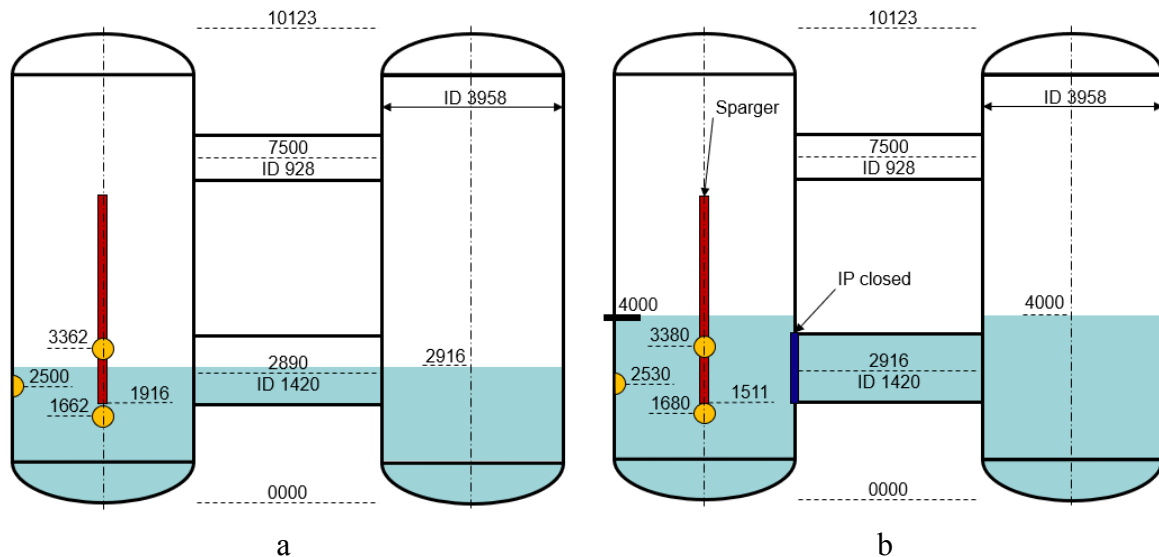


Figure 99. Calculation cases for two-vessel configuration with open IPs  
(a – Case 4; b – Case 1-3)

In all cases the results were similar in that after 15000 sec pool temperature was around 60°C, gas temperature was 45-60°C and system pressure 1.2 Bar. Heat transfer from vessel 3 pool to the vessel 4 pool significantly slows down system pressurization. Furthermore, connections between the two vessels introduce counter-current gravity driven flows in a pipe that are not relevant for plant conditions, difficult to measure in the test and not easy to model. For example, when water level is within the elevation of the bottom interconnecting pipe (IP), hot water from the left vessel will flow through the IP in to the right vessel and cold water from the right vessel will flow in opposite direction. The two counter-current flows will (i) be stratified (with hot layer above the cold layer), (ii) have different velocities due to varied cross section of the IP and (iii) partially mix due to the Kelvin-Helmholtz instability. Detailed modelling of flow in the IP will be necessary to capture the dynamics of thermal stratification in both vessels. The experiment is not well instrumented for measuring details of the flow in the interconnecting pipes and modelling of the IPs is not directly relevant from the perspective of a plant accident.

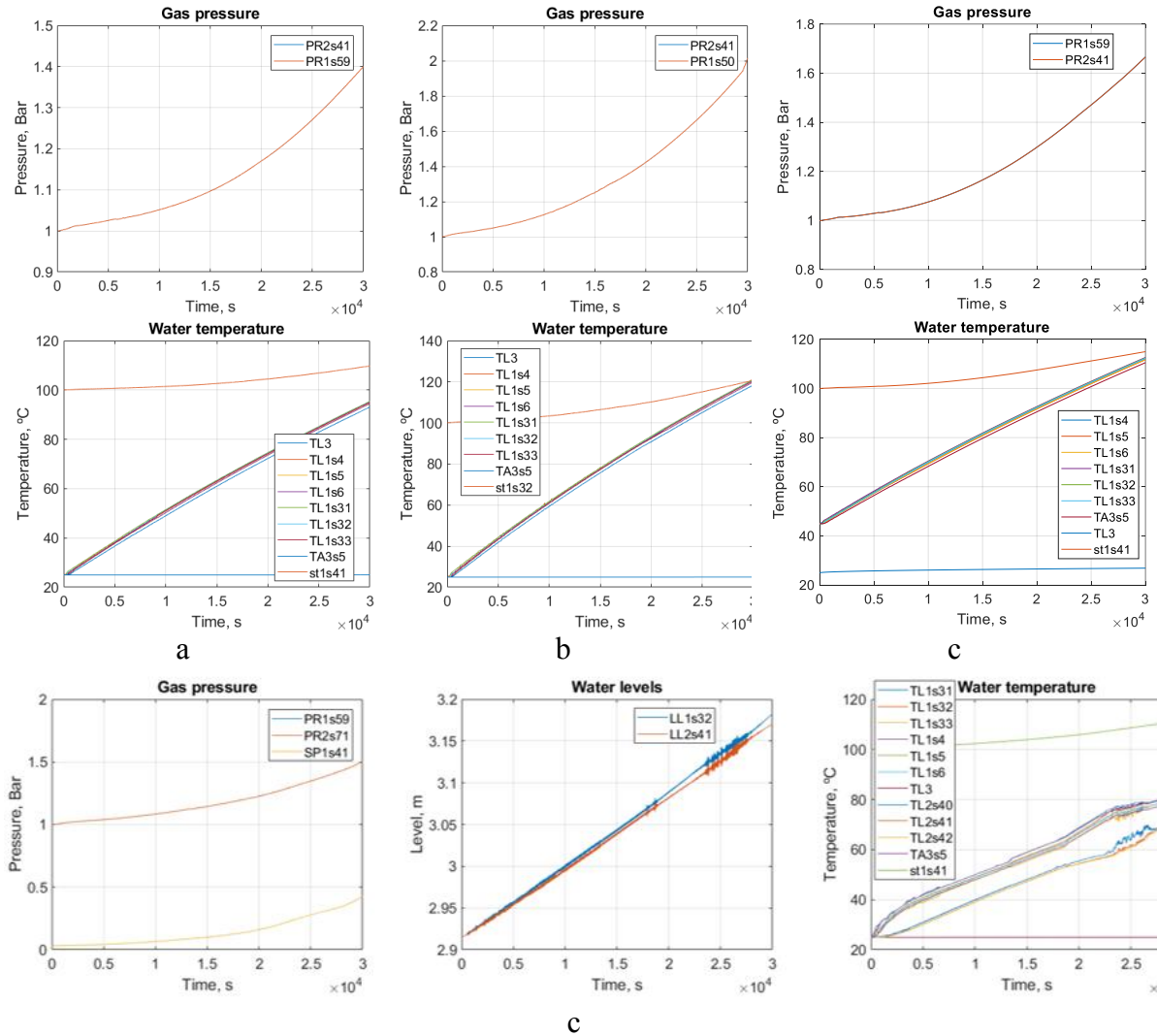


Figure 100. Calculation results for two vessel configuration with open IPs  
(a – Case 1; b – Case 2; c - Case 3; d – Case 4)

*Legend notation:*

*PR2, PR1 – gas pressure in the control volumes 2s and 1s*

*SP1 – saturation pressure in the control volume 1s*

*TL1, TL3 – water temperature in the control volumes 1s and 3*

*st1 – saturation temperature in the control volume 1s*

*LL1, LL2 – water level in the control volumes 1s and 2s*

Based on the results of the first series of calculations, it was suggested that both interconnecting pipes should be closed. Instead small diameter lines (interconnecting steam line and interconnecting water line) could be introduced to balance hydrostatic pressure of the two pools and pressure in the gas space in both vessels (see Figure 101).

## 7.5.2. Two-vessel configuration with closed bottom IP

A second series of calculations has been carried (refer to Table 14 for the list of the most relevant cases), including 4 cases for sparger injection, 2 cases for pool preconditioning and different configurations of interconnecting pipes and interconnecting lines. The results are summarized in the following subsections.

Table 14. List of simulations carried out in the second series of calculations

Case	Steam injection	Depth			Initial water temperature	Top interconnecting pipe	Interconnecting line		Spray	
		Therm ocline	Pool	Sparger			Bot.	Top	kg/s	position
	g/s	m	m	m	°C					
C10.01	161	1	3	2.5	25	open	yes	no	-	-
C10.02	262	1.4	3	2.5	25	open	yes	no	-	-
C10.03	161	1.4	3	2.5	25	open	yes	no	-	-
C10.04	262	1.9	3	2.5	25	open	yes	no	-	-
C10.01b	161	1	3	2.5	25	closed	yes	yes	-	-
C10.02b	262	1.4	3	2.5	25	closed	yes	yes	-	-
C10.03b	161	1.4	3	2.5	25	closed	yes	yes	-	-
C10.04b	262	1.9	3	2.5	25	closed	yes	yes	-	-
C11.01	161	1	6	5.5	25	open	yes	no	-	-
C11.02	262	1.4	6	5.5	25	open	yes	no	-	-
C11.03	161	1.4	6	5.5	25	open	yes	no	-	-
C11.04	262	1.9	6	5.5	25	open	yes	no	-	-
C11.01b	161	1	6	5.5	25	closed	yes	yes	-	-
C11.02b	262	1.4	6	5.5	25	closed	yes	yes	-	-
C11.03b	161	1.4	6	5.5	25	closed	yes	yes	-	-
C11.04b	262	1.9	6	5.5	25	closed	yes	yes	-	-
C08.01	161	3	4	2.5	25	open	no	no	-	-
C08.02	161	3	4	2.5	45	open	no	no	-	-
C10.01c	161	1	3	2.5	15	closed	yes	yes	-	-
C10.02s1	262	1.4	3	2.5	25	closed	yes	yes	5	V3-top
C10.02s2	262	1.4	3	2.5	25	closed	yes	yes	1	V3-top
C10.02s3	262	1.4	3	2.5	25	closed	yes	yes	5	V3-bot
C10.02s4	262	1.4	3	2.5	25	closed	yes	yes	5	V4-top
Preconditioning 1 – hot water injection for 1h at the top of pool										
Preconditioning 2 – hot water injection for 1h at 0.5 depth										

## 7.5.2.1. Effect of the water pool depth

Water pool depth (assumed initially the same in both vessels) changes the volume of gas that needs to be pressurized during the test. In addition, it brings the surface of the two pools closer to each other (closer to the top interconnecting pipe or line) and consequently can increase the rate of steam transport from the hot pool in Vessel 3 to the cold pool in Vessel 4. Initial conditions for calculations performed to investigate the effect of the water pool depth correspond to the cases C10.01, C10.02, C11.01, C11.02 (refer to Table 14) with C10 referring to shallow and C11 to deep pool cases (refer to Figure 101).

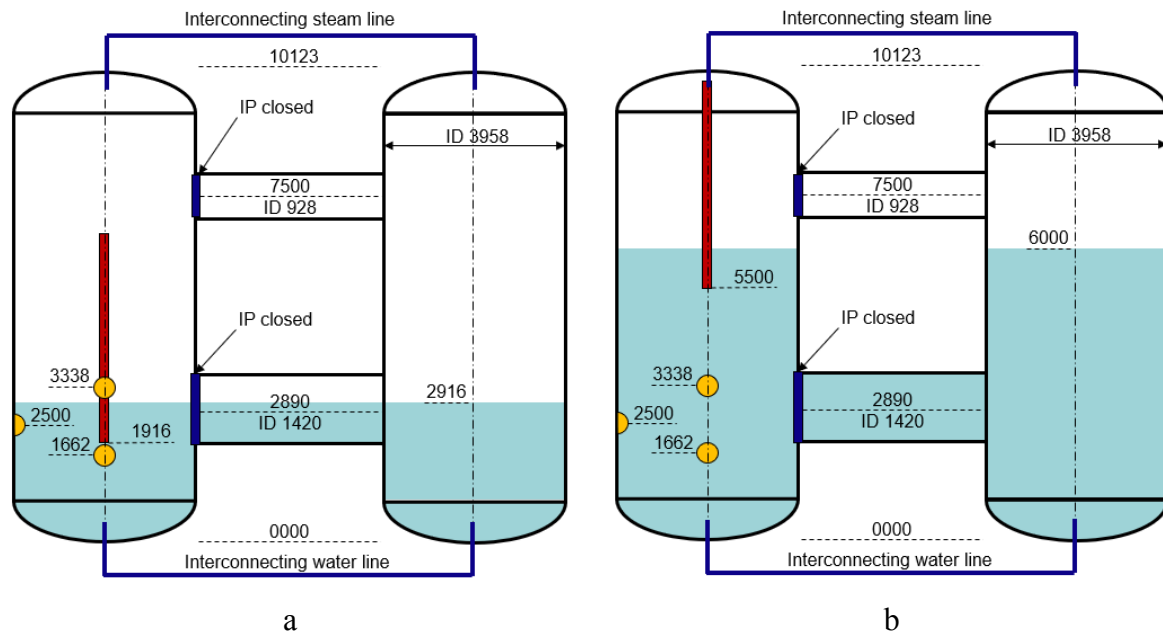


Figure 101. Calculation cases for two vessel configuration with closed IPs

In all cases sufficiently high temperatures have been established in the water pool. The initial pressure rise was found to be faster for deeper water pool cases. However, higher pressures were established in case of a shallow pool (see Figure 102). Follow-up analysis indicated that increased transport of steam in the simulations is established between the two vessels that prevented further pressurization in the case of deep water pool. Since increased transport of steam could be attributed to the used coarse mesh in the gas space a new set of calculations has been performed with refined mesh.

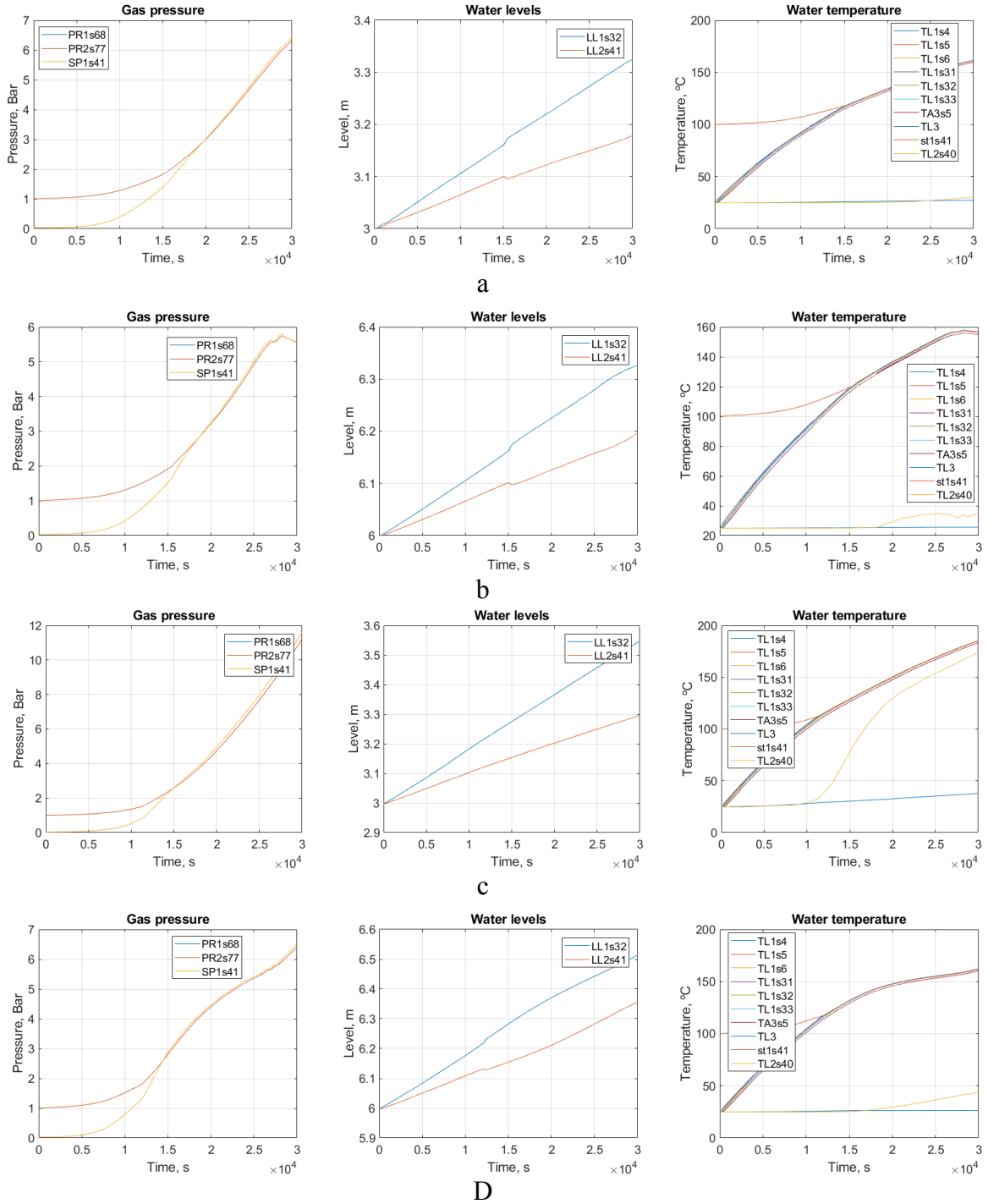


Figure 102. Calculation results for the effect of the water pool depth  
(a – C10.01; b – C11.01; c – C10.02; d – C11.02)

*Legend notation:*

*PR2, PR1 – gas pressure in the control volumes 2s and 1s*

*SP1 – saturation pressure in the control volume 1s*

*TL1, TL3 – water temperature in the control volumes 1s and 3*

*st1 – saturation temperature in the control volume 1s*

*LL1, LL2 – water level in the control volumes 1s and 2s*

The results for the cases with shallow pool depth were not affected by the mesh size. However, for the deep pool with finer mesh steam transport was reduced and higher pressure was

predicted in the simulation for deep water pool (see Figure 103 for the mesh effect and compare Figure 103a vs Figure 102c (left plot)).

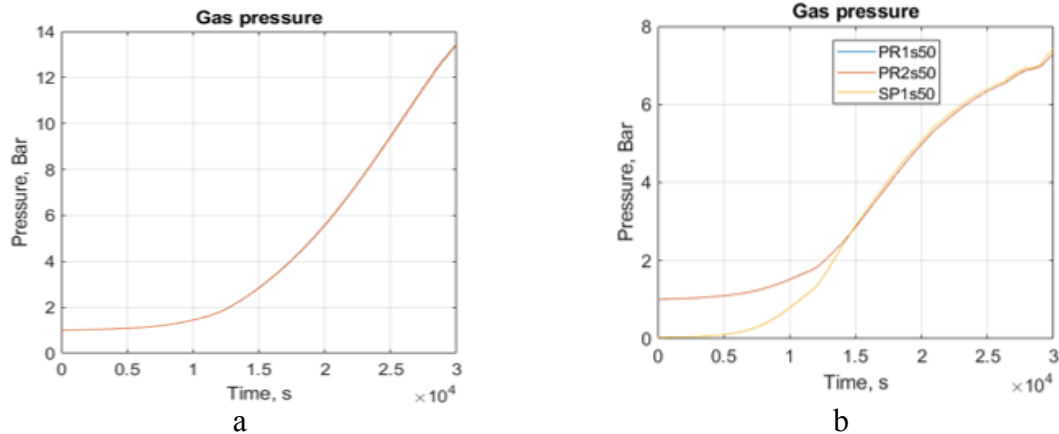


Figure 103. Effect of the mesh size for deep water pool case (a – fine mesh, b – coarse mesh)

Time required to establish 4 Bar pressure was predicted to be between 6.25h and 5.00h depending on the steam flow rate, the effect of the water pool depth was found to be less important with deep pools providing 20-30 min advantage.

#### 7.5.2.2. Effect of initial water pool temperature

Lower initial water temperature can facilitate thermal stratification, i.e. increase the stability of the cold layer to erosion due to larger density difference between the hot and cold layers. Two simulations have been carried out with shallow water to investigate the effect of initial water pool temperature on pressurization. It was found that reduction of initial pool temperature from 25 °C to 15 °C has a penalizing effect on the pressurization. At 20 000 sec pressure in the initially colder pool was 0.5 Bar lower than that in the initially hotter pool. The difference is increased to about 0.7 Bar at 25 000 sec (see Figure 104). The effect of the initial water pool temperature is likely enhanced by the initial temperature of the test section walls (which at the start of the calculation is assumed equal to the initial water pool temperature). The time delay due to reduction of the initial pool temperature from 25°C to 15°C is about 2250 sec.

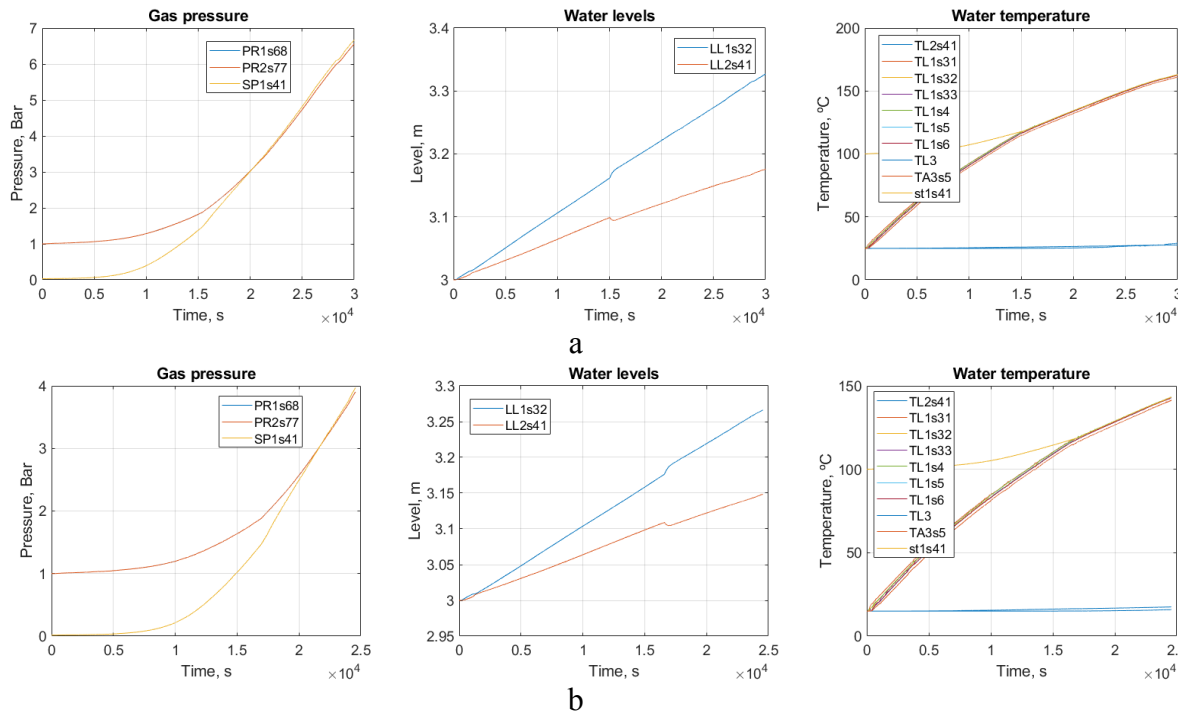


Figure 104. Calculation results for the effect of the initial water pool temperature  
(a – Case 10.02b initial temperature 25°C; b – Case 10.01c initial temperature 15°C)

*Legend notation:*

*PR2, PR1 – gas pressure in the control volumes 2s and 1s*

*SP1 – saturation pressure in the control volume 1s*

*TL1, TL3 – water temperature in the control volumes 1s and 3*

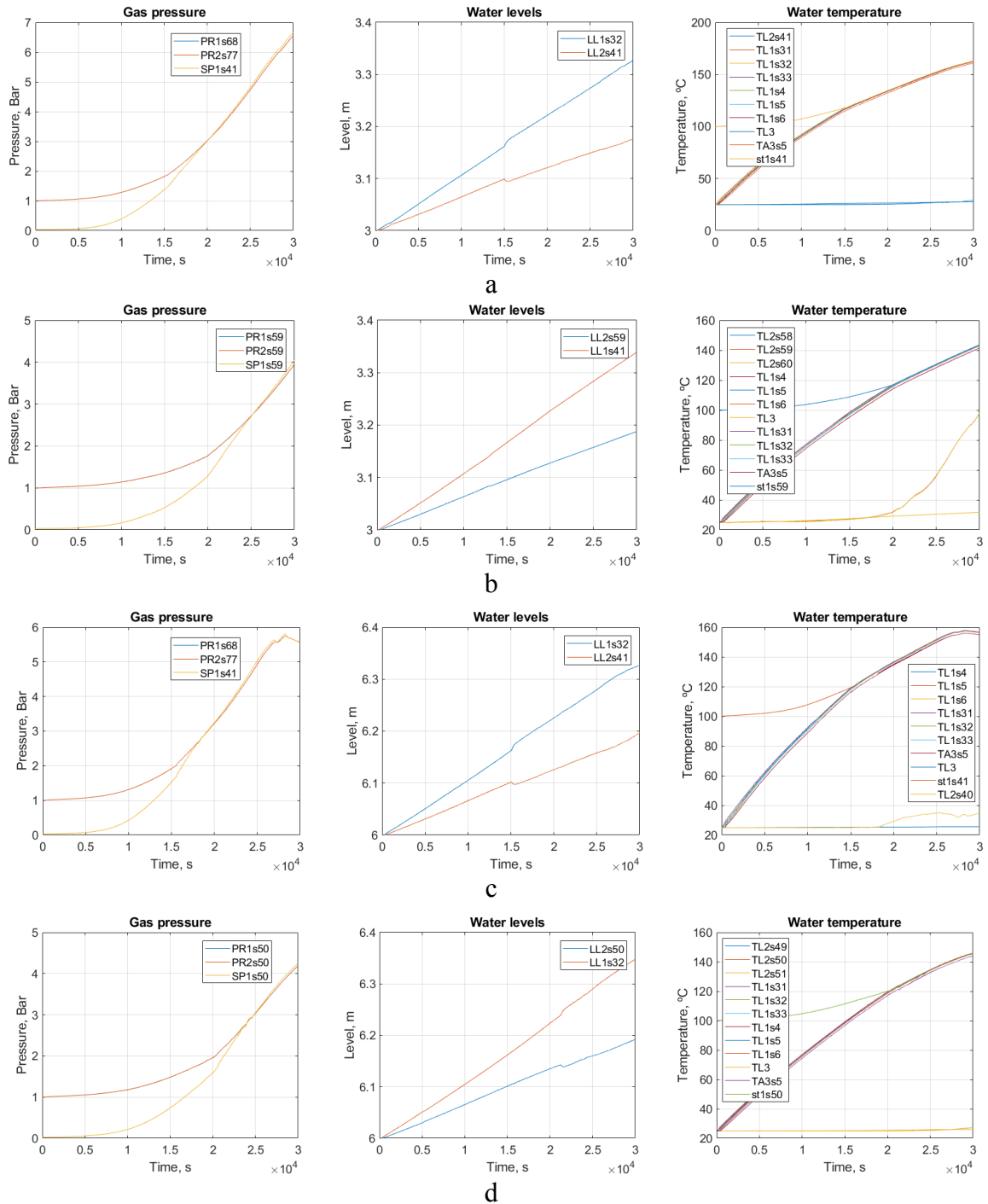
*st1 – saturation temperature in the control volume 1s*

*LL1, LL2 – water level in the control volumes 1s and 2s*

### 7.5.2.3. Effect of the hot layer thickness

The location of the thermocline below the sparger on the distance from the sparger head and is determined by the competition between the density difference between cold and hot water layers and the effective momentum generated by condensing steam, which depends on parameters such as water temperature and steam flow rate.

Implemented in this work model does not directly simulate effective steam momentum, using instead a fixed hot layer depth to represent the effect of partial pool mixing. We used this model to investigate the effect of the hot layer thickness on the pressurization. The effect was studied for both shallow and deep-water pools. The results of the simulations are summarized in Figure 105.





would be reduced from 8.3h to 6.25h if hot layer thickness could be sustained at 1m instead of 1.4.

High sensitivity of the pressure to the thickness of the hot layer suggests that proposed experimental configuration is well suited for validation of the effective momentum source models and the effect of pool stratification/mixing on containment pressurization.

#### 7.5.2.4. Effect of steam injection rate

Experimentally it is not possible to study separately the effect of the steam injection rate from other parameters. Change in the steam injection will change the effective momentum [4, 12, 15] and consequently the erosion rate of the cold layer. Two simulations have been carried out with different injection rates (161 and 262 g/s) and consequently different thermocline positions (1.0 and 1.4 m respectively – values obtained in HP5 series for given steam injection rates). The effect appeared to be comparable to the effect of hot layer thickness. Increase in the steam injection from 161 to 262 g/s almost doubled the rate of pressure rise (clarify Figure 106).

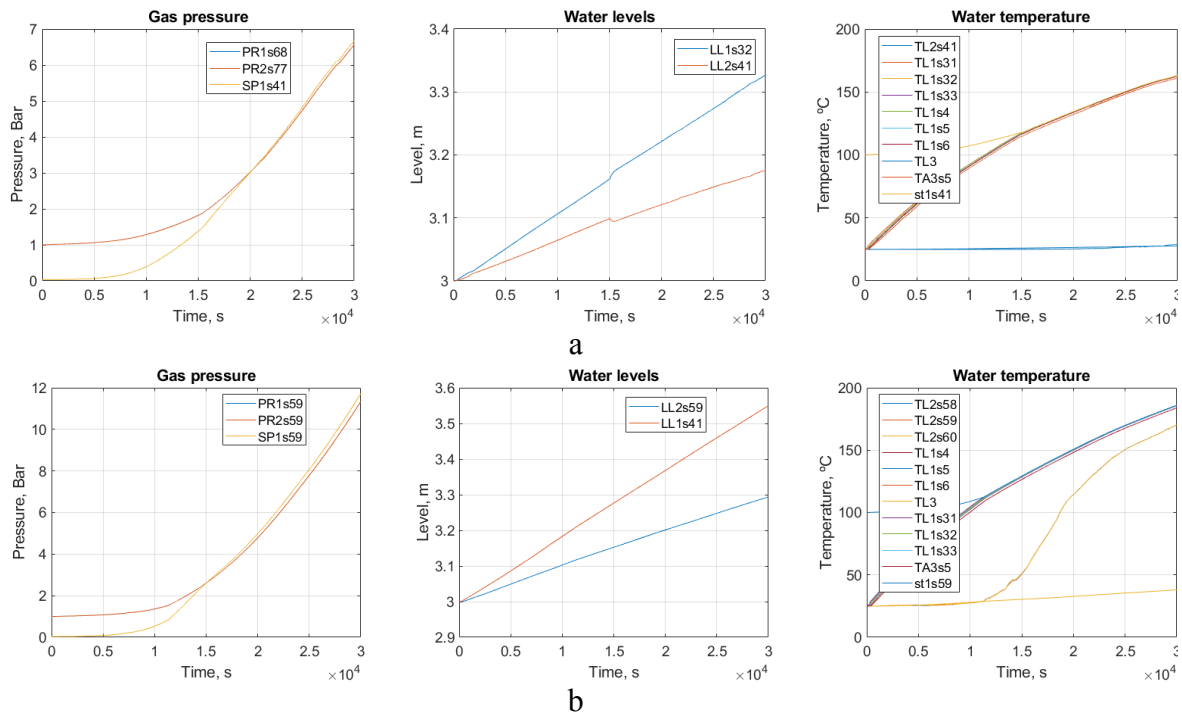


Figure 106. Calculation results for the effect of the initial water pool temperature  
(a – Case 10.01b; b – Case 10.02b)

*Legend notation:*

*PR2, PR1 – gas pressure in the control volumes 2s and 1s*

*SP1 – saturation pressure in the control volume 1s*

*TL1, TL3 – water temperature in the control volumes 1s and 3*

*st1 – saturation temperature in the control volume 1s*

*LL1, LL2 – water level in the control volumes 1s and 2s*

#### 7.5.2.5. Effect of nozzle spray location

Investigation of the effect of spray on the depressurization of the vessels is planned in the H2P4 series. In the pre-test analysis we studied effects of (i) water mass flow rate on the rate of depressurization and (ii) spray nozzles location (refer to Figure 107).

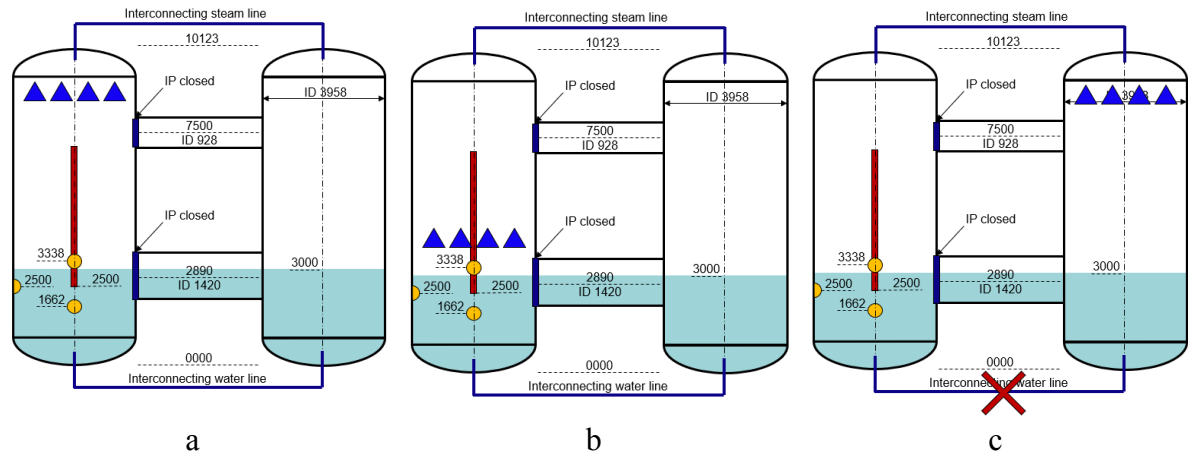


Figure 107. Simulated configurations of spray nozzles in the PANDA facility  
(a – spray at the top of vessel 3; b – spray above the water level of vessel 3; c – spray at the top of vessel 4)

It was found that moving spray nozzles down to the water surface had marginal effect on system depressurization (at least at 5 kg/s of water supply to sprays). Depressurization might be dominated by the surface temperature of the water pool (see Figure 108a and b). The data further shows that shortly after spray activation system pressure rises above the saturation pressure causing volumetric condensation of steam and depressurization.

Placing spray into the vessel 4, i.e. above the cold-water pool produced counter intuitive result, i.e. depressurization rate was similar to the case where sprays were located above the hot water pool. However, the mechanisms of depressurization appeared to be different. In case when sprays are in vessel 3 depressurization is driven by cooling of the hot pool, and gas pressure is above saturation pressure. In case when sprays are in the cold vessel the pressure drops due to increased evaporation from the hot pool and gas pressure is below the saturation pressure (compare Figure 108b and c). From experimental point of view, system pressure rapidly falling below saturation point may lead to volumetric boiling of the hot pool potentially endangering instrumentation.

System depressurization appeared to be most sensitive to the water mass flow rate of spray water. At 5 kg/s of coolant flow rate the system pressure reduced by 92% within 1h, at 1kg/s only 16% reduction was established within the same period (compare Figure 108a and d).

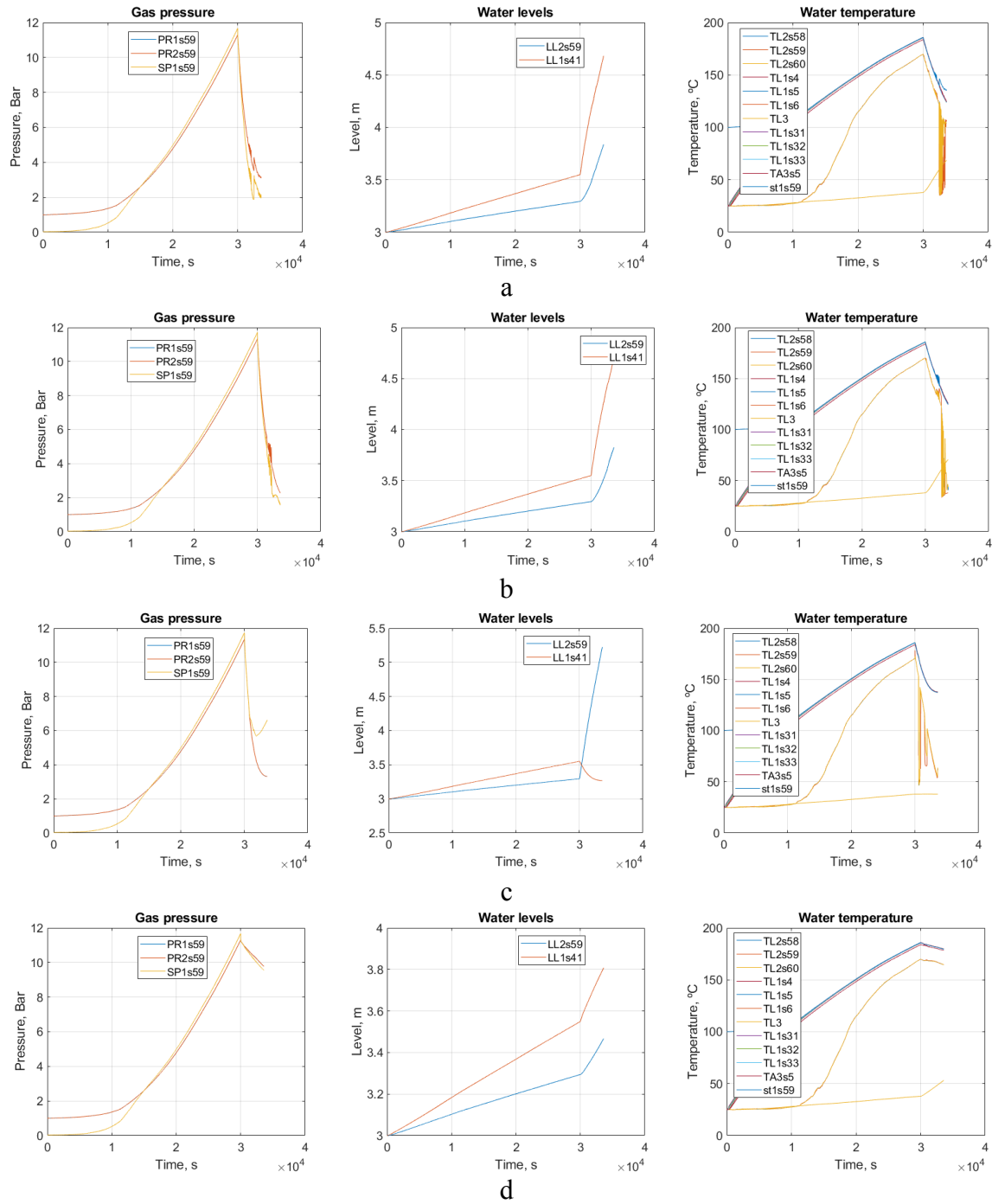


Figure 108. Calculation results for the effect of spray nozzles elevation  
(a – Case 10.02s1; b – Case 10.02s3; c – Case 10.02s4; d – Case 10.02s2)

*Legend notation:*

*PR2, PR1 – gas pressure in the control volumes 2s and 1s;*

*SP1 – saturation pressure in the control volume 1s;*

*TL1, TL3 – water temperature in the control volumes 1s and 3;*

*st1 – saturation temperature in the control volume 1s*

*LL1, LL2 – water level in the control volumes 1s and 2s*

### 7.5.3. Pool preconditioning

To reduce overall duration of the experiment and thus providing more time for observation and measurement of more important phenomena two pool preconditioning procedures were suggested and simulated. Both procedures aim at artificial development of stratified pool by injection of hot water during filling procedure.

The first option includes the following (Procedure #1):

- connect vessel 3 and vessel 4 using bottom interconnecting line
- establish cold water pool in both vessels with water level according to H2P4 test conditions
- for the period of 3600 s:
  - inject hot water (95°C) just under water surface at a rate of 5 l/s and simultaneously
  - remove cold water from the bottom of the pool at a rate of 5 l/s

This procedure will allow to establish hot water layer at the surface of the cold pool and gradually extend the hot layer downwards. Simulation of this procedure predicted an hour reduction of the experiment duration if the hot water could be prepared in advance. Results of the simulation are shown in Figure 109.

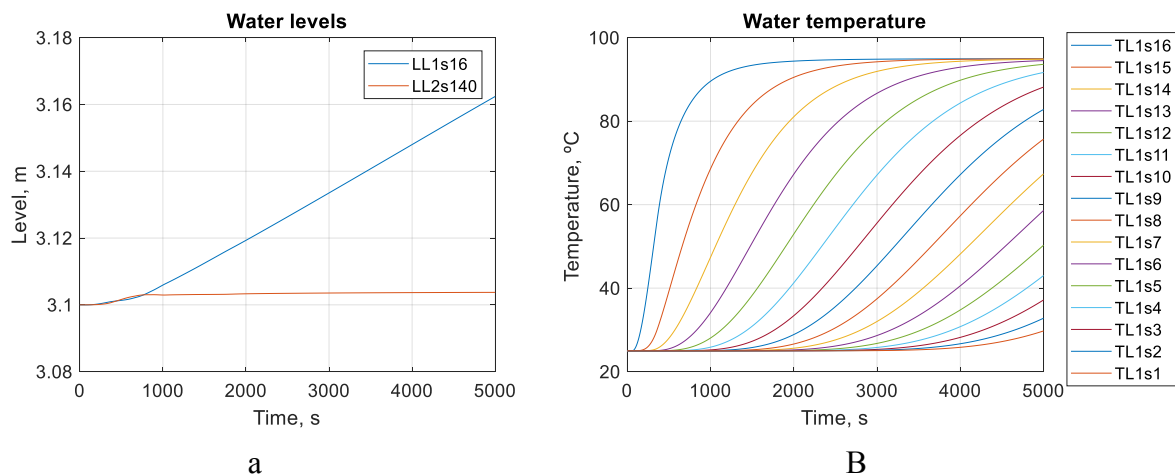


Figure 109. Pool heat up during filling procedure #1 (a – water level, b – temperature evolution)

The second option is based on the following (Procedure #2):

- connect vessel 3 to the vessel 4 at the bottom using interconnecting line
- establish cold water pool in both vessels with water level 0.5 m below H2P4 test conditions
- for the period of ~3600 s:
  - Inject hot water (95°C) at the initial pool level at a rate of 5 l/s
  - Stop injection when water level reaches H2P4 predefined level
  - water level can be adjusted by supplying or removing cold water into / from vessel 4

Since hot water injection will create momentum, some mixing with cold layer may occur. Also injection into a pool while level gradually increases will create a temperature gradient resulting in the pool temperature profiles shown in Figure 110.

While both procedures will reduce experiment time, their implementation might meet difficulties from practical perspective. It should be noted that Procedure #2 requires much less control over the supply of hot and cold water and therefore can be easier to implement.

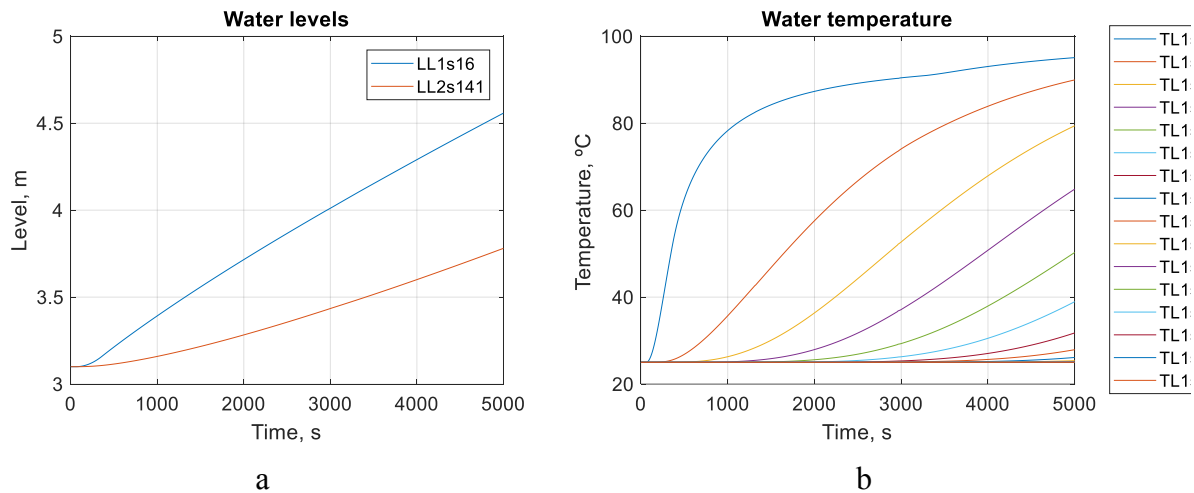


Figure 110. Pool heat up during filling procedure #1 (a – water level, b – temperature evolution)

## 7.6. Summary of H2P4 scoping analysis

In shallow water pool configuration, opened bottom interconnecting pipe, can significantly increase time for pressurization caused by additional amount water that will be heated up in the second vessel. Two most influential model input parameters are steam injection rate, hot layer thickness and spray water injection rate. Experimentally, only steam and water injection rates can be controlled, actual hot layer thickness is not known for high-pressure high-temperature conditions.

The characteristics times to reach 4 Bar pressure are in the range between 23000-30000 sec for 161 g/s and between 17000 to 24000 for 261 g/s. It was further predicted that those times can be reduced by ~3600 s if a special procedure for water pool preheating is performed.

Furthermore, opened top and bottom IPs in the experiment will introduce counter-current two-phase flows that will be difficult to measure and model, suggesting that both IP should be closed.

System pressurization is sensitive to the depth of the hot layer. Initial water position at 0.5 m above the sparger head would be desirable. However, more intensive erosion of the cold layer may occur if the hot layer is too thin to dissipate momentum. In addition, reduced sparger submergence may increase the likelihood for steam bypass (incomplete condensation in the pool). A pre-test could be useful to clarify these phenomena.

Comparison of shallow and deep water pool configuration suggests that deep water pool provides faster pressurization and in addition is a “safer” choice for maintaining the

thermocline during the whole transient. There is no data on the behavior of the stratified pool when steam is injected into near saturated water in in-stable condensation regime. Loss of stratification will make any other stage of the test (except for spray activation) meaningless.

As a result of the analysis four options have been developed for the test configuration. Those are currently under consideration by the PANDA experimental team. From phenomenological perspective the best configuration is a deep pool setup with closed interconnecting pipes, opened top and bottom interconnecting lines. Steam injection at 262 g/s and sparger submergence 1 m. Sprays should be located above the pool surface to separate effect of steam condensation on the surface of the pool over steam condensation in the gas space above.

At present time several concerns have been raised by the experimentalist and scoping simulations. First is the possibility of rapid pressure rise during sparger actuation due to the water evaporation from the hot walls of the vessel 3. Such situation may lead to the rupture of pressure safety diaphragm or operator opening of venting valve. Both will disrupt the experiment. Another concern is possibility of volumetric boiling in the pool upon spray activation. Due to the rapid cooling and condensation in the gas space the system pressure may fall below the saturation point and promote rapid pool expansion. This may lead to the damage of instrumentation in the pool and disrupt the spray injection phase of the H2P4 test. Both issues are currently being investigated.

## 8. Analysis of SEF-POOL tests

### 8.1. Motivation and background

SEF-POOL is a separate effect experimental facility build and operated at LUT (Finland) for measurement of the effective momentum generated by direct condensation of steam in a water pool and investigation of the relevant physical mechanisms. Specifically, the facility is used to experimentally determine a relation between a theoretical momentum rate  $M_{th}$  of the injected steam and effective momentum rate  $M_{eff}$  developed in water induced by the injected steam:

$$M_{eff} = CM_{th} = C\rho_s A_0 U_s^2,$$

where  $\rho_s$  is steam density;  $A_0$  nozzle cross-section; and  $U_s$  steam velocity at the nozzle outlet;  $C$  is a proportionality coefficient that can be a function of different parameters including steam mass flux or Mach number, water pool subcooling, steam superheat, nozzle geometry, etc.

The goal of the experiments at the SEF facility is to provide data for the development of EMS model for prediction of the time-averaged momentum generated by steam injection through sparger in pressure suppression pool of a nuclear reactor in sonic and subsonic regimes. The EMS model introduces (time averaged) momentum source that creates a single phase liquid jet with specific values of the effective (i) momentum, (ii) centerline velocity, and (iii) jet expansion ratio. These parameters affect transfer of the momentum into the bulk liquid and development of thermal mixing / stratification in the pool.

SEF tests aim to indirectly measure the effective and superheat) of steam injection into a subcooled water pool through single and multiple nozzles. The jet centerline velocity and expansion rate can be deduced from the measurement of the jet entrainment rate. Entrainment rate can be deduced from the velocity field around the jet. The following sections describe the status of the experimental and analytical work carried out to measure effective momentum and entrainment generated by condensing and non-condensing jets and estimate velocity field in the vicinity of the jet. Specifically, we provide (i) the theoretical background of singular round jets and derive correlations between jet momentum, centerline velocity and entrainment rate, (ii) describe the experimental setup, (iii) evaluate uncertainty in image analysis and provide (iv) results of the ongoing entrainment analysis for SEF tests.

### 8.2. Flow entrainment in round jets

#### 8.2.1. Relation between axial and radial volumetric flow rate

In this section, the relation between the axial and radial volumetric flow rate of the round jet is presented. By using this relation, the expansion rate of the jet can be deduced if its entrainment velocity is measured.

According to Eqs. (29) and (30), the axial velocity profile of an axis-symmetry round jet can be described by

$$U(x, r) = \frac{U_0 dB}{(x - x_0)} e^{\left(-K \frac{r^2}{(x - x_0)^2}\right)} \quad (53)$$

where the term before the exponent is the centerline velocity  $U_c$  and the exponent describes a Gaussian distribution of the jet axial velocity profile in the radial direction. Coefficients  $B$  and  $K$  uniquely define the jet axial velocity profile  $U(x, r)$  for the given injection velocity  $U_0$  and initial jet diameter  $d$ .

The momentum rate in axial direction can be expressed as:

$$\int_0^{\infty} 2\pi r U^2 dr = \frac{\pi U_0^2 d^2 B^2}{2K}$$

From the momentum conservation (neglecting dissipation of momentum) it then follows:

$$\frac{\pi U_0^2 d^2 B^2}{2K} = \frac{\pi d^2 U_0^2}{4}$$

$$K = 2B^2 \quad (54)$$

The last equation suggests that the rate of jet expansion is related to the decay rate of the jet centerline velocity.

Integrating Eq. (53) over  $r$  we obtain that the volumetric flow rate  $\dot{Q}_a$  is linearly increasing with axial distance  $x$ , which can only be explained by the flow radial entrainment:

$$\dot{Q}_a = \int_0^{\infty} 2\pi r U dr = \frac{\pi d U_0 B}{K} (x - x_0) \quad (55)$$

For constant density jets, the relation between the axial  $\dot{Q}_a$  and radial  $\dot{Q}_r$  volumetric flow rates (see Figure 111) can be written as

$$\frac{d\dot{Q}_a(x, R)}{dx} = \dot{Q}_r(x, R) \quad (56)$$

$$\dot{Q}_r(x, R) = 2\pi R V_e(x, R) \quad (57)$$

$$\dot{Q}_a(x, R) = \int_0^R 2\pi r U(x, r) dr = \frac{\pi U_0 d B (x - x_0)}{K} \cdot \left( 1 - e^{\left( -K \frac{R^2}{(x - x_0)^2} \right)} \right) \quad (58)$$

where  $R$  is the radius of the control volume,  $V_e$  is the entrainment velocity.

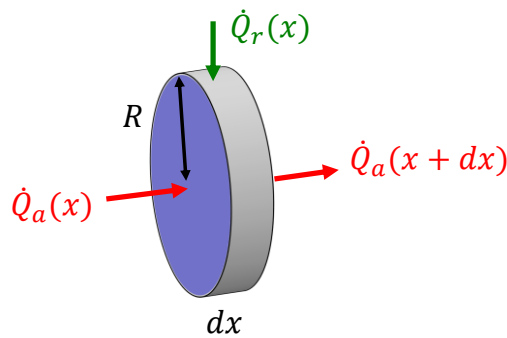


Figure 111. Schematic of volumetric flow rate balance

By substituting Eqs. (57) and (58) in Eq. (56) and assuming  $\xi = R/(x - x_0)$ , we get

$$R V_e(x, R) = \frac{U_0 d B}{2K} \left[ 1 - (1 + 2K \xi^2) e^{-K \xi^2} \right] \quad (59)$$



From Eq. (59), we can see that the product of the entrainment velocity and the radius  $RV_e(x, R)$  is constant along  $\xi = R/(x - x_0)$  and for large values of  $K\xi^2$  it asymptotically approaches  $\frac{U_0 dB}{2K}$ . With the relation in Eq. (54), both  $K$  and  $B$  can be solved if entrainment velocity is known.

Comparison of the contours of  $RV_e(x, R)$  is shown in Figure 112. The simulation and analytical results were obtained by the single jet study in Section 5.2.4 and Eq. (59) with parameters in Table 15.

Table 15: Water jet parameters

	$Re$	$B$	$K$	$x_0$	$d$	$U_0$
	[-]	[-]	[-]	[mm]	[mm]	[m/s]
Theory	95500	5	50	25	10	9.6

As expected, the product  $RV_e(x, R)$  is almost constant when it is far away from the mainstream (large values of  $K\xi^2$ ). Inside the mainstream, the distinguished contours suggest that the products are constant along the curve with the slope of  $\xi$ .

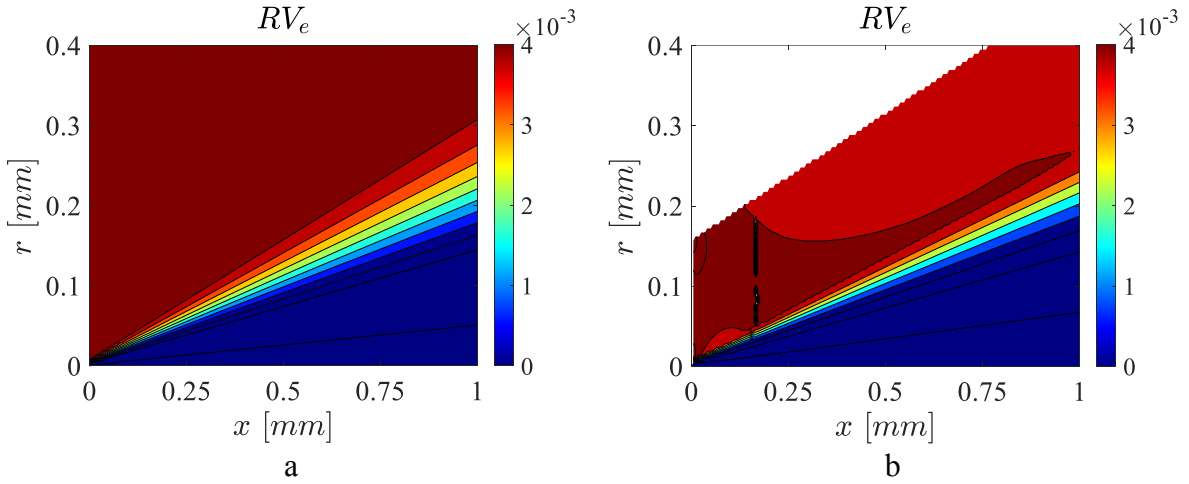


Figure 112. Contours of the product of entrainment velocity and radius of (a) analytical solution and (b) Fluent simulation. Note the entrainment velocity is positive when it points to the centerline.

### 8.2.2. Effects of $\dot{S}_{\tilde{k}_1}$ on entrainment velocity

The effects of  $\dot{S}_{\tilde{k}_1}$  (introduced in Section 5.5.5) on the product of entrainment velocity and radius are investigated. The motivation is to study whether  $\dot{S}_{\tilde{k}_1}$  can be uniquely identified with the measured entrainment induced by the steam injection into the pool in SEF.

Sensitivity study with the model introduced in Section 5.5.3 was performed. A single round jet was injected through the inlet with a uniform velocity of 2.65 m/s which is estimated by Eq. (35) with the conditions in phase 1 of PPOOLEX SPA-T3. Other setups remained unchanged except the implementation of the high level turbulence induced by steam condensation. TKE-DS was used to provide such turbulence. This source was distributed within a region (Figure

60) of  $x_1 = 0.15 \text{ m}$ ,  $x_2 = 0.5 \text{ m}$  and  $h = 0.036 \text{ m}$  for a single jet.  $\dot{S}_{\tilde{k}_1}$  varies from  $0 \text{ kg/ms}^3$  ( $I = 800\%$ ,  $\mu_t/\mu = 40000$ ) to  $540 \text{ kg/ms}^3$  ( $I = 30\%$ ,  $\mu_t/\mu = 1000$  for rest cases). More details regarding turbulence setup can be found in Section 5.5.

The profiles of the product of entrainment velocity and radius at different slices are presented in Figure 113. We can find that far-field  $VeR$  (e.g.  $r > 0.1 \text{ m}$ ) of cases with  $\dot{S}_{\tilde{k}_1} = 0$  and  $60 \text{ kg/ms}^3$  agrees well with Eq. (59) where it should equal to  $U_0 dB/2K$  at different slices. The deviation of case with  $\dot{S}_{\tilde{k}_1} = 0 \text{ kg/ms}^3$  at  $x = 0.1 \text{ m}$  can be caused by the extremely high turbulence introduced by  $I = 800\%$ ,  $\mu_t/\mu = 40000$  at the orifice. For the same reason, the difference of cases with  $\dot{S}_{\tilde{k}_1} = 180$  and  $540 \text{ kg/ms}^3$  at different slices can be attributed to the too high turbulence introduced by the source term, resulting in the jet are no longer the round jet.

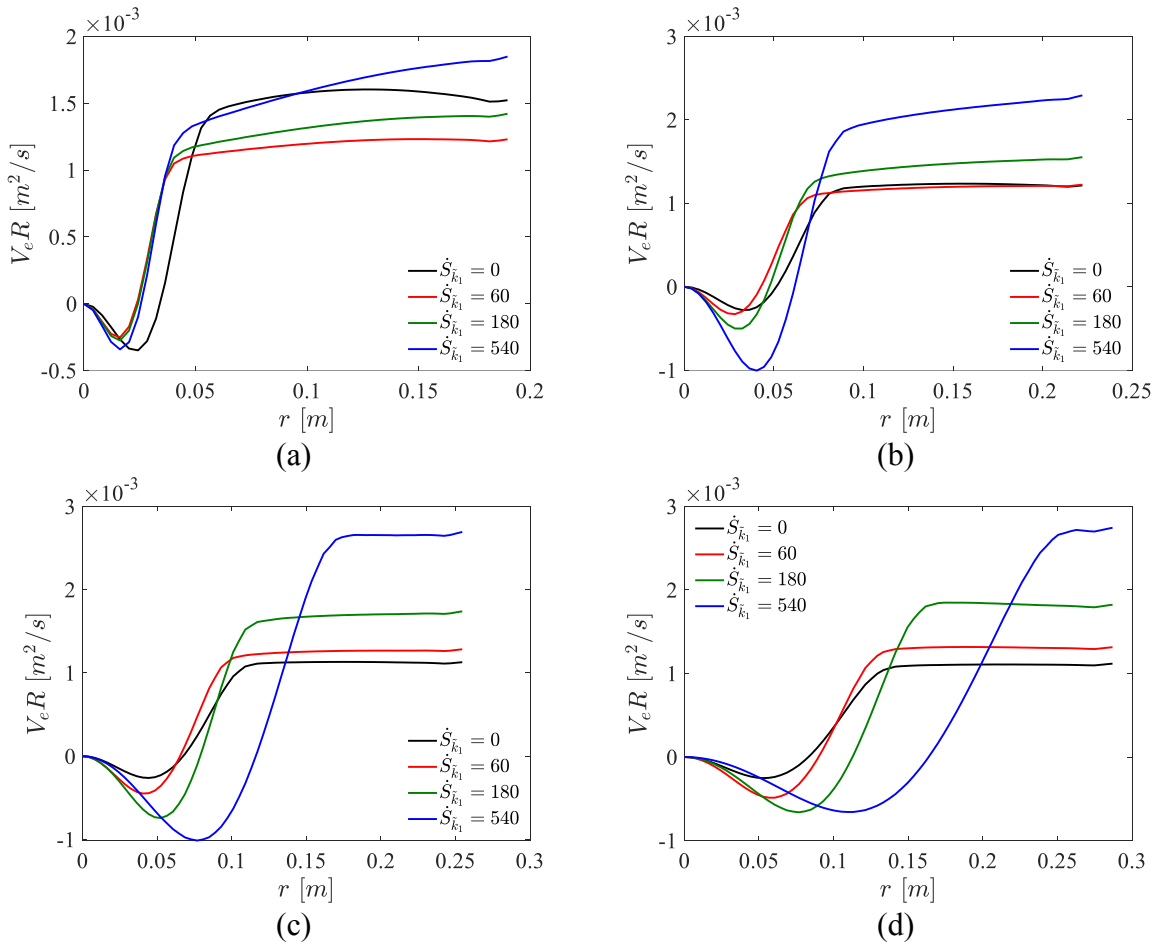


Figure 113. Profiles of the product of entrainment with radius at (a)  $x = 0.1 \text{ m}$  (b)  $x = 0.2 \text{ m}$  (c)  $x = 0.3 \text{ m}$  (d)  $x = 0.4 \text{ m}$ .

However, the significant difference of  $VeR$  profiles at the same slice suggests that it is possible to calibrate the  $\dot{S}_{\tilde{k}_1}$  by entrainment measurement. Compared to TKE-BC where the turbulence is provided at the orifice and rapidly dissipated by the turbulence model, the introduction of the turbulence source in a region (TKE-DS) would significantly affect the downstream jet profiles (e.g.  $x = 300 \sim 600 \text{ mm}$ ) and therefore,  $\dot{S}_{\tilde{k}_1}$  could be uniquely identified with the measured entrainment.

### 8.3. Experimental setup

The schematic of the experimental setup is shown in Figure 114. It consists of a test section with 0.4x0.5x1.2 m water pool and an injection nozzle for steam supply. The nozzle is positioned in the middle of the pool on a rotating pipe. During steam injection, the force exerted on the pipe / nozzle is measured using a force sensor located on an external rigid frame and connected to the rotating pipe using a steel rod. The experimental facility is instrumented with thermocouples to measure water and steam temperature, vortex flow meter to measure the steam mass flux and pressure transducers inside the steam line and water pool.

A fast video camera is used to record the process of steam injection and condensation inside the pool through one of the two Plexiglas windows at the sides of the test section. During the test, the condensation process is periodically recorded at different water pool temperatures. Each recording is performed at ~6000 fps for a period of 0.25-0.50 s.

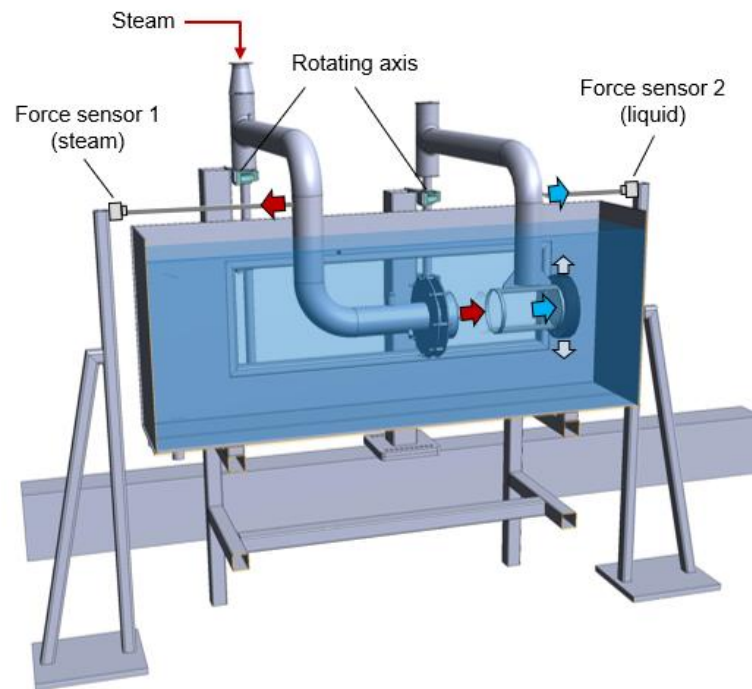


Figure 114. SEF-POOL test facility

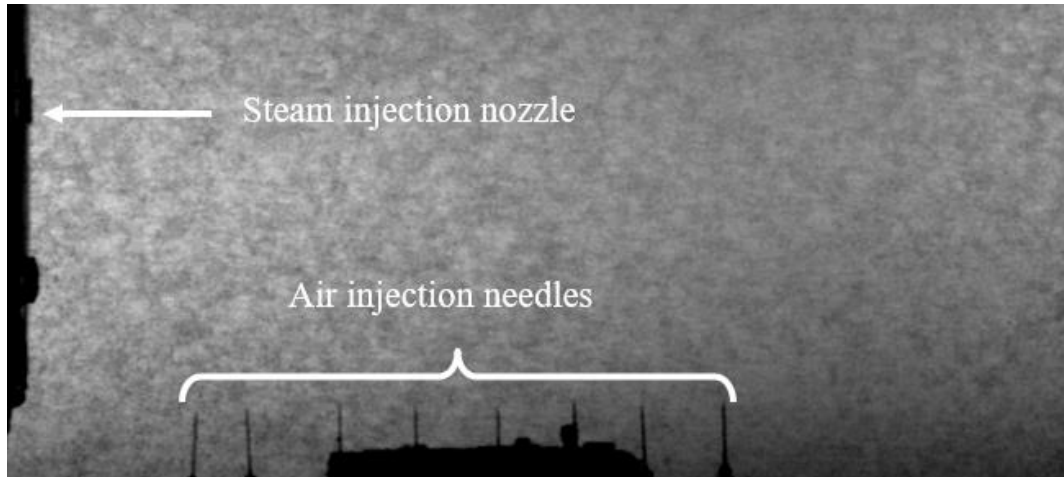


Figure 115. Gas injection needles (example)

To measure the flow velocity around the condensing jet, it was suggested to track movement of gas bubbles inside the pool. Two modifications to the experimental setup were introduced:

1. Eight needles (ID 0.2mm) connected to a collector have been placed at the bottom of the test section pool underneath the steam condensation region. The nozzles were positioned in the plane of the jet. The pitch between the needles is 15-18 mm. Compressed air supplied into the collector will flow through the needles and generate  $\sim \varnothing 2$  mm bubbles inside the pool (see Figure 115).
2. Two fast video cameras were placed in front of the test section side window for stereoscopic video recording of the pool. The cameras would film the same region of view from two different angles (see Figure 116); the two video recordings are used for triangulation and 3D tracking of individual bubbles in the flow. The stereo imaging is needed to track bubbles position relative to the jet.



a



Figure 116. Snapshots of the stagnant pool from left (a) and right (b) cameras

The method would require first to measure characteristic bubble velocity in a stagnant pool and then use it as a reference for the estimation of the flow velocity in a pool with condensing jet.

It should be notice that in the course of the experimental campaign the experimental setup was modified several times: position and number of the injection nozzles have been changed. Specifics can be found in the respective tests descriptions.

#### 8.4. Image calibration and error analysis

Testing stereoscopic setup has been carried out at KTH in conditions similar to the potential setup at LUT. Mapping of distances between the cameras, error in image analysis and respective error in the estimation of depth was obtained (see Figure 117). Results suggested that optimal distance between the cameras is in the range between 350 to 550 mm, further increase in the distance is not likely to improve image accuracy and will make it difficult to correlate objects between the two video footages. Specific recommendation for alignment, distance between the cameras and image calibration procedure were then provided to LUT.

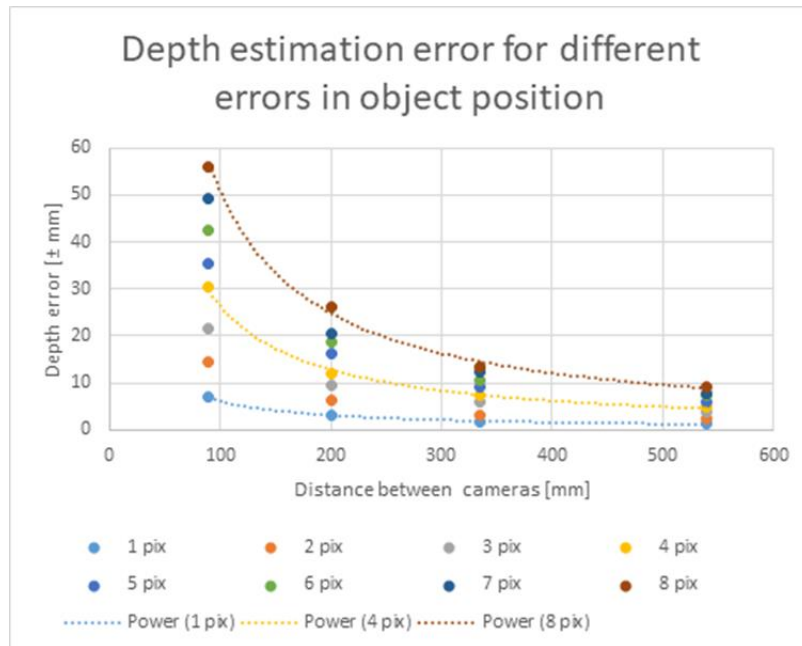


Figure 117. Error in depth estimation as a function of distance between the cameras

The stereoscopic imaging calibration was carried out using >160 pair of snapshots of a checkerboard plate inside the water pool. The results of the calibration and estimation of the reprojection error are shown in Figure 118. The mean reprojection error appeared to be <0.5 pix, which is sufficient for our application.

Uncertainty in 3D position of the bubble is expected to be dominated by the error in the estimation of the bubble position in the video images. The components of the maximal error vector (i.e. vector between the actual bubble position and the estimated one) resulting from random sampling of point location within given ranges of image error are listed in Table 16. For an average bubble diameter of 2-3 mm an image error in bubble position is not likely to exceed  $\pm 0.7$  mm. This corresponds to a maximal error vector with magnitude of 3.11 mm and for the vertical component of the position  $\pm 0.68$  mm.

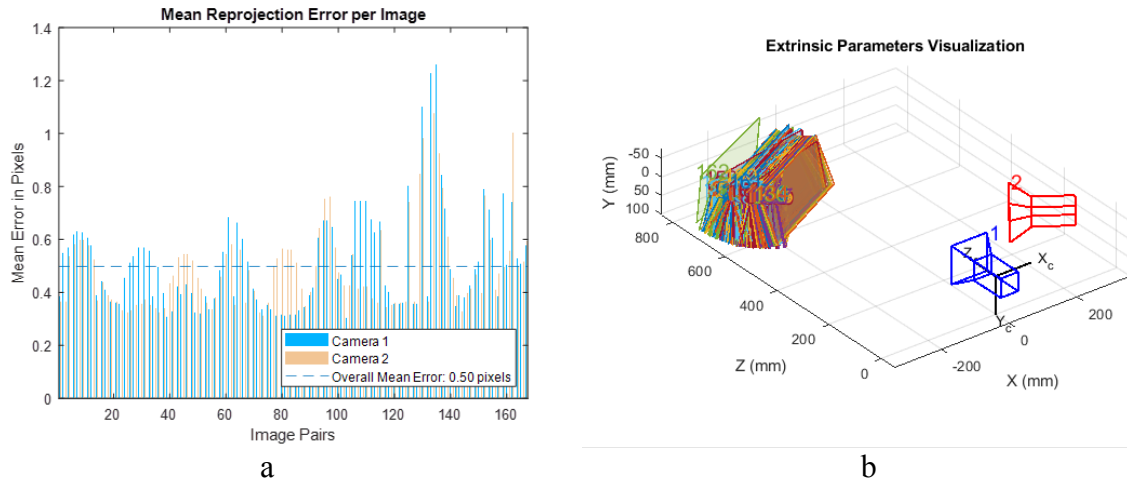


Figure 118. MATLAB generated figures for mean reprojection error (a) and visualization of extrinsic parameters (b)

Table 16. Error assessment for bubble triangulation

Error in image coordinates		Error in world coordinates <sup>*</sup>			
Col, Row [pix]	Col, Row [mm]	Z, mm	Y, mm	X, mm	Magnitude
±1	±0.34	±1.28	±0.39	±0.79	1.55
±2	±0.69	±2.60	±0.68	±1.57	3.11
±3	±1.03	±3.70	±1.23	±2.33	4.54
±4	±1.38	±4.98	±1.50	±2.90	5.95
±5	±1.72	±6.05	±1.90	±3.88	7.43
±6	±2.07	±6.92	±2.53	±4.20	8.48

<sup>\*</sup>Refer to coordinate system in Figure 3b

## 8.5. Entrainment rate analysis

### 8.5.1. SEF stagnant pool

A video of bubbles rising in a stagnant pool has been recorded in SEF-POOL facility. The recording was done at 6300 fps for a period of 261 ms. The snapshots of the first frame from left and right cameras with superposition of coordinates of the tracked bubbles are shown in Figure 120. Results from the 3D triangulation of 146 bubbles are shown in Figure 119.

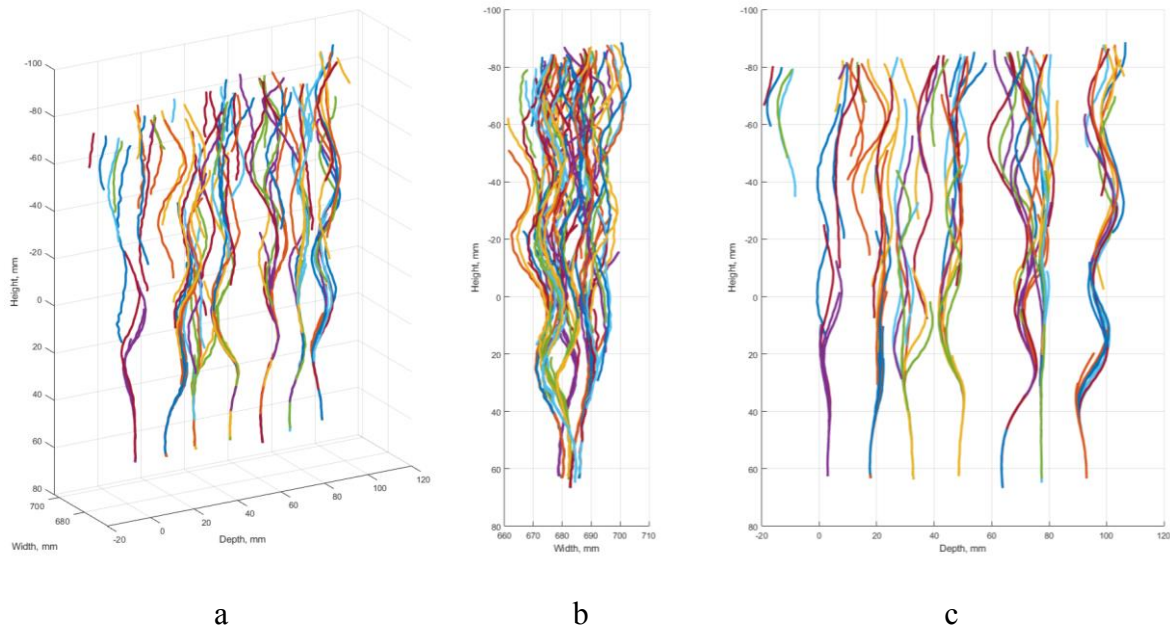


Figure 119. Trajectories of 146 bubbles in stagnant pool  
(a – isometric projection; b – ZY projection; c – XY projection)

Upon detachment from the needle each bubble for  $\sim 40$  mm follows a trajectory characteristic to the needle by which the bubble is generated. The difference in the initial trajectories might be due to the different orientation of the needles (which are cut at some angle at the top). Once the memory of the “origin” effect is gradually lost in random fluctuations, all bubbles follow more stochastic helicoidal paths. During the rise all bubbles remain within the vicinity of vertical central plane of the jet.



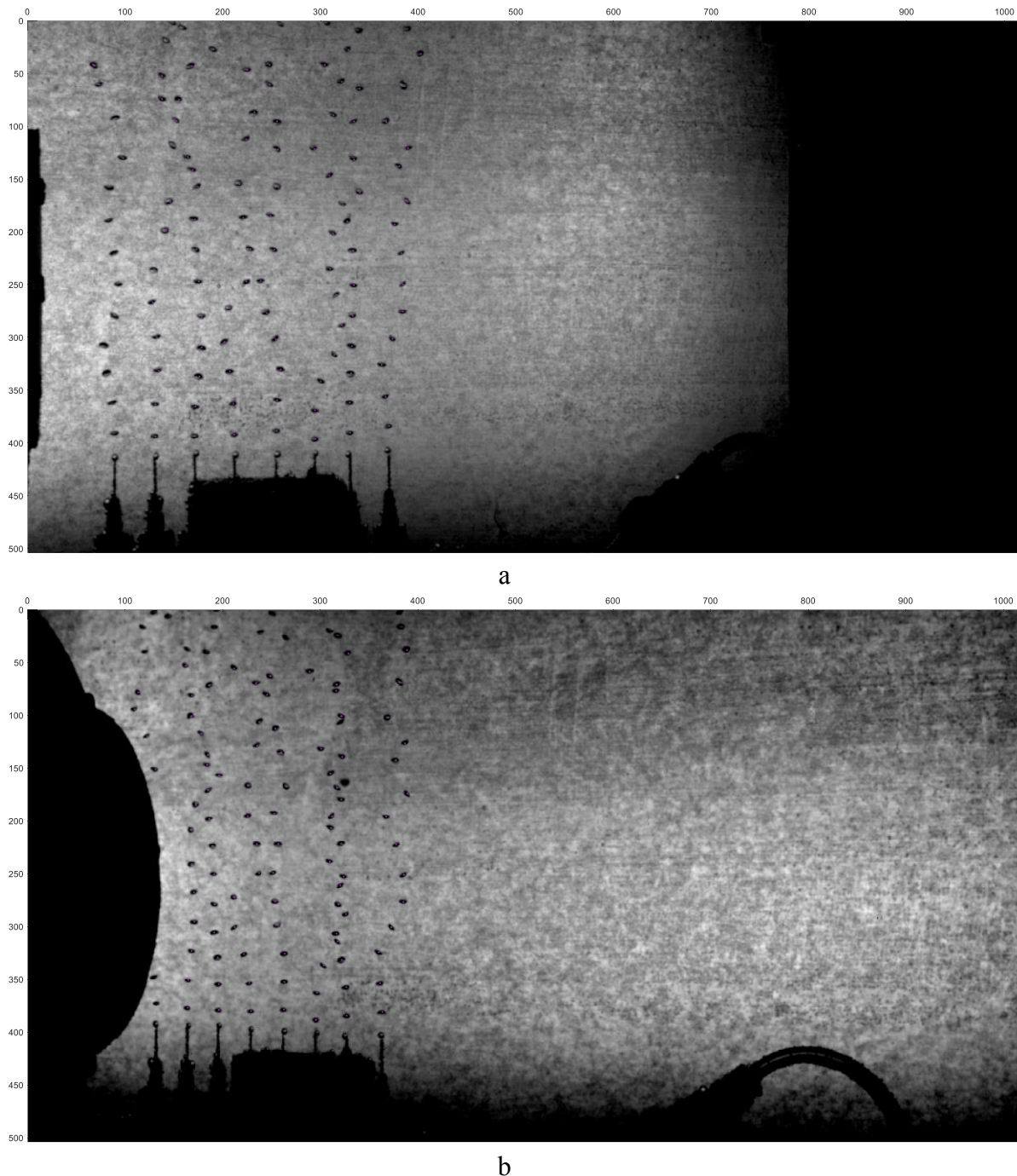


Figure 120. Snapshots of bubbles in a stagnant pool  
(a – left camera; b – right camera)

The results of the estimation of the vertical velocity component for bubbles originating from several needles and covering the distance from release till the steam ejection nozzle are shown in Figure 121. The magnitude of the velocity vector shows periodic oscillations, which are attributed to the periodic oscillation of bubbles shape. In the range between 60 to 15 mm bubbles velocities reproduce each other well. Difference is mainly between the nozzles. The average (expected) value of the vertical velocity component from the full history of 146 bubbles is 0.322 m/s.

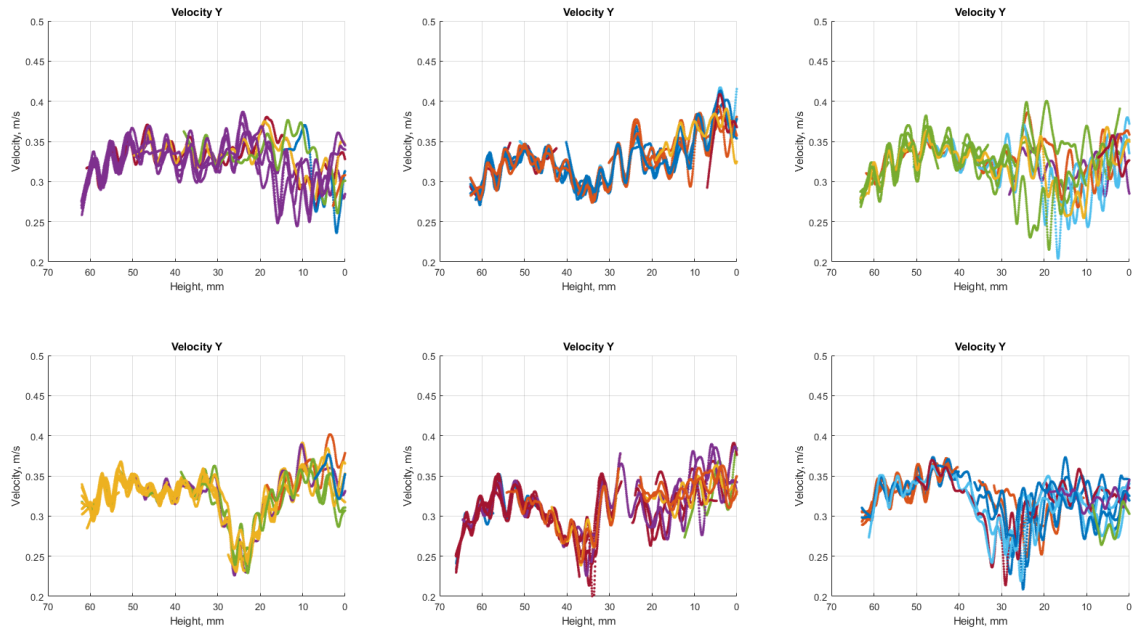


Figure 121. Vertical velocity component from different nozzles.  
(zero in the abscissa corresponds to the elevation of the nozzle)

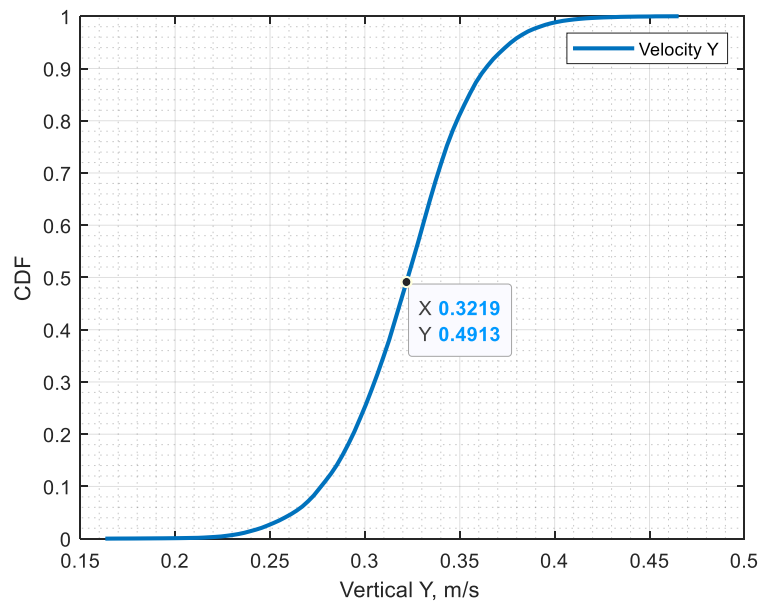


Figure 122. Cumulative distribution of the vertical velocity component

Image analysis of bubble trajectories inside a stagnant pool show some promising results. The bubbles can be tracked and their 3D trajectory and velocity vectors can be estimated. However, the data suggests that few issues should be addressed for measurement of the fluid flow velocity and estimation of the entrainment rate:

- There is a periodic variation of the bubble velocity. This phenomenon is likely to be due to the oscillation of the bubble shape. Such oscillations can be suppressed if smaller bubbles could be generated. Several solutions can be investigated:

- Change the shape and/or diameter of the bubble injection needle.
- Increase wettability at the needle tip by applying a hydrophilic coating. The aim is to achieve earlier pinch-off and detachment of the bubble. Possible caveats are stability of the introduced coating during steam injection and variation in the bubble sizes and respective terminal velocity.
- Reduce surface tension of the liquid in which bubbles are released. A possible solution is to install a sleeve around each needle filled with oil. One may expect 2-10 times reduction in the surface tension and respective reduction in the bubble size. Possible caveats are (i) bubble penetration through oil / water interface, (ii) oil back flow into the needle and adverse effects of the oil higher viscosity.
- Bubbles have two characteristic parts in their trajectories: one that is well reproduced and dominated by the bubble injection needle, and another one that has a more stochastic nature. By placing needles closer or farther away from the jet it will be possible to impose desired reference velocity profile.
- Phenomena of steam condensation has periodic nature which effectively results in the periodic variation of the flow velocity around jet. To obtain / measure entrainment velocity one would need somewhat longer data acquisition sequences to provide more data for proper statistical treatment of the bubble's movement in the water pool.

#### 8.5.2. SEF-W7 test analysis

The SEF-W7 test aimed to investigate the feasibility of the jet entrainment measurement and estimation of the jet expansion coefficient by injecting a water jet into the initially stagnant water pool. The test included a calibration phase and the injection phase.

During the calibration phase gas bubbles were injected at the bottom of the test section into the stagnant pool of water. The image analysis of resulting trajectories and bubble size distribution is shown in Figure 123. From the point of gas bubble injection, the terminal velocity is achieved after about 100 mm. The terminal bubble rise velocity (see Figure 124) was estimated 0.364 m/s (note that velocity is negative in the figures as the image vertical axis Y is directed downwards), which is in good agreement with the expected value for the measured bubble equivalent diameter of ~1.6 mm. However, there is significant noise in the measured data. The noise can be attributed to the:

- *periodic bias*, due to axisymmetric oscillation of bubbles shape,
- *random variability*, due to the variability of bubble sizes and possible interaction between bubbles (bubble moving in the wake of another bubble).

The noise imposes a limitation on the minimal size of the ROI (Region Of Interest) within which bubble rise velocity can be reliably averaged. The limitation is illustrated in Figure 125. The histograms show the distribution of the mean relative (to terminal) velocity for different ROI sizes. A distribution shall fall within a range of the velocity that is sufficiently smaller than the magnitude of the entrainment velocity.

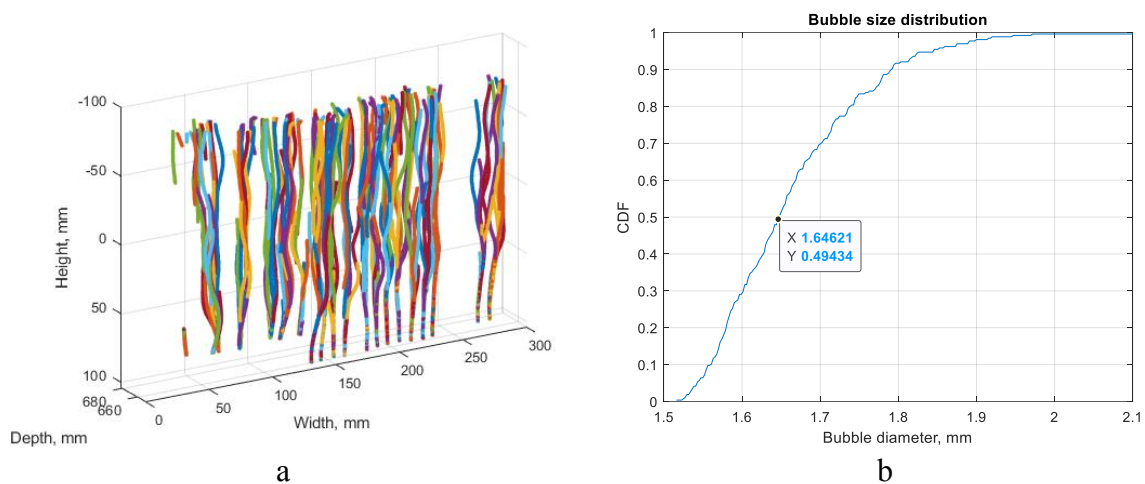


Figure 123. SEF-W7 stationary pool, bubble trajectories (a) and bubble size distribution (b)

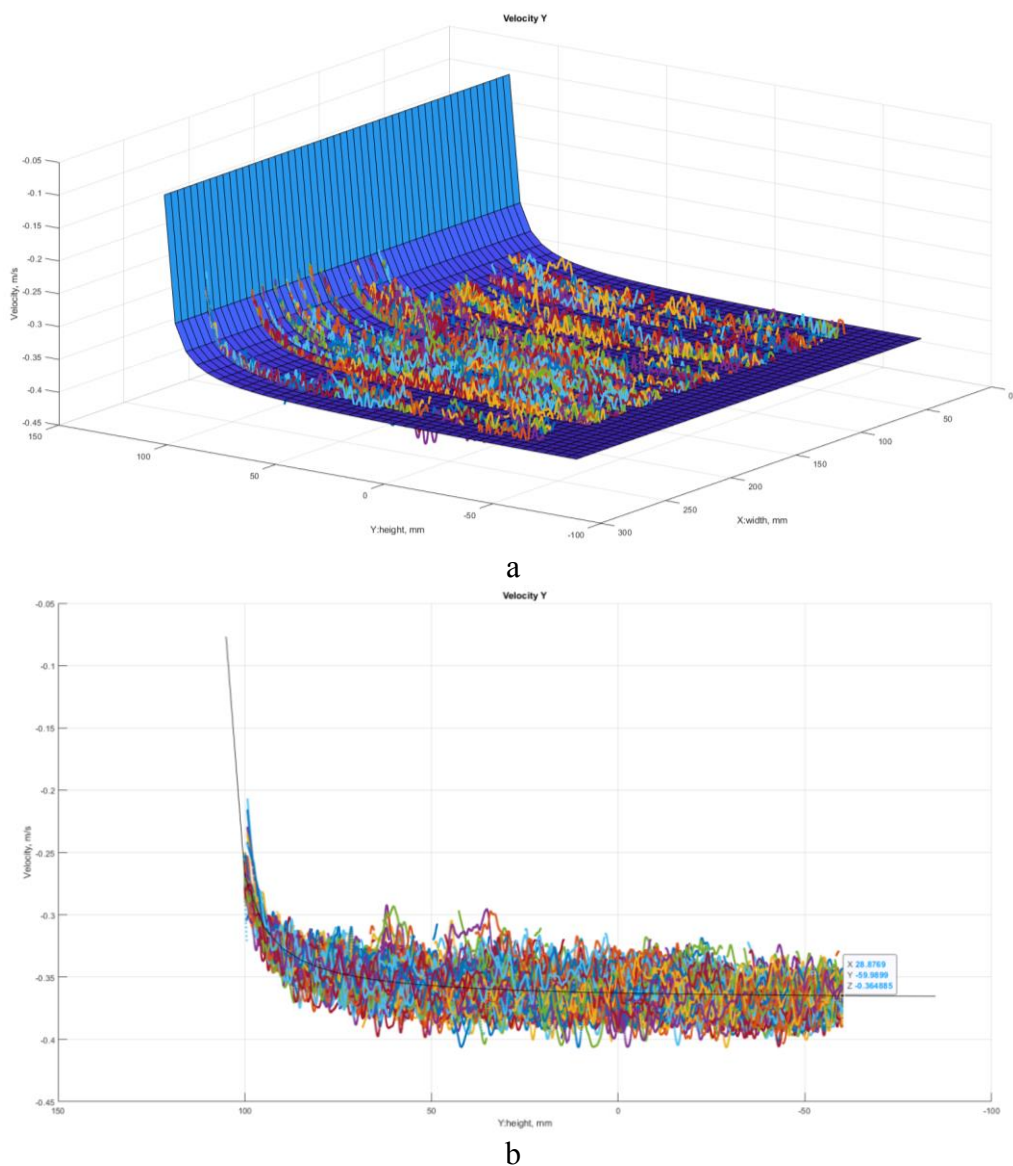


Figure 124. SEF-W7 stationary pool, bubble rise velocity and the reference velocity plane

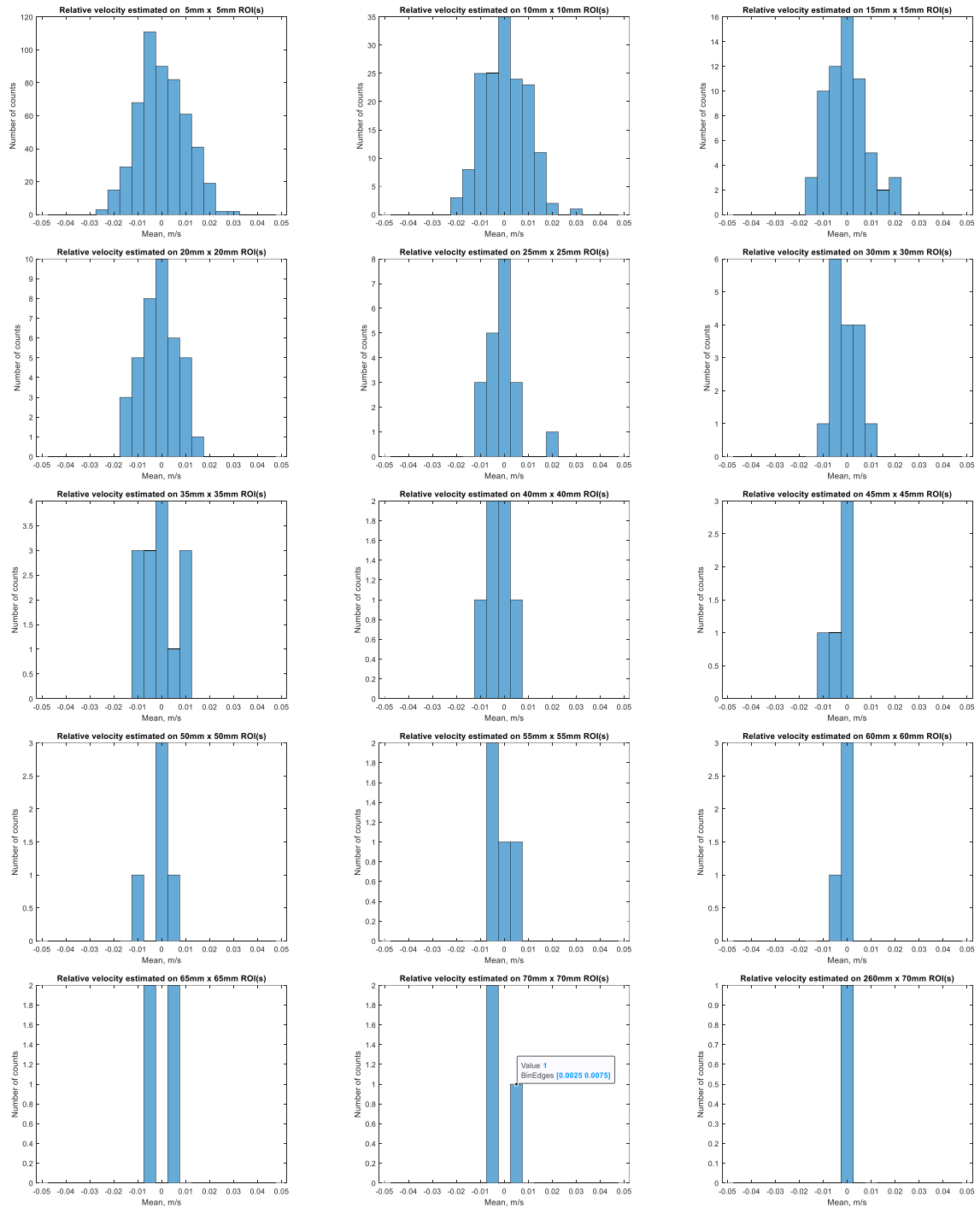


Figure 125. SEF-W7 Dependence of mean relative bubble rise velocity on the ROI size

The results suggest that for the measurement error to remain below  $\pm 1$  cm/s the size of the ROI should be at least 55x55 mm. In order to bring the level of accuracy of the 10x10 mm ROI to the one of the 55x55 mm the duration of the video recording should be increased  $\sim 30$  times. In the following analysis a ROI of 6 cm<sup>2</sup> was selected (X30xR20 mm) as a tradeoff between accuracy and size of the averaging window.

The estimation of the entrainment velocity in a stagnant pool should provide zero. For confirmation, the results of such analysis are show in Figure 126. The entrainment velocity was calculated in the lower part of the image (underneath injection line) between 45 and 80 mm in

vertical (radial) direction, and between 50 and 250 mm in axial direction. The size of the averaging (median) window was selected 20 mm in radial direction and 30 mm in axial direction. As expected, the resulting entrainment curves scatter around zero within about  $\pm 1$  cm/s range.

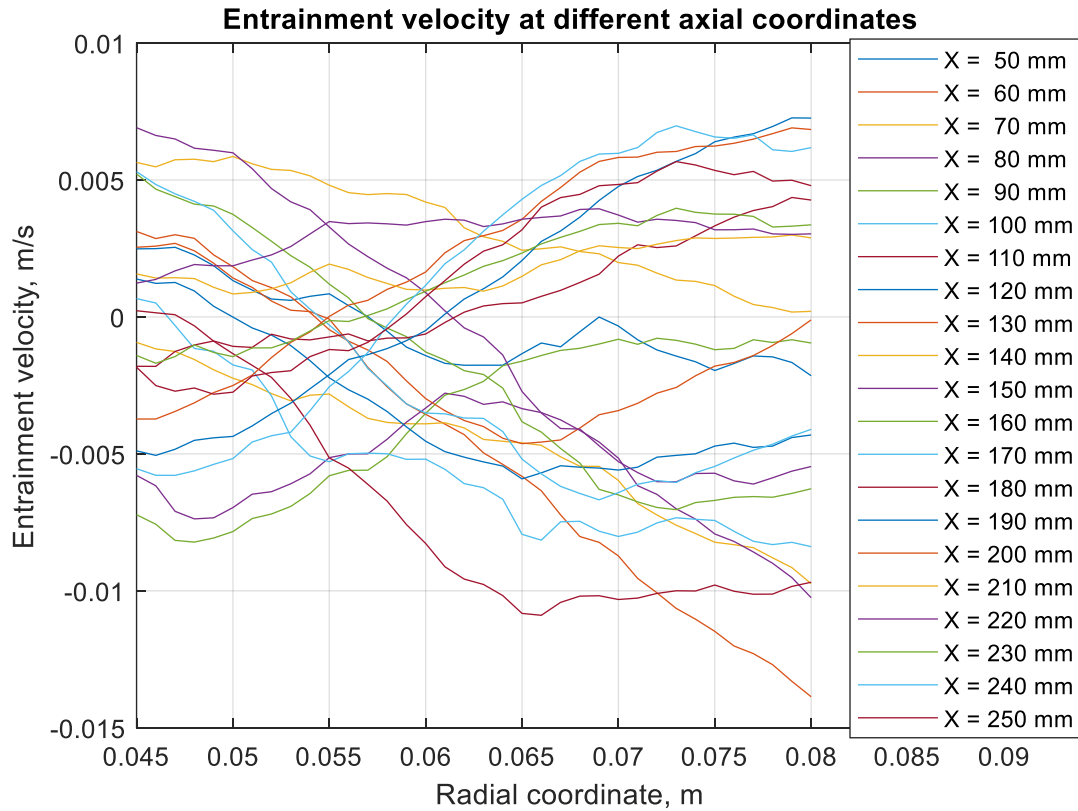


Figure 126. SEF-W7 Entrainment velocity at different axial distances estimated for stagnant pool. (The coordinate system used here is the same as in Figure 123a)

During the injection phase the water jet injection velocity in the nozzle was changed step-wise at increments of 1.41 m/s, 3.81 m/s, 4.97 m/s, 6.21 m/s, 8.95 m/s. From the jet theory summarized in Section 8.2 the expected entrainment velocity for a round jet can be estimated. The results of the calculation show that entrainment velocity falls in the range between 0.016 m/s and 0.18 m/s depending on the injection rate and location within the image. Such measurement should be feasible even considering  $\pm 1$  cm/s uncertainty. Note that measurement of the entrainment velocity should be done at the radial distance where the product  $RV_e$  becomes constant (see the example calculation in Figure 127), i.e. before bubbles are entrained inside the jet. As jet expands, the minimum radial distance at which entrainment measurement should be carried out increases. E.g. at 230 mm axial coordinate the minimum radial distance is 100 mm, which falls outside the image range in SEF-W7 test. On the other hand, measurement of the entrainment at axial distances below 6 jet diameters (96 mm) is also not recommended. This region of the jet corresponds to the flow development zone where jet expansion does not follow analytical equations presented in Section 8.2. Therefore, the optimal distance for the estimation of the entrainment is in the section of the image between 100 and 230 mm in axial direction and between 45 and 90 mm in vertical direction.



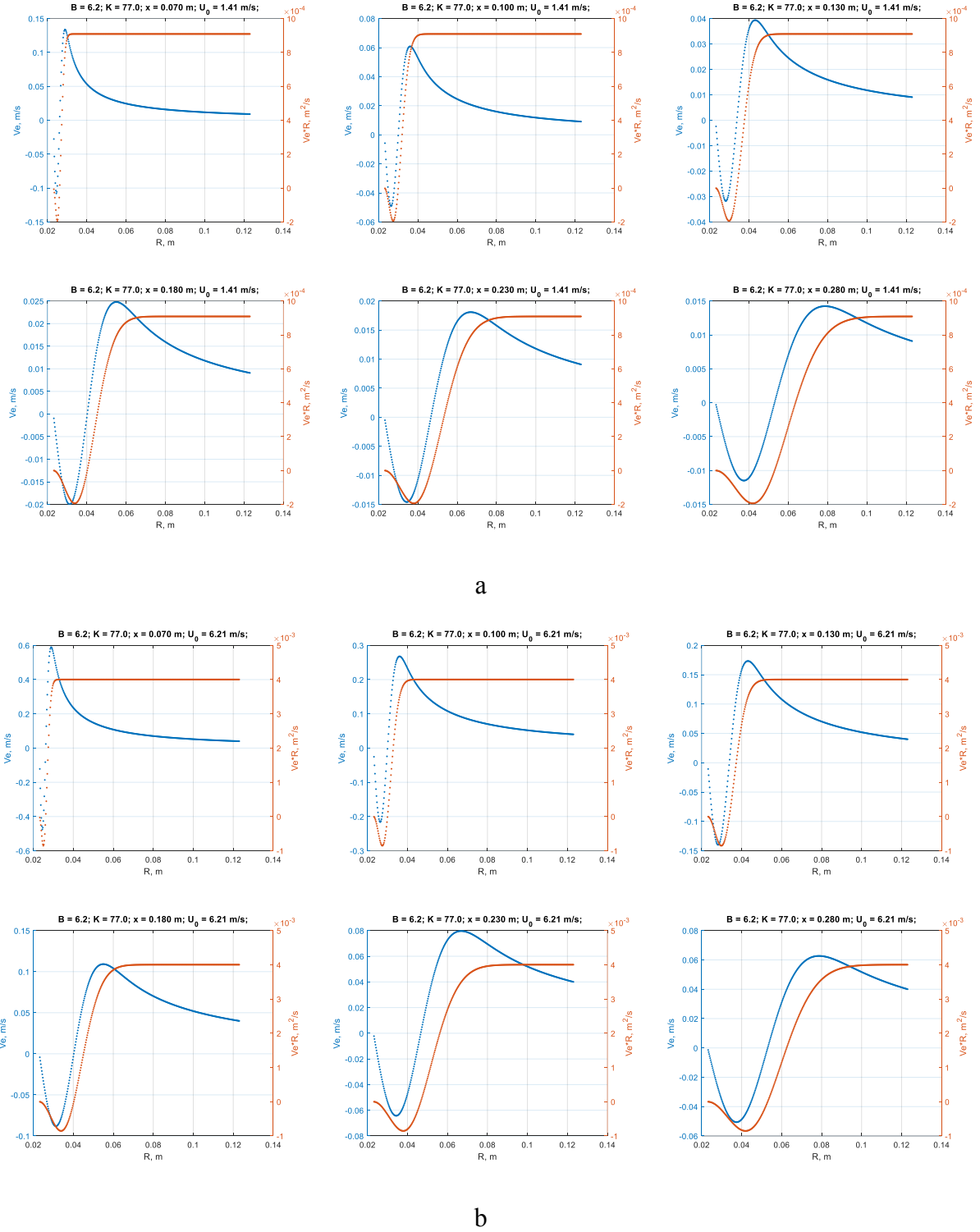


Figure 127. SEF-W7 Theoretical entrainment velocity and  $RV_e$  product for the jet expansion ratio  $K = 77$  and injection rate  $1.41\text{ m/s}$  (a) and  $6.32\text{ m/s}$  (b) at different axial distances  $x$ . (The coordinate system used here is the same as in Figure 123a)

Example of bubbles trajectories during injection is shown in Figure 128. One can notice that trajectories inside the jet become more chaotic and often divert strongly in  $Z$  direction (horizontally). This is caused by bubble breakup and superposition of multiple bubbles inside the jet – a situation which is not yet fully resolved by the image analysis algorithm.

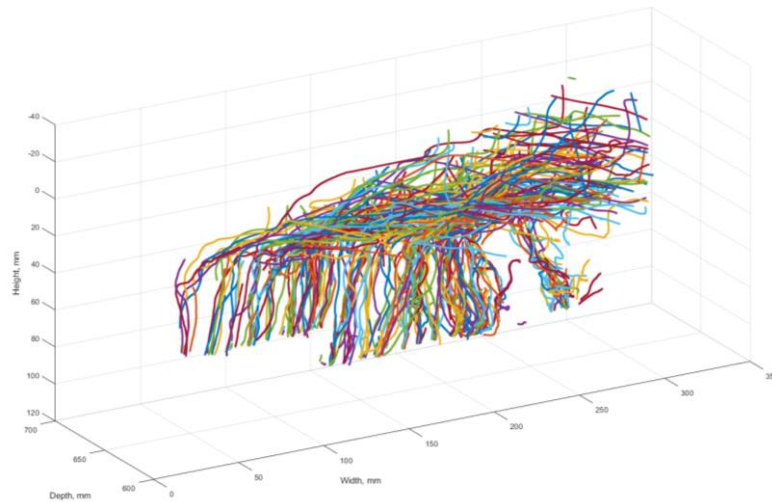
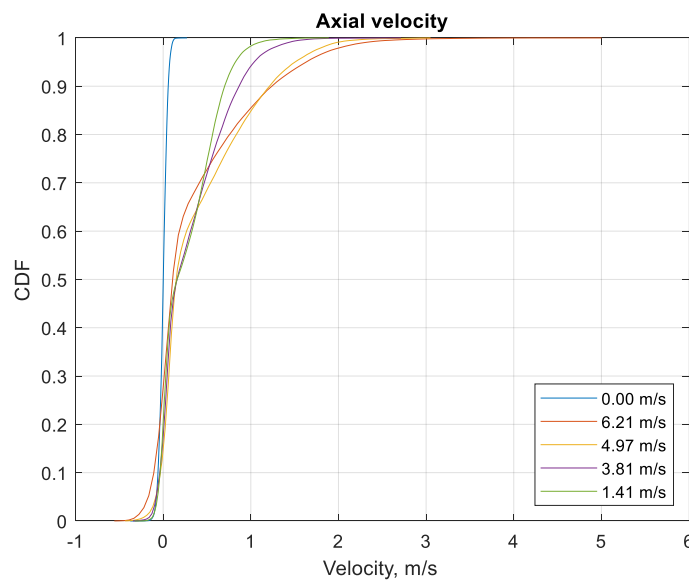


Figure 128. SEF-W7 Bubble trajectories during water jet injection at 4.97 m/s

The obtained distributions of axial velocities of the bubbles are provided in Figure 129 along with an insert that lists maximal axial velocity measured during each injection period. As expected with increase of the injection rate axial velocity of the bubbles inside the jet increases. The maximum value of the axial velocity is as expected smaller than the injection velocity except for the 1,41 m/s case where higher velocity was estimated (1.89 m/s). This could be attributed to (i) variability in the axial velocity of individual bubbles ( $\pm 0.27$  m/s) and (ii) non-uniform velocity profile at the nozzle cross-section.



Velocity, m/s	
$U_0$	$U_a \text{ max}$
0	0.27
1.41	1.89
3.81	2.71
4.97	3.05
6.21	5.00

Figure 129. SEF-W7 Distribution of axial velocity component for different injection velocities

The results of the estimation of the entrainment velocity are illustrated in Figure 130 **Error! Reference source not found.** together with the theoretical entrainment velocity (dotted curves) assuming characteristic for round jets expansion coefficient  $K = 77$ . The entrainment velocity was computed as the difference between bubble rise velocity with jet injection and bubble rise velocity without jet injection, i.e., in the stagnant pool. A median value was then taken from the ROI as the characteristic entrainment velocity for given coordinates of the ROI center.



The measured entrainment velocity underestimates the theoretical one by a significant margin. The scatter in the results is larger comparing to the stagnant pool indicating that flow structure might be more complex than anticipated. There could be several reasons for the underestimation:

- The flow structure around the jet is transient and its proper evaluation requires longer time for observation. It is instructive to note that if maximum instead of median is taken for the estimation of the entrainment the resulting curves overshoot the theoretical ones by a large margin (see Figure 131).
- The selected ROI size is prohibitively large to accurately capture entrainment velocity. Reduction of the ROI does increase the scatter in the entrainment velocity bringing some curves closer to the theoretical values (see Figure 132).

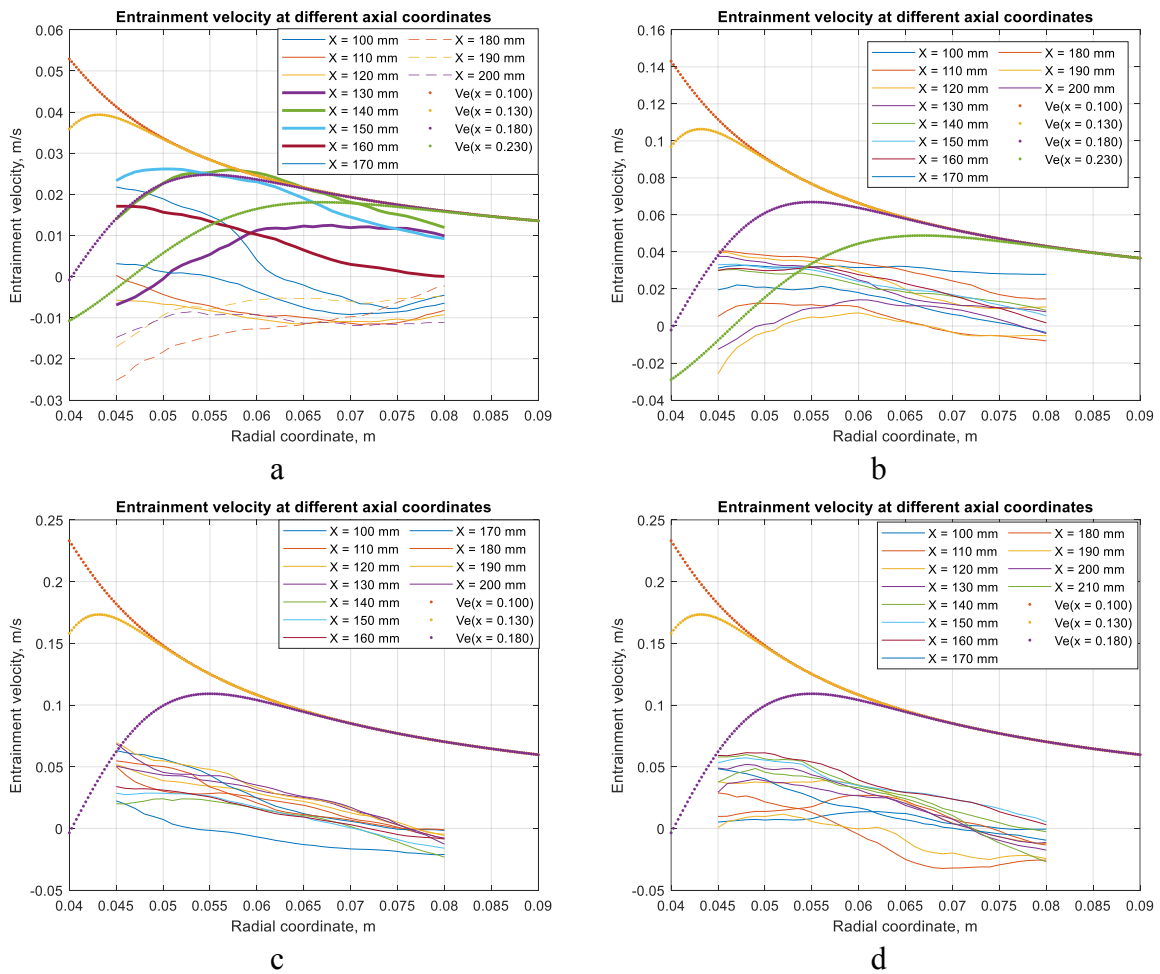


Figure 130. SEF-W7 Comparison of experimental and analytical entrainment velocity at different axial distances (a – 1.41 m/s, b – 3.81 m/s, c – 4.97 m/s, d – 6.21 m/s)

- Entrainment velocity measured in the vicinity of the nozzle shows an inverse trend (Figure 133). On one hand this suggests that entrainment is significantly reduced close to the injection. In such case mass conservation in that section of the jet would imply the centerline velocity to reduce with the square of the axial distance  $\frac{U_0 dB}{(x-x_0)^2}$  making actual centerline velocity in the established part of the jet lower than what is expected

in the model. On the other hand, the observed reversed trend indicates formation of a clockwise vortex that affects the entrainment flow around the jet.

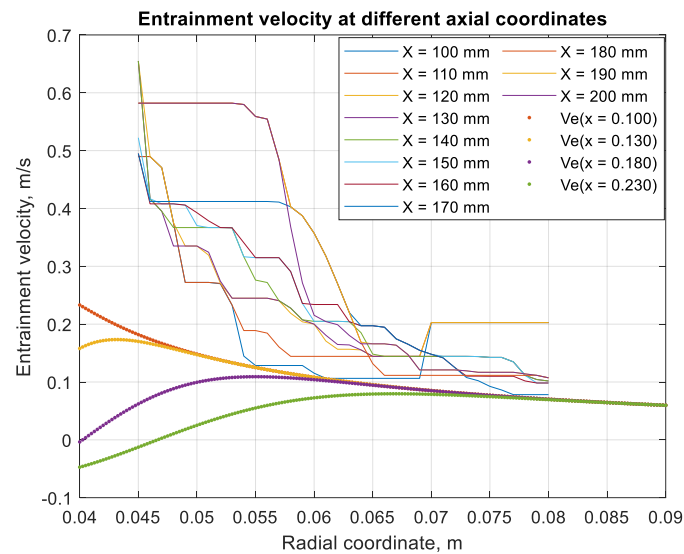


Figure 131. SEF-W7 Entrainment velocity estimated using max instead of the median statistics

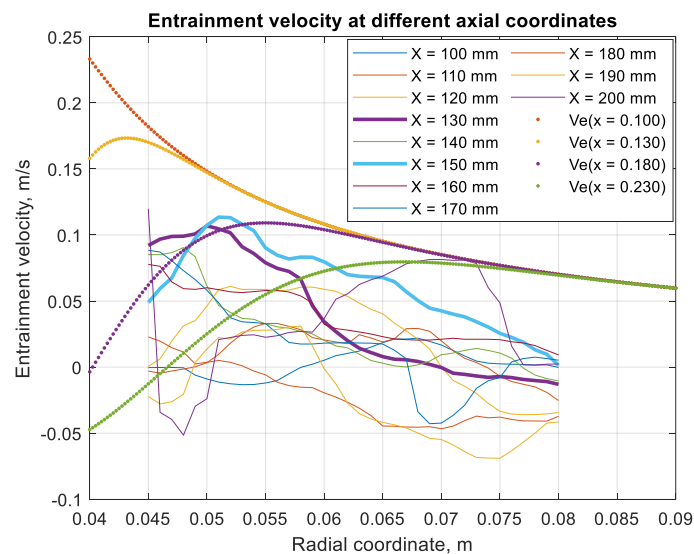


Figure 132. SEF-W7 Comparison of experimental and analytical entrainment velocity using a smaller ROI (10x10 mm)

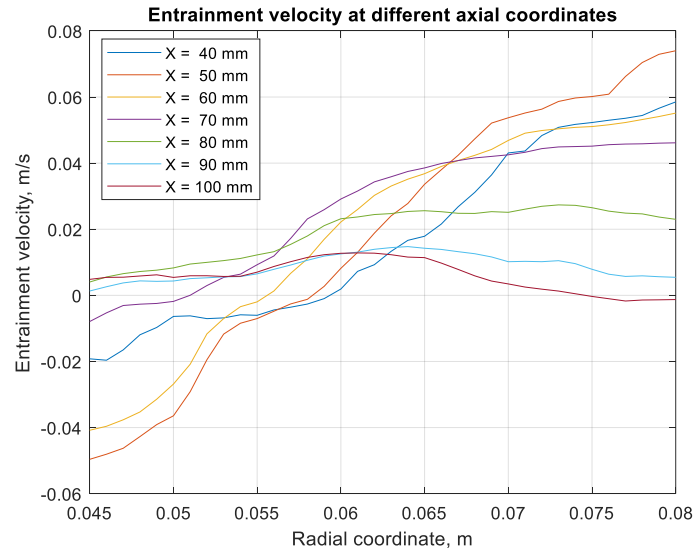


Figure 133. SEF-W7 Entrainment velocity in the vicinity of the nozzle

### 8.6. Summary of development of image analysis for SEF-POOL experiment

The first data from the analysis of the bubbles rise in a stagnant pool and pool with injection of a water jet was obtained and results have been analyzed. The current work is focused on the analysis of the tests with injection of a stream of water. The objective is to validate the methodology and confirm that measured entrainment rates agree well with theoretical ones. Currently, experimental data underestimates the theoretical entrainment velocity by about two times, and the reasons are being investigated.

Further work will aim to (i) optimize the experimental setup and image analysis and (ii) develop reliable approach to the estimation of the flow velocity and the entrainment rate.

## 9. SUMMARY

Containment is an essential part of the reactor safety design and is the last physical barrier that prevents the release of radioactive fission products into the environment. Pressure Suppression Pool (PSP) in Boiling Water Reactor (BWR) is used to condense steam released from the primary system in normal operation and in accident conditions. The PSP also serves as a source of water for the Emergency Core Cooling System (ECCS), spray, and as a scrubber in case of a core damage accident with release of radioactive aerosols. The PSP and overall containment performance can be affected by physical phenomena such as mixing and stratification. A stratified pool will have higher temperature at the surface compared to completely mixed pool with the same averaged temperature. The pool surface temperature determines the steam partial pressure in the containment gas space. Higher pool temperature results in higher partial pressure of steam in the containment atmosphere and respectively higher total containment pressure, while bottom layer of the pool remains cold. For instance, in Fukushima Daiichi Unit 3 containment pressure was rapidly increasing, which was attributed to the development of thermal stratification in the PSP.

The prediction of thermal stratification and mixing in a PSP remains a challenging task, due to the lack of models for steam direct contact condensation phenomena that could be effectively used for modeling of large-scale pools with numerous steam injection devices operated during long-term transients.

Effective Heat Source (EHS) and Effective Momentum Source (EMS) models have been proposed to enable the prediction of thermal stratification and mixing phenomena in a BWR containment PSP. The aim of this project is to provide pre- and post-test analytical support to the HYMERES-2 and NKS-THEOS experimental activities that were proposed to support development and validation of the EHS/EMS models. In this report we describe the progress achieved in addressing main tasks, i.e.: (i) development validation of the EHS/EMS models for spargers using OECD/HYMERES-1 PANDA HP5 test series; (ii) pre-test analysis in support of the experimental for SEF-POOL facility at LUT and PANDA facility at PSI; (iii) post-test analysis using the new test data.

In Section 3 we provide an overview of the work on direct contact condensation, pool stratification/mixing phenomena and modeling approaches. The progress and the need for further development of the EHS/EMS models for spargers is described in Sections 4. Two approaches to EMS model implementation are discussed (i) based on the source terms in the momentum equation and (ii) using boundary conditions for liquid velocity. Advantages and disadvantages of both approaches are discussed in detail. Results of the EHS/EMS models implemented using a source term approach suggest that the temperature evolutions are sensitive to the geometrical characteristics of the domains where EHS/EMS source terms are introduced. Validation of the EHS/EMS model using steam condensation region (SCR) approach against PANDA HP5 tests suggest that this model can provide a reasonably accurate prediction of the pool behavior while avoiding uncertainty in the distribution of the momentum source.

In Section 5 results of “Unit Cell” (where individual injection hole is modelled individually) EHS/EMS model development and validation are discussed against PPOOLEX SPA-T3 test. The model can provide a reasonably accurate prediction of the pool behavior. Downward angles of the jets are estimated using the internal sparger flow simulations and then assessed using the temperature evolutions the TC mesh measurements. Increased turbulence intensity

induced by the steam condensation is modelled by either adding an extra source of  $k$  in the transport equation or providing turbulence in the boundary conditions.

In Section 6 application of the developed EHS/EMS models to pre-test analysis in support of the PANDA H2P3 tests with sparger injection are presented. Scoping calculations were carried out to specify geometrical setup (pool depth, elevation of the sparger and number of open LRR holes), initial pool temperature, injection procedures, arrangement of thermocouples, PIV setup, for sparger tests (H2P3-1,2,3) and LRR tests (H2P3-4,5,6).

In Section 7 we present results of the pre-test analysis for the integral H2P4 test series in PANDA facility. The aim of the tests is to study the effect of pool stratification and mixing phenomena on containment pressurization. Results of the analysis are used for selection of the test configuration, i.e. the vessels to be used and connections between them, water pool level, duration and mass flow rates for different injection phases. Results of the analysis suggest that it is feasible to achieve prototypic levels of pressurization during a reasonable time for the tests.

In Section 8 the progress in development of the image analysis for post-processing of the data from the SEF-POOL tests are presented. Gas bubbles are used in the tests in order to visualize water velocity in the vicinity of the jet induced by steam injection. The first data from the analysis of the bubbles rise in a stagnant pool was obtained and results are being analyzed. The current work is focused on the further analysis of bubbles flow during steam injection and the data from SEW-W7 and W8 tests with water jets is being processed. Further work will aim to optimize (i) experimental setup to resolve several issues related to bubble formation and size, and (ii) image analysis and develop reliable approach to the estimation of flow velocity and entrainment rate.

## **ACKNOWLEDGEMENTS**

Financial support from the SSM and Nordic Nuclear Safety Program (NKS) is greatly acknowledged. The authors are grateful to all the countries participating in the OECD/NEA HYMERES and HYMERES-2 projects. The authors would like to thank the secretariat and all the members of the Management Board and the Programme Review Group of the HYMERES and HYMERES-2 project for their help in defining the test programme and evaluating the test results.

GOTHIC is developed and maintained by the Numerical Applications Division of Zachry Nuclear Engineering under EPRI sponsorship. We would like to acknowledge NAI for providing access to the program for educational and research purposes.

NKS conveys its gratitude to all organizations and persons who by means of financial support or contributions in kind have made the work presented in this report possible.

**DISCLAIMER**

The views expressed in this document remain the responsibility of the author(s) and do not necessarily reflect those of NKS. In particular, neither NKS nor any other organization or body supporting NKS activities can be held responsible for the material presented in this report.

## REFERENCES

1. Pershagen, B., 1994. Light Water Reactor Safety. Pergamon Press.
2. Lahey, R.T., Moody, F.J., 1993. The Thermal Hydraulics of a Boiling Water Nuclear Reactor, 2nd edition, American Nuclear Society, La Grange Park, Ill, USA.
3. Li, H., Kudinov, P., 2010. Effective Approaches to Simulation of Thermal Stratification and Mixing in a Pressure Suppression Pool. OECD/NEA & IAEA Workshop CFD4NRS-3, Bethesda, MD, USA, September 14-16, 2010.
4. Li, H., Villanueva, W., Kudinov, P., 2014. Approach and Development of Effective Models for Simulation of Thermal Stratification and Mixing Induced by Steam Injection into a Large Pool of Water. Science and Technology of Nuclear Installations, 2014, Article ID 108782, 11 pages.
5. Laine, J., Puustinen, M., Räsänen, A., 2013. PPOOLEX experiments on the dynamics of free water surface in the blowdown pipe. Nordic Nuclear Safety Research, NKS-281.
6. J. Laine, M. Puustinen, A. Räsänen, PPOOLEX Experiments with a Sparger, Nordic Nuclear Safety Research, 2015, NKS-334.
7. Mizokami, S., Yamada, D., Honda, T., Yamauchi, D., Yamanaka, Y., 2016. Unsolved issues related to thermal-hydraulics in the suppression chamber during Fukushima Daiichi accident progressions. Journal of Nuclear Science and Technology, 53, 630-638.
8. Mizokami, S., Yamanaka, Y., Watanabe, M., Honda, T., Fuji, T., Kojima, Y., PAIK, C.Y., Rahn, F., 2013. State of the art MAAP analysis and future improvements on TEPCO Fukushima-Daiichi NPP accident. NURETH-15: The 15th International Topical Meeting on Nuclear Reactor Thermal Hydraulics, Pisa, Italy, May 12-17, paper number 536.
9. Tanskanen, V., Jordan, A., Puustinen, M., Kyrki-Rajamäki, R., 2014. CFD simulation and pattern recognition analysis of the chugging condensation regime. Annals of Nuclear Energy, 66, 133-143.
10. Patel, G., Tanskanen, V., Hujala, E., Hyvärinen, J., 2017. Direct contact condensation modeling in pressure suppression pool system. Nuclear Engineering and Design, 321, 328-342.
11. Pellegrini, M., Naitoh, M., 2016. Application of two-phase flow DFC to the phenomena expected in Fukushima Daiichi S/C. OECD/NEA & IAEA Workshop CFD4NRS-6.
12. Li, H., Villanueva, W., Puustinen, M., Laine, J., Kudinov, P., 2014. Validation of Effective Models for Simulation of Thermal Stratification and Mixing Induced by Steam Injection into a Large Pool of Water. Science and Technology of Nuclear Installations, 2014, Article ID 752597, 18 pages.
13. Li, H., Villanueva, W., Puustinen, M., Laine, J., Kudinov, P., 2017. Thermal stratification and mixing in a suppression pool induced by direct steam injection. Annals of Nuclear Energy, 111, 487-498.
14. Villanueva, W., Li, H., Puustinen, M., Kudinov, P., 2015. Generalization of experimental data on amplitude and frequency of oscillations induced by steam injection into a subcooled pool. Nuclear Engineering and Design, 295, 155-161.
15. Li, H. and Kudinov, P., 2009. An Approach to Simulation of Mixing in a Stratified Pool with the GOTHIC code. ANS Transactions, paper 210976.
16. Li, H., Villanueva, W., Kudinov, P., 2011. Development and implementation of effective models in GOTHIC for the prediction of mixing and thermal stratification in a BWR pressure suppression pool. Proceedings of ICAPP 2011, Nice, France, May 2-5, 2011, Paper 11256.
17. Li, H. and Kudinov, P., 2008. An approach toward simulation and analysis of thermal stratification and mixing in a pressure suppression pool. NUTHOS-7, Seoul, Korea, October 5-9, Paper 243.



18. Gallego-Marcos, I., Villanueva, W., Kudinov, P., 2018. Modelling of Pool Stratification and Mixing Induced by Steam Injection through Blowdown Pipes. *Annals of Nuclear Energy*, 112, 624-639.
19. Li, H. and Kudinov, P., 2009. Condensation, Stratification and Mixing in a Boiling Water Reactor Suppression Pool. NORTHNET Roadmap 3 Report, Division of Nuclear Power Safety, Royal Institute of Technology (KTH), Stockholm, Sweden, 70p.
20. Li, H., Villanueva, W., Kudinov, P., 2010. Investigation of containment behavior with activation of rupture disks in system 361/362 with GOTHIC simulation. Swedish Radiation Safety Authority (SSM) Project Report, Royal Institute of Technology (KTH), Stockholm, Sweden, 25p.
21. Li, H., Kudinov, P., Villanueva, W., 2010. Modeling of Condensation, Stratification and Mixing Phenomena in a Pool of Water. NKS Report, NKS-225, Division of Nuclear Power Safety, KTH, Stockholm, Sweden, 91p.
22. Li, H., Kudinov, P., Villanueva, W., 2010. Condensation, Stratification and Mixing in a Boiling Water Reactor Suppression Pool. NORTHNET Roadmap 3 Report, Division of Nuclear Power Safety, Royal Institute of Technology (KTH), Stockholm, Sweden, 88p.
23. Li, H., Villanueva, W., Kudinov, P., 2012. Development, Implementation and Validation of EHS/EMS Models for Spargers. Westinghouse project report. Division of Nuclear Power Safety, Royal Institute of Technology (KTH), Stockholm, Sweden, 98p.
24. Li, H., Villanueva, W., Kudinov, P., 2012. Effective Momentum and Heat Flux Models for Simulation of Stratification and Mixing in a Large Pool of Water. NKS-ENPOOL Research report, NKS-266, 58p.
25. Li, H., Villanueva, W., Kudinov, P., 2012. Effective Models for Prediction of Stratification and Mixing Phenomena in a BWR Suppression Pool. NORTHNET Roadmap 3 Report, Division of Nuclear Power Safety, Royal Institute of Technology (KTH), Stockholm, Sweden, 87p.
26. Li, H., Villanueva, W., Kudinov, P., 2014. Effective Models for Simulation of Thermal Stratification and Mixing Induced by Steam Injection into a Large Pool of Water. Nordic Nuclear Safety Research, NKS-316.
27. Gallego-Marcos, I., Villanueva, W., Kapulla, R., Paranjape, S., Paladino, D., Kudinov, K., 2016. Modeling of thermal stratification and mixing induced by steam injection through spargers into a large water pool. OECD/NEA & IAEA Workshop CFD4NRS-6, Cambridge, MA, USA, September 13-15.
28. Gallego-Marcos, I., Villanueva, W., Kapulla, R., Paranjape, S., Paladino, D., Kudinov, K., 2016. Scaling and CFD Modelling of the Pool Experiments with Spargers Performed in the PANDA Facility. NUTHOS-11: The 11th International Topical Meeting on Nuclear Reactor Thermal Hydraulics, Operation and Safety Gyeongju, Korea, October 9-13, N11P0670.
29. Gallego-Marcos, I., Villanueva, W., Kudinov, P., 2016. Scaling of the Erosion of a Thermally Stratified Layer in a Large Water Pool during a Steam Injection Through Spargers. NUTHOS-11: The 11th International Topical Meeting on Nuclear Reactor Thermal Hydraulics, Operation and Safety, Gyeongju, Korea, October 9-13, N11P0525.
30. Gallego-Marcos, I., Villanueva, W., Kudinov, P., 2016. Modeling of Thermal Stratification and Mixing in a Pressure Suppression Pool Using GOTHIC. NUTHOS-11: The 11th International Topical Meeting on Nuclear Reactor Thermal Hydraulics, Operation and Safety, Gyeongju, Korea, October 9-13, N11P0524.
31. Gallego-Marcos, I., Kudinov, P., Villanueva, W., Kapulla, R., Paranjape, S., Paladino, D., Laine, J., Puustinen, M., Räsänen, A., Pyy, L., Kotro, E., 2019. Pool Stratification and Mixing Induced by Steam Injection through Spargers: CFD modeling of the PPOOLEX and PANDA experiments. *Nuclear Engineering and Design*, 347, 67-85.

32. Gallego-Marcos, I., Filich, L., Villanueva, W., Kudinov, P., 2015. Modelling of the Effects of Steam Injection through Spargers on Pool Thermal Stratification and Mixing. NKS Report 347.
33. Gallego-Marcos, I. Villanueva, W., Kudinov, P., 2016. Thermal Stratification and Mixing in a Large Pool Induced by Operation of Spargers, Nozzles, and Blowdown Pipes". NKS Report 369.
34. Gallego-Marcos, I., Villanueva, W., Kudinov, P., 2017. Modelling of a Large Water Pool during Operation of Blowdown Pipes, Spargers, and Nozzles. NKS-393.
35. Puustinen, M., Laine, J., Räsänen, A., 2009. PPOOLEX experiments on thermal stratification and mixing. Research report CONDEX 1/2008, NKS-198.
36. Gallego-Marcos I., Kudinov P., Villanueva W., Kapulla R., Paranjape S., Paladino D., Laine J., Puustinen M., Räsänen A., Pyy L., Kotro E., 2018. Pool Stratification and Mixing Induced by Steam Injection through Spargers: analysis of the PPOOLEX and PANDA experiments. Nuclear Engineering and Design, 337, 300-316.
37. Song, C.H., Cho, C., Him, H.Y., et al., 1998. Characterization of direct contact condensation of steam jets discharging into a subcooled water, Proceedings of IAEA Technical Committee Meeting, PSI, Villigen.
38. Kerney, J., Feath, G.M., Olson, D.R., 1972. Penetration characteristics of a sub-merged steam jet. AIChE Journal 18(3) 584-553.
39. Gulawani, S.S., Dahikar, S.K., Mathpati, C.S., et al., 2009. Analysis of flow pattern and heat transfer in direct contact condensation. Chemical Engineering Science, 64 1719-1738.
40. Wu, X.Z., Yan, J.J., et al., 2009. Experimental study on sonic steam jet condensation in quiescent subcooled water. Chemical Engineering Science, 64 (23), 5002-5012.
41. Y.J. Choo, C.H. Song, PIV measurements of turbulent jet and pool mixing produced by a steam jet discharge in a subcooled pool, Nuclear Engineering and Design 240 (9) (2010) 2215-2224.
42. Ju, S.H., et al., 2000. Measurement of heat transfer coefficients for direct contact condensation in core makeup tanks using holographic interferometer. Nuclear Engineering and Design, 199, 75-83.
43. Chan, C.K., Lee, C.K.B., 1982. A regime map for direct contact condensation. International Journal of Multiphase Flow, 8, 11-20.
44. Simpson, M.E., Chan, C.K., 1982. Hydrodynamics of a subsonic vapor jet in subcooled liquid. Journal of Heat Transfer, 104 (2), 271-278.
45. Fukuda, S., 1982. Pressure Variations due to Vapor Condensation in Liquid, (II). Journal of the Atomic Energy Society of Japan, 24 (6), 466-474.
46. Hong, J., Park, G.C., Cho, S., Song, C.H., 2012. Condensation dynamics of submerged steam jet in subcooled water. International Journal of Multiphase Flow 39, 66-77.
47. Cho, S., Chun, S.Y., Baek, W.P., Kim, K., 2004. Effect of multiple holes on the performance of sparger during direct contact condensation. Experimental Thermal and Fluid Science, 28 (6), 629-638.
48. Tang, J., Yan, C., Sun, L., 2015. A study visualizing the collapse of vapor bubbles in a subcooled pool. International Journal of Heat and Mass Transfer, 88, 597-608.
49. Aya, I., Nariai, H., Kobayashi, M., 1980. Pressure and Fluid Oscillations in Vent System due to Steam Condensation, (II) High-Frequency Component of Pressure Oscillations in Vent Tubes under at Chugging and Condensation Oscillation. Journal of Nuclear Science and Technology, 20(3), 213-227.
50. Youn, D.H., Ko, K.B., Lee, Y.Y., Kim, M.H., Bae, Y.Y., Park, J.K., 2003. The Direct Contact Condensation of Steam in a Pool at Low Mass Flux. Nuclear Science and Technology 40(10), 881-885.

51. E. Aust, D. Seeliger. Pool dynamics and dynamic loads in pressure suppression containment systems. Transactions of the American Nuclear Society 41 (1982) 696-699.
52. Aya, I., Nariai, H 1987. Boundaries between regimes of pressure oscillations induced by steam condensation in pressure suppression containment. Nuclear Engineering and Design, 99, 31-40.
53. Liang, K.S., Griffith, P., 1994. Experimental and analytical study of direct contact condensation of steam in water, Nuclear Engineering and Design, 147 (3), 425-435.
54. Cho, S., Song, C.H., Park, C.K., Yang, S.K., Chung, M.K., 1998. Experimental study on dynamic pressure pulse in direct contact condensation of steam jets discharging into subcooled water. Proceedings of NTHAS98. Korea-Japan symposium on nuclear thermal hydraulics and safety; Pusan Korea, 291-298.
55. A. Petrovic de With, R.K. Calay, G. de With, 2007. Three dimensional condensation regime diagram for direct contact condensation of steam injected into water. International Journal of Heat and Mass Transfer, 50 (9-10), 1762-1770.
56. G. Gregu, M. Takahashi, M. Pellegrini, R. Mereu, 2017. Experimental study on steam chugging phenomenon in a vertical sparger, International Journal of Multiphase Flow 88, 87-98.
57. X.Z. Wu, J.J. Yan, W.J. Li, D.D. Pan, G.Y. Liu, W.J. Li, 2009. Condensation regime diagram for supersonic/sonic steam jet in subcooled water, Nuclear Engineering and Design 239 (12), 3142-3150.
58. Song, 2010. PIV measurements of turbulent jet and pool mixing produced by a steam jet discharge in a subcooled pool. Nuclear Engineering and Design 240 (9) 2215-2224.
59. R.J.E. Van Wissen, K.R.A.M. Schreel, C.W.M Van Der Geld, 2005. Particle image velocimetry measurements of a steam-driven confined turbulent water jet. Journal of Fluid Mechanics 530, 353-368.
60. F. D'Auria, G.M. Galassi, Scaling of nuclear reactor system thermal-hydraulics, Nuclear Engineering and Design 240 (10) (2010) 3267-3293.
61. MARVIKEN-FSCB-I, 1973. Marviken Full Scale Containment Blowdown Experiments Series I.
62. W. Kennedy, D. McGovern, R. Maraschin, K. Wolfe. Rigid and flexible vent header testing in the quarter scale test facility. Mark I containment program, task 5.3.3. Technical report, General Electric Co., San Jose, CA (USA), 1978. Alternate Energy Division.
63. T.R. McIntyre, M.A. Ross, L.L. Myers. Mark II pressure suppression test program: Phase I tests. Technical report, General Electric Co., San Jose, CA (USA), 1976. Boiling Water Reactor Systems Dept.
64. W.A. Grafton, T.R. McIntyre, M.A. Ross. Mark II pressure suppression test program: Phase II and III tests. Technical report, General Electric Co., San Jose, CA (USA), 1977. Boiling Water Reactor Projects Dept.
65. T.R. McIntyre, L.L. Myers, J.E. Torbeck, R.J. Booker. Mark III confirmatory test program: one third scale, three vent air tests. Technical report, General Electric Co., San Jose, Calif. (USA), 1975. Boiling Water Reactor Systems Dept.
66. A.M. Varzaly, W.A. Grafton, H. Chang, M.K. Mitchell. Mark III confirmatory test program: 1/root 3 scale condensation and stratification phenomena, test series 5807. Technical report, General Electric Co., San Jose, Calif. (USA), 1977. Boiling Water Reactor Systems Dept.
67. T.H. Chuang. Mark III one-third area scale submerged structure tests. Technical report, General Electric Co., San Jose, CA (USA), 1977. Boiling Water Reactor Systems Dept.

68. K. Namatame, Y. Kukita, I. Takeshita, 1983. Evaluation of primary blowdown flow rate and vent pipe steam mass flux (Tests 00002, 0003, 0004, 1101, 2101, 3101, 3102) - Full-Scale Mark II CRT program Test Evaluation Report No 1, JAERI-M 83-185.
69. Y. Kukita, I. Takeshita, K. Namatame, M. Kato, K. Moriya, M. Shiba, 1981. Statistical evaluation of steam condensation loads in pressure suppression pool (1) – Full-Scale Mark II CRT program. Test Evaluation Report No. 2, JAERI-M 9665.
70. J. Hart, W.J.M. Slegers, S.L. de Boer, M. Huggenberger, J. Lopez Jimenez, J.L. Munoz-Cobo Gonzalez, F. Reventos Puigjaner., 2001. TEPSS-Technology enhancement for passive safety systems. Nuclear Engineering and Design 209, 243-252.
71. C.D. Walsche, F.D. Cachard., 1996. Experimental investigation of condensation and mixing during venting of a steam/non-condensable gas mixture into a pressure suppression pool. Technical report, IAEA Report 53-61.
72. Y.T. Moon, H.D. Lee, G.C. Park., 2009. CFD simulation of steam jet-induced thermal mixing into a subcooled water pool, Nuclear Engineering and Design 239, 2849-2863.
73. Y. Zhang, D. Lu, Z. Wang, X. Fu, Q. Cao, Y. Yang, G. Wu., 2016. Experimental research on the thermal stratification criteria and heat transfer model for the multi-holes steam ejection in IRWST of AP1000 plant, Applied Thermal Engineering 107, 1046-1056.
74. J. Laine, M. Puustinen., 2005. Condensation Pool Experiments with Steam Using DN200 Blowdown Pipe, Nordic Nuclear Safety Research NKS-111.
75. J. Laine, M. Puustinen., 2006. Thermal stratification experiments with the condensation pool test rig, Nordic Nuclear Safety Research NKS-117.
76. J. Laine, M. Puustinen., 2009. A. Räsänen, PPOOLEX Experiments on Thermal Stratification and Mixing, Nordic Nuclear Safety Research NKS-198.
77. M. Puustinen, J. Laine., 2011. A. Räsänen, Multiple blowdown pipe experiments with the PPOOLEX facility, Nordic Nuclear Safety Research NKS-241.
78. J. Laine, M. Puustinen., 2013. A. Räsänen, PPOOLEX experiments on the dynamics of free water surface in the blowdown pipe, Nordic Nuclear Safety Research NKS-281.
79. J. Laine, M. Puustinen, A. Räsänen., 2014. PPOOLEX Mixing Experiments, Nordic Nuclear Safety Research, NKS-309.
80. Kapulla, R., Mignot, G., Paranjape, P., Paladino, D., Fehlmann, M., Suter, S., 2015. OECD/NEA HYMERES project: HP5 Test Results. In: 6th Meeting of the Programme Review Group and Management Board of the HYMERES Project, PSI Villigen, Switzerland, 17–19 November.
81. M. Solom, K.V. Kirkland, Experimental investigation of BWR Suppression Pool stratification during RCIC system operation, Nuclear Engineering and Design 310 (2016) 564-569.
82. H.J.S. Fernando., 1991. Turbulent mixing in stratified fluids, Annual Review of Fluid Mechanics 23, 455-93.
83. D. Song, N. Erkan, B. Jo, K. Okamoto, 2014. Dimensional analysis of thermal stratification in a suppression pool, International Journal of Multiphase Flow 66, 92-100.
84. H.J.S. Fernando, Turbulent mixing in stratified fluids, Annual Review of Fluid Mechanics 23 (1991) 455-93.
85. H.J.S. Fernando, J.C.R. Hunt, 1997. Turbulence, waves and mixing at shear-free density interfaces. Part 1. A theoretical model, Journal of Fluid Mechanics 347, 197-234.
86. J.L. McGrath, H.J.S. Fernando, J.C.R. Hunt, 1997. Turbulence, waves and mixing at shear-free density interfaces. Part 2. Laboratory experiments, Journal of Fluid Mechanics 347, 235-261.
87. C.H. Chen, V.K. Dhir. Hydrodynamics of a bubble formed at vent pipe exit. International Journal of Multiphase Flow 8(2) (1982) 147-163.

88. F. Yuan, D. Chong, Q. Zhao, W. Chen, J. Yan, Pressure oscillation of submerged steam condensation in condensation oscillation regime, *International Journal of Heat and Mass Transfer* 98 (2016) 193-203.
89. J.H. Pitts, Steam chugging in a boiling water reactor pressure-suppression system, *International Journal of Multiphase Flow* 6 (1980) 329-344.
90. M. Ali, V. Verma, A.K. Ghosh, Analytical thermal hydraulic model for steam chugging phenomenon, *Nuclear Engineering and Design* 237(19) (2007) 2025-2039.
91. C. Brennen, A Linear Dynamic Analysis of Vent Condensation Stability, Annual Meeting of the American Society of Mechanical Engineers, Chicago, Illinois, November 16-21, 1980.
92. T.J.H. Pättikangas, J. Niemi, J. Laine, M. Puustinen, H. Purhonen. 2010. CFD modelling of condensation of vapor in the pressurized PPOOLEX facility. *CFD4NRS-3*, 14-16 September, Washington D.C., USA.
93. R.E. Gamble., T.T. Nguyen., B.S. Shiralkar., P.F. Peterson., R. Greifc., H. Tabatad., 2001. Pressure suppression pool mixing in passive advanced BWR plants, *Nuclear Engineering and Design* 204, 321-336.
94. H.S. Kang., C.H. Song., 2008. CFD analysis for thermal mixing in a subcooled water tank under a high steam mass flux discharge condition. *Nuclear Engineering and Design*, 238. 492-501.
95. H.S. Kang., C.H. Song., 2010. CFD analysis of a turbulent jet behavior induced by a steam jet discharge through a single hole in a subcooled water tank. *Nuclear Engineering and Design*, 240, 2160-2168.
96. C.H. Song., S. Cho., H.S. Kang., 2012. Steam Jet Condensation in a Pool: From Fundamental Understanding to Engineering Scale Analysis. *Journal of Heat Transfer*, 134, 031004-1.
97. Gallego-Marcos, I., Grishchenko, D., Kudinov, P., 2019. Thermal stratification and mixing in a Nordic BWR pressure suppression pool. *Annals of Nuclear Energy*, 132, 442-450.
98. Gallego-Marcos, I. Kudinov P., Villanueva W., Puustinen M, Räsänen A., Tielinen K., Kotro E., 2019. Effective momentum induced by steam condensation in the oscillatory bubble regime. *Nuclear Engineering and Design*, 350, 259-274.
99. GOTHIC Thermal Hydraulic Analysis Package, Version 8.1(QA). EPRI, Palo Alto, CA: 2014.
100. RELAP5/MOD3.3 Code Manual Volume IV. US Nuclear Regulatory Commission, Washington DC, 2006.
101. I. Aya, H. Nariai. Chugging Phenomenon Induced by Steam condensation into pool water (amplitude and frequency of fluid oscillation). Translated from: *Transactions of the Japan Society of Mechanical-Engineers* 50 (1984) 2427-2435.
102. C.E. Brennen. *Fundamentals of Multiphase Flow*. Cambridge University Press (2005), section 15.6.3.
103. C.K.B Lee, C.K. Chan, Steam chugging in pressure suppression containment: final report July 1976 - July 1979, US Nuclear Regulatory Commission (1980).
104. I. Gallego-Marcos, W. Villanueva, P. Kudinov. Possibility of Air Ingress into a BWR Containment during a LOCA in case of Activation of Containment Venting System. NUTHOS-10: The 10th International Topical Meeting on Nuclear Reactor Thermal Hydraulics, Operation and Safety, Okinawa, Japan, December 14-18, (2014) paper number 1292.
105. Pellegrini, M., et al., 2016. Benchmark study of the accident at the Fukushima Daiichi NPS: best-estimate case comparison. *Nuclear Technology*. 196 (2), 198-210.

106. Gallego-Marcos, I., 2018. Steam condensation in a water pool and its effect on thermal stratification and mixing. PhD thesis, KTH Royal Institute of Technology, Stockholm, Sweden.
107. A.A. Sonin. Scaling laws for small-scale modeling of steam relief into water pools, *Nuclear Engineering and Design* 65 (1) (1981) 17-21.
108. Paladino, D., Dreier, J., 2012. PANDA: a multipurpose integral test facility for LWR safety investigations. *Science and Technology of Nuclear Installations*, Article ID 239319.
109. Kapulla, R., Mignot, G., et al., 2018. PIV Measurements in the Vicinity of a Steam Sparger in the PANDA Facility. *Nuclear Engineering and Design*, 336, 112-121.
110. X. Li, M. Zhang, Z. Du, X. Fu. Scaling analysis of coolant spraying process in automatic depressurized system, *Annals of Nuclear Energy* 72 (2014) 350-357.
111. N.W.M. Ko, K.K. Lau, Flow structures in initial region of two interacting parallel plane jets, *Experimental Thermal and Fluid Science* 2 (4) (1989) 431-449.
112. D. Heinze, T. Schulenberg, L. Behnke. A Physically Based, One-Dimensional Two-Fluid Model for Direct Contact Condensation of Steam Jets Submerged in Subcooled Water. *Journal of Nuclear Engineering and Radiation Science*, 1(2) (2015) 8 pages.
113. E.S Gadis, A. Vogelpohl. Bubble formation in quiescent liquids under constant flow conditions. *Chemical Engineering Science* 41 (1986) 97-105.
114. S. Ramakrishnan, R. Kumar, N.R. Kuloor. Studies in bubble formation - Bubble formation under constant flow conditions. *Chemical Engineering Science* 24 (1969) 731-747.
115. L. Zhang, M. Shoji. Aperiodic bubble formation from a submerged orifice. *Chemical Engineering Science* 56 (2001) 5371-5381.
116. I. Aya, H. Nariai. Evaluation of heat-transfer coefficient at direct-contact condensation of cold water and steam. *Nuclear Engineering and Design* 131 (1991) 17-24.
117. O. Zeitoun, M. Shoukri, V. Chatoorgoon. Interfacial Heat Transfer Between Steam Bubbles and Subcooled Water in Vertical Upward Flow. *Journal of Heat Transfer* 117 (2) (1995) 402-407.
118. G.R. Warriar, N. Basu, V.K. Dhir. Interfacial heat transfer during subcooled flow boiling. *International Journal of Heat and Mass Transfer* 45 (2002) 3947-3959.
119. A. Prosperetti, M.S. Plesset. Vapour-bubble growth in a superheated liquid. *Journal of Fluid Mechanics* 85 (2) (1978) 349-368.
120. Pope. S.B., 2020. *Turbulent Flow*. Section 5.1, Cambridge University Press, Cambridge UK.
121. Hussein. H., et al., 1994. Velocity measurements in a high-Reynolds-number, momentum-conserving axisymmetric, turbulent jet. *Journal of Fluid Mechanics*, 258, 31-75.
122. T.B. Benjamin, A.T. Ellis. The collapse of cavitation bubbles and the pressures thereby produced against solid boundaries. *Philosophical Transactions of the Royal Society* 260 (1966) 221-240.
123. J.R. Blake. The Kelvin Impulse: Application to Cavitation Bubble Dynamics. *Journal of the Australian Mathematical Society* 30 (1988) 127-146.
124. D. Obreschkow, M. Tinguely, N. Dorsaz, P. Kobel, A. Bosset, M. Farhat. A Universal Scaling Law for Jets of Collapsing Bubbles. *Physical Review Letters* 107 (2011) 204501.
125. O. Supponen, D. Obreschkow, M. Tinguely, P. Kobel, N. Dorsaz, M. Farhat. Scaling laws for jets of single cavitation bubbles. *Journal of Fluid Mechanics* 802 (2106) 263-293.
126. ANSYS® Academic Research, 2019 R3, ANSYS Fluent Theory Guide, ANSYS, Inc.

127. A.M. Bahari, K. Hejazi. Investigation of Buoyant Parameters of  $k-\varepsilon$  Turbulence Model in Gravity Stratified Flows. World Academy of Science, Engineering and Technology 55 (2009).
128. J.W. Miles. On the stability of heterogeneous shear flows. Journal Fluid Mechanics 10 (1961) 496-508.
129. H.D. Abarbanel, D.D. Holm, J.E. Marsden, T. Ratiu. Richardson Number Criterion for the Nonlinear Stability of Three-Dimensional Stratified Flow. Physical Review Letters 52 (1984) 2352-2355.
130. I.P.D. De Silva, A. Brandt, L.J. Montenegro, H.J.S. Fernando. Gradient Richardson number measurements in a stratified shear layer. Dynamics of Atmospheres and Oceans 30 (1999) 47-63.
131. P. Van Gastel, J.L. Pelegrí. Estimates of gradient Richardson numbers from vertically smoothed data in the Gulf Stream region. Scientia Marina 68 (4) (2004) 459-482.
132. Paranjape. S, Fehlmann. M, Kapulla, R. et al., 2016. OECD/NEA HYMERES project: PANDA Test HP5\_3 Quick-Look Report. Paul Scherrer Institute, (report restricted to project participants).
133. Cha. J.H, et al., 2017. The effect of the Reynolds number on the velocity and temperature distributions of a turbulent condensing jet. International Journal of Heat and Mass Transfer, 67, 125-132.
134. Benoit. C.R, 2008. Environmental Fluid Mechanics, Chapter 9: Turbulent Jets, Wiley-Blackwell.
135. Mignot G. R. Kapulla, S. Paranjape, R. Zboray, M. Fehlmann, W. Bissels, S. Sutter, D. Paladino, OECD/NEA HYMERES project: PANDA test facility description and geometrical specifications, HYMERES-P-13-03, 2013.
136. Wang, X., Gallego-Marcos, I., Grishchenko, D., Kudinov, P. 2019. Post-test calibration of the Effective Momentum Source (EMS) model for steam injection through multi-hole spargers. *NURETH-18*. Portland, USA, 6176-6189.
137. Wang, X., Gallego-Marcos, I., Grishchenko, D., Kudinov, P. 2019. Pre-test analysis for HYMERES-2 PANDA tests series for steam injection into pool through spargers., *NURETH 18*, Portland, USA, 6190–6203.
138. Kudinov, P., Wang, X., Grishchenko, D., Puustinen, M., Räsänen, A., Kotro, E., Tielinen, K., Pättikangas, T., Silde, A. 2020. Thermal Hydraulic Phenomena of the Suppression Pool. NKS-THEOS Report, NKS-439.
139. Puustinen, M., Pyy, L., Laine, J., Räsänen, A. 2017. Sparger Tests in PPOOLEX on the Behaviour of Thermocline. Nordic Nuclear Safety Research NKS-382.
140. Wang, X., Grishchenko, D, Kudinov, P. 2020. Development of Effective Momentum Model for Steam Injection Through Multi-Hole Spargers Using a Condensation Region Approach. *ICONE-2020*. Virtual, Online. August 4–5, V001T03A025. ASME.
141. Wang, X., Grishchenko, D, Kudinov, P. 2021. Development of Effective Momentum Model for Steam Injection Through Multi-Hole Spargers: Unit Cell Model. *ICONE-28*. Virtual, Online. August 4–6
142. [https://www.cfd-online.com/Forums/fluent/228201-boundary\\_heat\\_flux-f-t.html](https://www.cfd-online.com/Forums/fluent/228201-boundary_heat_flux-f-t.html)
143. Menter, F. R., Lechner. R., Ansys German GmbH., et al., 2020. Best Practice: Generalized  $k - \omega$  Two-Equation Turbulence Model in Ansys CFD (GEKO). Technical Report.
144. Ghahremanian, S., Moshfegh, B. 2014. Evaluation of RANS models in predicting low reynolds, free, turbulent round jet. Journal of Fluids Engineering, Transactions of the ASME, 136(1), 1–13.

## **Appendix B**

### **SEF-POOL tests on jet entrainment**



Technical Report  
LUT University  
Nuclear Engineering

**SPASET 1/2020 (D1.2.1)**

**SEF-POOL tests on jet entrainment**

*Markku Puustinen, Antti Räsänen,  
Eetu Kotro, Kimmo Tielinen, Lauri Pyy*



Lappeenranta-Lahti University of Technology LUT  
School of Energy Systems  
Nuclear Engineering  
P.O. Box 20, FIN-53851 LAPPEENRANTA, FINLAND  
Phone +358 294 462 111

Lappeenranta, 3.3.2021

<b>Research organization and address</b> LUT University School of Energy Systems Nuclear Engineering P.O. Box 20 FIN-53851 LAPPEENRANTA, FINLAND <b>Project manager</b>  Markku Puustinen  <b>Diary code</b> 360/322/2018	<b>Customer</b> VYR / SAFIR2022 NKS  <b>Contact person</b> Jari Hämäläinen (SAFIR2022) Ari-Pekka Leppänen (NKS)  <b>Order reference</b> Drno SAFIR 19/2020				
<b>Project title and reference code</b>  SAFIR2022-SPASET	<table> <tr> <th>Report identification &amp; Pages</th><th>Date</th></tr> <tr> <td>SPASET 1/2020 (D1.2.1) 33 p. + app. 3+1 p.</td><td>3.3.2021</td></tr> </table>	Report identification & Pages	Date	SPASET 1/2020 (D1.2.1) 33 p. + app. 3+1 p.	3.3.2021
Report identification & Pages	Date				
SPASET 1/2020 (D1.2.1) 33 p. + app. 3+1 p.	3.3.2021				

**Report title and author(s)**

SEF-POOL TESTS ON JET ENTRAINMENT

Markku Puustinen, Antti Räsänen, Eetu Kotro, Kimmo Tielinen, Lauri Pyy

**Summary**

The main goal of the SEF-POOL tests in 2020 was to provide data of the characteristics of small-scale phenomena, which affect the effective heat and momentum sources in case of steam injection through a sparger into a sub-cooled pool of water. This information will then be used in the validation of the simplified EHS/EMS models by KTH. Furthermore, the SEF-POOL tests support the validation effort of the DCC and interfacial area models of CFD codes for steam injection through spargers at VTT and LUT. Particular interest in the 2020 tests was in capturing good quality high-speed camera stereo recordings of the steam jet behaviour and jet entrainment visualized with the help of air bubbles injected into the pool.

Six steam injection tests were performed in the SEF-POOL facility in 2020. In addition, two water injection tests were performed. The main varied parameter was the mass flux of injected steam. The possible effect of multiple injection holes was also studied by using a three-hole plate in some of the tests. The water injection tests were done in order to check the operation of the air bubble generator and to find suitable camera imaging parameters and lighting conditions so that KTH can effectively use their in-house tools in the analysis of the recordings for tracking the movement of the air bubbles and thus ultimately assess the liquid velocity and the amount of jet entrainment.

Steam injection with the same steam mass flux through a three-hole plate seemed to produce slightly larger force measurement values than injection through a single-hole plate. The most important outcome of the 2020 tests was the successful refining of the air bubble generator configuration and the high-speed camera set-up.

**Distribution**

Members of the SAFIR2022 Reference Group 4

A-P. Leppänen (NKS), P. Kudinov (KTH), W. Villanueva (KTH), J. Hämäläinen (VTT), V. Suolanen (VTT), T. Pättikangas (VTT), I. Karppinen (VTT), S. Hillberg (VTT)

**Principal author or Project manager**

Markku Puustinen  
Senior Research Scientist

**Approved by**

Heikki Purhonen  
Research Director

**Reviewed by**

Joonas Telkkä  
Project Researcher

**Availability statement**

SAFIR2022 limitations

## Acknowledgement

NKS conveys its gratitude to all organizations and persons who by means of financial support or contributions in kind have made the work presented in this report possible.

## Disclaimer

The views expressed in this document remain the responsibility of the author(s) and do not necessarily reflect those of NKS. In particular, neither NKS nor any other organisation or body supporting NKS activities can be held responsible for the material presented in this report.

## **PREFACE**

Tests done in the Separate Effect Facility (SEF-POOL) have been planned together by Kungliga Tekniska Högskolan (KTH) and the Nuclear Engineering research group at Lappeenranta-Lahti University of Technology LUT (LUT University). The work has been performed under the Finnish Research Programme on Nuclear Power Plant Safety 2019–2022 (SAFIR2022) in the SPASET project. Financial support for the work has been provided by the National Nuclear Waste Management Fund (VYR), Nordic Nuclear Safety Research (NKS) and LUT.

# CONTENTS

<b>NOMENCLATURE .....</b>	<b>6</b>
<b>1 INTRODUCTION.....</b>	<b>7</b>
<b>2 EMS/EHS MODELS AND EFFECTIVE MOMENTUM .....</b>	<b>9</b>
<b>3 SEF-POOL FACILITY .....</b>	<b>10</b>
3.1 GENERAL.....	10
3.2 CONDENSATION POOL .....	11
3.3 SPARGER SYSTEM .....	11
3.4 BUBBLE GENERATION SYSTEM .....	11
3.5 FORCE MEASUREMENT .....	12
3.6 OTHER MEASUREMENTS .....	12
3.7 DATA ACQUISITION .....	13
3.8 CAMERA SYSTEM SET-UP FOR 2020 TESTS .....	13
<b>4 SEF-POOL TESTS .....</b>	<b>20</b>
4.1 SINGLE-HOLE VS. MULTI-HOLE TESTS .....	23
4.2 EFFECT OF POOL TEMPERATURE ON BUBBLE SIZE .....	25
4.3 WATER INJECTION TESTS.....	26
<b>5 CONCLUSIONS .....</b>	<b>30</b>
<b>REFERENCES .....</b>	<b>31</b>
<b>APPENDIX A: TEST RIG DRAWINGS</b>	
<b>APPENDIX B: BASIC INSTRUMENTATION</b>	

## NOMENCLATURE

### Symbols

$A$	area
$\dot{m}$	mass flow rate
$M_{\text{eff}}$	effective momentum
$M_s$	steam momentum
$\rho$	density

### Abbreviations

BWR	Boiling Water Reactor
CFD	Computational Fluid Dynamics
DCC	Direct Contact Condensation
EHS	Effective Heat Source
EMS	Effective Momentum Source
INSTAB	Couplings and INSTABilities in Reactor Systems Project
KTH	Kungliga Tekniska Högskolan
LOCA	Loss-of-coolant accident
LUT	Lappeenranta-Lahti University of Technology LUT, LUT University
NKS	Nordic Nuclear Safety Research
P	Pressure measurement
PACTEL	PArallel Channel TESt Loop
PC	Polycarbonate
PPOOLEX	Pressurized Condensation POOL EXperiments Test Facility
SAFIR	SAfety of Nuclear Power Plants - Finnish National Research Programme
SEF-POOL	SEparate Effect Test Facility
SPASET	SParger SEparate Effect Tests Project
SRV	Safety Relief Valve
T	Temperature measurement
TC	ThermoCouple
VTT	Technical Research Centre of Finland Ltd
VYR	National Nuclear Waste Management Fund

# 1 INTRODUCTION

Steam injection through spargers induces heat, momentum and mass sources that depend on the steam injection conditions and can result in thermal stratification or mixing of the suppression pool. The development of thermal stratification in the suppression pool is of safety concern since it reduces the steam condensation capacity of the pool, increases the pool surface temperature and thus leads to higher containment pressures, compared with completely mixed pool conditions.

Prediction of thermal stratification and mixing induced by steam injection into a sub-cooled pool with computational fluid dynamics (CFD) codes is time consuming and requires lots of computational capacity because the associated direct-contact condensation (DCC) phenomenon needs to be solved. The simplified effective heat source (EHS) and effective momentum source (EMS) models for simulation of steam injection into a pool filled with sub-cooled water, proposed by KTH, would reduce the needed computational capacity [1, 2]. The models have been implemented in the GOTHIC code and validated against the PPOOLEX experiments with blowdown pipes done at LUT University (LUT) under the SAFIR2018/INSTAB project [3, 4]. These semi-empirical effective heat and momentum source correlations have already been successfully used at KTH to model a full-scale Nordic BWR containment and suppression pool behaviour during a loss-of-coolant accident (LOCA) with GOTHIC 8.1 [5]. The EHS/EMS models can be used in any thermal-hydraulic code, which currently cannot reliably model direct contact condensation phenomena.

The concepts of the EHS/EMS models are being extended to the condensation regimes, particularly the oscillatory bubble and oscillatory cone jet regime, appearing in safety relief valve (SRV) spargers. The oscillatory bubble and oscillatory cone jet regimes are relevant for BWR plant conditions when spargers inject steam at mass fluxes between 75–300 kg/(m<sup>2</sup>s) [6]. A validation effort has been carried out against the PANDA and PPOOLEX experiments done with a model of a SRV sparger [7]. This validation effort has shown that the injection angle, total momentum, and momentum profile have a large effect on the pool behaviour [8]. Due to the uncertainty on these parameters, a separate effect test facility named SEF-POOL has been designed at LUT in collaboration with KTH to measure/define the effective momentum and reduce the uncertainty of the simulations. Effective momentum induced by steam injection through the sparger can be measured directly for different condensation regimes with the help of force sensors. A high-speed camera system will allow recordings of the condensation regimes and collapsing bubbles. With high-frequency pressure measurements, the detachment and collapse frequency of the bubbles will be obtained.

LUT has performed OpenFOAM calculations of selected SEF-POOL sparger tests with several different simulation models. 2D-axisymmetric simulations with different grids of the SEF-INF2 test are reported in [9]. The calculated total DCC rate differed somewhat from the measured value and a longer simulated transient is needed to assess the validity of the DCC and interfacial area models in sparger cases. The results of the 2D and 3D simulations done in 2020 are presented in [10].

VTT has developed, improved and validated numerical simulation models of direct contact condensation for steam discharge through blowdown pipes on the basis of PPOOLEX experiments. In 2018, VTT tested the suitability of these CFD models for direct contact condensation phenomenon associated with a sparger operation. A simulation model based on the LUT's separate effect test facility for sparger studies was developed and a selected test case was calculated [11].

The SEF-POOL facility was constructed at LUT and a series of preliminary and characterizing tests were conducted with the facility in autumn 2017. The first tests with the facility revealed that some modifications for the design are needed in order to be able to define the effective momentum. After these modifications were implemented, more preliminary tests were run at the end of the year [12]. The test campaign continued in 2018, first with the same facility design as at the end of 2017 and later in spring with a design that had been changed considerably by adding a second support arm for an independent propulsion volume to allow a direct measurement of the effective momentum [13].

In 2019, the SEF-POOL tests concentrated on the effect of chamfer at the injection holes, regime transition and high steam mass fluxes [14]. The basic design of the SEF-POOL facility remained unchanged in the 2019 tests. However, a part of the tests was done with the propulsion volume in use and part without it. Different options for the high-speed camera arrangement were tested during the test campaign in 2019. Particularly, stereo imaging was tried in couple of last tests.

For the SEF-POOL tests in 2020, many improvements were made for the imaging system. The biggest difference between the previous SEF tests and the tests performed in 2020 was the change to stereo viewing perspective, i.e. both high-speed cameras were in angle towards the pool. In addition, the calibration procedure was completely changed. The main objective in the 2020 tests was to study jet entrainment in low and high Mach number cases with the help of high-speed imaging and air bubble generation and tracing. The test parameters were decided together with KTH.

Experiments in the SEF-POOL facility at LUT will provide necessary data to understand which characteristics of small-scale phenomena affect the effective heat and momentum sources and will thus help in the validation of the simplified EHS/EMS models. Furthermore, the SEF-POOL tests support the validation effort of the DCC and interfacial area models of CFD codes for steam injection through spargers as well as implementation of the EHS/EMS models to the Apros system code. As a result of this validation effort of the simulation tools, capabilities for a realistic evaluation of the steam condensation capacity of the suppression pool in different thermal stratification scenarios will improve.

This report summarizes the SEF-POOL tests done in 2020. The concept behind the EMS/EHS models is first shortly discussed in chapter 2. Next, the geometry of the SEF-POOL facility, the installed instrumentation and the high-speed camera set-up are introduced in chapter 3. The main observations from the tests done with the SEF-POOL facility in 2020 are then presented in chapter 4. Conclusions are drawn in chapter 5. Evaluation of the amount of jet entrainment is performed by researchers at KTH as they have developed in-house tools for the purpose. Analysis results of the SEF-POOL tests done in 2020 by KTH can be found from a NKS research report to be published in 2021.



## 2 EMS/EHS MODELS AND EFFECTIVE MOMENTUM

The general idea behind the EMS/EHS models is that, to predict the global pool behaviour, the small-scale phenomena occurring at the level of direct contact condensation does not need to be resolved [1, 2]. Instead, it is the time averaged heat and momentum transferred from the steam to the large-scale pool circulation that needs to be provided. The premise behind this idea is that the averaged effects of the small-scale direct contact condensation phenomena determine the integral heat and momentum sources, which in turn determine the large-scale pool circulation and temperature distribution. With this approach, computational efficiency can be improved considerably, when large domains such as pressure suppression pools of BWRs and long-term transients, are modelled. Particularly, the modelling of steam jets at the injection holes of a sparger requires very fine meshes and short time steps. Furthermore, instability issues will arise if we attempt to resolve the direct contact condensation of such jets.

In the EMS/EHS model approach, simplified conservation equations of mass, momentum and energy in a control volume, where the steam jets are expected to condense completely, are solved and a mean (time-averaged) condensate flow at the control volume boundary is defined. Steam momentum ( $M_s$ ) is defined as the momentum of steam at the injection hole (before condensing) and can be expressed by  $\dot{m}^2/(\rho A)$ , where  $\dot{m}$  is steam the mass flow rate,  $\rho$  the steam density and  $A$  the cross-sectional flow area. Effective momentum ( $M_{\text{eff}}$ ) is the amount of momentum transferred from the steam to the liquid. These two momentums are not equal in two-phase flow (for example: chugging). It is the  $M_{\text{eff}}$  term that needs to be known in the EMS model approach. Separate-effect tests in the SEF-POOL facility allow to measure and visualize directly the difference between  $M_s$  and  $M_{\text{eff}}$ . The tests help to map the effective momentum of different condensation regimes and will thus provide closures for the EMS model development for spargers by KTH.

The focus in the test series with the SEF-POOL facility in 2018 was to determine the effect of the injection hole diameter, the number of holes, the pool temperature, the steam mass flux, etc., on the effective momentum [13]. Furthermore, the bubble radius and the velocity as well as the detachment and collapse frequencies of the bubbles could be obtained with the help of high-frequency measurements and high-speed video recordings. However, important variables affecting the effective momentum magnitude in full-scale plant needed to be further analysed in order to provide closures for the EMS model development for spargers. Tests in SEF-POOL in 2019 thus concentrated on the effect of chamfer at the injection holes, regime transition and high steam mass fluxes [14].

The entrainment velocity for the jet created by the steam injection is a crucial parameter for the implementation of the EMS model. It is needed in order to impose proper boundary conditions in modelling of the large pool response to steam injection. Entrainment defines such characteristics of the jet as the initial turbulent kinetic energy, the decay of the maximum velocity and the velocity profile in the cross-section of the jet. These have been shown as important factors in predicting large pool behaviour. Stereoscopic high-speed imaging and bubble (particle) tracking were applied in the 2020 SEF-POOL tests for assessing the liquid velocity.

### 3 SEF-POOL FACILITY

The reference system for the SEF-POOL facility is a SRV sparger pipe of a BWR plant. Hence, the SEF-POOL facility is designed in such a way that discharge of steam through the injection holes at the sparger lower end into sub-cooled pool water can be simulated representatively.

The goal in the tests with the facility is to define the effective momentum for a given steam condensation regime, particularly for the oscillatory bubble regime. For this purpose, the design of the test facility is such that the effective momentum can be directly measured with a force sensor or it can be calculated on the basis of measured steam momentum. Because the focus is on measuring the separate effects of steam injection through the sparger holes and not on the stratification/mixing phenomena, the water pool itself, where the sparger is submerged, is relatively small in volume.

For helping to recognize different flow regimes and for obtaining the bubble diameter as a function of time, the test facility allows high-speed video recordings of the DCC of steam. In addition, a high-frequency pressure measurement helps to obtain the detachment and collapse frequencies of the bubbles. Steam needed in the tests is generated with the nearby PACTEL test facility [15]. The design principles, geometry and installed instrumentation of the SEF-POOL facility are presented in more detail in reference [16]. Appendix A presents some drawings on the facility geometry and Appendix B the locations of the measurements. The flexibility of the facility provides an appropriate possibility to extend the facility set-up according to the future research needs.

#### 3.1 GENERAL

The main parts of the SEF-POOL facility are the sparger piping and the condensation pool. The sparger piping is connected with a pipeline to the PACTEL test facility, which supplies the steam needed in the tests. The sparger pipe is pivoted on a vertical axis with low friction bearings in order to allow the direct force measurement. The lower end of the sparger pipe mounts a flow plate with injection holes. Steam is discharged through the injection holes and it condenses in the pool.

In front of the flow plate there is a polycarbonate (PC) pipe, which is independent from the sparger piping and it has its own support arm, which is allowed to rotate around its axis. The purpose of the PC pipe is to act as a propulsion volume and to create a parallel flow pattern so that the amount of momentum transferred from the steam to the liquid at the outlet of the PC pipe can be estimated. The condensed flow is guided through the PC pipe to impinge on the disk stack. The disk stack is designed to maximize the amount of flow driven radially outwards from the PC pipe. Backflow in the axial direction would induce an artificial increase of the force measured at the PC pipe. Axial distance between the disks is 5 mm. The steam force at the injection hole and the liquid force carried by the condensate liquid (effective momentum) can thus be measured independently by using force sensors connected to the fixed supports in the floor. The configuration of the SEF-POOL facility with the propulsion volume is shown in Figure 1. **Note: The tests in 2020 were carried out without the PC pipe, i.e. with only the sparger piping submerged in the pool and with a single force measurement.**

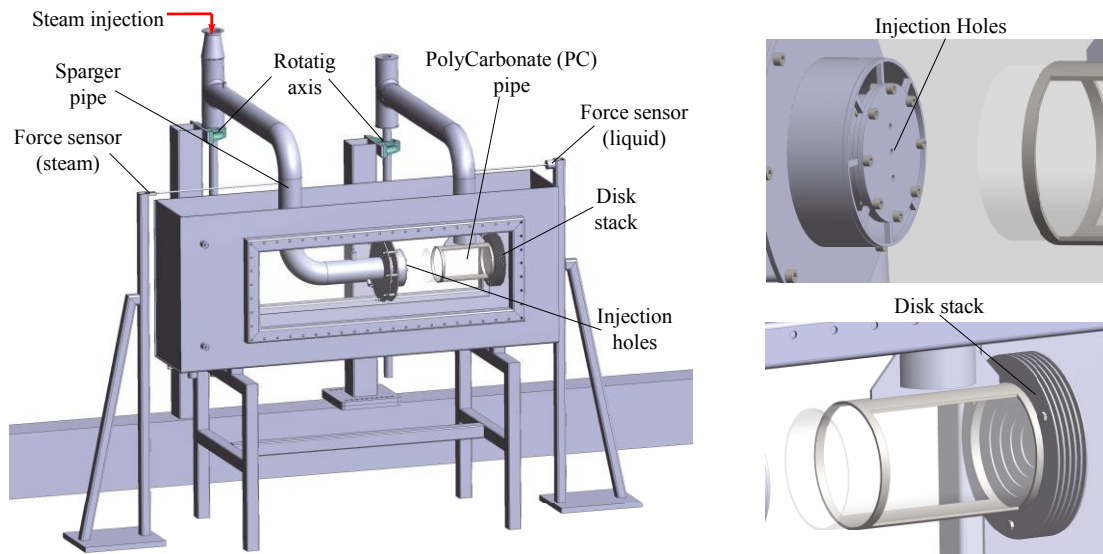


*Figure 1. General view of the SEF-POOL facility configuration where the propulsion volume (PC pipe) is independent and attached to its own support arm.*

### 3.2 CONDENSATION POOL

The condensation pool is made of stainless steel. It is 1500 mm long, 300 mm wide and 600 mm tall. The pool is open on top and it is uninsulated. Windows on both sides are 1000 mm wide and 300 mm tall. The pool is mounted on a support made of 50x50 box section. A cover (lid) can be installed to the top to prevent any spill over or splashing of water during the tests. As the pool is open on top, atmospheric pressure will prevail in the pool in all the tests. Figure 1 in Appendix A presents the condensation pool in more detail.

### 3.3 SPARGER SYSTEM

The sparger piping is made of sections of DN80 stainless steel pipes and it is insulated with 13 mm thick AP Armaflex® XG flexible elastomeric thermal insulation. Dimensions of the piping are shown in Figure 2 in Appendix A. A perforated flow plate for steam injection is mounted to the end of the sparger pipe. A set of plates with different diameter injection holes and pitch have been manufactured.

The independent PC pipe is 250 mm long and its inner diameter is ~127 mm. The distance between the injection plate and the PC pipe is 100 mm. A disk stack at the outlet of the PC pipe directs the flow radially outwards from the PC pipe. **Note: The PC pipe was not used in the 2020 tests.**

### 3.4 BUBBLE GENERATION SYSTEM

An in-house air bubble injection system was built for generating bubbles into the pool to be tracked with the help of the high-speed camera system in order to assess jet entrainment. The system utilized the compressed air network of the laboratory. Eight individual bubble injectors (syringes) were used in the first tests. The system was

upgraded to a 32-injector system during the test series in 2020. Figure 2 shows the design of the first version of the system.

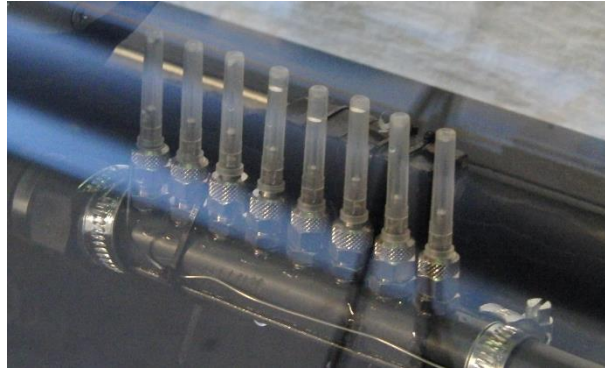


*Figure 2. Air bubble generator system with eight syringes.*

### 3.5 FORCE MEASUREMENT

The direct force measurements are arranged with load cells. They are located outside the condensation pool and are attached to support poles made of 50x50 mm box section bolted to the floor of the laboratory. The first load cell is at that end of the condensation pool, where the sparger piping is submerged. Another cell is at the end of the pool, where the support arm of the PC pipe is installed. Force is transmitted from the sparger piping and the support arm to the sensors via thin horizontal rods.

When steam is injected through the sparger piping and the flow plate, momentum is created, and as a result the sparger piping tends to rotate around the pivot bearing. Momentum transferred to the pool liquid tends to rotate the support arm of the PC pipe. These rotating movements cause compression to the load cells and the generated forces can be thus measured. Because the force measurement compression distances are almost non-existent, the angle of the sparger piping or the angle of the support arm compared to the condensation pool does not change during the tests. **Note: The PC pipe and the force measurement connected to it was not used in the 2020 tests.**

### 3.6 OTHER MEASUREMENTS

Two pressure transducers for steam pressure measurement are mounted in the sparger piping. One is near the steam inlet point and the other one is 140 mm upstream from the perforated flow plate. The measurement range of each transducer is 0.1-1.0 MPa.

A kHz-range pressure sensor is used for capturing the detachment and collapse frequencies of the steam bubbles. It is fixed to a vertical support structure laying at the pool bottom and it can be positioned in front of the flow plate with a desired distance from the plate. The range of the sensor can be up to 0.2 MPa, 1 MPa or 2 MPa depending on the test in question (**Note: this sensor was not functioning properly and it was removed together with its support structure from the pool for the last tests in 2020**). An additional pressure sensor with the range of 0-0.2 MPa is attached to the pool wall near the pool bottom.

Temperatures are measured with calibrated k-type thermocouples (TC). The temperature of incoming steam is measured with one TC near the inlet point at the same location as the pressure. The steam temperature is also measured in the sparger piping at about 190 mm before the perforated flow plate. In the pool side, one TC is positioned inside the PC pipe, one at the inlet of the PC pipe and one at the outlet of the PC pipe close to the disk stack. **(Note: Because the PC pipe was not used in the 2020 tests, the TCs (T2602, T2603 and T2604) attached to it were not used. However, there was one TC (T2607) in the pool, which was used for measuring water temperature along the flow path of the steam jet at about 300 mm distance from the injection plate and about 50 mm from the pool bottom.)** In addition, the pool water temperature is also measured with two TCs (T2605 and T2606) attached to the pool wall on different elevations.

Water level in the condensation pool is measured with a Yokogawa® differential pressure transducer. The transducer is mounted to the base of the pool. Water level is calculated from the differential pressure reading with the help of the liquid density. Temperature measurements in the pool are used to define the liquid density. Steam flow rate is measured with a vortex flow meter in the steam line.

Figure 1 in Appendix B shows the locations of the measurements. The type, frequency and range of the different sensors can be found in Table 1 at the end of Appendix B.

### 3.7 DATA ACQUISITION

The National Instruments PXIe PC-driven measurement system is used for data acquisition. The system enables high-speed multi-channel measurements. The maximum recording capacity depends on the number of measurements and is in the region of mega samples per second. The measurement software is LabView 2015.

### 3.8 CAMERA SYSTEM SET-UP FOR 2020 TESTS

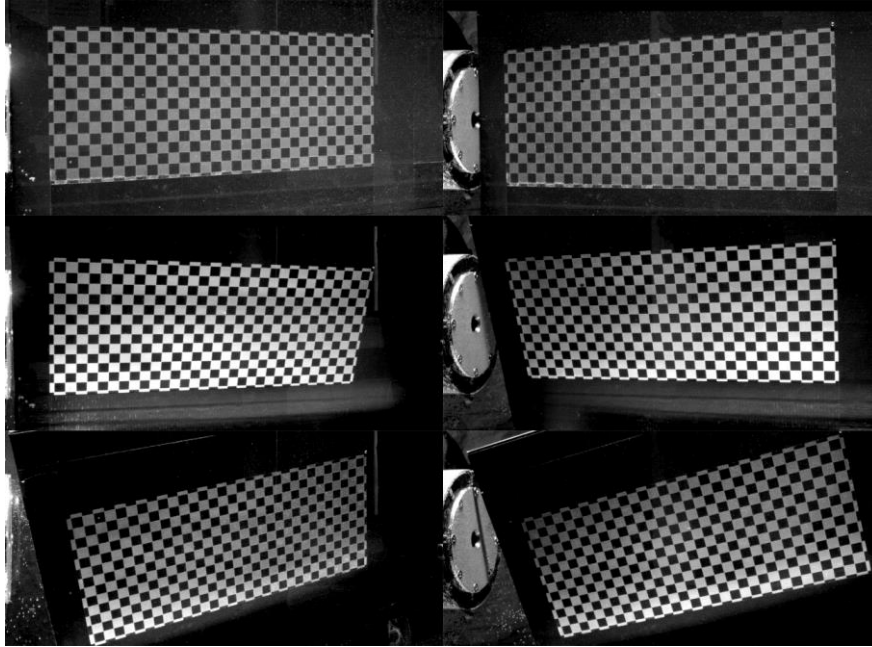
Windows on the both side walls of the condensation pool allow the capture of the DCC phenomenon of steam with a high-speed video system. Different flow regimes can be recognized and bubble diameters obtained with the help of the system.

The high-speed camera system consists of two monochromatic Phantom Miro M310 cameras. The maximum resolution is 1280x800 px, but in practise the picture area is cropped in order to increase the maximum amount of the images the 12 GB internal memory can hold, thus increasing the total time of the recordings.

For the tests conducted in 2020 in the SEF-POOL facility, many improvements were made for the imaging system in general. The biggest difference between the previous SEF tests and the tests performed in 2020 was the change to stereo viewing perspective, i.e. both high-speed cameras were in angle towards the pool. In addition, the calibration procedure was completely changed. Previously, the calibration board was positioned in the centreline of the steam jet, and calibration images were taken for the camera(s). From the SEF-S27 test onwards, the calibration plate was also placed at different distances in front and back of the jet outlet towards the cameras. For the tests performed in 2020, a calibration video was used where the calibration plate was moved in different angles towards the cameras. The video was captured with the framerate of 24 fps and could in

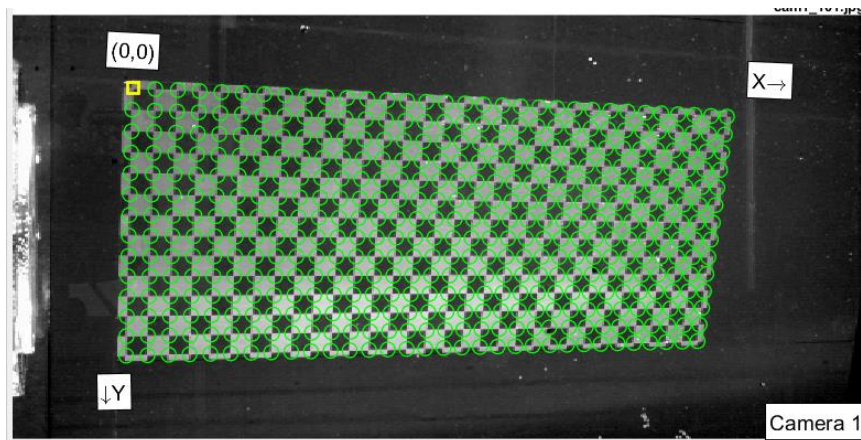


theory consist of thousands of calibration images (depending on the length of the calibration video) instead of static positions and a single image pair per position as was the case before. Example images from the calibration procedure are shown in Figure 3.



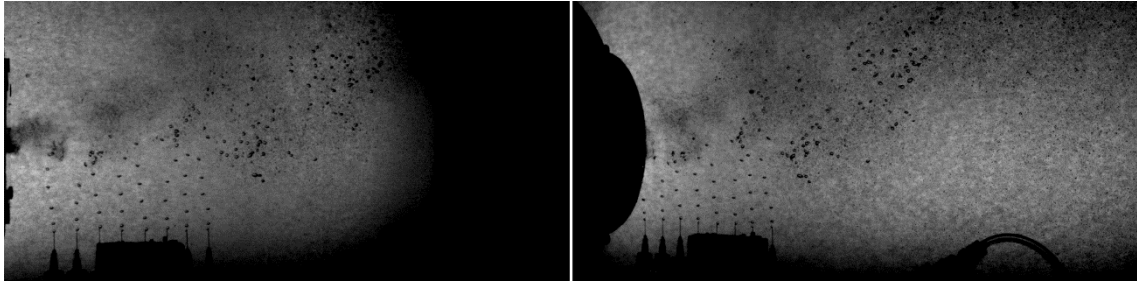
*Figure 3. Examples of calibration plate positions seen from left and right camera from initial calibration used in SEF-S29, SEF-S30 and SEF-S31 tests.*

Figure 3 presents three calibration image pairs chosen randomly from the calibration video. Image numbers from top to bottom are #0 (first image), #972 and #3455. For the tests SEF-S29, SEF-S30 and SEF-S31, the calibration plate was moved with a camera tripod in one static position. The calibration plate was partially taped in order to maximize the number of checkers visible in different angles and in every image of the video. For the calibration procedure to work, the same exact amount of checkers must be in every single image. An example of checker detection is presented Figure 4.



*Figure 4. Checker edge detection from calibration algorithm (MatLab) using in-house manufactured calibration plate.*

For the tests mentioned above, the image size in use was 1024 x 504 pixels. With the image acquisition rate of 6300 fps, this resulted in a video of 0.261 s, and the goal for the tests was to capture 10 individual video clips of the different pool and steam injection conditions. This is the maximum capacity of the Miro M310 high-speed cameras as the amount of RAM is 12 GB. An actual experiment image from the SEF-S29 test is presented in Figure 5.



*Figure 5. Experiment image from SEF-S29 (white line in the middle splits the left and right camera images).*

Eight individual bubble injectors were used in the tests for bubble tracking. The background lighting rig was updated for SEF-S29 with four additional LED panels with 2 x 160 W and 2 x 120 W in power making the total lighting power for the rig 720 W. In addition, a new transformer for the LEDs were acquired because in the previous tests in 2019, the backlight was flickering. This ensured constant lighting conditions. The back window of the pool was lined with normal parchment paper to diffuse the light. Before the SEF-S30 test, multiple new diffuser materials were tested for a smoother background illumination of the pool. An opaque glass was found to be the most suitable for this purpose and was installed on the backside of the pool. The new LED rig and the opaque diffuser glass window of the pool are presented in Figure 6.

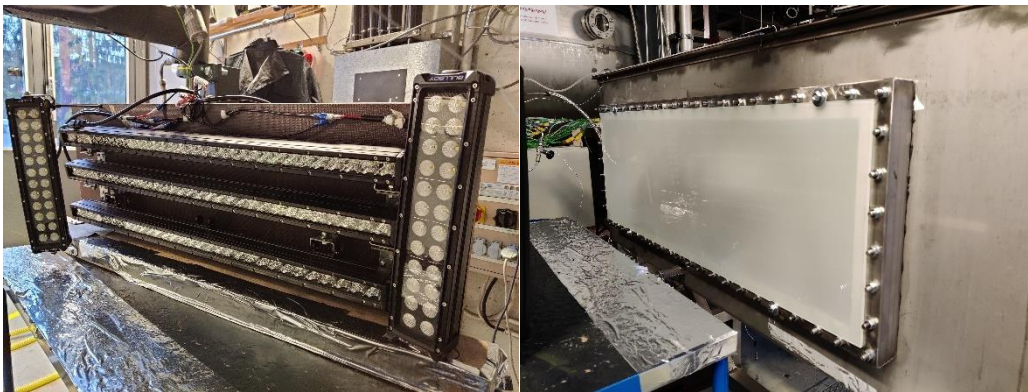


*Figure 6. Updated LED rig (top) and opaque diffuser glass of SEF-POOL (bottom).*

With these updates, the overall quality of the experiment images was enhanced. A comparison between the experiment images from SEF-S29 and SEF-S30 is presented in Figure 7.

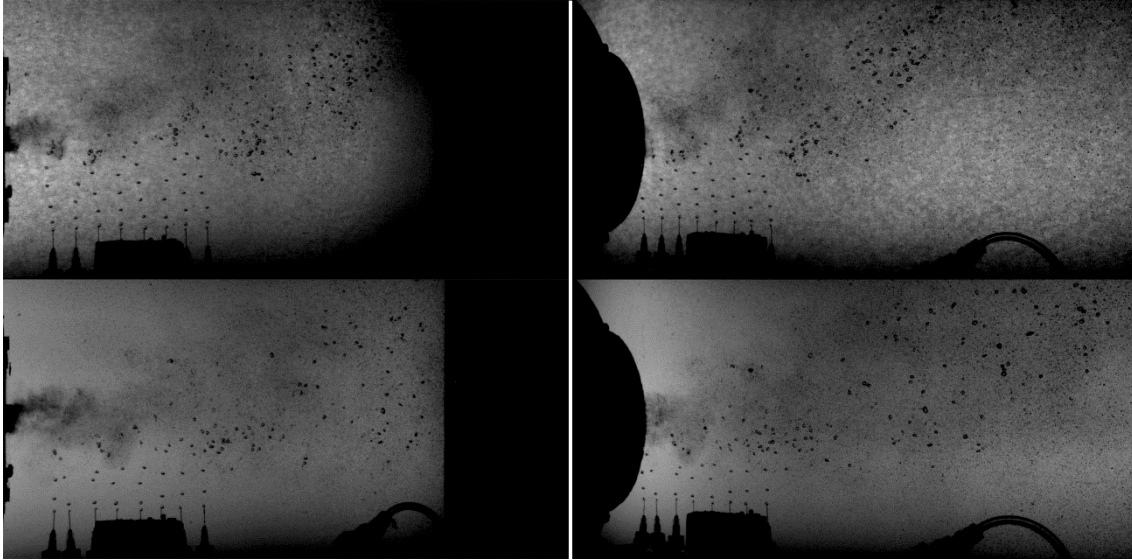


*Figure 7. Experiment image from SEF-S29 (top) vs. SEF-S30 (white line in the middle splits the left and right camera images).*

The straight edge (black area on the right) in the left camera image from SEF-S30 is the edge of the pool, which was not seen in SEF-S29 (and preceding tests) due to worse light diffusion. The background illumination is also drastically smoother with the new opaque glass.

Next calibration for the imaging system was done for the SEF-W7, SEF-S32 and SEF-S33 tests. The main difference between the prior and these tests was the image size, which was cropped to 768 x 504 pixels in order to achieve longer videos from the individual triggers. With this change, it was possible to capture 10 video clips with a duration of 0.348 s. The new image size also reduced the areas imaged that were not of interest, mainly the edge of the pool for the left camera. The calibration plate taping was changed in order to have checkers right next to the steam outlet. Due to the smaller image size, the calibration plate was further masked out with a tape in order to have all the checkers visible in different angles. Also, the calibration plate itself was moved freehandedly when capturing the calibration video. An example from the second calibration is presented in Figure 8.

For these tests, also a new bubble injector was manufactured in-house. The new bubble injector contained 32 individual syringes for bubble generation, of which all 32 were visible for the left camera and 29 for the right camera. The reason for the lesser amount of visible syringe heads for the right camera was the fact that moving the camera horizontally was not an option as the frame of the front pool window would have created visual obstruction and it was wanted that the angle for both cameras remain the same. The syringe needle size was smaller than before allowing smaller bubbles to be injected and tracked. An example experiment image is presented in Figure 9.



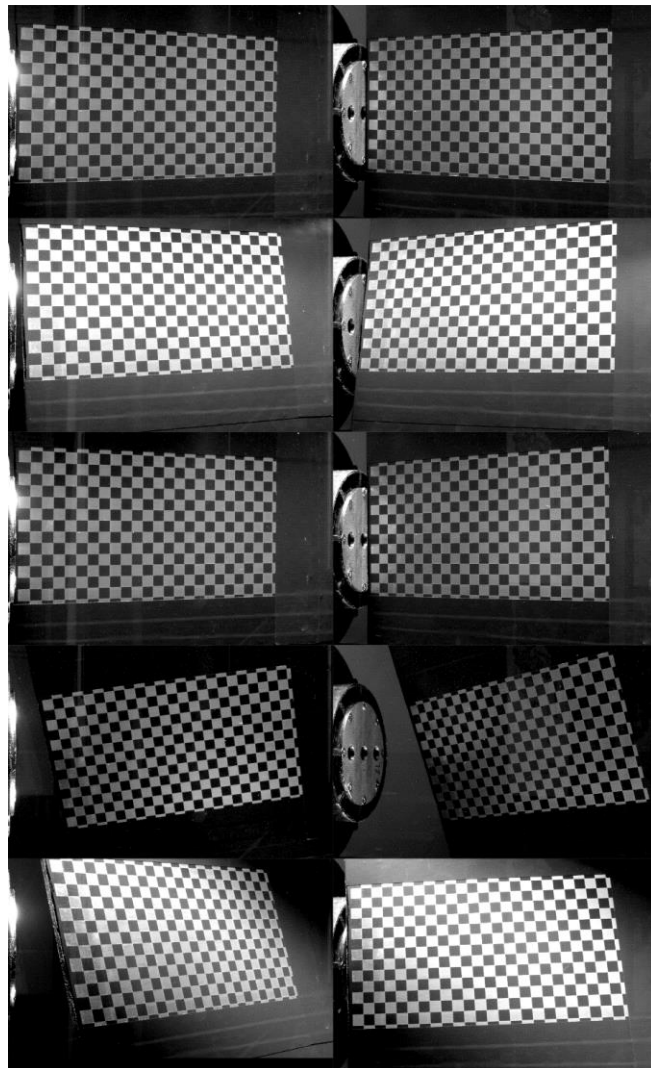


*Figure 8. Example images of second calibration set-up seen from left and right camera.*

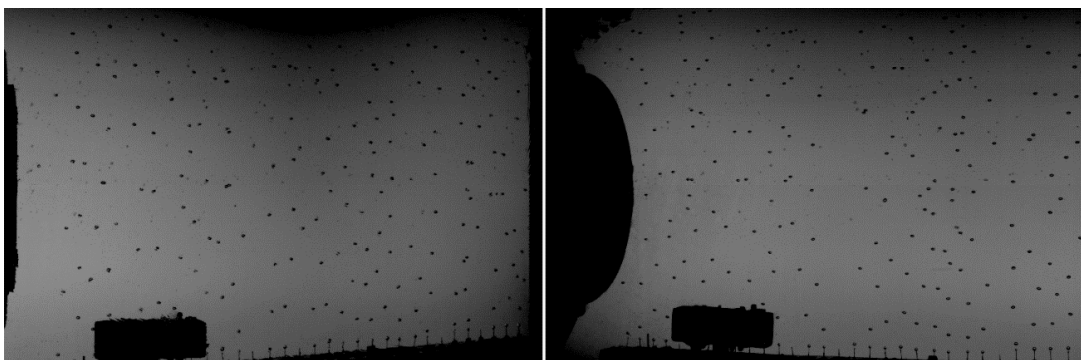


*Figure 9. Experiment image from SEF-S32.*

Figure 9 presented above has been recorded before the steam injection. Pool water is at 2 °C. The ice that was used for cooling the pool water can be seen in the right camera's

image on top left blocking the backlight. It was crucial to stretch out the bubble injector horizontally to the whole image area and to image as many syringe heads as possible in the bubble injector to further improve the bubble tracking.

For the final tests SEF-W8 and SEF-S34, some changes were made for the imaging system. This time, the lenses were changed to 50 mm ones. The image size was enlarged back to 1024 x 504 pixels for better pixels/mm resolution. The lens aperture was opened to the f-number of 11 to ensure that more light will be captured by the sensor. Opening the aperture of the lens will result in narrowing the depth-of-field of the image. A check-up of the depth-of-field was done in order to ensure that possible steam slugs would be in focus within the image plane.

In addition, the fast pressure transducer block was removed (can be seen in Figure 9 above behind the syringes next to steam outlet) and the bubble injector lowered out-of-image. Lowering of the syringe system was done to ensure that the bubbles would reach their terminal velocity caused by buoyancy before entering the entrainment of the steam jet. A separate test to check the terminal velocity was conducted before the tests as well. The image plane was lowered as well because for the bubble tracking the important information is more below the jet entrainment.

For SEF-W8, the calibration followed the procedure of prior tests (taping out the excess area of the calibration plate). Before conducting the SEF-S34 test, the calibration plate was cut into a smaller size instead of taping out the excess areas. By doing this the calibration plate could be moved with even more freedom. The calibration video was split into two parts where the first one was with angles within the image area and the second one with the calibration plate moved in parallel with the steam outlet. Example images of the calibration for SEF-S34 with a smaller plate are presented in Figure 10.

Note that the flow plate was changed after the calibration. The SEF-S34 test was also filmed with GoPro with 120 fps and Canon EOS 80D with 60 fps to capture the shaking of the steam outlet during the test. Especially towards the end of the test with higher pool water temperature, the steam outlet was shaking violently. GoPro and Canon were also used to capture the sound of the steam injection in different condensation regimes. The view for the Canon is presented in Figure 11. An experiment image from SEF-S34 is presented in Figure 12.

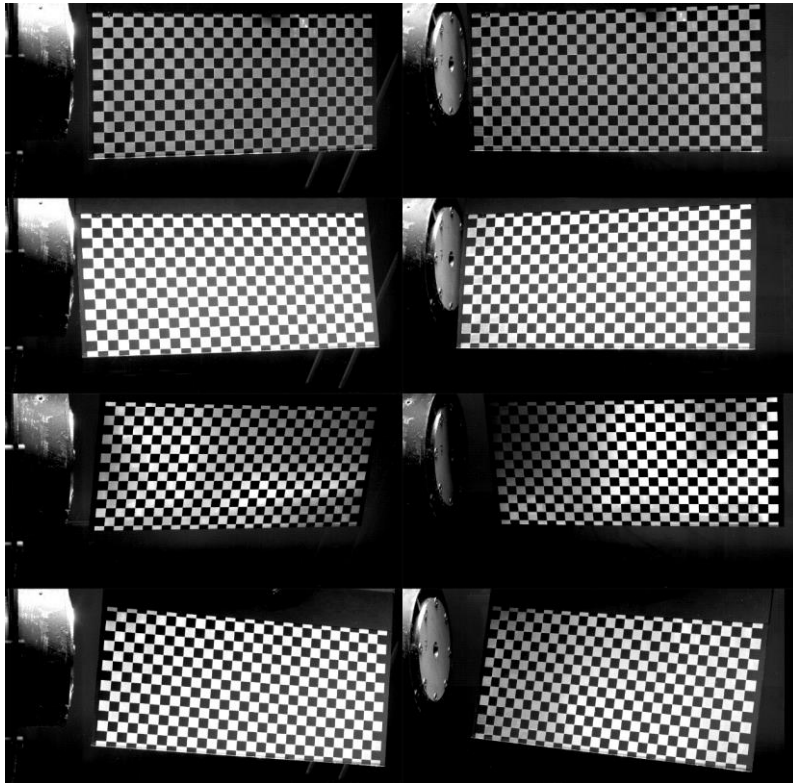


*Figure 10. Random calibration images with different plate positions for SEF-S34.*

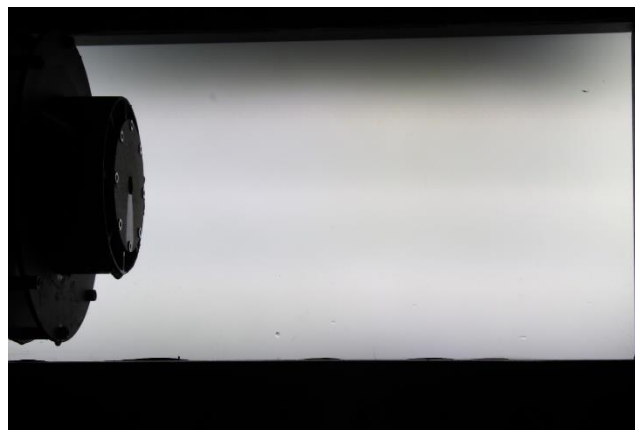


*Figure 11. The view for video captured with Canon EOS 80D.*

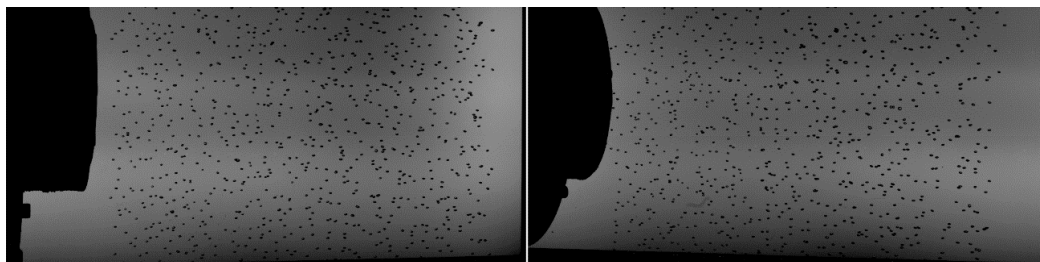


*Figure 12. Experiment image from SEF-S34 after steam injection was stopped.*

The pool water is at 94 °C in Figure 12 above. All the 32 steam injection syringes were visible for both cameras with the latest setup for SEF-W8 and SEF-S34 further improving the bubble tracking.

Table 1 summarizes the general imaging parameters used for the SEF-POOL tests performed in 2020.

*Table 1. General imaging parameters for SEF-POOL tests performed in 2020*

Test	Image acquisition rate	Image size	Lens focal length	Lens aperture, $f$	Video clips captured from experiment	Video clip duration	Camera angle towards the pool
SEF-S29	6300 fps	1024 x 504	24 mm	16	10	0.261 s	$\sim 17^\circ$
SEF-S30	6300 fps	1024 x 504	24 mm	16	10	0.261 s	$\sim 17^\circ$
SEF-S31	6300 fps	1024 x 504	24 mm	16	10	0.261 s	$\sim 17^\circ$
SEF-W7	6300 fps	768 x 504	24 mm	16	10	0.348 s	$\sim 17^\circ$
SEF-S32	6300 fps	768 x 504	24 mm	16	10	0.348 s	$\sim 17^\circ$
SEF-S33	6300 fps	768 x 504	24 mm	16	10	0.348 s	$\sim 17^\circ$
SEF-W8	6300 fps	1024 x 504	50 mm	11	10	0.261 s	$\sim 16^\circ$
SEF-S34	6300 fps	1024 x 504	50 mm	11	10	0.261 s	$\sim 16^\circ$

## 4 SEF-POOL TESTS

The main goal of the SEF-POOL tests in 2020 was to provide data of the characteristics of small-scale phenomena, which affect the effective heat and momentum sources. This information will then be used in the validation of the simplified EHS/EMS models by KTH. Furthermore, the SEF-POOL tests support the validation effort of the DCC and interfacial area models of the CFD codes for steam injection through spargers at VTT and LUT. Particular interest in the 2020 tests was in capturing good quality high-speed camera stereo recordings of the steam jet behaviour and jet entrainment visualized with the help of air bubbles injected into the pool.

The previous results from the SEF-POOL tests suggest that with respect to the effective momentum the difference between the single and multiple hole cases is small. Also, the effect of the injection hole diameter seems to be minor. The SEF-POOL tests in 2019 verified that the effect of the nozzle chamfer of the flow plate is also relatively small. On the other hand, it was found that there was a significant difference between the sonic and subsonic injection regimes. Furthermore, high subcooling of pool water didn't affect sonic jets, while it had an influence on the subsonic injection. The main varied parameter in the 2020 tests was chosen to be the mass flux of the injected steam. The possible effect of multiple injection holes was also studied further by using a three-hole plate in some of the tests.

For the most part the 2020 tests focused, however, on setting up and tuning the high-speed camera system so that KTH can effectively use their in-house tools in the analysis of the recordings for tracking the movement of the air bubbles and thus ultimately assess the liquid velocity and the amount of jet entrainment. The camera set-up, the lighting conditions and the air bubble generation system was improved along the test series according to the feedback received from KTH with adjustments made to them as described in chapter 3.8. It can be considered that all the tests preceding the last one were more or less rehearsals or pre-tests, and the last test then had the optimal arrangements and conditions for capturing good quality high-speed imaging.

A total of six steam injection tests were performed in the SEF-POOL facility in 2020. In addition, two water injection tests were performed. The main purpose of these water injection tests was to check the operation of the air bubble generator (without the disturbance of steam injection) and to find suitable camera imaging parameters and lighting conditions. All the test parameters and procedures were agreed with KTH.

The force generated by the steam injection and other parameters were measured during the tests. Based on this high-resolution measurement data, KTH will refine the semi-empirical correlations for the effective momentum and define the bubble collapsing frequency, radius, velocity, pressure gradient and heat transfer coefficients in more detail.

Table 2 lists the main parameters of the steam injection tests and Table 3 of the water injection tests done in 2020.

*Table 2. SEF-POOL steam injection tests in 2020*

Test	Steam flow rate [g/s]	Initial pool water level/temp [m/°C]	Flow plate	Steam temp. at sparger inlet [°C]	High speed video	Stereo imaging
SEF-S29	~15	0.45/1	1x16 mm	~103	6300 fps	yes
SEF-S30	~10	0.47/2	1x16 mm	~102	6300 fps	yes
SEF-S31	~27	0.44/3	1x16 mm	~109	6300 fps	yes
SEF-S32	~46	0.47/2	3x16 mm	~104	6300 fps	yes
SEF-S33	~31	0.44/5	3x16 mm	~102	6300 fps	yes
SEF-S34	~21-29	0.45/7	3x16 mm	~101	6300 fps	yes

*Table 3. SEF-POOL water injection tests in 2020*

Test	Water flow rate [kg/s]	Initial pool water level/temp [m/°C]	Flow plate	Temperature of injected water [°C]	High speed video	Stereo imaging
SEF-W7	0.25-1.75	0.44/12	1x16 mm	~12	6300 fps	yes
SEF-W8 Phase 1	0.25-0.55	0.46/67	1x16 mm	~53	6300 fps	yes
SEF-W8 Phase 2	0.25-0.60	0.48/17	1x16 mm	~17	6300 fps	yes



As a large part of the tests dealt with the modifications and adjustments of the camera set-up, it makes no sense to present the same measurement curves from all the tests here. The following chapters present only some selected results from the steam and water injection tests in 2020 and discuss the key observations based on those results.

Figure 13 presents a regime map for direct contact condensation developed by Chan and Lee [6]. The boundaries of various condensation modes on the flow regime map are established by two criteria: (a) the location of the steam region relative to the pipe exit and (b) the location at which steam bubbles detach from the source. The horizontal boundary (solid line from the left edge to the right edge) in Figure 2 shows whether the steam region is completely below the pipe exit or has expanded to encapsulate part of the pipe. The vertical boundaries indicate how steam is being released from the pipe exit.

The flow modes covered in the previous SEF-POOL steam injection tests are the oscillatory bubble regime, the oscillatory cone jet regime and partly the ellipsoidal jet regime. The oscillatory bubble and cone jet regimes are relevant for the BWR plant conditions when spargers inject at mass fluxes between 75–300 kg/m<sup>2</sup>s [6]. In the SEF-POOL tests in 2020, the steam mass flux varied between 35–134 kg/m<sup>2</sup>s placing the tests mainly in the oscillatory bubble regime on the map. In some of the tests (SEF-S30, SEF-S33, SEF-S34), the flow mode was at least partly external chug with detached bubble or external chug with encapsulating bubble depending on the pool water temperature.

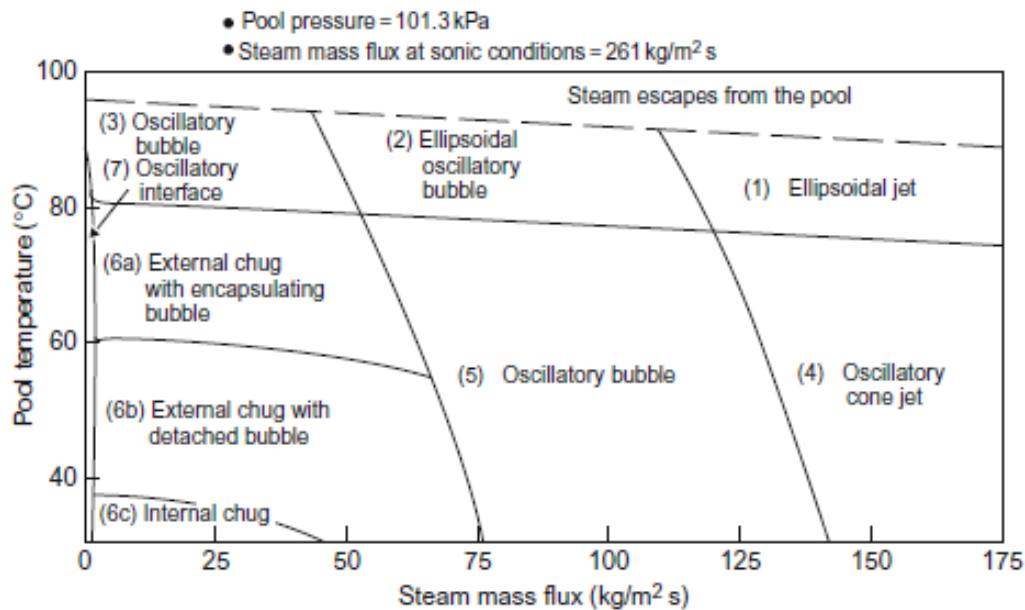


Figure 13. Condensation regime map for a sparger [6].

One goal of the tests in 2020 was to verify the validity of the EMS/EHS models in highly sub-cooled conditions. Therefore, during the preparations for the steam injection tests, a few kilograms of ice was put in the pool before filling it with water. The initial pool water temperature was thus between 1 °C and 7 °C (see Table 2).

In each steam injection test, the mass flow rate was first adjusted to the desired value and then it was kept constant for the rest of the test. Adjustment of the flow rate was challenging, especially with the small flow rates, and could take a few hundred seconds in some cases. The tests were continued until the pool water temperature was approaching 95 °C. Fast data (pressure, forces and video) was usually recorded from ten short sequences as the pool temperature increased. The high-speed video clips were recorded with the frame-rate of 6300 fps allowing a clip length of 0.261 s or 0.348 s depending on the used resolution.

The SEF-W7 water injection test was done with cold pool and injection water (~12 °C). In the SEF-W8 test, pre-heated pool water and warm injection water (phase 1) as well as cold pool and injection water (phase 2) were used. The exact temperature values can be found from Table 3 above. In the SEF-W7 test, several water injection flow steps at intervals of about 0.25 kg/s both in the ascending and descending direction were measured. The SEF-W8 test consists of two flow steps both in phase 1 and 2.

In some earlier facility configurations, there was a PC pipe attached directly to the injection plate or attached to a support arm in front of the plate a short distance away. This PC pipe was not used either in the steam injection or water injection tests in 2020. As a result, only one force measurement, the one connected to the steam piping, was used in the 2020 tests.

#### **4.1 SINGLE-HOLE VS. MULTI-HOLE TESTS**

Single-hole vs. multi-hole injection has been dealt slightly in the previous SEF-POOL tests and it has been found out that there is no noticeable difference between the cases with respect to the effective momentum. The issue was studied further in the 2020 tests by conducting the tests with the same steam mass flux both in a single-hole and three-hole facility configuration. In the SEF-S29 and SEF-S32 tests, the steam mass flux was about 75 kg/m<sup>2</sup>s but the first one was done by using a single-hole injection plate while the latter one by using a three-hole plate. Also, in the SEF-S30 and SEF-S33 tests, the mass flux was the same (about 50 kg/m<sup>2</sup>s) while injection was through one hole in SEF-S30 and through three holes in SEF-S33. The absolute steam mass flow rate in kilograms per second was thus about three times larger in the three-hole tests than in the single-hole tests.

Comparison of the measured time-averaged force values from the latter pair of tests is presented in Figures 14 and 15. It can be seen that the measured force in the SEF-S30 test for example at pool temperatures of 30, 50 and 70 °C was about 1.6, 1.9 and 2.4 N, respectively (Figure 14). In the SEF-S33 test the force values for the same pool water temperatures were 3.0, 3.7 and 3.9 N, respectively (Figure 15). Steam injection with the same steam mass flux through a three-hole plate thus seems to produce slightly larger force measurement values than injection through a single-hole plate. The same kind of behaviour can be found from the first pair of tests (SEF-S29 vs. SEF-S32) but the comparison is more troublesome due to the interruption of steam injection in the middle of the test and due to some other disturbances in the measured values. Curves from those tests are not presented here.

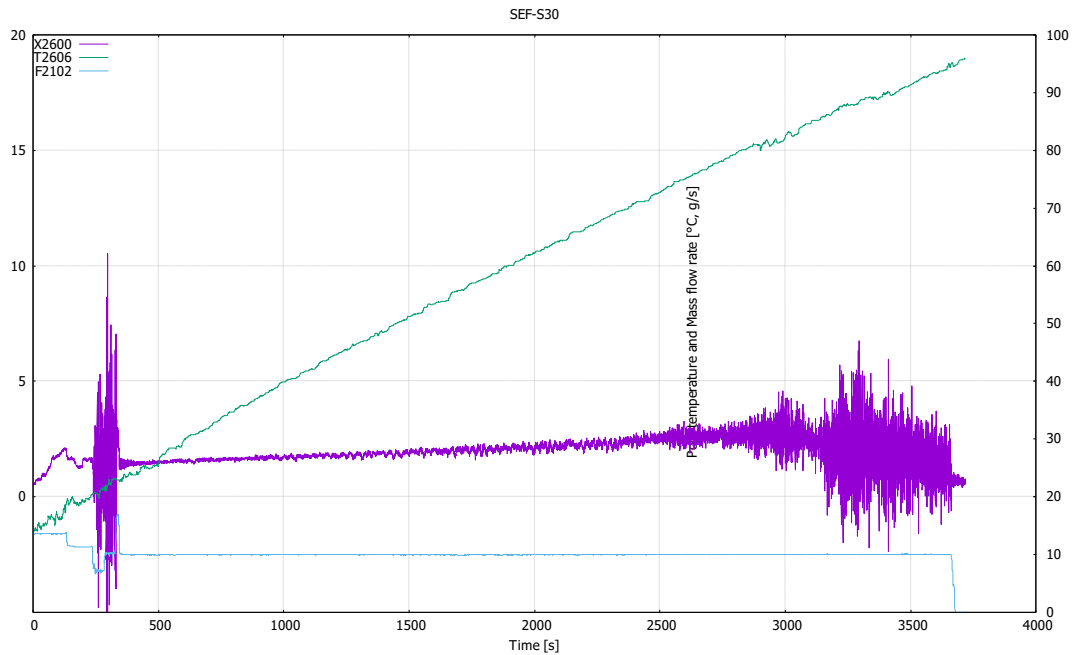


Figure 14. Steam injection mass flow rate ( $F_{2102}$ ), pool temperature ( $T_{2606}$ ) and force ( $X_{2600}$ ) in SEF-S30 test.

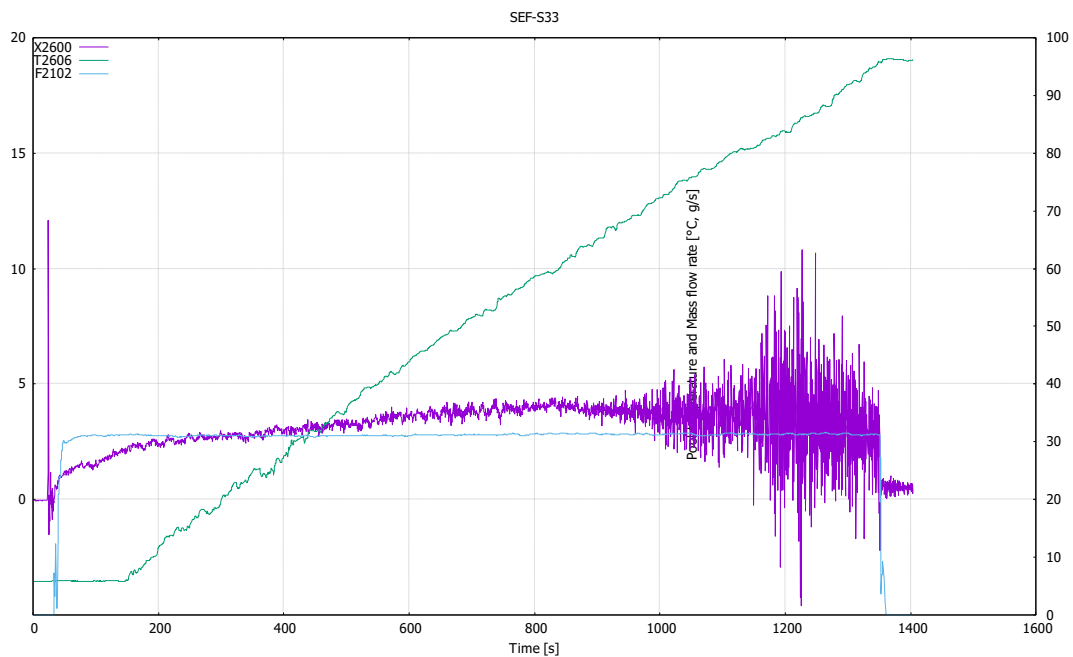


Figure 15. Steam injection mass flow rate ( $F_{2102}$ ), pool temperature ( $T_{2606}$ ) and force ( $X_{2600}$ ) in SEF-S33 test.

Another interesting trend that can be observed from the force curves in the figures above is the fact that in the three-hole case the curve reaches its peak value at the pool temperature of about 60 °C and then turns very slightly downwards, while in the single-



hole case the peak occurs at the pool temperature of about 80 °C. The other two three-hole tests indicate the same kind of behaviour of earlier peak in the force curve.

The heavy shaking of the sparger piping clearly visible in the force curves and associated with the pool water heat-up, and seen also in many previous tests, starts in the three-hole cases a little bit earlier, i.e. with a lower pool water temperature than in the single-hole cases. KTH will further analyse the violent shaking of the steam outlet with the help of the GoPro and Canon EOS video captures from the SEF-S34 test delivered to them.

Earlier single-hole tests in SEF-POOL revealed that high subcooling of pool water has an influence on the shape of the force curve in the sub-sonic injection cases. In the sonic cases such effect was not seen. The tests in 2020 confirm that the same kind of force curve shape can be found with the sub-sonic injection also in the three-hole configuration. From Figure 15 one can see that when the steam injection is started, the measured force value does not immediately jump up but instead it starts to follow a bending curve. Only when the pool water temperature is close to 20 °C, the force curve reaches a more linear slightly increasing trend. In the single-hole sonic cases tested in 2019, the force value had a clearly abrupt jump after the initiation of the steam injection and after that almost a linear trend. Sonic tests with the three-hole injection plate have not been done so far.

## **4.2 EFFECT OF POOL TEMPERATURE ON BUBBLE SIZE**

The oscillatory motion of the steam bubbles in the pool can be divided into three parts. That is, the bubble begins to grow attached to the injection hole, detaches when the force balance becomes positive in the direction of the steam injection and collapses as the neck connecting the bubble to the injection hole reduces the steam flow into the bubble.

The collapse phase at large sub-cooling can lead to a steam-water cloud with no clear boundary between vapour and liquid. At low sub-cooling, detached bubbles can move a large enough distance from the injection hole and allow the formation of a new bubble before their collapse. As the sub-cooling of the pool water decreases, the size of the forming steam bubbles before their detachment increases. Figure 16 presents a series of images captured from the high-speed camera recording during the SEF-S31 test. The used steam mass flux in the test was about 134 kg/m<sup>2</sup>s. The images show the increasing size of steam bubbles along the test as the pool water heats up. The last image shows how a new developing bubble has almost caught up with the previous detached bubble, which has not completely condensed yet. Collision and fusion of two successive bubbles was witnessed in some cases during the last phase of the test.

Both in the single-hole and three-hole tests done with the smallest steam injection rate incomplete condensation occurs as the pool temperature approaches saturation conditions. The forming steam bubbles are large in size and they start to rise upwards due to buoyancy forces even when they are still attached to the injection plate. The detached bubbles continue the rising movement and seem to reach the pool surface (which is outside of the video image) before they collapse. In these cases, the steam flow velocity is so small that the forming steam bubbles slow down and are unable to travel horizontally far from the injection plate. Instead, the buoyancy forces take control and start to lift the bubbles upwards.

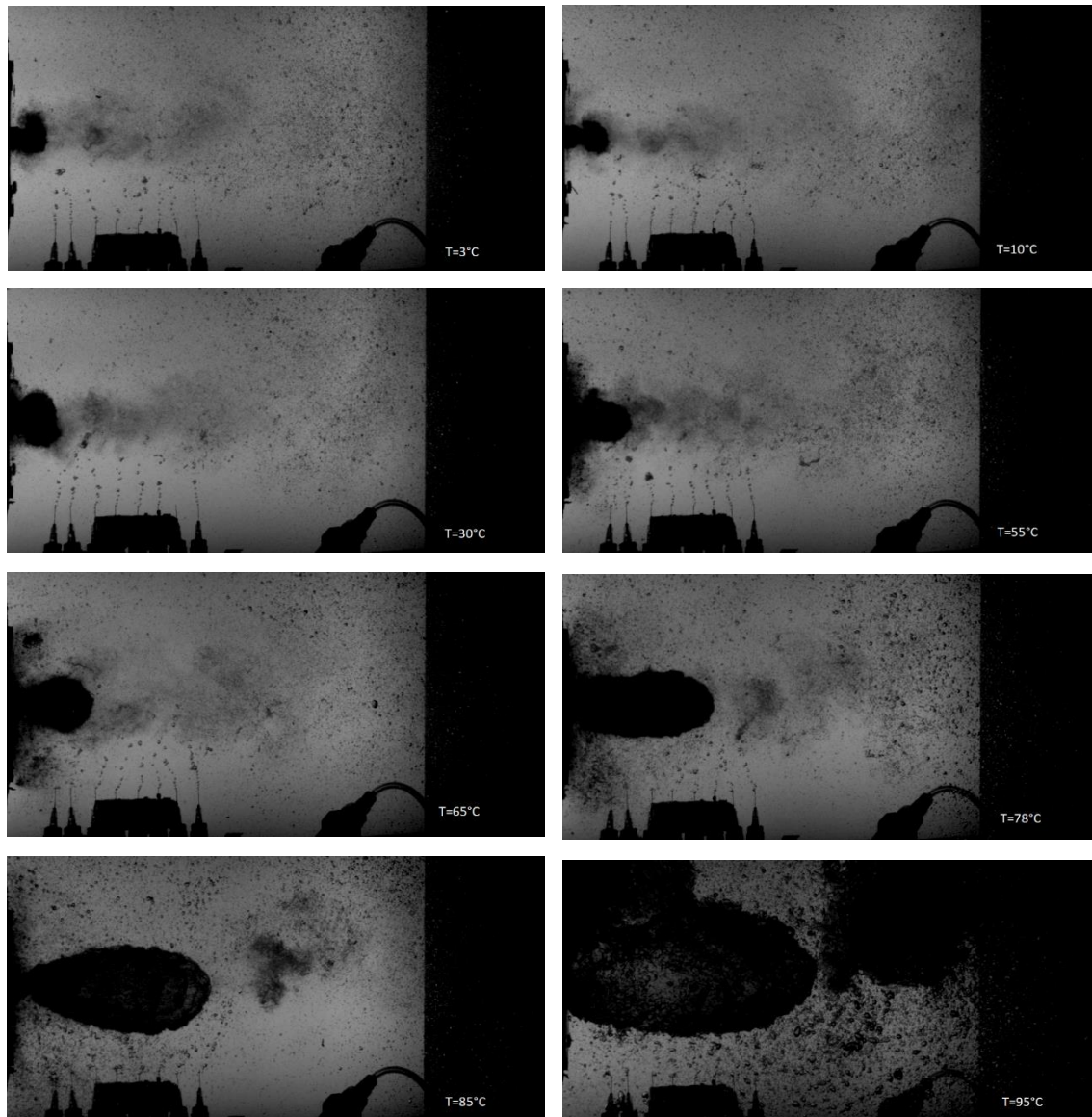


*Figure 16. Effect of pool water temperature on size of developing steam bubbles in SEF-S31 test.*

### 4.3 WATER INJECTION TESTS

In 2020 tests, one objective was to further develop the image analysis approach to evaluate flow velocity around the steam jet. Currently, KTH relies on the movement of (air) bubbles in the image to compute flow velocity. For this approach to work properly the bubbles must locate in the same plane as the jet. As a possible method to ensure this it was suggested in 2019 that the extra bubbles could be generated in the central plane. For that purpose, a horizontal pipe with small holes drilled on the upper side was installed to the central line of the pool below the elevation of the steam jet. During the tests, a small amount of air was injected into the pipe so that a stream of small bubbles escaping from

the holes on the upper side was formed. The air bubbles were then drawn into the bypassing liquid flow before finally being entrained into the steam jet.

The main purpose of the water injection tests SEF-W7 and SEF-W8 in 2020 was to verify that the new configuration of the air bubble injector works as desired, i.e. the generated bubbles are optimal in size and the release interval and distance between individual rising air bubbles are such that the in-house tracking tool of KTH can be used effectively. The new air bubble injector manufactured in the middle of the 2020 tests contains 32 individual syringes for bubble generation. The previous version had eight syringes. The syringe needle size is also smaller than before allowing smaller bubbles to be injected and tracked.

The vertical position of the bubble generator was changed between the SEF-W7 and SEF-W8 tests. The system was slightly lowered to ensure that the bubbles would reach their terminal velocity caused by buoyancy before entering the entrainment of the steam jet.

In the water injection tests, air bubbles were injected into the pool from the bubble generator, and at the same time water was injected through a single-hole injection plate used normally for steam injection. The behaviour of the air bubbles as they were drawn into the water jet was captured with the help of the high-speed camera system.

In the steam tests, where the air bubble generation system had been used, it had been noticed that the interval between the generated bubbles as well as the bubble diameter partly depends on the pool water temperature. In order to adjust the operation of the air bubble generation system to be optimal for bubble tracking purposes also during those phases of the steam injection tests when the pool water is heated up, it was decided that the second water injection test (SEF-W8) is done with warm pool and injection water. Before the test, the pool water was pre-heated (up to 67°C) with electrical heaters and during the injection, warm water (about 52 °C) from the tap was taken. In the SEF-W7 test, cold water directly from the tap was used both for filling up the pool and for injection.

There were several different water injection flow steps in the SEF-W7 test. The minimum used flow rate value was 15 l/min and the maximum 105 l/min. For each new step the flow was increased (or decreased) by about 15 l/min. In the SEF-W8 test, only two flow steps were used (15 and 33 l/min). The high-speed camera was triggered in each flow step to capture the movement of the air bubbles. The measured time-averaged injection water flow rate and the temperature of the injection and pool water in SEF-W7 are shown in Figure 17.

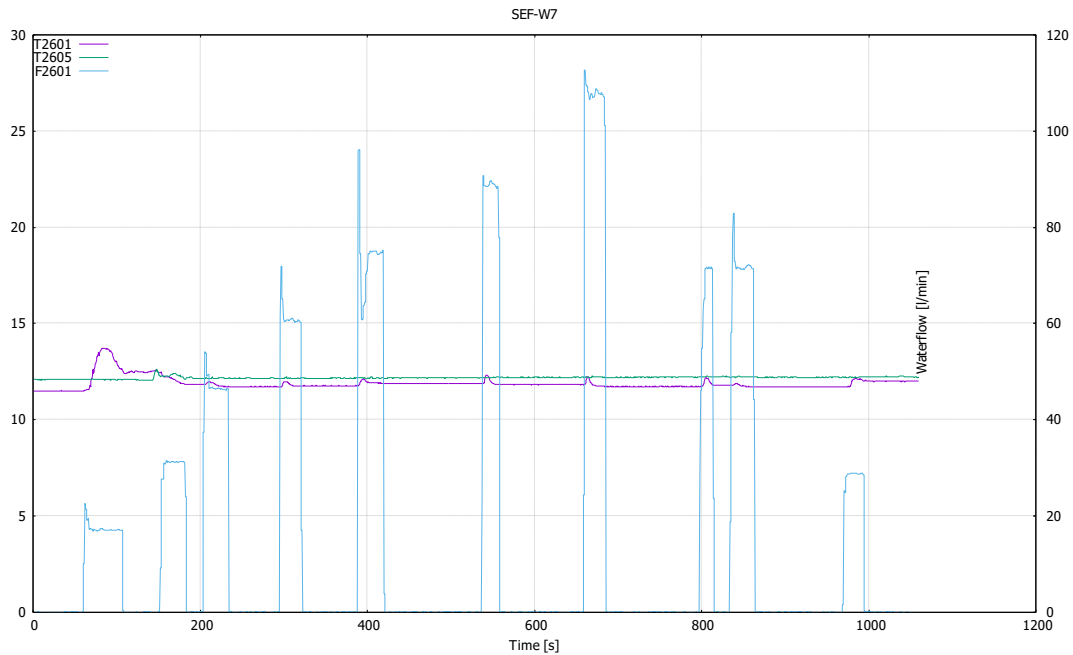


*Figure 17. Injection water flow rate (F2601), injection water temperature (T2601) and pool water temperature (T2605) in SEF-W7 test.*

Figure 18 shows four captured images of the air bubble cloud generated with the help of the system from the SEF-W7 test. The images are taken about 16 ms apart from each other (i.e. every 100<sup>th</sup> frame) during the 60 l/min water injection flow step. They should illustrate how the vertically rising air bubbles start to move also horizontally as they reach the zone affected by the water jet coming from the flow plate on the the left side of the images.

With frozen images, only an incomplete conception of the speed and route of drifting air bubbles can be accomplished. By looking at the live video recordings, a much more precise understanding of how the air bubbles accelerate along the fluid flow can be gained.

The image analysis approach developed by KTH and applied to the recorded high-speed clips from the SEF-POOL tests has given some encouraging preliminary results in determining the flow velocity around the jet. Also bubble radius, velocity and collapsing frequencies will be obtained through the analysis of the video images, as the work with the clips continues at KTH.

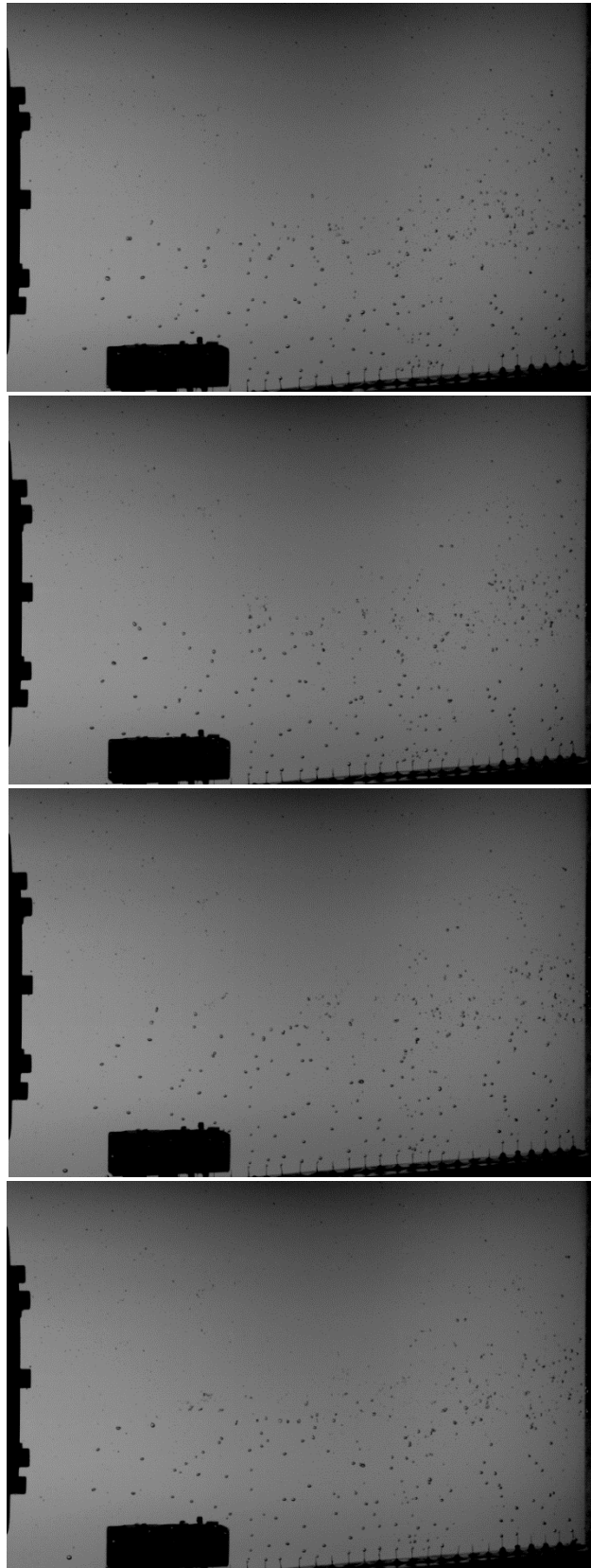


*Figure 18. Rising air bubble cloud colliding with horizontal water jet in SEF-W7.*



## 5 CONCLUSIONS

Prediction of the effective momentum induced by the oscillatory bubble and oscillatory cone jet regimes is necessary for the modelling of the pool behaviour. This is especially relevant for BWRs, where the development of thermal stratification or mixing during a steam injection through spargers can affect the performance of the suppression pool. In order to directly measure the effective momentum, the SEF-POOL facility has been built at LUT University and an extensive test series has been carried out. The reference system for the SEF-POOL facility is an SRV sparger pipe of a BWR plant. Hence, the facility is designed in such a way that discharge of steam through the injection holes at the sparger lower end into the sub-cooled pool water can be simulated representatively.

The analysis of the previous tests by KTH has shown that oscillatory bubble motions are a very efficient mechanism of transferring the force from the steam to the mean flow liquid. The test results have been helpful for the understanding of the key effects and factors that can be neglected when the EMS/EHS models are developed further [17].

The main goal of the SEF-POOL tests in 2020 was to provide data of the characteristics of the small-scale phenomena, which affect the effective heat and momentum sources in case of steam injection through a sparger into a sub-cooled pool of water. This information will then be used in the validation of the simplified EHS/EMS models by KTH. Furthermore, the SEF-POOL tests support the validation effort of the DCC and interfacial area models of CFD codes for steam injection through spargers at VTT and LUT. Particular interest in the 2020 tests was in capturing good-quality high-speed camera stereo recordings of the steam jet behaviour and jet entrainment visualized with the help of air bubbles injected into the pool.

Six steam injection tests were performed in the SEF-POOL facility in 2020. In addition, two water injection tests were performed. The main varied parameter was the mass flux of injected steam. The possible effect of multiple injection holes was also studied further by using a three-hole plate in some of the tests. The water injection tests were done in order to check the operation of the air bubble generator and to find the suitable camera imaging parameters and lighting conditions so that KTH can effectively use their in-house tools in the analysis of the recordings for tracking the movement of the air bubbles and thus ultimately assess the liquid velocity and the amount of jet entrainment. The camera set-up and the air bubble generation system were adjusted along the test series according to the feedback received from KTH. All the test parameters and procedures were agreed with KTH.

The test matrix in 2020 contained tests both with a single-hole and three-hole injection plate configuration. Steam injection with the same steam mass flux through a three-hole plate seemed to produce slightly larger force measurement values than injection through a single-hole plate. In addition, in the three-hole case the measured force curve reached its peak value at the pool temperature of about 60 °C and then turned very slightly downwards while in the single-hole case the peak occurred at the pool temperature of about 80 °C.

Earlier single-hole tests in SEF-POOL had revealed that in sub-sonic injection cases high subcooling of the pool water has an effect on the shape of the force curve. When steam

injection is started, the measured force starts to follow a bending curve (instead of immediately jumping up). After the pool water temperature reaches 20 °C, the force curve starts to follow a more linear, slightly increasing trend. The tests in 2020 confirmed that the same kind of force curve shape can be found with sub-sonic injection also in the three-hole configuration. In the single-hole sonic injection cases tested in 2019, the bending shape of the force curve was not observed. Sonic tests with the three-hole injection plate have not been done so far.

As the sub-cooling of the pool water decreases, the size of the forming steam bubbles increases. The high-speed video clips reveal that at low sub-cooling detached bubbles can move a long distance from the injection hole and allow the formation of a new bubble before they collapse. Close to saturation conditions a new developing bubble can catch up with the previous detached bubble, which has not condensed completely yet, collide with it and even merge with it.

Both in the single-hole and three-hole tests done with the smallest steam injection rate incomplete condensation occurred as the pool temperature approached saturation conditions. The forming steam bubbles were large in size and they started to rise upwards due to buoyancy forces even when they were still attached to the injection plate. The detached bubbles continued the rising movement and seemed to reach the pool surface before they collapsed. In these cases, the steam flow velocity was so small that the forming steam bubbles slowed down and were unable to travel horizontally far from the injection plate. Instead, the buoyancy forces took control and started to lift the bubbles upwards.

Violent shaking of the sparger piping had been observed in the earlier tests as the pool water was heated over 80 °C. In the three-hole cases, this happened even with a little bit lower pool water temperature. To analyse the phenomenon in more detail GoPro and Canon EOS video clips were captured from the SEF-S34 test and delivered to KTH.

The most important outcome of the 2020 tests was the successful refining of the air bubble generator configuration and the high-speed camera set-up. Two water injection tests were carried out for this purpose. On the basis of the feedback from KTH the operation of the air injector was fine-tuned and optimal parameters for stereo imaging were selected so that the movement of the air bubbles can be tracked and finally, the liquid velocity and the amount of jet entrainment can be assessed. Additional bubble parameters, which will be estimated through the image processing of the high-speed videos of the SEF-POOL tests by KTH, include the collapse and bubble life frequencies, maximum bubble radius, bubble velocities, pressure gradients, and heat transfer coefficients.

## REFERENCES

- [1] Li, H., Kudinov, P., Effective Approaches to Simulation of Thermal Stratification and Mixing in a Pressure Suppression Pool. OECD/NEA & IAEA Workshop CFD4NRS-3, September 14-16, 2010, Bethesda, MD, USA.
- [2] Li, H., Villanueva, W., Kudinov, P., Approach and development of effective models for simulation of thermal stratification and mixing induced by steam

- injection into a large pool of water. *Sci. Technol. Nucl. Ins.* 2014, <http://dx.doi.org/10.1155/2014/108782>, (Article ID 108782).
- [3] Li, H., Villanueva, W., Puustinen, M., Laine, J., Kudinov, P., Validation of effective models for simulation of thermal stratification and mixing induced by steam injection into a large pool of water. *Sci. Technol. Nucl. Ins.* 2014, <http://dx.doi.org/10.1155/2014/752597>, (Article ID752597).
  - [4] Li, H., Villanueva, W., Puustinen, M., Laine, J., Kudinov, P., Thermal stratification and mixing in a suppression pool induced by direct steam injection. *Annals of Nuclear Energy*. 2018, 111, <https://doi.org/10.1016/j.anucene.2017.09.014>.
  - [5] Estévez-Albuja, S., Gallego-Marcos, I., Kudinov, P., Jiménez, G., Modelling of a Nordic BWR containment and suppression pool behavior during a LOCA with GOTHIC 8.1. *Annals of Nuclear Energy*. 2020, 136, <https://doi.org/10.1016/j.anucene.2019.107027>.
  - [6] Chan, C.K., Lee, C.K.B., A regime map for direct contact condensation. *International Journal of Multiphase Flow*, 8 (1982), pp. 11-20.
  - [7] Gallego-Marcos, I., Kudinov, P., Villanueva, W., Kapulla, R., Paranjape, S., Paladino, D., Laine, J., Puustinen, M., Räsänen, A., Pyy, L., Kotro, E., Pool Stratification and Mixing Induced by Steam Injection through Spargers: Analysis of the PPOOLEX and PANDA experiments. *Nuclear Engineering and Design*, 337 (2018), pp. 300-316. <https://doi.org/10.1016/j.nucengdes.2018.07.004>.
  - [8] Gallego-Marcos, I., Kudinov, P., Villanueva, W., Kapulla, R., Paranjape, S., Paladino, D., Laine, J., Puustinen, M., Räsänen, A., Pyy, L., Kotro, E., Pool Stratification and Mixing during a Steam Injection through Spargers: CFD modelling of the PPOOLEX and PANDA experiments. *Nuclear Engineering and Design*, 347 (2019), pp. 67-85. <https://doi.org/10.1016/j.nucengdes.2019.03.011>.
  - [9] Patel, G., Hujala, E., Tanskanen, V., Puustinen, M., OpenFOAM simulations and pattern recognition analysis of the SEF-POOL tests. Lappeenranta-Lahti University of Technology, LUT School of Energy Systems, Nuclear Engineering, Research Report SPASET 2/2019. Lappeenranta 2019.
  - [10] Patel, G., Hujala, E., Puustinen, M., CFD simulations and pattern recognition analysis of the SEF-POOL tests. Lappeenranta-Lahti University of Technology, LUT School of Energy Systems, Nuclear Engineering, Research Report SPASET 2/2020. Lappeenranta 2020.
  - [11] Pättikangas, T., Hovi, V., CFD Simulation of Condensation of Vapor Jets. Research Report VTT-R-00993-18. Espoo 2018.
  - [12] Puustinen, M., Laine, J., Räsänen, A., Kotro, E., Tielinen, K., Characterizing Tests in SEF-POOL Facility. Lappeenranta University of Technology, School of Energy Systems, Nuclear Engineering, Research Report INSTAB 3/2017. Lappeenranta 2018.
  - [13] Puustinen, M., Laine, J., Räsänen, A., Kotro, E., Tielinen, K., SEF-POOL Tests. Lappeenranta-Lahti University of Technology, School of Energy Systems, Nuclear Engineering, Research Report INSTAB 1/2018. Lappeenranta 2019.
  - [14] Puustinen, M., Räsänen, A., Kotro, E., Tielinen, K., SEF-POOL tests on small-scale phenomena of steam discharge into sub-cooled water, Lappeenranta-Lahti



- University of Technology, LUT School of Energy Systems, Nuclear Engineering, Research Report SPASET 1/2019. Lappeenranta 2020.
- [15] Tuunanen, J., Kouhia, J., Purhonen, H., Riikonen, V., Puustinen, M., Semken, R. S., Partanen, H., Saure, I., Pylkkö, H., General Description of the PACTEL Test Facility. Espoo: VTT. 1998. VTT Research Notes 1929. ISBN 951-38-5338-1.
- [16] Tielinen, K., Räsänen, A., Kotro, E., Saure, I., General description of SEF-POOL test rig. Lappeenranta University of Technology, School of Energy Systems, Nuclear Engineering, Research Report INSTAB 2/2017. Lappeenranta 2018.
- [17] Gallego-Marcos, I., Kudinov, P., Villanueva, W., Puustinen, M., Räsänen, A., Tielinen, K., Kotro, E., Effective Momentum Induced by Steam Injection in the Oscillatory Bubble Regime. Nuclear Engineering and Design, 350 (2019), pp. 259-274. <https://doi.org/10.1016/j.nucengdes.2019.05.011>.

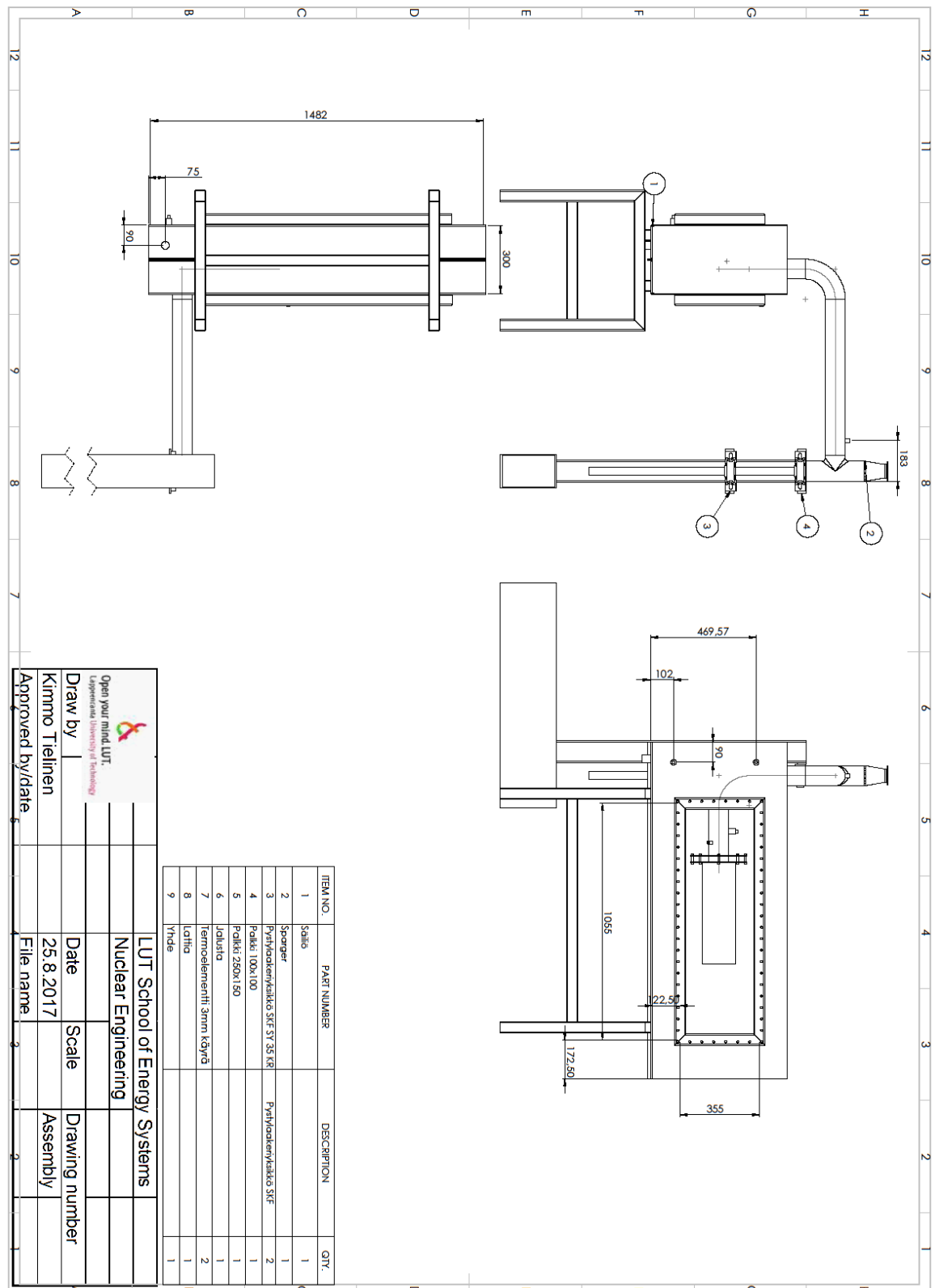


Figure 1. Condensation pool.

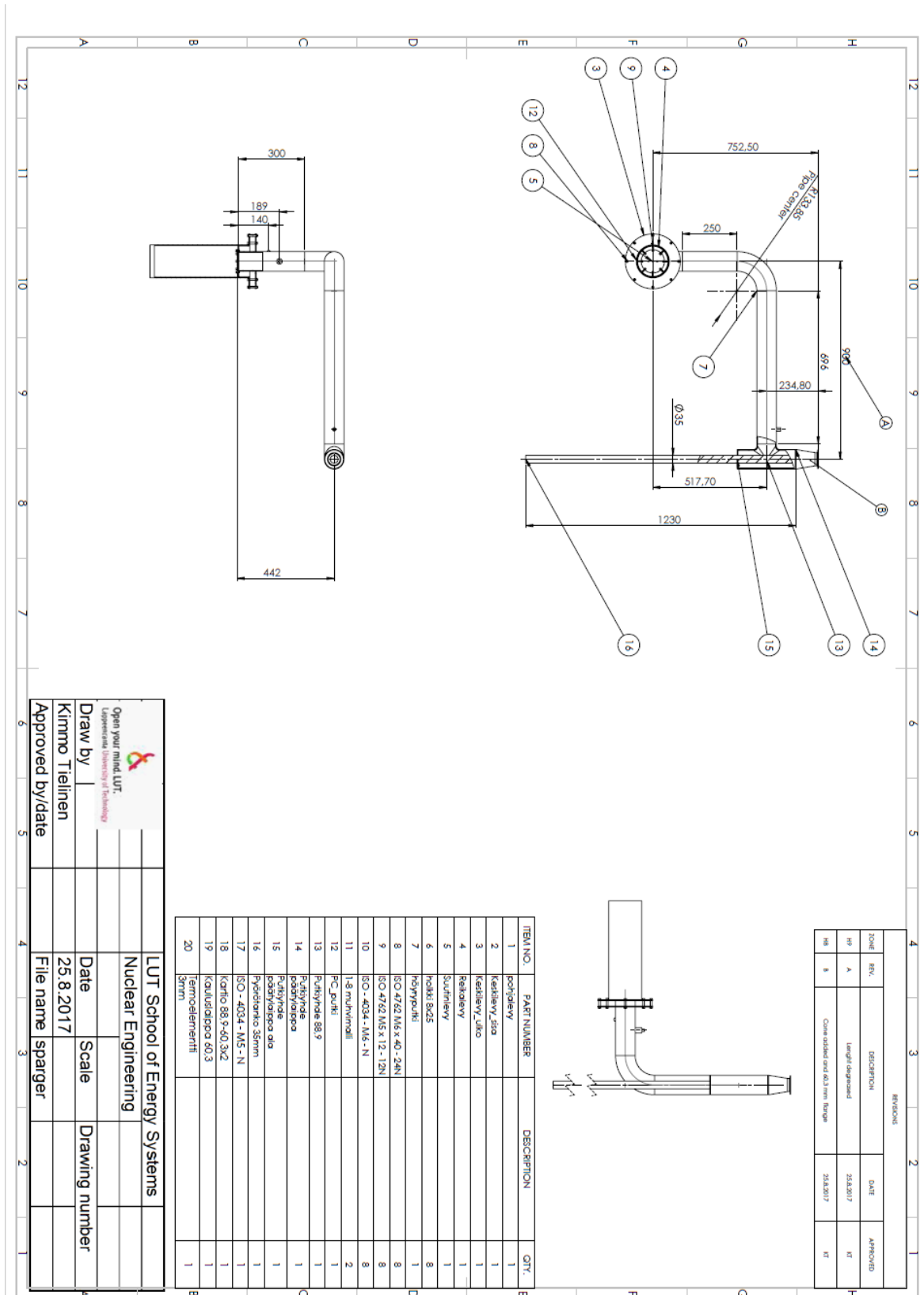


Figure 2. Sparger piping.

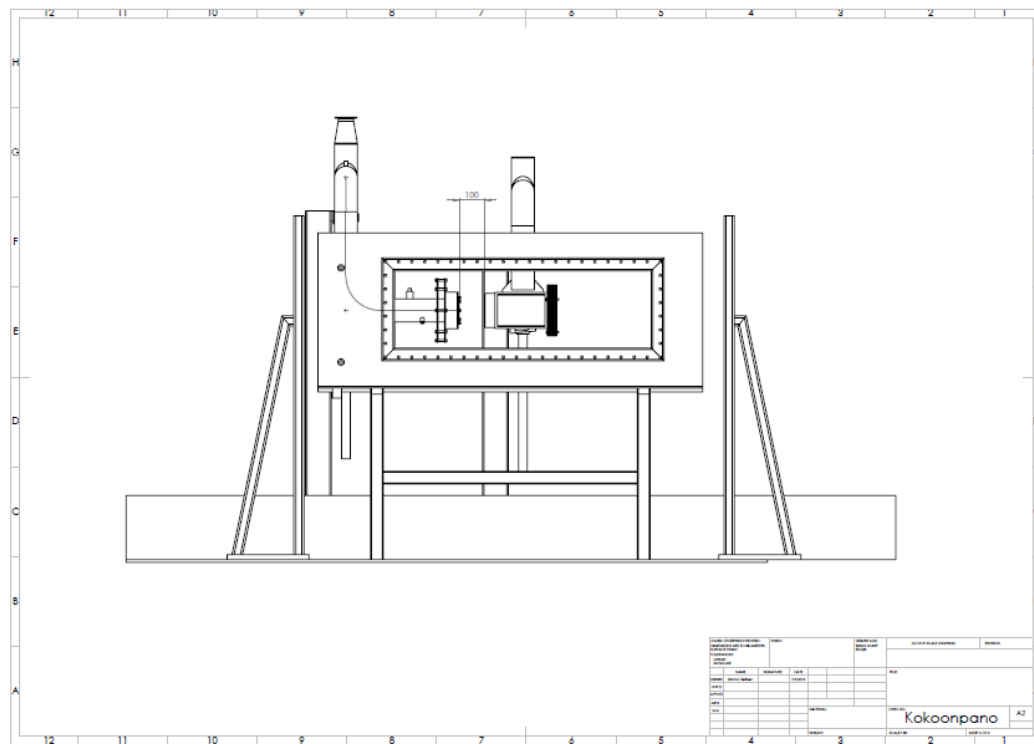


Figure 3. Sparger system and independent PC pipe.

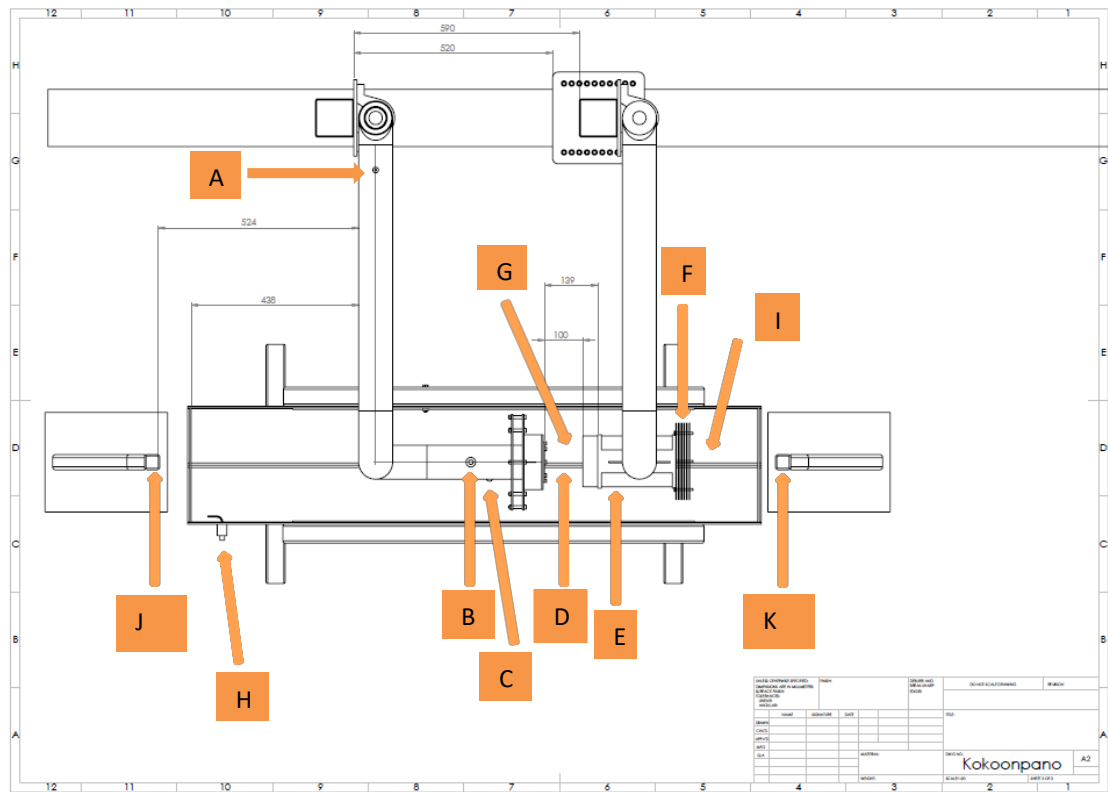


Figure 1. Measurements of the sparger system and PC pipe.

Table 1. Instrumentation of the SEF-POOL facility

Figure code	Data code	Sensor type	Manufacturer/ type	Measurement frequency	Measurement range
A	P2600	Pres. transducer	Wikatronic	2 Hz	0-1 MPa
A	T2600	TC, K- type	Ø3 mm <sup>1</sup>	70 Hz	0-200 °C
B	T2601	TC, K- type	Ø1 mm <sup>1</sup>	70 Hz	0-200 °C
C	P2601	Pressure sensor <sup>2</sup>	Kyowa PHS-B	7 KHz	0-1 MPa
D <sup>4</sup>	P2602	Pressure sensor <sup>2</sup>	Kyowa PS-2KC <sup>3</sup>	7 kHz	0-0.2 MPa
E <sup>4</sup>	T2602	TC, K- type	Ø 0.5 mm <sup>1</sup>	70 Hz	0-200 °C
F <sup>4</sup>	T2603	TC, K- type	Ø 0.5 mm <sup>1</sup>	70 Hz	0-200 °C
G <sup>4</sup>	T2604	TC, K- type	Ø 0.5 mm <sup>1</sup>	70 Hz	0-200 °C
H	T2605	TC, K- type	Ø 3.0 mm <sup>1</sup>	70 Hz	0-200 °C
H	T2606	TC, K- type	Ø 3.0 mm <sup>1</sup>	70 Hz	0-200 °C
I	T2607	TC, K- type	Ø 0.5 mm <sup>1</sup>	70 Hz	0-200 °C
J	X2600	Force sensor <sup>2</sup>	Kyowa LUX-B-50N	7 kHz	±50 N
K <sup>4</sup>	X2601	Force sensor <sup>2</sup>	FUTEK LRM200	7 kHz	±222 N

<sup>1</sup> Diameter of the sensing element

<sup>2</sup> These are used in conjunction with a Strain/Bridge Input Module

<sup>3</sup> Type used depends on the range, the number denotes the measurement range in bars

<sup>4</sup> Sensor not used in 2020 tests!

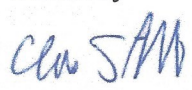
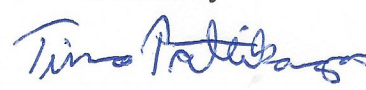
## **Appendix C**

### **Modelling of thermal stratification in suppression pool using the Apros thermahydraulic model**

# Modelling of thermal stratification in suppression pool using the Apros thermahydraulic model

Authors: Ari Silde

Confidentiality: Public

<b>Report's title</b> Modelling of thermal stratification in suppression pool using the Apros thermalhydraulic model		
<b>Customer, contact person, address</b> 1. Yli-insinööri Jorma Aurela, Valtion ydinjäterahasto, PI 32, 00023 Valtioneuvosto 2. Cristian Linde, Programme Manager NKS-R, Strålsäkerhetsmyndigheten, Se-171 16 Stockholm, Sweden		<b>Order reference</b> Dnro SAFOR 11/2019 AFT/NKS-R(19)130/8
<b>Project name</b> CFD methods for reactor safety assessment (CFD4RSA)		<b>Project number/Short name</b> 12496/ SAFIR2022_CFD4RSA_2020
<b>Author(s)</b> Ari Silde		<b>Pages</b> 27
<b>Keywords</b> Apros, suppression pool, pool stratification, BWR, EMS/EHS model		<b>Report identification code</b> VTT-R-00664-20
<b>Summary</b> <p>The goal of this work was to study stratification modeling capability of Apros thermal-hydraulic model using so called pseudo 2D nodalisation. The PPOOLEX stratification test SPA-T3 was simulated. The sensitivity studies included e.g. the effect of nodalisation concept, loss coefficient, direction of momentum transfer from steam source, discretization scheme and steam mass flow during the pool mixing phase.</p> <p>The simulation results show that the pool stratification phase was predicted well with the 2-column nodalisation used. However, the pool mixing phase could not be predicted reasonably. The best agreement with the experiment is obtained when using the higher order discretisation scheme for enthalpy solution and the larger loss coefficient for the horizontal branches than for the vertical ones. Sensitivity study showed that a significant increase in steam mass flow (and momentum) did not improve the predicted pool mixing. Therefore, implementation of the EHS/EMS model in Apros would not probably solve alone the deficiencies found in the mixing calculation. Maybe the EHS/EMS approach should be modified or totally different approach should be tailored to Apros's need in order to model better the pool mixing phenomena.</p> <p>The Shah condensation correlation of Apros, which is the default correlation, did not model realistically the steam condensation in the pool. The Chen correlation without Vierow-Schrock correction (option 7) seemed to predict reasonably the steam condensation inside water pool.</p>		
<b>Confidentiality</b>	Public	
30.03.2021 <div style="display: flex; justify-content: space-between;"> <div style="width: 30%;"> <b>Written by</b>    Ari Silde  Senior scientist </div> <div style="width: 30%;"> <b>Reviewed by</b>    Timo Pättikangas  Research Team Leader,  Process Modelling </div> <div style="width: 30%;"> <b>Accepted by</b>    Antti Arasto  Vice President,  Industrial Energy and Hydrogen </div> </div>		
<b>VTT's contact address</b> VTT Technical Research Centre of Finland, PL 1000, 02044 VTT.		
<b>Distribution (customer and VTT)</b> SAFIR2022 Reference group		
The use of the name of VTT Technical Research Centre of Finland Ltd in advertising or publishing of a part of this report is only permissible with written authorisation from VTT Technical Research Centre of Finland Ltd.		



## Contents

---

Contents.....	2
1. Introduction.....	3
2. PPOOLEX experiment SPA-T3.....	4
3. Apros model for SPA-T3 experiment.....	7
4. Simulation results.....	11
4.1 Base case.....	11
4.2 Sensitivity study.....	15
4.2.1 Steam mass flow (momentum).....	15
4.2.2 Loss coefficient.....	16
4.2.3 Direction of steam source .....	18
4.2.4 Higher order upwind model.....	19
4.2.5 Size of inner node column.....	21
4.2.6 Number of nodes below the sparger elevation .....	22
4.2.7 Other observations.....	24
5. Conclusions .....	25
References.....	26

## 1. Introduction

---

The suppression pool system is installed in certain types of Boiling Water Reactor (BWR) Nuclear Power Plants to manage containment overpressurisation. Steam discharge coming from the primary coolant system through Safety Relief Valves (SRVs) lines and/or from the drywell through the vent pipe system is directed into suppression pool where the steam is condensed. The possible formation of thermal stratification in the pool is of safety concern since it has an influence on the steam condensation and pressure suppression capacity of the pool. If the pool is thermally stratified, the pool surface temperature and containment pressurization may be higher compared with homogeneous pool. The real example of this is the Fukushima accident (Jo et al 2016; Mizokami et al 2016.)

The numerical modelling of pool mixing/stratification have been widely studied at KTH Sweden where the Effective Heat Source (EHS) and Effective Momentum Source (EMS) models for modelling of pool stratification effects have been developed and validated (Gallego-Marcos et al. 2016; Gallego-Marcos 2018; Li et al. 2014a). The extensive experimental work has been done at e.g. Lappeenranta-Lahti University of Technology LUT at the PPOOLEX facility (LUT university) (Li et al. 2014b; Laine et al. 2009; Laine et al. 2014).

The previous VTT work relating to the stratification topic summarized the prerequisites of the lumped parameter (LP) containment model and thermalhydraulic model (TH) for simulating stratification phenomena of suppression pool (Silde 2019). Also the possibility to implement the EHS/EMS model in Apros was considered. The summary of the work was that the EHS/EMS model is not directly applicable in Apros LP modelling, but could be maybe utilized in the stratification calculation when using the Apros TH model. However, the main concern was that the Apros TH model applies 1D solution, whereas the EHS/EMS model is intended for coupling it with 2D or 3D flow solution.

The goal of this work is to study stratification modeling capability of Apros 1D TH model using so called pseudo-2D nodalisation. The PPOOLEX stratification test SPA-T3 is simulated. The nodalisation is constructed with aid of the experimental evidence and the experience gained from the CFD simulations (Pättikangas 2020). The sensitivity studies include e.g. the effect of nodalisation concept, loss coefficient, direction of momentum transfer from steam source, discretization scheme and steam mass flow rate during the pool mixing phase.

## 2. PPOOLEX experiment SPA-T3

---

LUT University has performed the pool thermal stratification and mixing experiments with the PPOOLEX test facility (Laine et al., 2015). The facility simulates the BWR containment system consisting of the drywell and wetwell gas volumes with interconnecting pipes between them and the suppression pool in the wetwell (Figure 2-1). Initial free volumes of the drywell and wetwell are 13.3 m<sup>3</sup> and 5.5 m<sup>3</sup>, respectively. Total height and diameter of the facility is 7.45 m and 2.4 m, respectively. Water initial elevation in the wetwell in PPOOLEX test SPA-T3 is 3.0 m. The initial pressure, and gas and water temperatures are 1 bar and 21 °C, respectively.

Steam is injected into the suppression pool through the sparger holes (32x8 mm) (Figure 2-2). The holes are arranged in four rows each containing eight orifices. The sparger bottom elevation is at level of 1.2 m, so the sparger end is submerged 1.8 m below the pool surface elevation. In test SPA-T3, actually only the wetwell is used, where the steam injection and pool stratification take place. The heat losses from the steam pipeline to the drywell gas space are modelled, because they affect the mass flow rate and temperature of steam coming out from the sparger orifices.

The steam pressure and temperature in the steam generator is 6.0 bar and 160 °C, respectively. Several meters long steam pipeline is insulated outside the vessel, but inside the drywell the pipeline is not insulated. In the drywell atmosphere, the pipeline turns vertically downwards and leads to the suppression pool. The steam injection mass flow was varied during test SPA-T3 (Table 2-1). The experiment started by a short heating phase (35 ... 235 s) when the pool is fully mixed. This phase is followed by the first stratification phase (235 ... 4303 s) at low mass flow rate of 120 g/s. After the stratification phase, the steam mass flow rate was increased to 260 g/s leading to effective pool mixing during (4303 ... 5005 s). This mixing phase is followed by the second stratification phase when the steam mass flow rate is only 95 g/s (5005 ... 10 793 s). Finally, the pool is once again mixed with steam mass flow rate of 120 g (10 793 s ... 11 735 s). The steam mass flow rate of 120 g/s during the first stratification phase corresponds to mass flux of 74.6 kg/m<sup>2</sup>s (Pättikangas 2020) which is on the borderline between internal and external chugging and oscillatory bubble regions (see the light blue line in the condensation map in Figure 2-3). The steam mass flow rate of 260 g/s during the first mixing phase corresponds to mass flux of 162 kg/m<sup>2</sup>s which is in the cone jet zone.

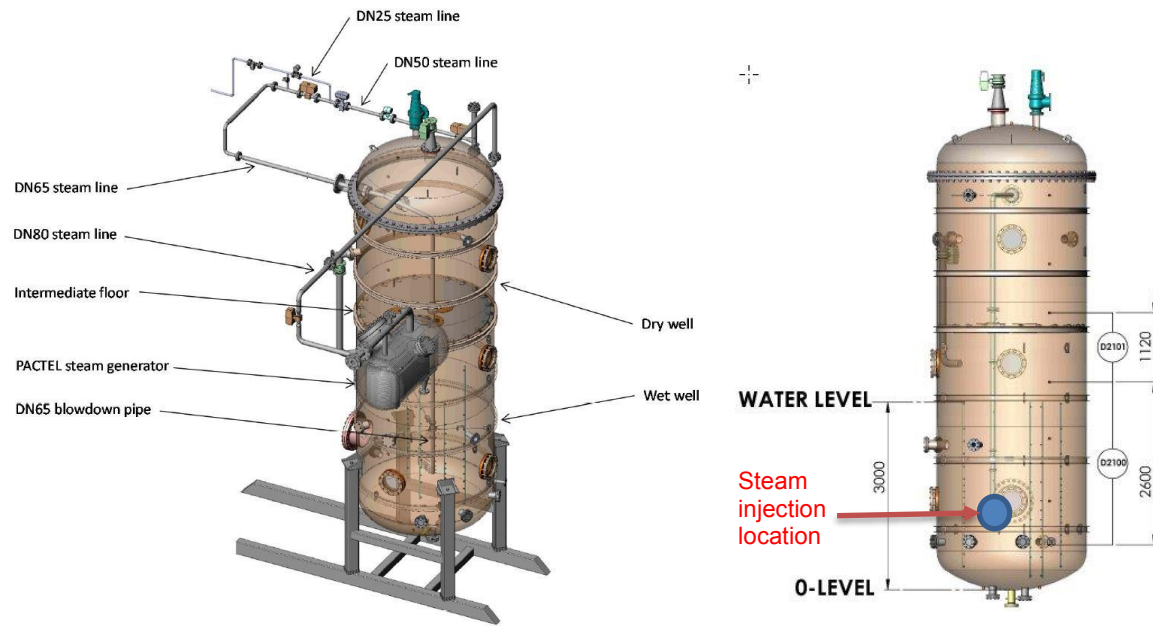


Figure 2-1. PPOOLEX test vessel (Laine et al., 2015).



Figure 2-2. Sparger of the PPOOLEX test facility (Laine et al., 2015).

Table 2-1. Steam mass flow rates in PPOOLEX SPA-T3 experiment.

Test phase	Time period [s]	Mass flow rate [g/s]
Mixing phase	35 ... 235	220
Stratification phase	235 ... 4303	120
Mixing phase	4303 ... 5005	260
Stratification phase	5005 ... 10 793	95
Mixing phase	10 973 ... 11 735	125

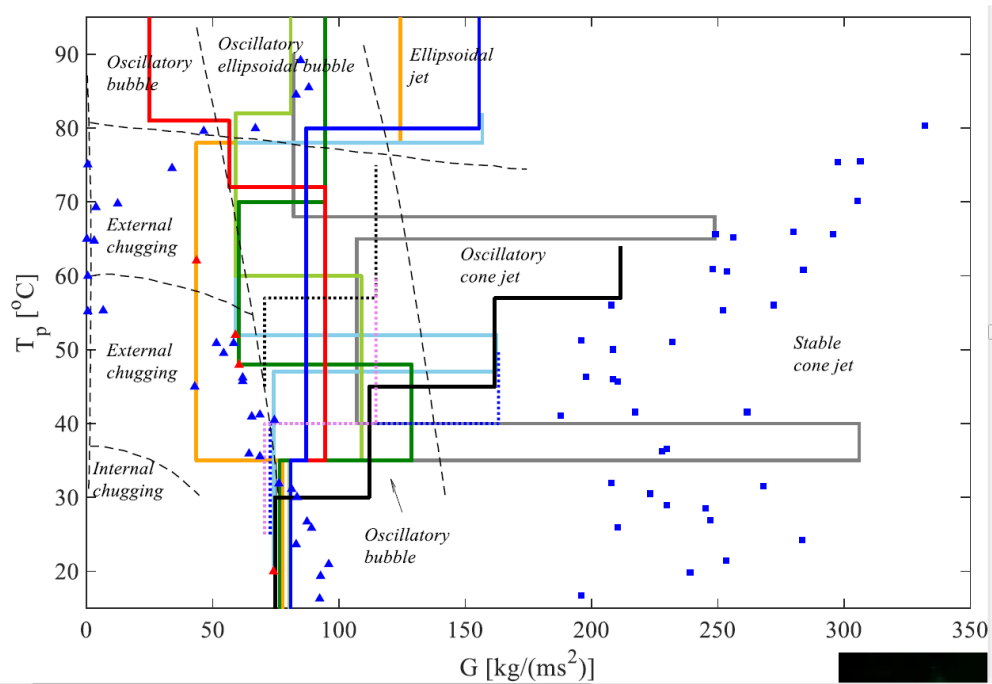


Figure 2-3. Condensation map obtained from PPOOLEX and PANDA data (Gallego-Marcos, 2018).

### 3. Apros model for SPA-T3 experiment

---

The drywell and wetwell gas spaces of the PPOOLEX facility and the environment node were modelled with the Apros LP containment model (Figure 3-1), whereas the steam pipeline and the sparger (Figure 3-2), and the suppression water pool (Figure 3-3 and Figure 3-4) were modelled with the six-equation thermalhydraulic model. The drywell is insulated and the drywell wall structures were not modelled, whereas the heat structure between the wetwell gas space and the environment was included (Figure 3-1).

The steamline was modelled with the TH heat pipes (Figure 3-2). The pipeline outside the vessel is insulated, and hence, only heat transfer from the pipeline inside the vessel was modelled with Apros. The closer the heat pipe is to the lower end of the sparger, the denser the nodalisation of the heat pipe was. Very close to the sparger end, the node length was about 3 cm, but near the steam generator only around 1 m. The holes (orifices) of the sparger were modelled with one pipe, whose flow area corresponds to the total flow area of all sparger holes and the hydraulics diameter corresponds to the diameter of single hole.

The suppression pool nodes which are filled up with liquid water were modelled with the Apros thermalhydraulic nodes. There were 9 nodes above the sparger end corresponding to node height of 0.2 m (Figure 3-3). Two different nodalisation below the sparger elevation were tested: 12 or 6 vertical nodes corresponding to the node height of 0.1 m and 0.2 m, respectively (Figure 3-4). The whole pool nodalisation was divided into two node columns representing the cross sectional configuration shown in Figure 3-3. Two different nodalisation was made for the innermost node: assuming 0.2 m and 0.8 m diameter. The two-column configuration was constructed according to the experimental observations of the main flow field in the pool and the experiences gained from the CFD simulations (Pättikangas 2020) which demonstrated that during the hot steam injection the warm water rises up in the region near the sparger line and the colder water flows down farther from the line. The Apros node configuration allows a qualitative simulation of this kind of flow field. Note that in reality the sparger pipeline of the PPOOLEX facility is not located exactly in the middle axis of the facility, but the Apros pseudo 2D nodalisation assumes a axially symmetrical geometry due to lack of modelling any 3D phenomena.

A direct connection of the wetwell gas space and TH nodes in the suppression pool was not possible, because the connecting branch does not include a separation option, which would have been needed in the simulation. Instead, the uppermost thermahydraulic nodes of the pool were connected to the external point. Because the objective of the work was to study only pool stratification phenomena, this simplification is justified.

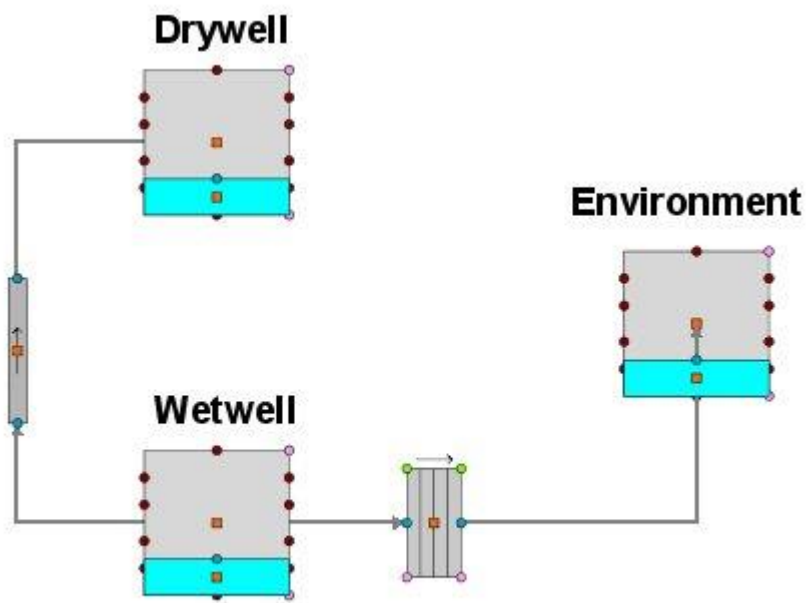


Figure 3-1. Apros model for drywell and wetwell.

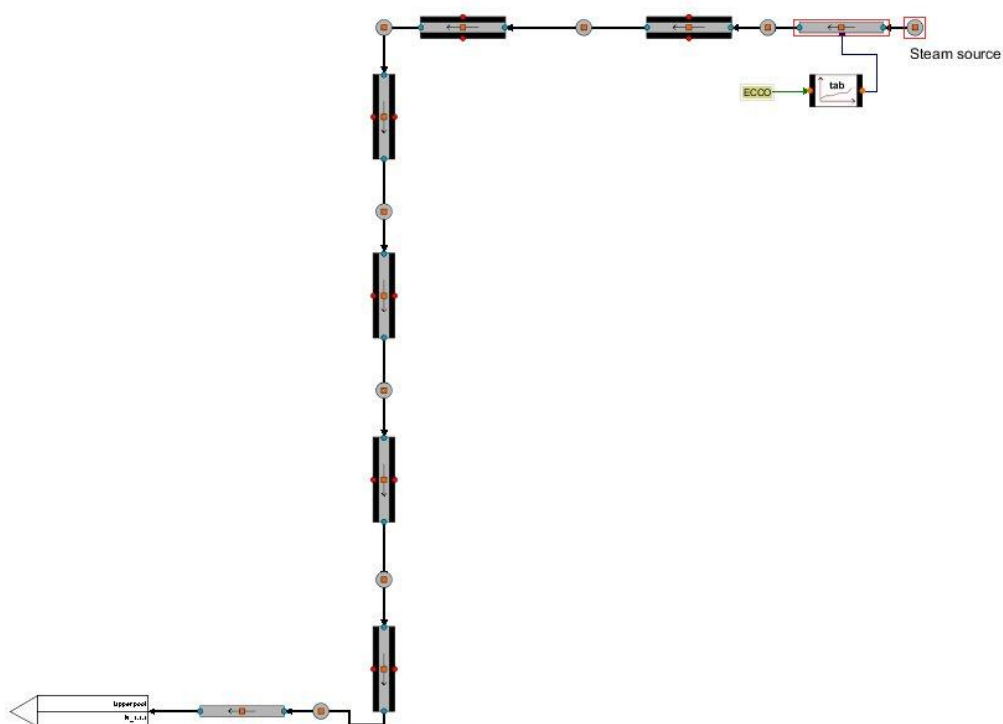


Figure 3-2. *Apros model for steam injection pipeline and the sparger.*

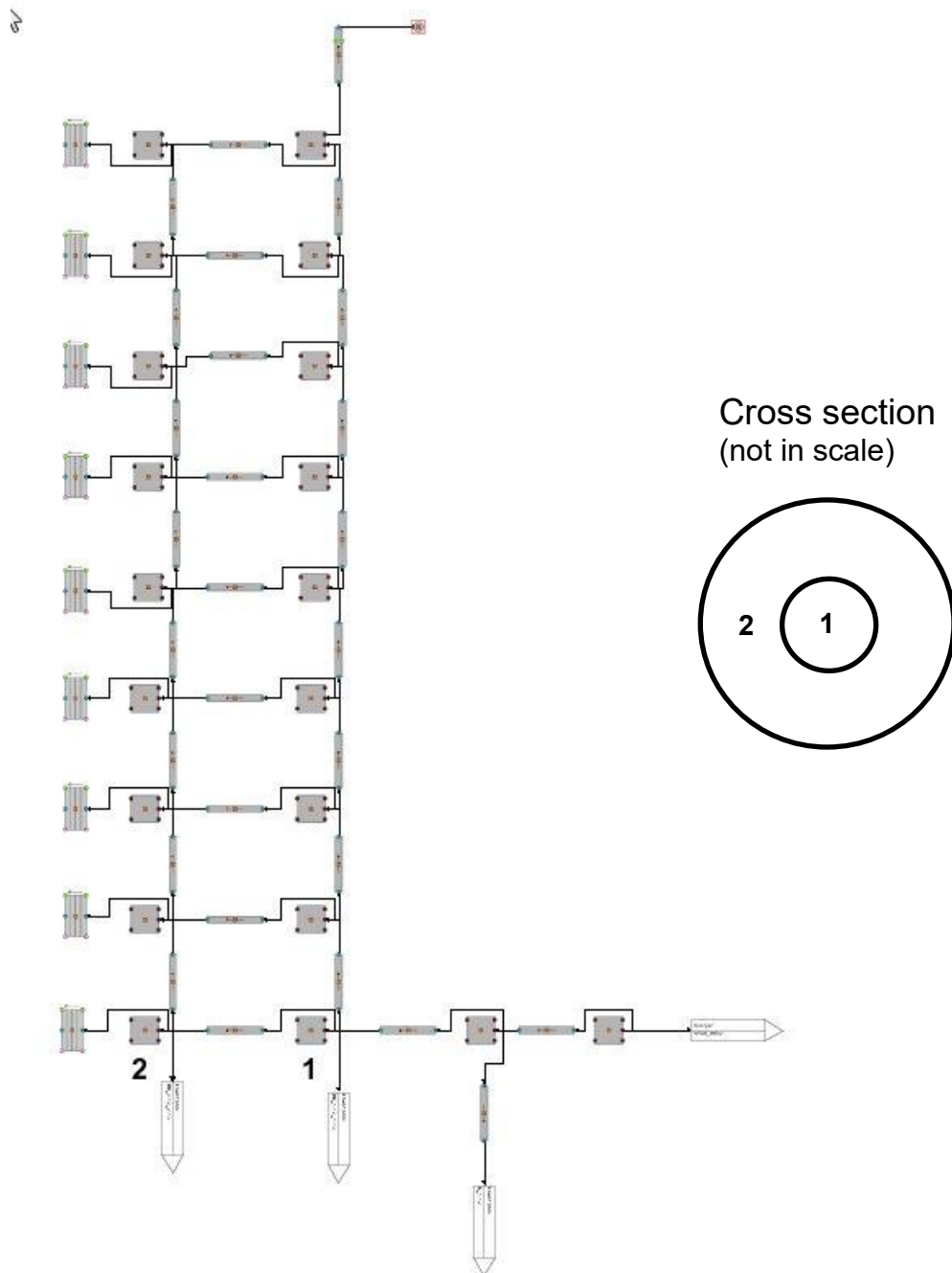


Figure 3-3. Apros nodalisations for the suppression pool above the sparger end.



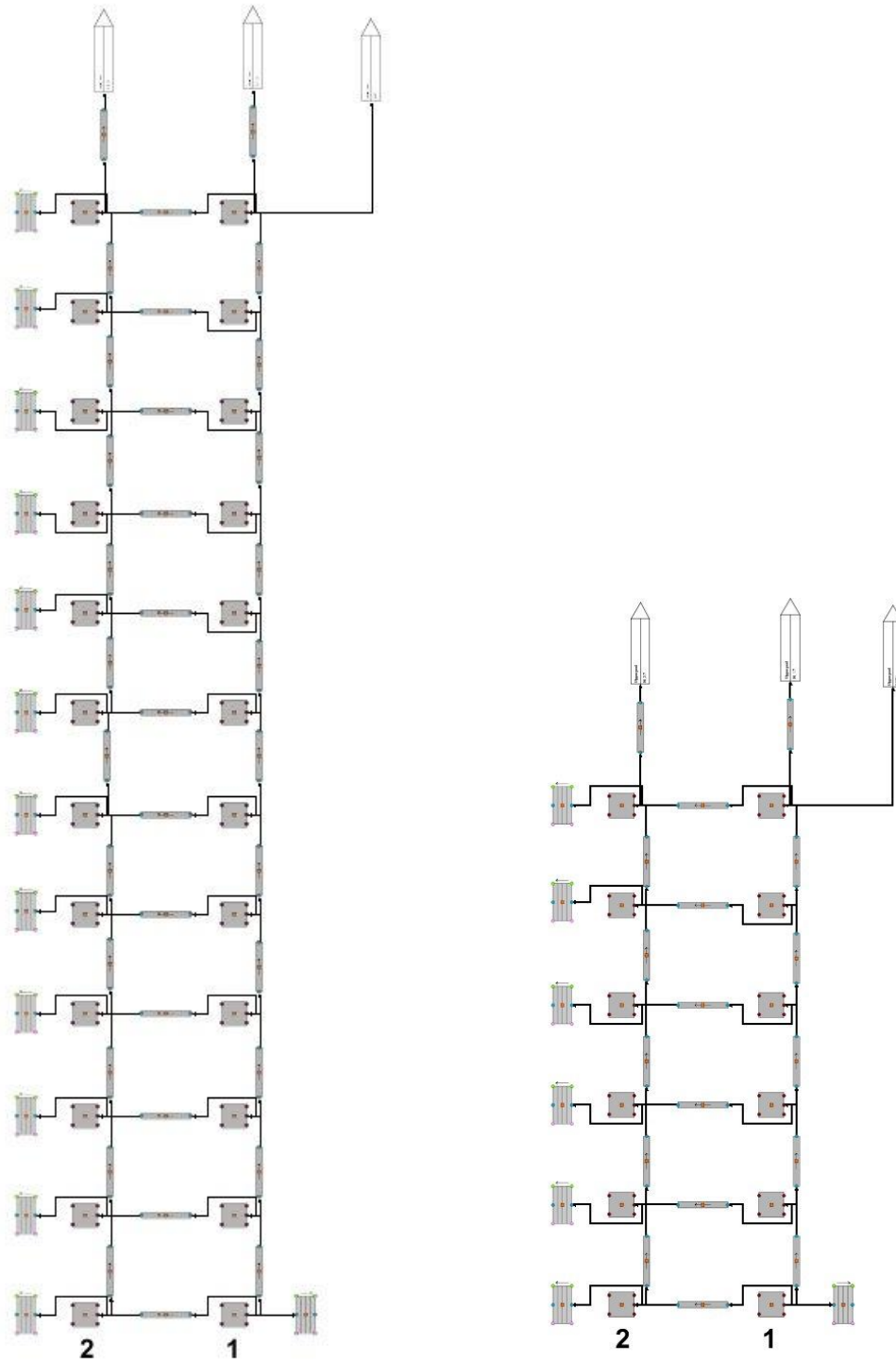


Figure 3-4. Apron nodalisations for the suppression pool below the sparger end (a dense nodalisation on the right, a simple nodalisation on the left).

## 4. Simulation results

---

The general purpose of the work was to assess the capability of Apros to simulate the pool stratification phenomena when using the 6-equation thermalhydraulic model and the pseudo 2D nodalisation for the pool. PPOOLEX test SPA-T3 was selected as an example case. One simulation is selected as a base case, which was assumed to be a best-estimate case. In addition, some sensitivity analyses were conducted.

### 4.1 Base case

The base case calculation had the most dense nodalisation where the pool above the sparger elevation is modelled with 9 vertical nodes (node height 0.2 m) and below the sparger with 12 node levels (node height 0.1 m). Therefore, the total amount of pool nodes was 42. The “inner” node column represented the area having 0.2 m diameter around the sparger line (total diameter of vessel is 2.4 m). The higher order upwind model was used for the pool enthalpy solutions in the vertical flow paths of the pool. Momentum transfer was activated only in the vertical flow paths. The flow loss coefficient (LC) of the vertical flow paths was 0.1, whereas a value 10 was used for the horizontal flow paths. Background of selection of LCs are discussed more in Chapter 4.2. The condensation correlation was the Chen correlation without Vierow-Schrock correction (input option 7).

The steam mass flow (and momentum) through the sparger holes into the pool water were directed sideways and downwards. This is based on the experimental observations where the steam jet coming out from the sparger holes were observed to have a downwards injection angle of about 10° (Gallero-Marcos 2018). This was attributed to the downward steam velocity inside the sparger pipeline, which cannot be re-directed at the sharp injection holes.

The measurements and simulation results of pool temperatures during the first stratification phase up to 4300 s are shown in Figure 4-1. The measurement are along the measuring bar L4 which is located at 0.8 m distance from the sparger vertical pipeline representing the node column 2 of the simulation model (see Figure 3-3 and Figure 3-4). The legends of the Figures indicate the distance from the pool bottom. The simulation results show that the final pool temperatures at 4300 s are in good agreement with the experiment indicating that the energy balance of pool including the heat losses to structures and from the pool surface are modelled reasonably. Also the simulated pool stratification and the position of thermocline match fairly well with the measurements that can be seen also in Figure 4-2 where the simulated and measured vertical temperature profiles at 4300 s are presented. Figure 4-3 illustrates the simulated temperature distribution at the same time instant made by StarNode post-processor software.

The measurements and simulation results during the whole test period including both the stratification and mixing phases are compared in Figure 4-4. The mixing phases of pool water cannot be simulated correctly with the current Apros model. During the first mixing phase at 4300 ... 5000 s, the simulated pool temperatures on at level of +0.5 m and above it increase slightly, but on the lower position the temperatures remain nearly intact until the end of the experiment. On the contrary, the measurement shows very good uniformity of all pool temperatures during the both mixing phases i.e. a very effective mixing of the whole pool takes place (Figure 4-5).

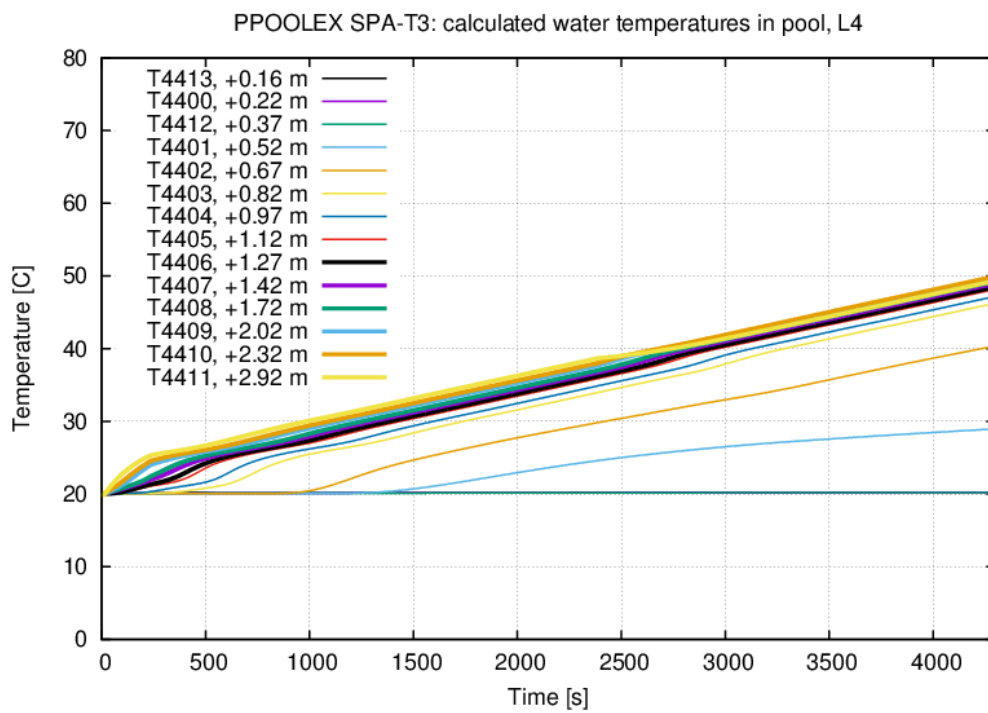
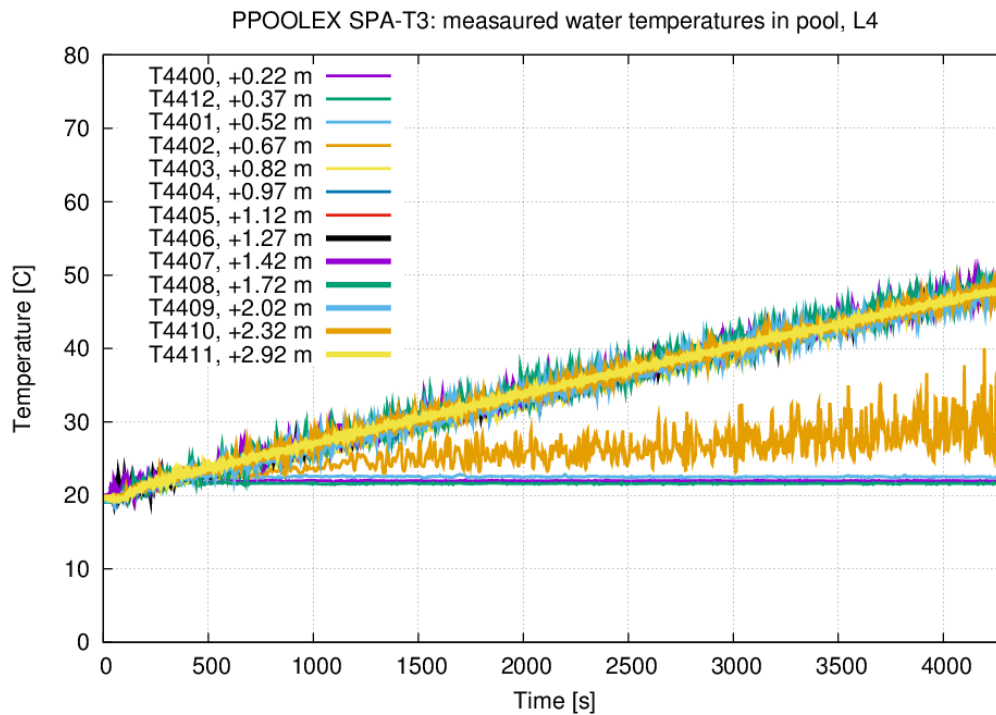


Figure 4-1. Pool temperatures in the first stratification phase up to 4303 s: measurements (up) and simulation (down).

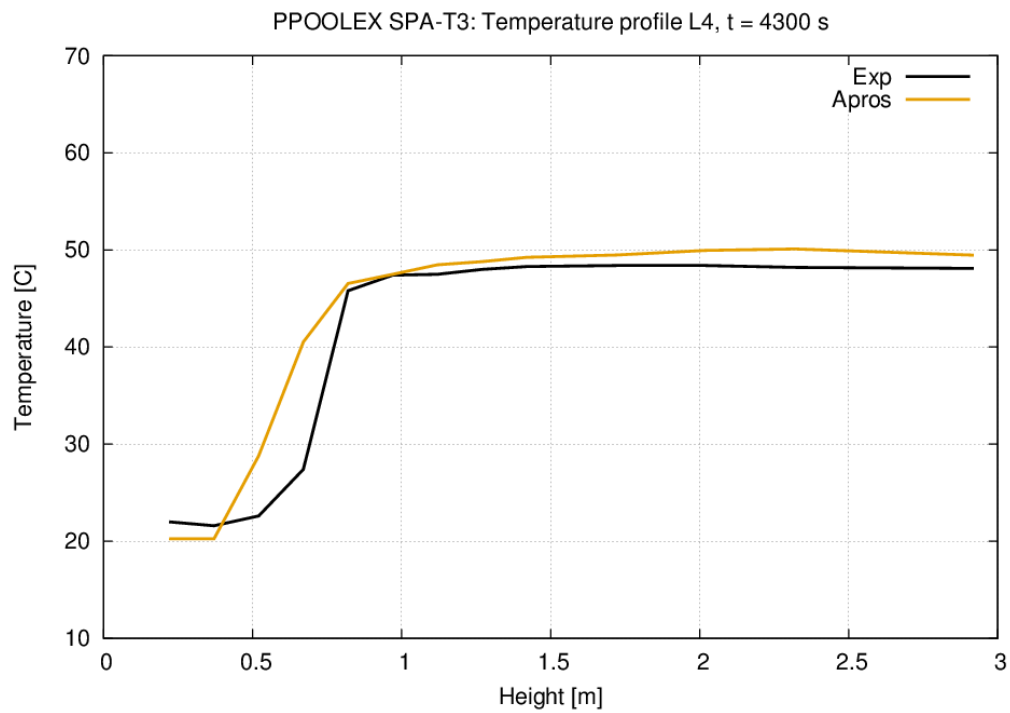


Figure 4-2. Vertical temperature profile along the vertical line L4 at 4300 s (stratification phase).

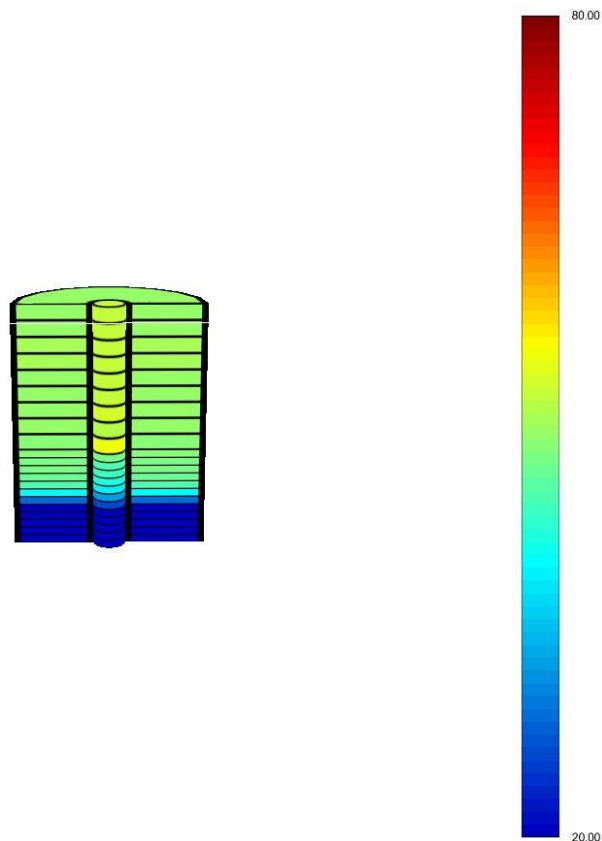


Figure 4-3. Calculated pool temperatures at 4300 s (stratification phase).

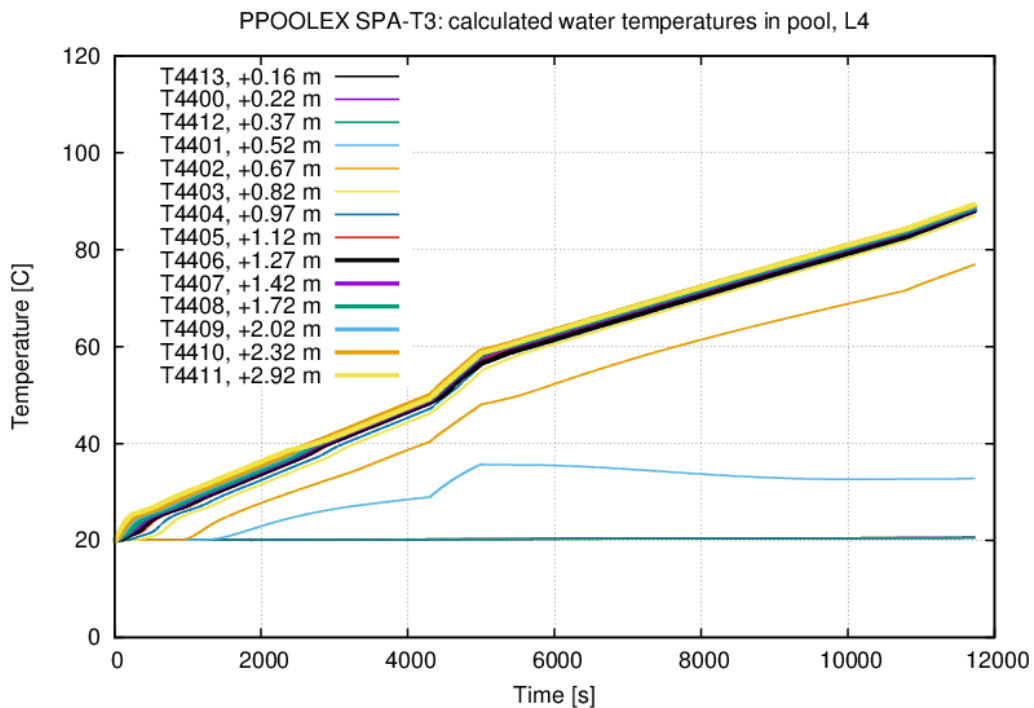
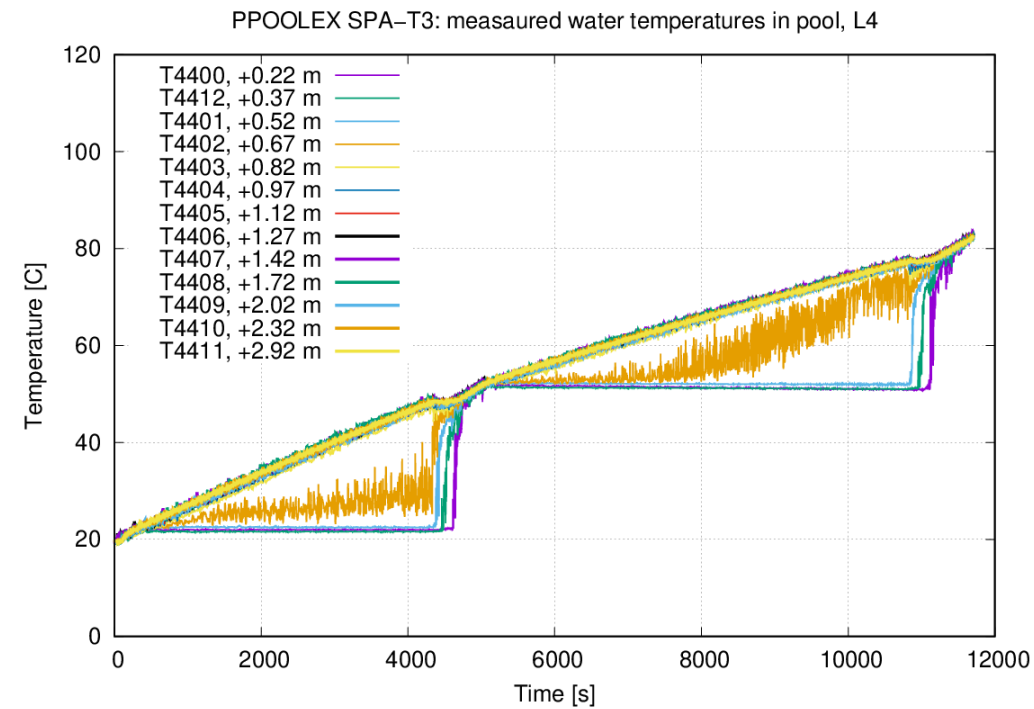


Figure 4-4. Pool temperatures during the whole tests period: measurements (up) and simulation (down).

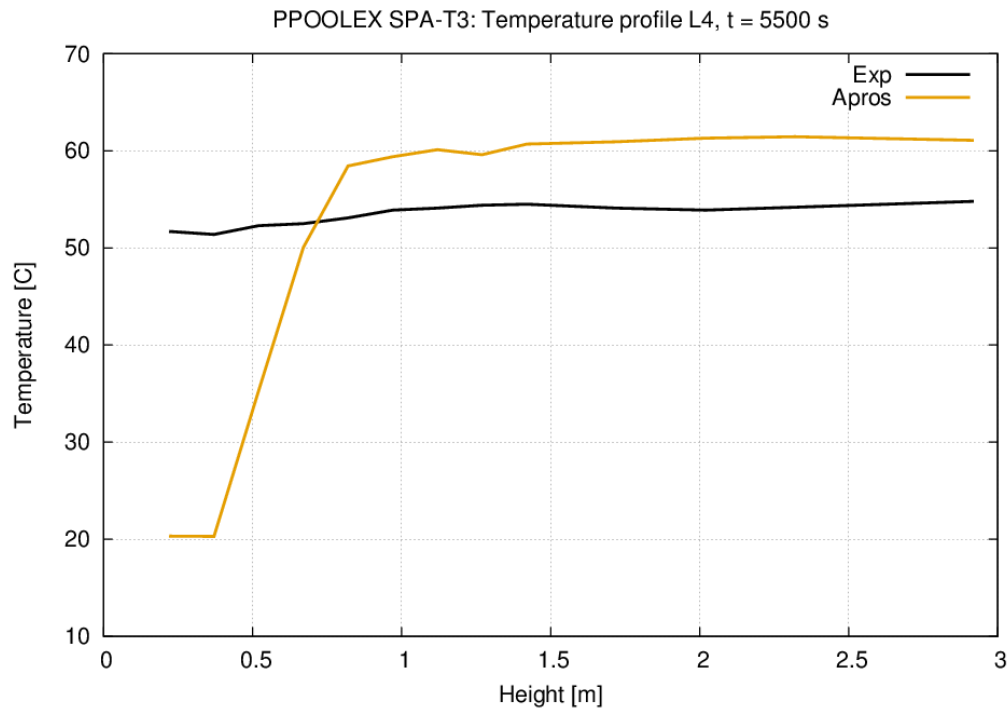


Figure 4-5. Vertical temperature profile along the vertical line L4 at 5500 s (mixing phase).

## 4.2 Sensitivity study

### 4.2.1 Steam mass flow (momentum)

Due to the difficulties in simulating pool mixing phases, a sensitivity study was made to find out whether the pool mixing can be reached, if the steam injection rate (and momentum) is higher. In this study, the simulated steam injection rate during the mixing phases (4300 ... 5000 s and 10 793 ... 11 735 s) was two times higher than in the experiment (Figure 4-6). Comparing the results to the Apros base case calculation and measurements in Figure 4-4, it is obvious that Apros is not able to simulate pool mixing despite a clear increase in the steam mass flow rate.

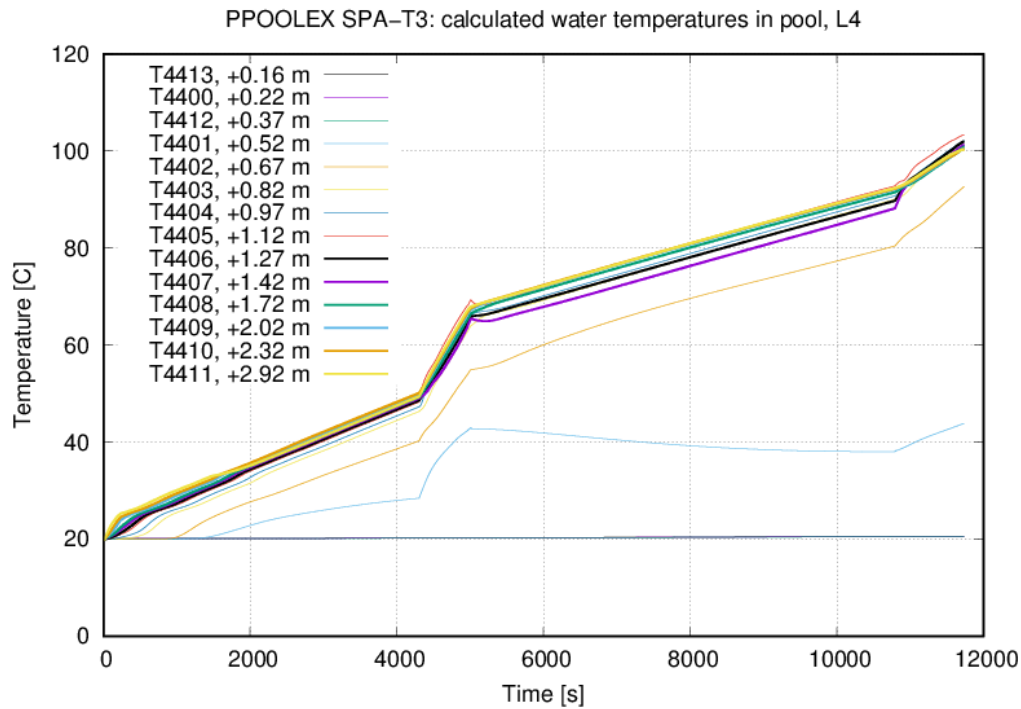


Figure 4-6. Simulated pool temperatures in the case of increased steam injection rate.

#### 4.2.2 Loss coefficient

In the base case simulation, the flow loss coefficient (LC) of the vertical flow paths was 0.1, whereas a value 10 was used for the horizontal flow paths. This was done to prevent

Figure 4-7 shows simulation results in the case, where the LCs are 0.1 for all flow paths of the pool. Otherwise, the input values and the boundary conditions are the same as in the base case. Figure 4-8 show the measured and simulated temperature profile at 4300 s in case where the loss coefficients are 0.1 and 10 (base case), and in case where the loss coefficient is 0.1 for all flow paths in the pool. Results shows that an increase in the loss coefficient in the horizontal flow paths leads to weaker horizontal mixing in the upper part of the pool, and correspondingly, stronger natural convection water flow from the upper pool below the sparger elevation. Consequently, the position of thermocline becomes lower during the stratification phase.

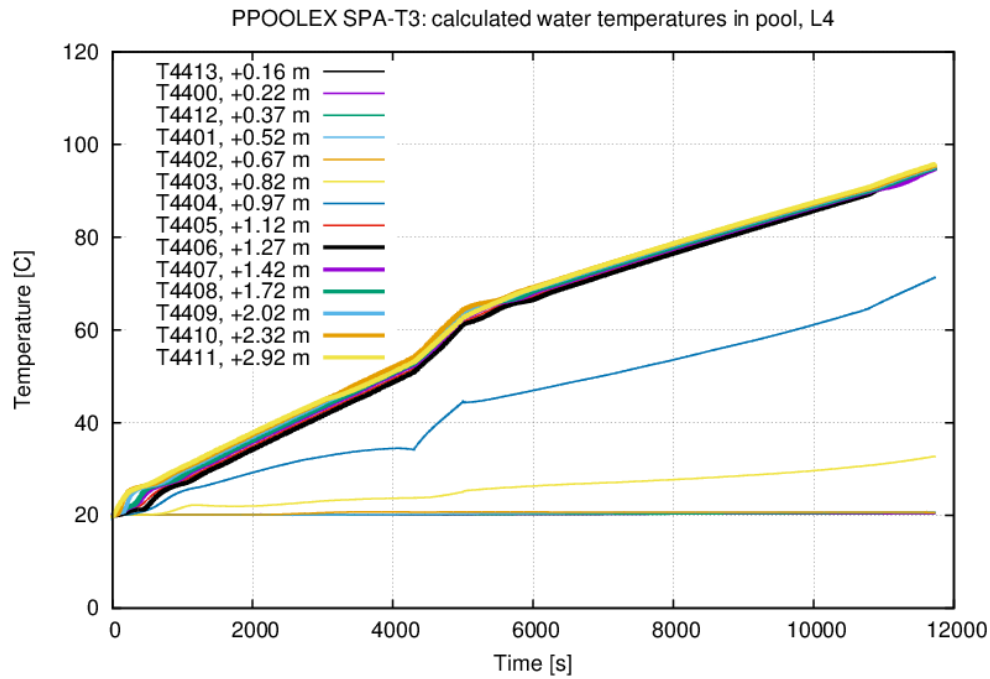


Figure 4-7. Simulated pool temperatures, LC 0.1 for all pool flow paths. Chen condensation with the Vierow-Schrock correction.

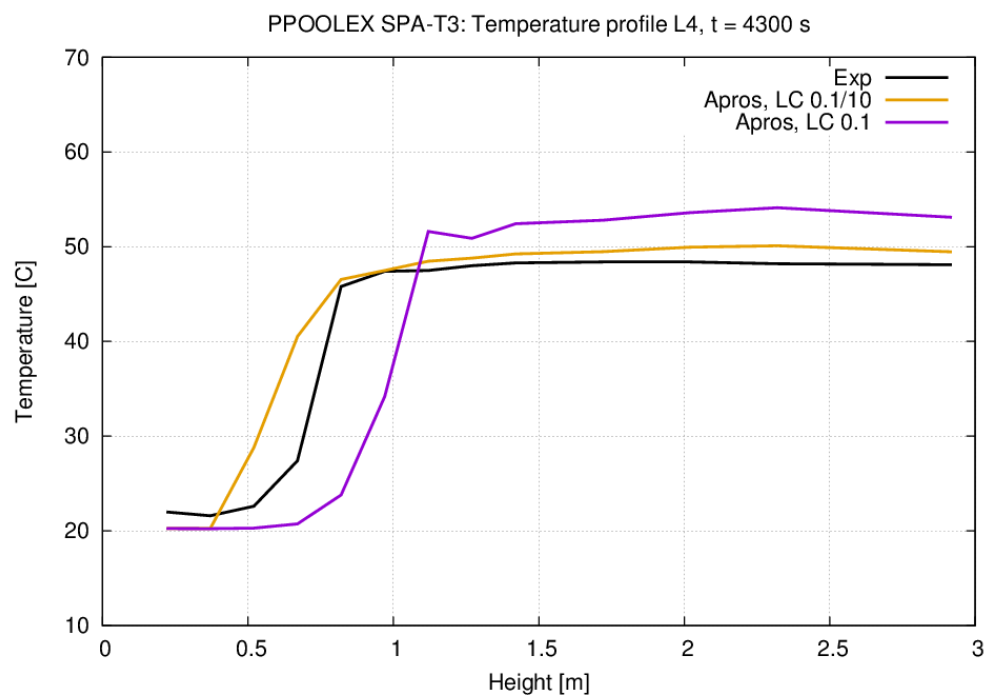


Figure 4-8. Vertical temperature profile along the vertical line L4 at 4300 s, effect of LCs (stratification phase).



### 4.2.3 Direction of steam source

In the base case simulation, the steam source is directed partly sideways and partly downwards according to the experimental observations (Gallero-Marcos 2018). Snapshots of the pool temperature and velocity fields during the PANDA pool stratification test HP5-2 shows that in the low steam injection phase buoyancy drives the water flow upwards to form a hot layer (Gallero-Marcos et al. 2018). In the high steam injection phase the larger momentum induced by the steam jets caused a faster erosion of the cold layer.

For comparison, a sensitivity study was performed with Apros where the steam source was directed only upwards to pronounce the buoyancy effect (Figure 4-9 and Figure 4-10 ). Otherwise, the input values and the boundary conditions are the same as in the base case. The results shows that the pool stratification phase up to 4300 s is extremely well predicted. The predicted location of thermocline in the case where steam is injected upward is better than in the base case simulation. However, the lack of modelling the pool mixing regimes remains.

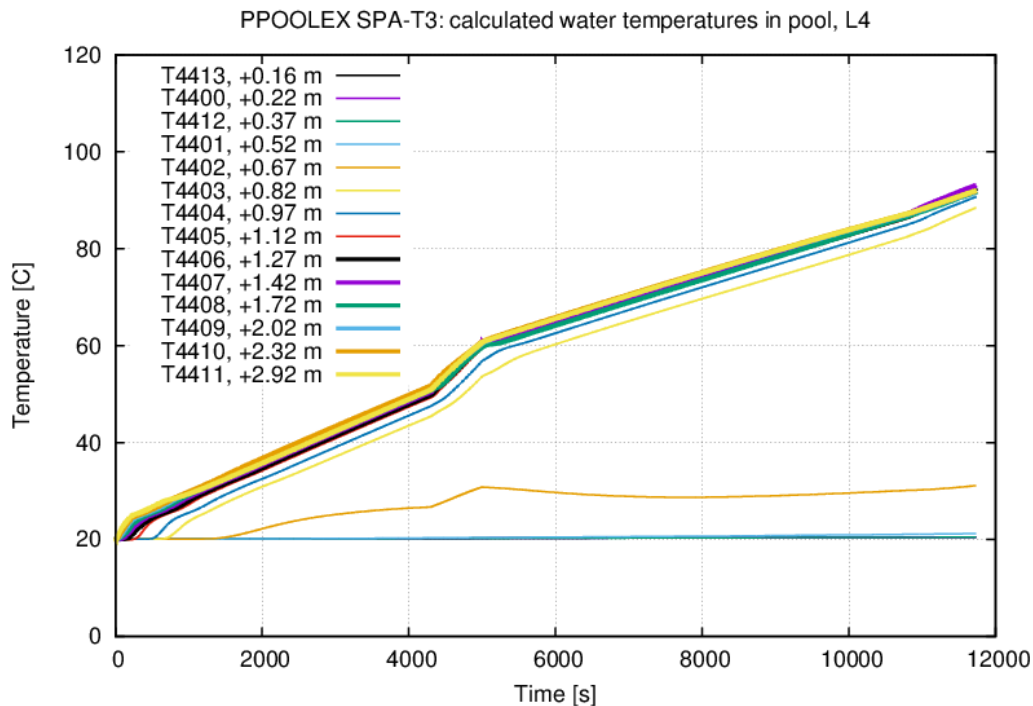


Figure 4-9. Simulated pool temperatures, steam source upwards.

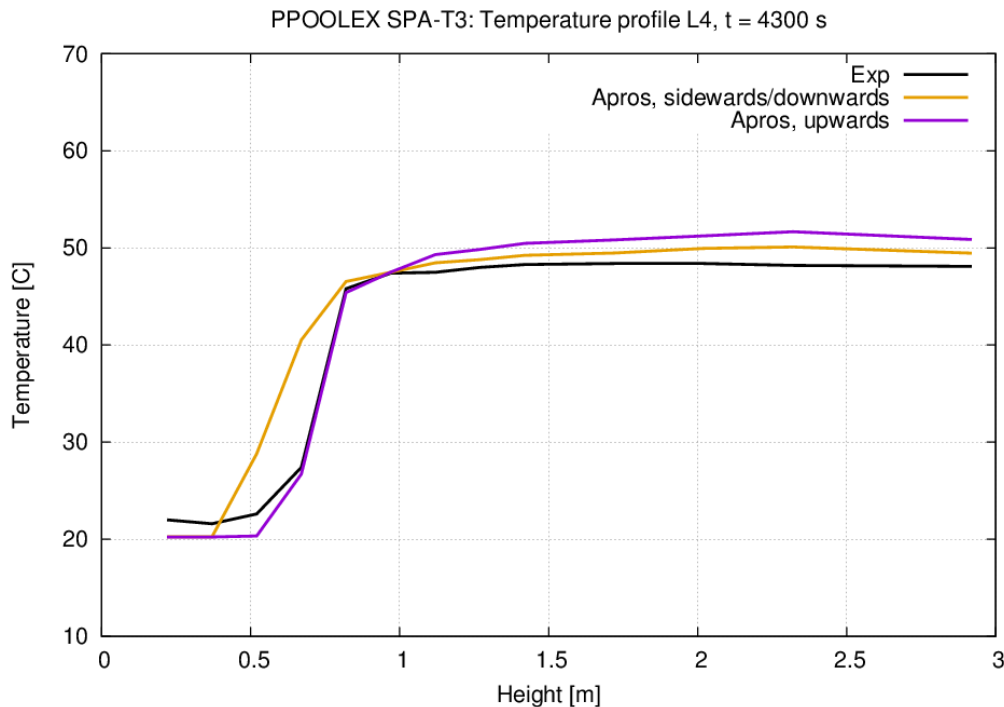


Figure 4-10. Vertical temperature profile along the vertical line L4 at 4300 s, effect of steam injection direction (stratification phase).

#### 4.2.4 Higher order upwind model

The simulations with conventional one-dimensional thermalhydraulic codes using the upwind discretisation scheme and averaged enthalpy in node have shown the difficulties in accurate simulation of thermal stratification in water tank (pool) (Hänninen 2009; Vihavainen et al. 1999). The sharp enthalpy distribution is unphysically smoothed when the fluid proceeds over several calculation meshes, i.e., numerical diffusion smoothens the temperature distribution inside the tank. The phenomenon can be attenuated by using a dense nodalisation and small time step, but the basic problem cannot be fully removed. Therefore, an alternative discretization scheme has been implemented in Apros, where the liquid first order upwind enthalpy transported from node to node in the area close to the thermally stratified layer was defined using information from three consecutive nodes (Hänninen 2009). Using the higher order discretisation scheme the numerical diffusion can be largely eliminated in most cases. Sufficient dense nodalisation is however needed to capture the real sharp stratification, because the temperature is calculated as function of the solved enthalpy which still represents the average enthalpy of node.

Figure 4-11 and Figure 4-12 show simulation results where the first order upwind discretization is used for pool enthalpy solution. Otherwise, the input values and the boundary conditions are the same as in the base case. The simulation with the higher order discretisation predicts better the deep stratification thermocline, and this discretisation scheme was used in all other simulations of this work.

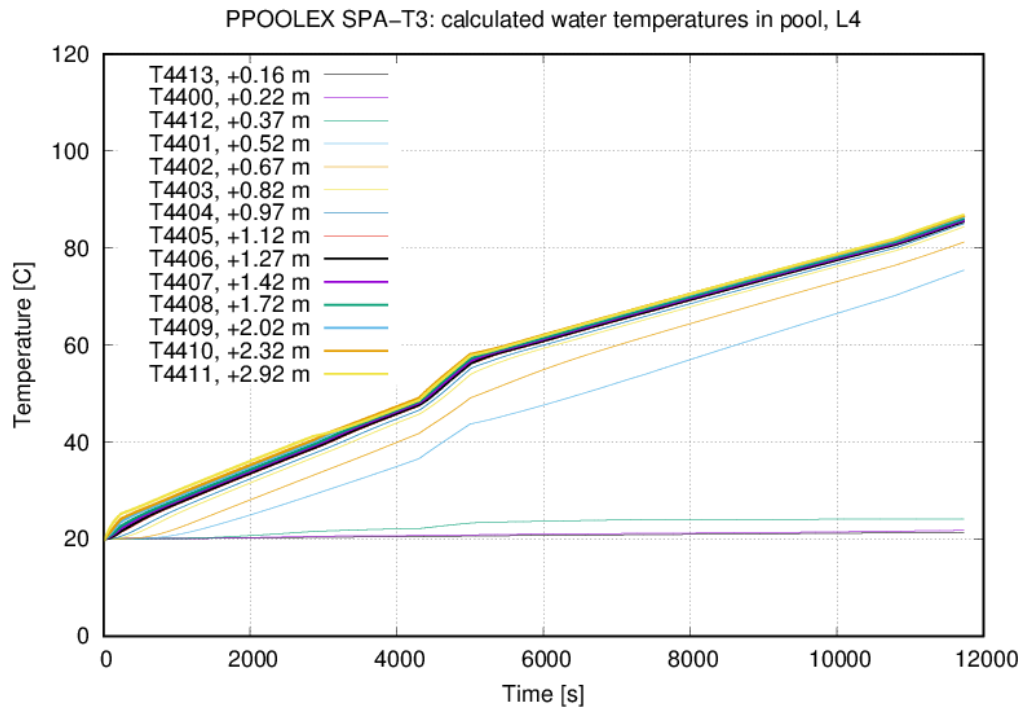


Figure 4-11. Simulated pool temperatures, first order upwind discretization.

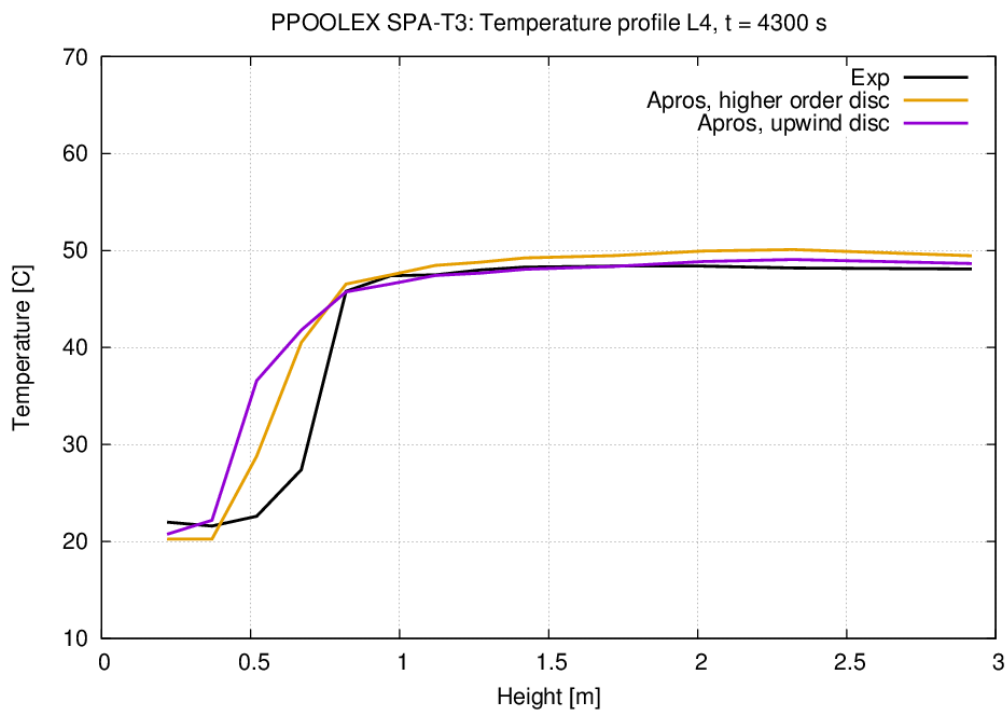


Figure 4-12. Vertical temperature profile along the vertical line L4 at 4300 s, effect of discretization scheme (stratification phase).

#### 4.2.5 Size of inner node column

The cross section area of the inner node column of Apros base case nodalisation represents the situation where the circular inner node has a diameter of 0.2 m. The comparison calculations where the inner node column has a 0.8 m diameter is also performed. Otherwise, the input values and the boundary conditions are the same as in the base case.

Results show that when the volume of the inner node column is smaller, the pool stratification below the sparger elevation is much better predicted (Figure 4-13 and Figure 4-14). But neither of the case can predict the pool mixing realistically when comparing to measurements.

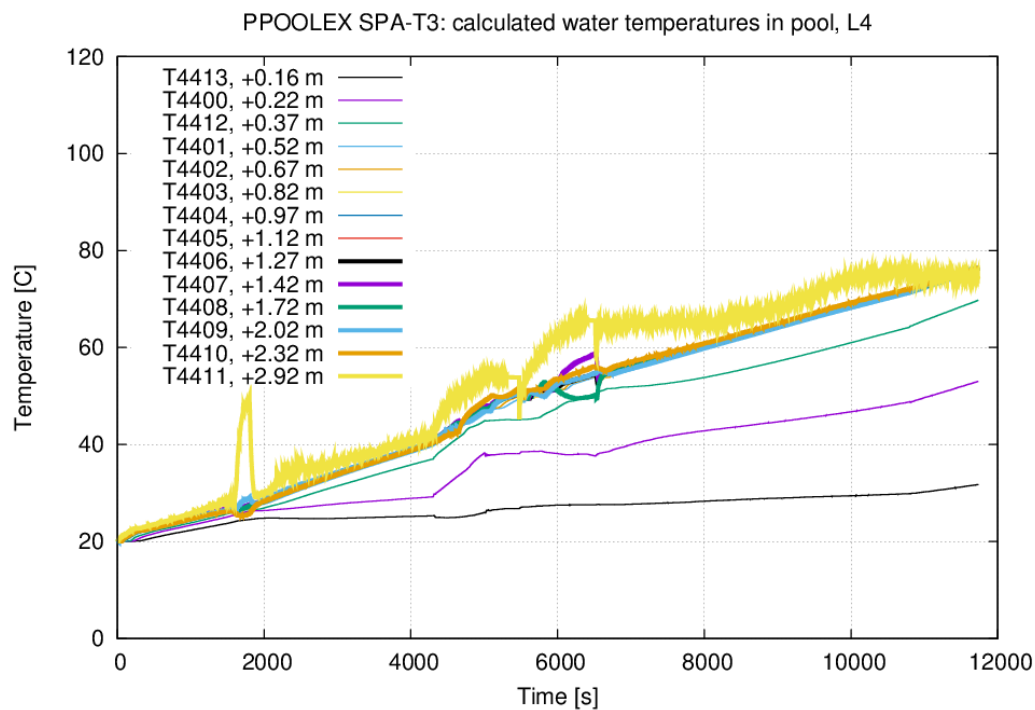


Figure 4-13. Simulated pool temperatures, large node column 1.

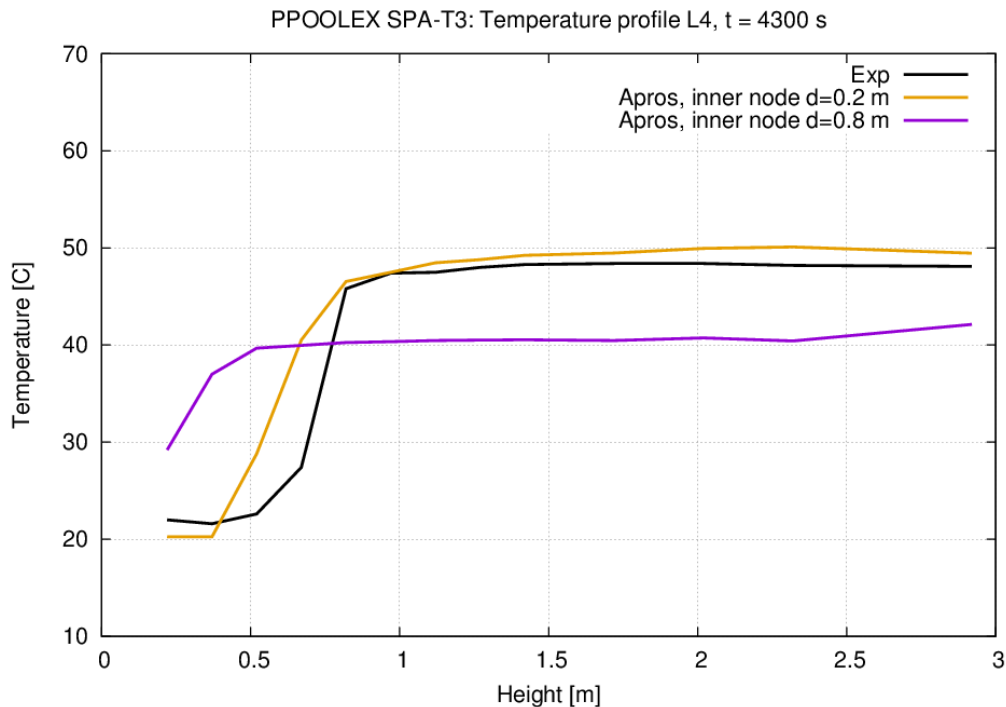


Figure 4-14. Vertical temperature profile along the vertical line L4 at 4300 s, effect of inner node column (stratification phase).

#### 4.2.6 Number of nodes below the sparger elevation

In the base case model, 12 vertical node levels corresponding to 0.1 m node height was used below the sparger level. In one comparison case, the nodalisation below the sparger elevation was coarser (6 versus 12 vertical node levels representing the total number of vertical nodes 15 and 21, respectively). Otherwise, the input values and the boundary conditions are the same as in the base case.

Simulation results with the coarser nodalisation indicates that the lower parts of the pool start warming and mixing after the time instant of 1500 s (Figure 4-15 and Figure 4-16). The gradient of warming of both the upper and lower parts of the pool are fairly similar and the temperature difference between the pool top and bottom remains fairly constant until the end of simulation. It is obvious that too coarse nodalisation cannot capture the pool stratification phenomena. This is maybe caused by the numerical diffusion. Sufficient dense nodalisation is needed to capture the real sharp stratification, because the temperature is calculated as function of the solved enthalpy which still represents the average enthalpy of node. The simulation with the coarse nodalisation cannot either predict the pool mixing correctly.

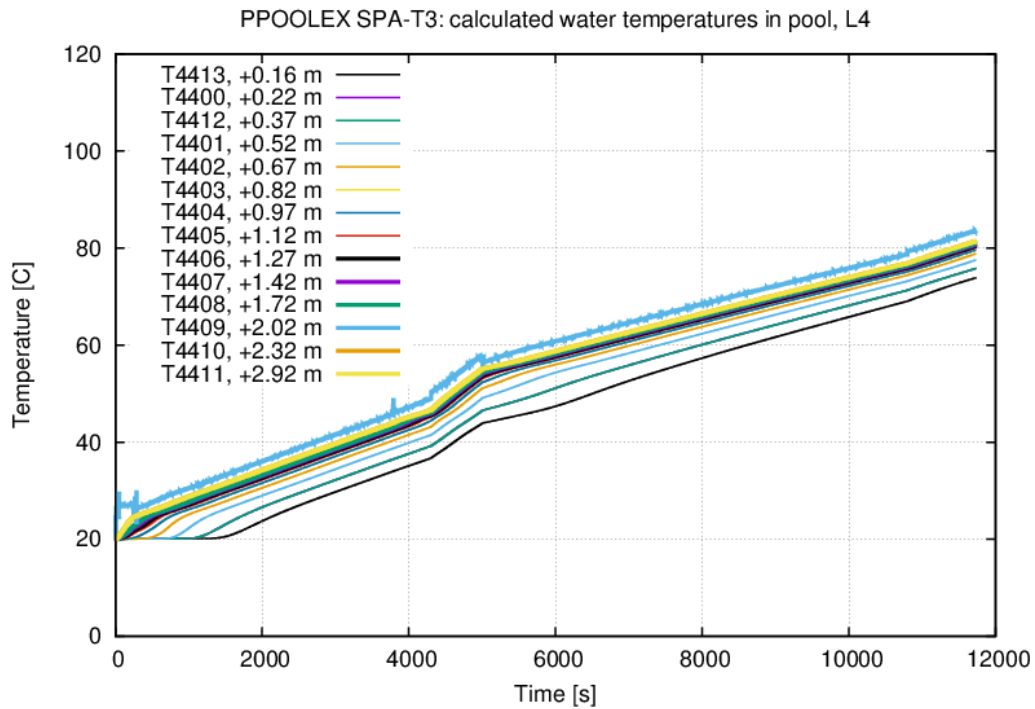


Figure 4-15. Simulated pool temperatures, 30 cell nodalisation.

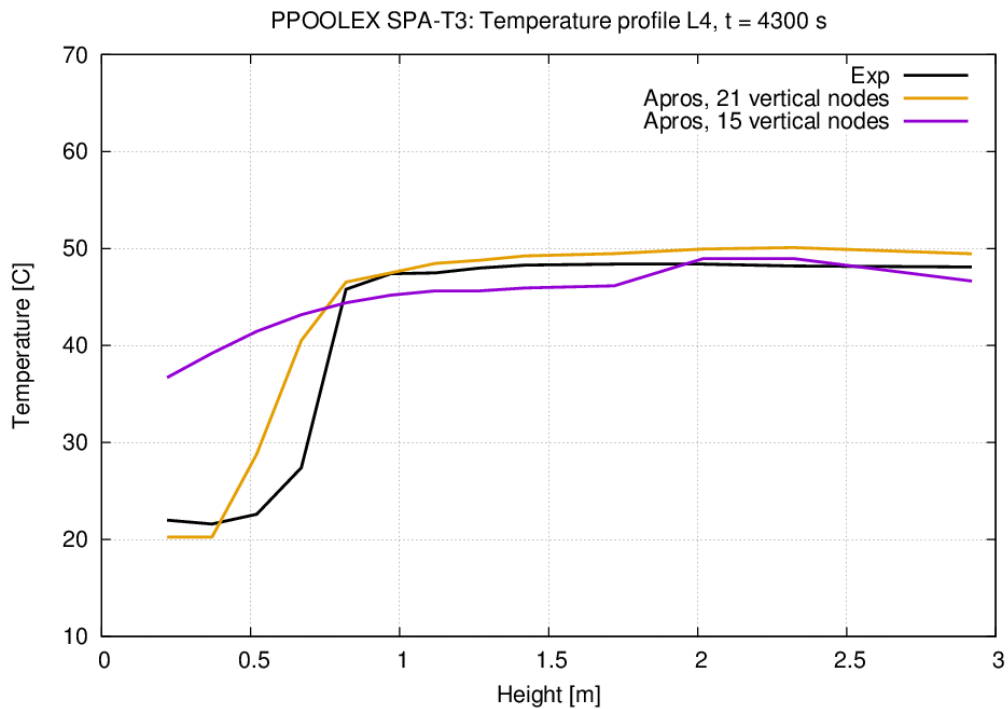


Figure 4-16. Vertical temperature profile along the vertical line L4 at 4300 s, effect of vertical nodalisation (stratification phase).

#### 4.2.7 Other observations

When varying maximum time step between 1 ... 10 ms, there was no significant deviations in the calculation results. Longer time step was not tested. Value of 5 ms was used in the final simulations, and the ratio of simulation time to required CPU time using the denser 42 cell pool nodalisation was around 0.4 ... 0.5. The corresponding ratio with the 30 cell pool nodalisation was around 0.6 ... 0.7. Minimum number of pressure iterations in each time step was 7. Allowed mass error was  $1.0\text{e-}4$  (default value).

The Shah condensation correlation of Apros could not model the steam condensation in the pool realistically. The Chen correlation without the Vierow-Schrock correction (input option 7) predicts the steam condensation reasonably.

## 5. Conclusions

---

KTH has developed and validated the Effective Heat Source (EHS) and Effective Momentum Source (EMS) models providing computational efficiency and sufficient accuracy in the modelling of pool stratification effects. The previous work at VTT studied and summarized the prerequisites of the Apros lumped parameter containment model and thermalhydraulic model for simulating stratification phenomena of suppression pool. Also the possibility to implement the EHS/EMS model in Apros was considered. The summary of the work was that the EHS/EMS model is not directly applicable in Apros LP modelling, but could be maybe utilized in the stratification calculation when using the Apros thermalhydraulic model. However, the concern was that the Apros thermalhydraulic model applies 1D flow solution, whereas the EHS/EMS model is developed to be coupled with 2D or 3D flow solver.

The goal of this work was to study stratification modeling capability of Apros 1D thermalhydraulic model using so called pseudo-2D nodalisation. The PPOOLEX stratification test SPA-T3 was simulated. The sensitivity studies included e.g. the effect of nodalisation concept, loss coefficient, direction of momentum transfer from steam source, discretization scheme and steam mass flow during the pool mixing phase.

The simulation results show that the pool stratification phase was predicted well with the 2-column nodalisation used. Sufficient dense nodalisation is needed to capture the real sharp stratification, because the temperature is calculated as function of the solved enthalpy which still represents the average enthalpy of node. The best agreement is obtained when using the higher order discretisation scheme for enthalpy solution and the larger loss coefficient for the horizontal branches than for the vertical ones.

The results also showed that the pool mixing phase could not be predicted reasonably. If the nodalisation is very coarse, pool mixing takes place, but it is then mostly caused by numerical diffusion or inaccuracy in modelling the real sharp stratification thermocline.

Sensitivity study showed that a significant increase in steam mass flow (and momentum) did not improve the predicted pool mixing. Therefore, implementation of the EHS/EMS model in Apros would not probably solve alone the deficiencies found in the mixing calculation. Maybe the EHS/EMS approach should be modified or totally different approach should be tailored to Apros's need in order to model better the pool stratification/mixing phenomena.

The Shah condensation correlation of Apros, which is the default correlation, could not model realistically the steam condensation in the pool. The Chen correlation without Vierow-Schrock correction (option 7) seemed to predict reasonably the steam condensation inside water pool.



## References

---

- Hänninen, M. 2009. Phenomenological extensions to Apros six-equation model. Doctoral thesis. VTT Publications 720.
- Jo, B. et al. 2016. Thermal stratification in a scaled-down suppression pool of the Fukushima Daiichi nuclear power plant. *Nuclear Engineering and Design* 305(2016)39-50.
- Mizokami, S. et al. 2016. Unsolved issues related to thermal-hydraulics in the suppression chamber during Fukushima Daiichi accident progression. *Journal of Nuclear Science and Technology*, 53, 630-638.
- Gallero-Marcos, I., Villanueva, W., Kudinov, P. 2016. Thermal stratification and mixing in a large pool induced by operation of spargers, nozzles, and blowdown pipes. *Nordic Nuclear Safety Research*, NKS-369. ISBN 978-87-7893-454-3. July 2016.
- Gallero-Marcos, I. 2018. Steam condensation in a water pool and its effect on thermal stratification and mixing. KTH School of Engineering Sciences. Doctoral thesis.
- Gallero-Marcos, I. et al. 2018. Pool stratification and mixing induced by steam injection through spargers: analysis of the PPOOLEX and PANDA experiments. *Nuclear Engineering and Design* 337(2018) 300-316.
- Laine, J., Puustinen, M., Räsänen, A. 2009. PPOOLEX experiments on thermal stratification and mixing. *Nordic Nuclear Safety Research*, NKS-117.
- Laine, J., Puustinen, M., Räsänen, A. 2014. PPOOLEX mixing experiments. *Nordic Nuclear Safety Research*, NKS-309.
- Li, H., Villanueva, W., Kudinov, P. 2014a. Approach and development of effective models for simulation of thermal stratification and mixing induced by steam injection into a large pool of water. *Science and Technology of Nuclear Installations*, 2014, Article ID 108782, 11 pages.
- Li, H., Villanueva, W., Puustinen, M., Laine, J., Kudinov, P. 2014b. Validation of effective models for simulation of thermal stratification and mixing induced by steam injection into a large pool of water. *Science and Technology of Nuclear Installations*, 2014, Article ID 752597.
- Pättikangas, T. 2020. CFD analysis of pressure suppression pool by using effective heat and momentum source models. Research report no. VTT-R-00228-20. VTT Technical Research Centre of Finland. 25.03.2020.
- Silde, A. 2019. Assessment of implementation of the effective heat and momentum source models in Apros. Research report no. VTT-R-01029-19. VTT Technical Research Centre of Finland. 29.22.2019.

Vihavainen, J., Hänninen, M., and Tuunanen, J. 1999. Improved thermal stratification modeling in the Apros code simulations of passive safety injection experiments. 9<sup>th</sup> International Topical Meeting in Nuclear Reactor Thermal Hydraulics (NURETH-9). San Francisco, California, October 3-8-, 1999.

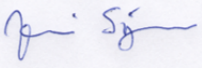

## **Appendix D**

**CFD study of condensation test SPA-T3 in PPOOLEX test vessel with VOF, k- $\omega$  turbulence and EMS/EHS condensation models**

# CFD study of condensation test SPA-T3 in PPOOLEX test vessel with VOF, $k-\omega$ turbulence and EMS/EHS condensation models

Authors: Jouni Syrjänen

Confidentiality: Public

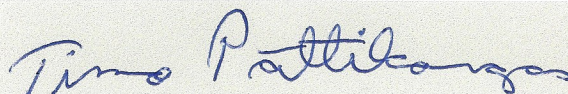
<b>Report's title</b> CFD study of condensation test SPA-T3 in PPOOLEX test vessel with VOF, $k-\omega$ turbulence and EMS/EHS condensation models	
<b>Customer, contact person, address</b> 1. Yli-insinööri Jorma Aurela, Valtion ydinjätehuoltorahasto, PL 32, 00023 Valtioneuvosto 2. Programme Manager NKS-R Ari-Pekka Leppänen, STUK, Lähteentie 2, 96400 Rovaniemi, Finland	<b>Order reference</b> Dnro SAFIR 12/2020  ATF/NKS-R(20)130/6
<b>Project name</b> CFD methods for reactor safety assessment (CFD4RSA)	<b>Project number/Short name</b> 124962 - SAFIR2022_CFD4RSA_2020
<b>Author(s)</b> Jouni Syrjänen	<b>Pages</b> 14
<b>Keywords</b> Pressure suppression pool, BWR, CFD, EMS/EHS, VOF, $k-\omega$	<b>Report identification code</b> VTT-R-00144-21
<b>Summary</b> <p>The stratification and mixing phases of the SPA-T3 condensing test performed in the PPOOLEX test vessel were simulated with the CFD software ANSYS Fluent v.19.5 using the volume of fluid (VOF) model for free surface and <math>k-\omega</math> turbulence model. The VOF model was included to describe the water surface elevation and to improve the heat transfer on the water surface, which issues were noted in the earlier simulation (Pättikangas, 2020). The steam jets of the SPA-T3 test were modelled with the effective momentum source and the effective heat source (EMS/EHS) models, which simplify the CFD modelling task and save computational resources.</p> <p>The model combination of EMS/EHS, VOF and <math>k-\omega</math> was combined in the ANSYS Fluent v.19.5 simulation. The simulation underpredicted the mixing of pool water to some degree. It suggested stronger stratification of temperature both in stratification and mixing phases of the experiment than observed. When the EMS/EHS source location was extended for the mixing phase simulation, the mixing improved considerably.</p> <p>The weaker than expected mixing might have been caused partly by less accurate discretization schemes, which were used for convergence or compatibility reasons. For future improvements, convergence might benefit from using polyhedral grid. Also, <math>k-\omega</math> turbulence model may predict lower level of turbulence and thus weaker heat transfer than <math>k-\epsilon</math> model used in the earlier simulation (Pättikangas, 2020). Extending the EMS/EHS source location, if necessary, could be done in more optimal way. Including heat losses from the steam pipe to EHS model and the through the vessel wall would further improve the model, the latter by enhancing circulation from the top of the vessel to the bottom.</p>	
<b>Confidentiality</b>	Public
<b>Written by</b>  Jouni Syrjänen Senior Scientist	<b>Reviewed by</b>  Ari Silde Senior Scientist
<b>VTT's contact address</b> VTT Technical Research Centre of Finland Ltd, P.O.B 1000, FI-02044 VTT	
<b>Distribution (customer and VTT)</b> SAFIR2022 Reference group, NKS-R Programme Manager	
<i>The use of the name of VTT Technical Research Centre of Finland Ltd in advertising or publishing of a part of this report is only permissible with written authorisation from VTT Technical Research Centre of Finland Ltd.</i>	

**Approval**

Date:

5.4.2021 Espoo

Signature:

A handwritten signature in blue ink, reading 'Timo Pättikangas'.

Name:

Timo Pättikangas

Title:

Research Team Leader, Principal Scientist

## Contents

---

Contents.....	3
1. Introduction.....	4
2. Goal.....	4
3. Description.....	4
4. Limitations .....	6
5. Methods.....	6
6. Results.....	8
6.1 Comparison of predicted temperature, velocity and effective heat conduction fields.	8
6.2 Predicted water temperatures in stratification phase with original steam source location.....	10
6.3 Predicted water temperatures in mixing phase with original steam source location.	11
6.4 Predicted water temperatures in mixing phase with extended steam source location.....	12
7. Conclusions and summary.....	13
References.....	14

## 1. Introduction

---

Steam discharge resulting from accident is conveyed to water pool to condensate the steam in some types of boiling water reactors. The behaviour of steam and water in the pool affect the efficiency of the pool to act as a heat sink for the discharge. For example, thermal stratification of the water in the pool may result in higher surface temperature of the pool and increased pressure in the reactor containment.

The PPOOLEX test facility in Lappeenranta University of Technology has been set up to generate experimental data related to condensation studies. The data is then used to develop and validate numerical simulation models. In a series of SPA tests, steam is led through a pipe to a sparger submerged in the test vessel. The vessel is equipped with multiple thermocouples to record the water temperature during the different phases of experiments.

The experiments have been modelled recently at VTT using ANSYS Fluent (Pättikangas, 2020) in 3D simulation and using Apros (Silde, 2020) in 1D simulation with pseudo 2D nodalisation. The 3D simulation indicated that the description of the water surface heat transfer might be improved by including free surface model in the CFD simulation.

## 2. Goal

---

In the present study, a 3D flow simulation of SPA-T3 test is performed with the commercial CFD software ANSYS Fluent v.19.5 for model validation purposes. The heat and momentum induced by steam to water are described with effective heat (EHS) and momentum source (EMS) models. Turbulence is modelled with the  $k-\omega$  model and the free surface with volume of fluid (VOF) model. Fluid flow and temperature are solved in the vessel and predicted temperature is compared to measured data.

## 3. Description

---

Laine et al. (2015) describe the PPOOLEX test vessel in detail. It consists of wetwell (condensation pool) and drywell compartments, separated by a floor. The compartment volumes are scaled down from the Olkiluoto plant. The diameter of the vessel is 2.38 m, the wetwell height is 4.22 m, and the initial water surface height is 3.0 m.

In the SPA experiments, steam is blown via a sparger pipe in the wetwell. The vertical sparger pipe is located 0.42 m to the side from the centre of condensation pool. The height of the end of the sparger pipe is 1.2 m from the vessel bottom. There are a total of 32 holes with 8 mm diameter located in 4 axial and 8 circumferential locations in the sparger head in the end of the pipe releasing the steam in the water.

In the SPA-T3 test, the steam is blown through the sparger in the wetwell in alternating mixing and stratification sequences shown in Table 1. In the simulation, stratification phase from 235 to 4303 s and mixing phase from 4303 to 5000 s were studied.



Table 1. Phases of SPA-T3 condensation tests. Simulated phases indicated by asterisk \*.

Test phase	Time range (s)	Steam mass flow rate (g/s)
Mixing phase	35 ... 235	220
Stratification phase*	235 ... 4303	120
Mixing phase*	4303 ... 5005	260
Stratification phase	5005 ... 10 793	95
Mixing phase	10 973 ... 11 735	125

The temperature in the test vessel is monitored quite extensively (Laine et al., 2015). In the present study, water temperatures are recorded at vertical locations on the measuring lines L1, L2, L3 and L4. The measuring lines are shown in Figure 1 and the vertical locations in Table 2.

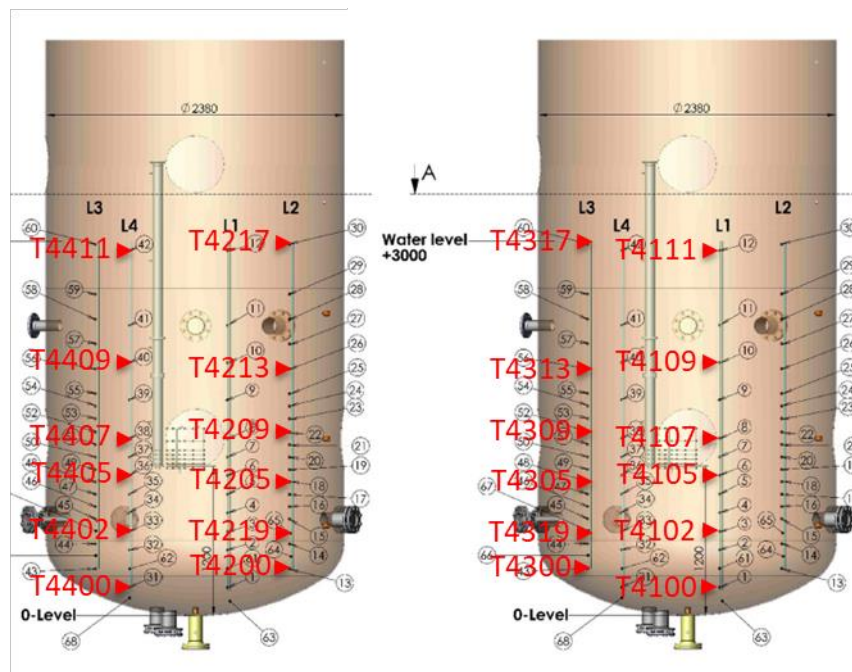


Figure 1. Measurement locations of water temperature in vessel for simulations of SPA-T3 experiment.

*Table 2. Heights of measuring locations along measuring lines L1, L2, L3 and L4 monitored in simulations.*

Line L1	Line L2	Line L3	Line L4	Height (mm)
				0 Vessel bottom
T4100			T4400	222
	T4200	T4300		372
T4102	T4219	T4319	T4402	672
	T4205	T4305		1072
T4105			T4405	1122
				1200 Sparger tip
T4107			T4407	1422
	T4209	T4309		1472
	T4213	T4313		1972
T4109			T4409	2022
T4111			T4411	2922
	T4217	T4317		2972
				3000 Initial Surface

## 4. Limitations

The following simplifications are used in the simulations: The flow field in the vessel is assumed to be stationary as an initial condition for the simulation at 235 s. All the vessel walls are assumed to be adiabatic. Heat loss from the steam pipe to pool water is not accounted for in the EHS source.

## 5. Methods

ANSYS Fluent v19.5 CFD software was used to simulate the SPA-T3 condensation experiment. Volume of fluid (VOF) model describing the free surface rising with the increasing water volume is used in multiphase calculation. Air, modelled as ideal gas, is defined as primary phase and water as secondary phase. Turbulence is modelled with the  $k-\omega$  model taking account of buoyancy effect. The computational domain is illustrated in Figure 2.

Pressure-velocity coupling was solved with the SIMPLE method. In spatial discretization, PRESTO! was used for pressure, and the second order upwind methods for density, momentum, turbulent kinetic energy and specific dissipation rate, as well as for energy. Volume fraction was solved using the geo-reconstruct scheme. First order implicit time discretization was used in the simulations. The computational grid consists of 540 000 hexahedral cells and it is refined with o-grid around the steam pipe and sparger. Parts of the grid are illustrated in Figure 3.

The steam blown in the vessel is modelled with the effective momentum source (EMS) and the effective heat source (EHS) models of Gallego-Marcos (2018, Gallego-Marcos et al., 2019a, Gallego-Marcos et al., 2019b) The application of the models in the CFD simulation of the SPA-T3 experiment with the ANSYS Fluent is described by Pättikangas (2020). The main idea is not to introduce a separate steam phase in the vessel, but transfer the effects of

condensing steam jets to pool water as sources, thus simplifying the CFD modelling task. In addition to mass and enthalpy sources from inflowing steam to water, momentum sources of the form

$$M = C\rho_s AU_s^2 \quad (1)$$

for pool water are set next to the orifice locations of the sparger where steam jets meet water and condensation takes place.  $A$  denotes the orifice area. Coefficient  $C$  depends on the steam mass flow, number of orifices and subcooling of pool water (Gallego-Marcos, 2018).  $C=1.0$  was used in the stratification phase and  $C=0.77$  in the mixing phase of the simulations of the experiment. Part of the momentum is also addressed to turbulence source. Enthalpy loss due to condensation of steam has been taken into account in the enthalpy source.

In the present simulation, the sources were originally set in computational cells next to orifice locations. In the extended source test, the EMS/EHS source locations were extended 0.23 m perpendicularly from the orifices keeping the magnitude of the sources equal to the original. The source locations are shown in Figure 4.

The pool water was at rest in the beginning of the simulation. Its uniform temperature was set to 21 °C and surface height to 3.0 m. The steam mass flow rates and the corresponding sources were then set according to Table 1. Time step sizes of 0.01 s and 0.02 s were used in the simulation. The vessel walls and top were assumed to be adiabatic. The steam pipe outer wall temperature was set to 106.43 °.

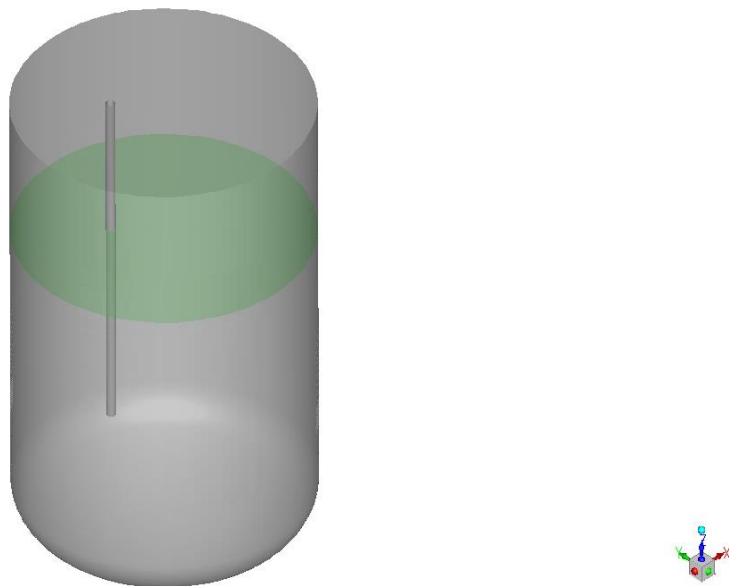


*Figure 2. Simulated vessel geometry. The initial water surface is indicated by green colour.*

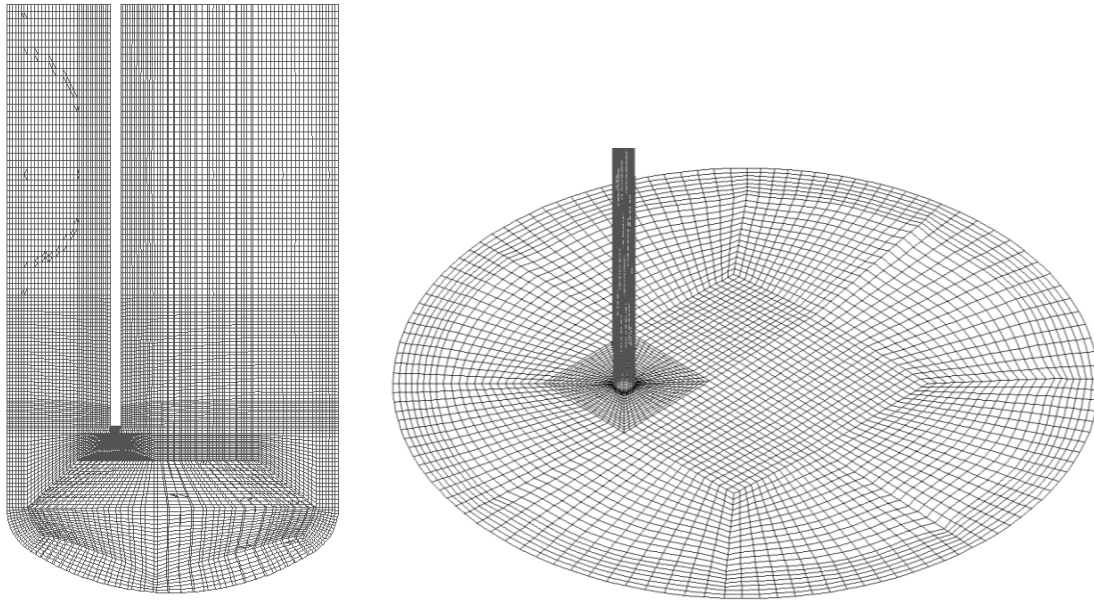


Figure 3. Computational grid used in simulations in vertical and horizontal cross sections of the vessel.

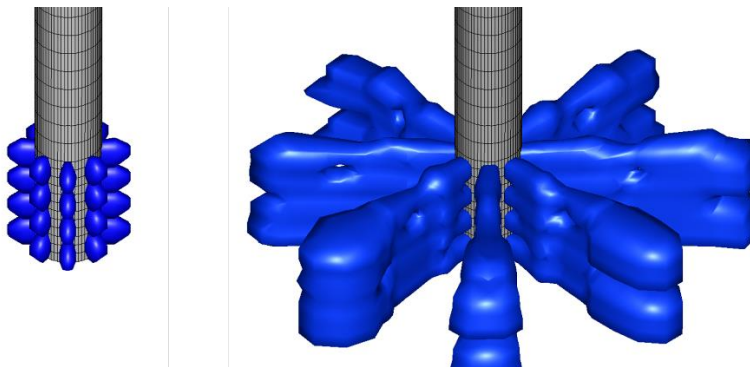


Figure 4. Source locations. Mass, momentum and enthalpy sources due to condensing steam entering the pool from sparger are described using EMS/EHS model. The original source locations are shown on the left and the extended source locations on the right.

## 6. Results

### 6.1 Comparison of predicted temperature, velocity and effective heat conduction fields

Simulated water temperatures, velocities and effective thermal conductivities of the simulations of stratification and mixing phases of the experiment are shown in Figures 5 to 7. The values are illustrated on vertical cross section of the vessel intersecting the steam pipe.

The initial state for the simulation of the SPA-T3 experiment is uniform water temperature 21 °C and stationary flow field in the vessel. During the stratification phase, the water near the

sparger and surrounding the steam pipe gets heated. It flows upward along the steam pipe toward the water surface. The predicted flow velocity remains quite low in other parts of the vessel, and no comprehensive circulation loop from top part of the vessel to the sparger level forms. Instead, some vertically stacked flow loops exist inside horizontal temperature layers. In the simulation, the water outside the pipe area gets heated from top to the sparger level presumably mostly by conduction, helped by turbulence near the pipe and in upper part of the vessel. The bottom part of the vessel remains near the initial temperature. In the end of the stratification phase, the temperature above the sparger level outside the vicinity of the pipe appears to be less uniform than in the earlier single phase simulation.

The simulated behaviour of the flow in the vessel during the mixing period using the original steam source location hardly differs from the stratification period qualitatively. The increased steam flow rate generates higher upward velocity for water along the pipe, higher temperature, and slightly more turbulence. The water layers above the sparger level get hotter but do not get mixed, and the unheated volume in the bottom area of the vessel remains nearly unchanged. This differs from observations from earlier simulation (Pättikangas, 2020), which suggests changing flow pattern and more effective mixing in the mixing phase.

The simulation of the mixing phase using extended steam source location is started from the end of stratification phase, which is calculated with the original steam source location. The extended steam source location causes the upwards directed flow to separate from the pipe and generates more turbulence, thus, mixing of the heated water volume is more efficient, resulting in more uniform temperature there, and reducing the unheated water volume in the bottom of the vessel.

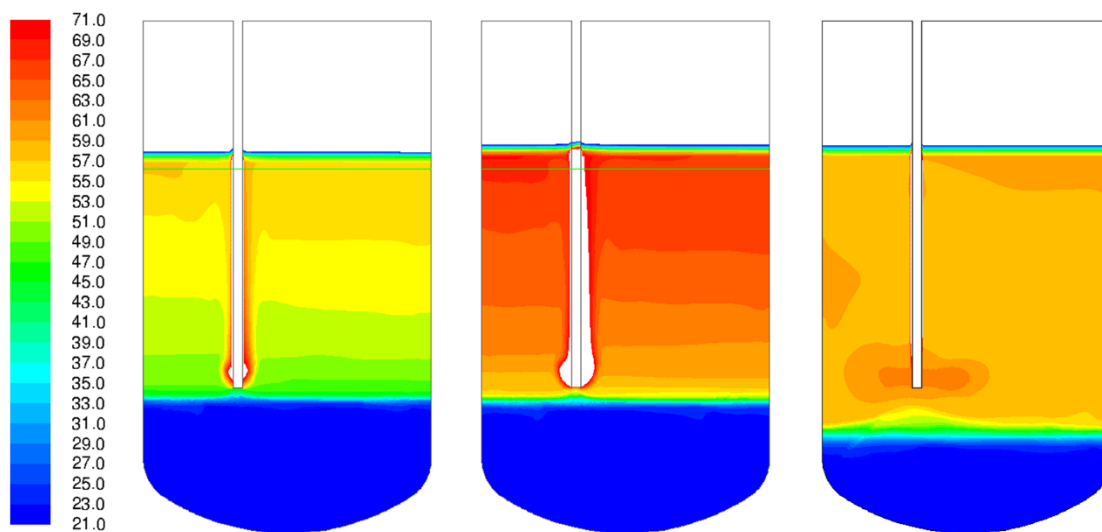


*Figure 5. Simulated water temperature (°C) in the end of stratification phase (4303 s) at left, and in the end of mixing phase (5000 s) with original steam source location (centre) as well as with extended steam source location (right).*



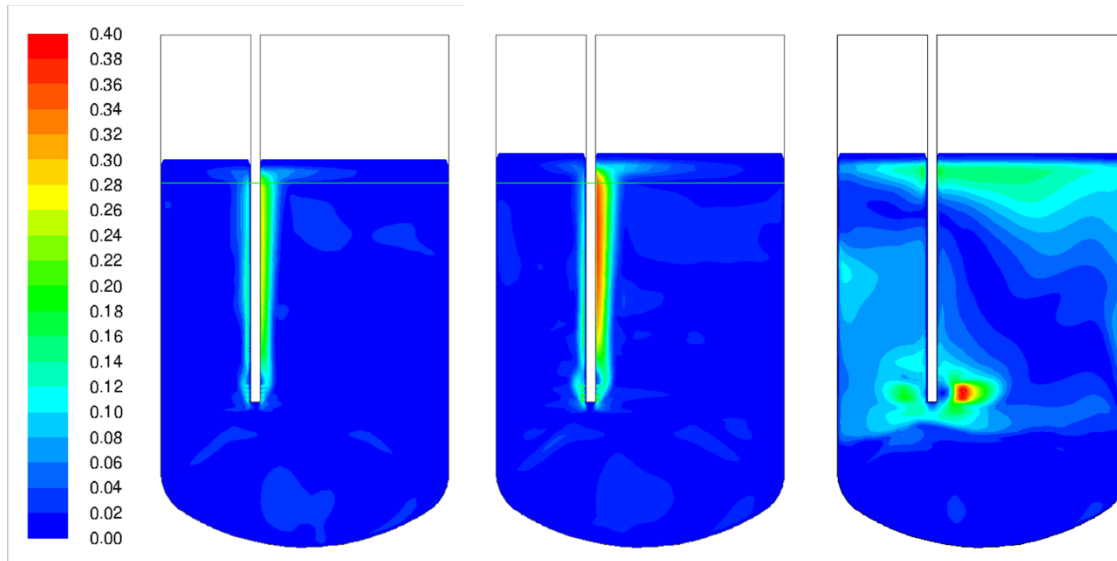


Figure 6. Simulated water velocity (m/s) in the end of stratification phase (4303 s) at left, and in the end of mixing phase (5000 s) with original steam source location (centre) as well as with extended steam source location (right).

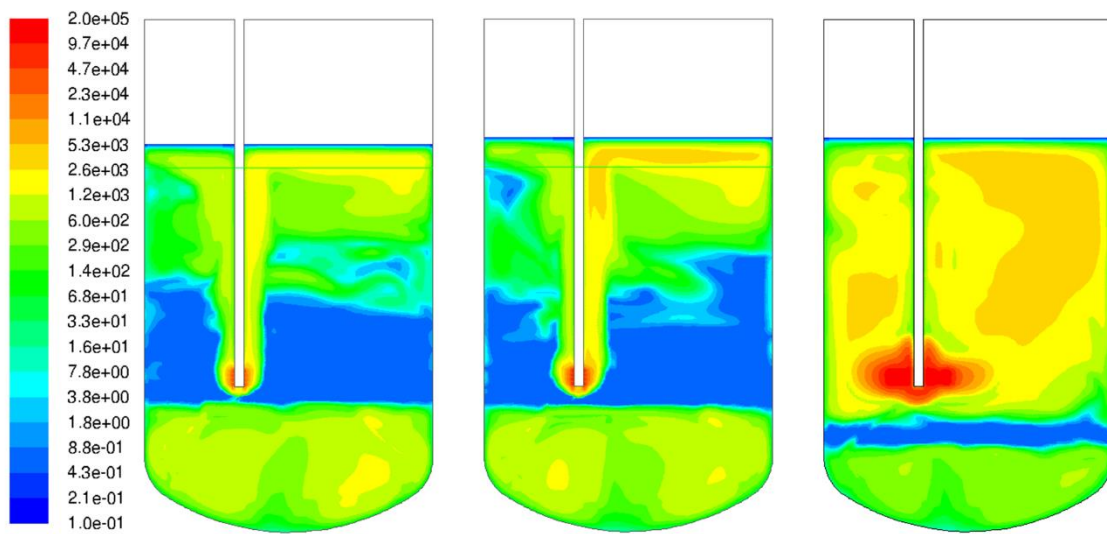


Figure 7. Simulated water effective thermal conductivity (W/m/K) in the end of stratification phase (4303 s) at left, and in the end of mixing phase (5000 s) with original steam source location (centre) as well as with extended steam source location (right).

## 6.2 Predicted water temperatures in stratification phase with original steam source location

Simulated water temperatures are shown in Figures 8 and 9 on selected vertical locations of measuring lines L1, L2, L3 and L4 of the vessel in the stratification phase of the experiment. The locations are shown in Figure 1 and Table 2. The steam source location used is shown in Figure 4 left.

Monitoring the simulated temperature changes in the vessel in more detail indicates that the temperature rise is very similar in all measuring line locations. In the upper part of the vessel, the temperature remains stratified through the stratification phase of the experiment. From

just above the sparger, at 1422 mm (monitor points T4107, T4407), to just below initial water surface at 2972 mm (T4217, T4317), the temperature increases from the initial 21 °C to about 50-56 °C.

In the lower part, the predicted temperature increases very little (1-2 °C) up to height 672 mm from the bottom (T4102, T4219, T4319, T4402). Above that at 1072 mm (T4205, T4305) the temperature increases to about 25-26 °C.

According to measurements (line L4) shown by Silde (2020), the temperature stays near the initial 21 °C below height 672 mm. At 672 mm, it increases to about 30 °C. Thus the size of the cool volume in the bottom of the vessel is somewhat overpredicted in the simulation. It also contributes to the higher simulated water temperatures in the upper part of the vessel. The measured temperatures above 672 mm rise uniformly to about 50 °C, suggesting stronger mixing in the vessel than in the simulation.

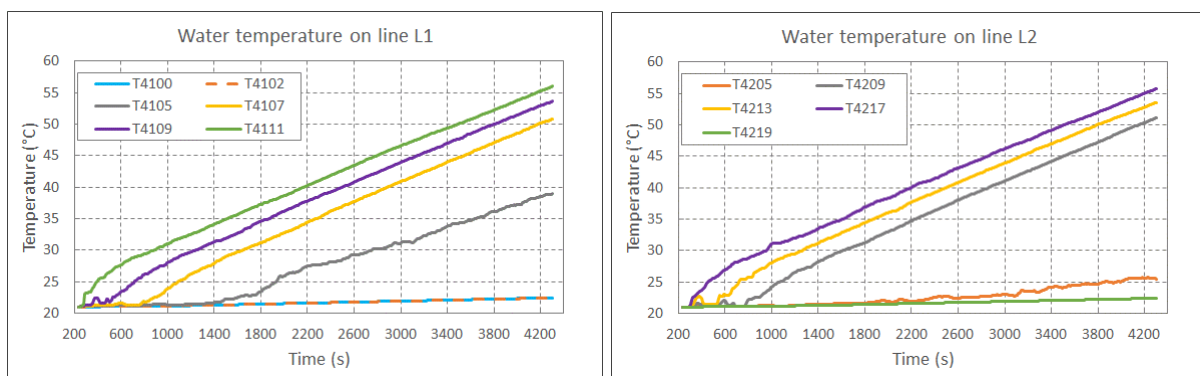


Figure 8. Simulated water temperature in stratification phase of SPA-T3 experiment from 235 to 4303 s on measuring line 1 and 2 positions.

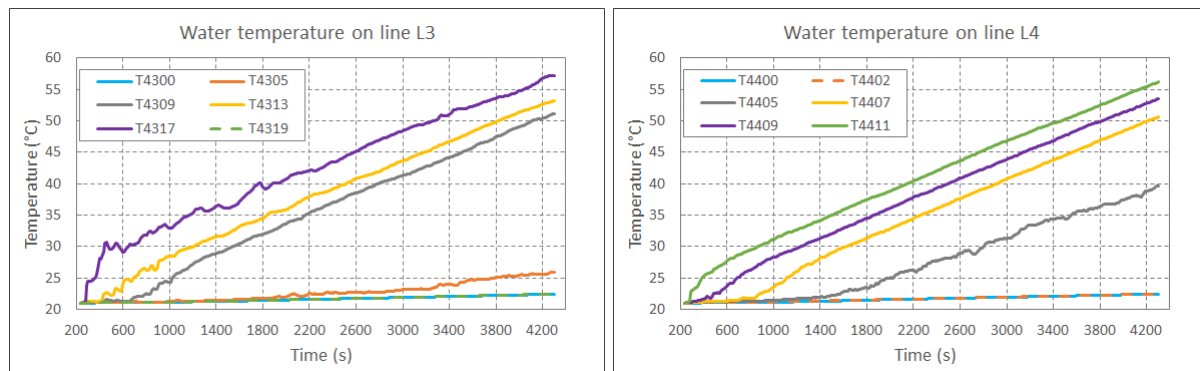


Figure 9. Simulated water temperature in stratification phase of SPA-T3 experiment from 235 to 4303 s on measuring line 3 and 4 positions.

### 6.3 Predicted water temperatures in mixing phase with original steam source location

Simulated water temperatures are shown in Figures 10 and 11 on selected vertical locations of measuring lines L1, L2, L3 and L4 of the vessel in the mixing phase of the experiment. The locations are shown in Figure 1.

The simulation results indicate that stratificated temperatures remain in the vessel through the mixing period. The temperature above the sparger in the vessel increases by about 9-10 °C to about 60-68 °C. The cool volume stays as in the stratification phase. No significant mixing takes place.

Earlier simulations (Pättikangas, 2020; Silde, 2020) and measurements suggest stronger mixing, probably by convection in the mixing phase of the experiment.

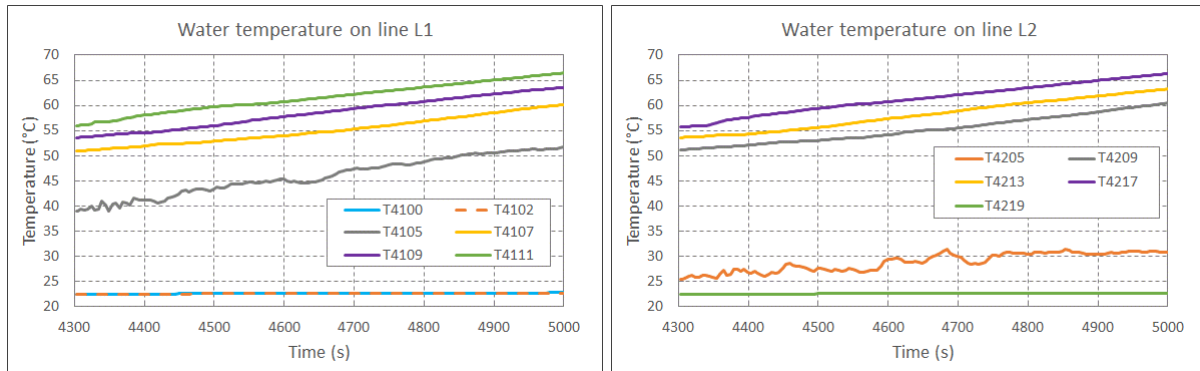


Figure 10. Simulated water temperature in mixing phase of SPA-T3 experiment from 4303 to 5005 s on measuring line 1 and 2 positions.

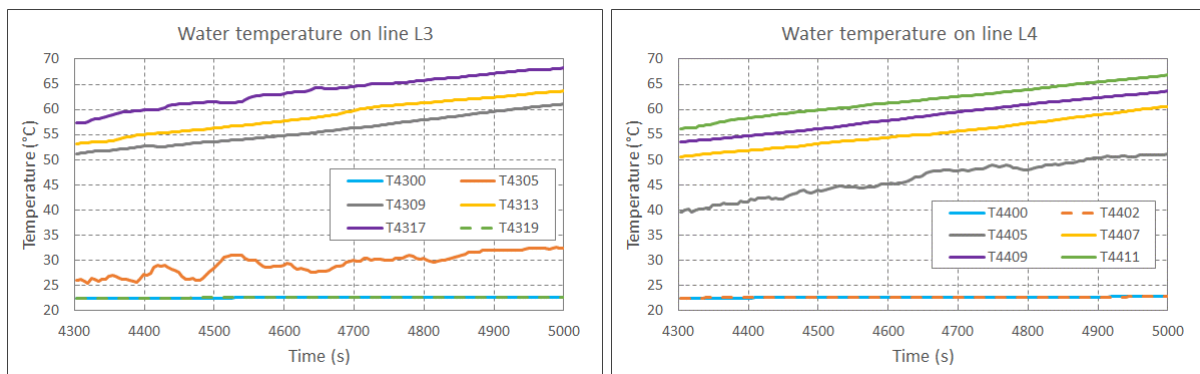


Figure 11. Simulated water temperature in mixing phase of SPA-T3 experiment from 4303 to 5005 s on measuring line 3 and 4 positions.

## 6.4 Predicted water temperatures in mixing phase with extended steam source location

Simulated water temperatures are shown in Figures 12 and 13 on selected locations of measuring lines L1, L2, L3 and L4 of the vessel in the mixing phase of the experiment. The locations are shown in Figure 1. The extended steam source location is shown in Figure 4, right.

With the extended source location in the simulation of the mixing phase, the velocity and turbulence levels increase, generating flow field which improves the mixing in the vessel above the sparger location considerably. The temperature in the mixed volume is more homogenous and the cool volume gets smaller. The final temperature in the mixed volume is about 57-60 °C. The resulting temperature field there is more in line with observations from earlier simulations and measurements.

The cool volume on the vessel bottom stays unmixed, but the location of the thermocline is lower than in the simulation with the original steam source location.



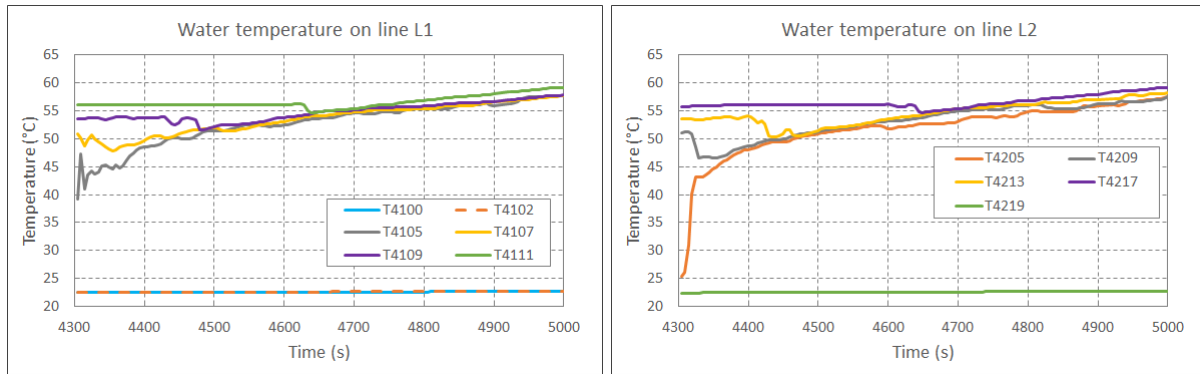


Figure 12. Simulated water temperature in mixing phase of SPA-T3 experiment from 4303 to 5005 s on measuring line 1 and 2 positions.

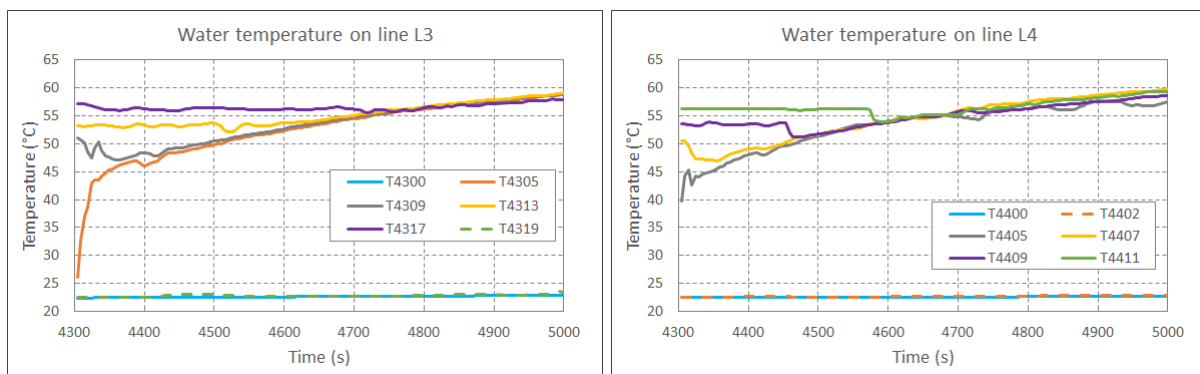


Figure 13. Simulated water temperature in mixing phase of SPA-T3 experiment from 4303 to 5005 s on measuring line 3 and 4 positions.

## 7. Conclusions and summary

The stratification and mixing phases of the SPA-T3 condensing test performed in the PPOOLEX test vessel were simulated with the CFD software ANSYS Fluent v.19.5 using the volume of fluid (VOF) model for free surface and  $k-\omega$  turbulence model. The VOF model was included to describe the water surface elevation and to improve the heat transfer on the water surface, which issues were noted in the earlier simulation (Pättikangas, 2020). The steam jets of the SPA-T3 test were modelled with the effective momentum source and the effective heat source (EMS/EHS) models, which simplify the CFD modelling task and save computational resources.

The model combination of EMS/EHS, VOF and  $k-\omega$  was combined in the ANSYS Fluent v.19.5 simulation. The simulation underpredicted the mixing of pool water to some degree. It suggested stronger stratification of temperature both in stratification and mixing phases of the experiment than observed. When the EMS/EHS source location was extended for the mixing phase simulation, the mixing improved considerably.

The weaker than expected mixing might have been caused partly by less accurate discretization schemes, which were used for convergence or compatibility reasons. For future improvements, convergence might benefit from using polyhedral grid. Also,  $k-\omega$  turbulence model may predict lower level of turbulence and thus weaker heat transfer than  $k-\varepsilon$  model used in the earlier simulation (Pättikangas, 2020). Extending the EMS/EHS source location, if necessary, could be done in more optimal way. Including heat losses from the

steam pipe to EHS model and the through the vessel wall would further improve the model, the latter by enhancing circulation from the top of the vessel to the bottom.

## References

---

- Gallero-Marcos, I. 2018. Steam condensation in a water pool and its effect on thermal stratification and mixing, Doctoral Thesis, KTH Royal Institute of technology, Stockholm, Sweden.
- Gallero-Marcos, I., Kudinov, P., Villanueva, W., Puustinen, M., Räsänen, A., Tielinen, K., Kotro, E., 2019a. Effective momentum induced by steam condensation in the oscillatory bubble regime. *Nuclear Engineering and Design* 350, 259--274.
- Gallero-Marcos, I., Kudinov, P., Villanueva, W., Kapulla, R., Paranjape, S., Paladino, D., Laine, J., Puustinen, M., Räsänen, A., Pyy, L., Kotro, E., 2019a. Pool stratification and mixing induced by steam injection through spargers: CFD modelling of the PPOOLEX and PANDA experiments, *Nuclear Engineering and Design* 347, 67--85.
- Laine, J., Puustinen, M., Räsänen, A. 2015. PPOOLEX experiments with a sparger, Nordic Nuclear Safety Research, NKS-334.
- Pättikangas, T. 2020. CFD analysis of pressure suppression pool by using effective heat and momentum source models, VTT Technical Research Centre of Finland, Research report VTT-R-00228-20.
- Silde, A. 2020. Modelling of thermal stratification in suppression pool using the Apros thermalhydraulic model, VTT Technical Research Centre of Finland, Research report VTT-R-00664-20.

Title	Thermal Hydraulic Phenomena of the Suppression Pool Summary of 2020 activities
Author(s)	Pavel Kudinov <sup>1</sup> , Xicheng Wang <sup>1</sup> , Dmitry Grishchenko <sup>1</sup> , Markku Puustinen <sup>2</sup> , Antti Räsänen <sup>2</sup> , Eetu Kotro <sup>2</sup> , Kimmo Tielinen <sup>2</sup> , Lauri Pyy <sup>2</sup> , Timo Pättikangas <sup>3</sup> , Ari Silde <sup>3</sup> , Jouni Syrjänen <sup>3</sup>
Affiliation(s)	<sup>1</sup> Division of Nuclear Engineering, Kungliga Tekniska Högskolan (KTH), <sup>2</sup> Lappeenranta-Lahti University of Technology (LUT), <sup>3</sup> VTT Technical Research Centre of Finland Ltd
ISBN	978-87-7893-542-7
Date	August 2021
Project	NKS-R / THEOS
No. of pages	242
No. of tables	23
No. of illustrations	180
No. of references	215
Abstract	<p>Effective Momentum Source and the Effective Heat Source (EMS/EHS) models for spargers are further developed using source terms, boundary conditions and “unit cell” approaches. The models implemented in Fluent and GOTHIC have been used to support design of the sparger (H2P3) and integral (H2P4) tests series in PANDA facility in HYMERES-2 project. The progress on the image analysis for post processing the data from the SEF-POOL tests is discussed.</p> <p>Steam injection tests in SEF-POOL facility at LUT University were carried out to clarify effective momentum behavior at low Mach numbers with a single and multiple hole injections. Small gas bubbles and high speed stereo imaging were used in water and steam injection tests to collect data on the jet entrainment characteristics. Also, high temporal resolution data was collected on the dynamic force measurements created by the steam injection in different regimes.</p> <p>VTT studied stratification modeling capability of Apros 1D thermalhydraulic model using pseudo-2D nodalization for the PPOOLEX SPA-T3 test. The simulations showed that (i) dense nodalisation is needed to capture the sharp stratification (ii) pool mixing phase could not be predicted reasonably without a tailored to Apros’s approach. The EMS/EHS, volume of fluid (VOF) and <math>k-\omega</math> were combined in the ANSYS Fluent v.19.5 simulation of SPA-T3</p>

test. The simulation underpredicted the mixing of pool water to some degree. When the EMS/EHS source location was extended for the mixing phase simulation, the mixing improved considerably.

Key words

Steam Condensation, Pool Stratification, Mixing, Pressure Suppression Pool, Thermal Hydraulic, BWR, Containment, CFD, GOTHIC

---

Available on request from the NKS Secretariat, P.O.Box 49, DK-4000 Roskilde, Denmark.  
Phone (+45) 4677 4041, e-mail [nks@nks.org](mailto:nks@nks.org), [www.nks.org](http://www.nks.org)